



Contribution to the design and realization of a HTS insert to obtain high magnetic field

Tara Benkel

► To cite this version:

Tara Benkel. Contribution to the design and realization of a HTS insert to obtain high magnetic field. Electric power. Université Grenoble Alpes, 2018. English. NNT : 2018GREAT009 . tel-01861261

HAL Id: tel-01861261

<https://theses.hal.science/tel-01861261>

Submitted on 24 Aug 2018

HAL is a multi-disciplinary open access archive for the deposit and dissemination of scientific research documents, whether they are published or not. The documents may come from teaching and research institutions in France or abroad, or from public or private research centers.

L'archive ouverte pluridisciplinaire **HAL**, est destinée au dépôt et à la diffusion de documents scientifiques de niveau recherche, publiés ou non, émanant des établissements d'enseignement et de recherche français ou étrangers, des laboratoires publics ou privés.

THÈSE

Pour obtenir le grade de

DOCTEUR DE LA COMMUNAUTE UNIVERSITE GRENOBLE ALPES

Spécialité : **Génie électrique**

Arrêté ministériel : 25 mai 2016

Présentée par

Tara BENKEL

Thèse dirigée par **Pascal TIXADOR**
et codirigée par **Arnaud BADEL** et **Xavier CHAUD**

préparée au sein des **Laboratoires LNCMI, INSTITUT NEEL et
G2ELAB**
dans **l'École Doctorale EEATS**

**Contribution à la conception et réalisation
d'un insert supraconducteur haute
température critique pour l'obtention de
champ magnétique intense.**

**Contribution to the design and realization
of a HTS insert to obtain high magnetic
field.**

Thèse soutenue publiquement le **16 février 2018**,
devant le jury composé de :

M. Arnaud BADEL

Chargé de Recherche, CNRS, Co-encadrant de thèse

M. Eric BEAUGNON

Professeur UGA, Président du jury

M. Marco BRESCHI

Professeur à l'université de Bologne, Rapporteur

M. Xavier CHAUD

Ingénieur de recherche, CNRS, Co-encadrant de thèse

M. Bernhard HOLZAPFEL

Directeur IMS, l'Institut Technologique de Karlsruhe (KIT), Rapporteur

M. Pascal TIXADOR

Professeur Grenoble-INP, Directeur de thèse

M. Pierre VEDRINE

Ingénieur docteur, chef du département DACM, CEA Saclay, Examineur



ACKNOWLEDGEMENT - REMERCIEMENTS

Firstly, I would like to kindly thank my PhD supervisor Pascal Tixador who was always open for discussion and ready to help whenever I needed it. I also thank my two supervisors Arnaud Badel and Xavier Chaud for sharing their knowledge and never saying no for extra hours of work together. I thank all of them for the opportunities they gave me during these three years.

I would like to warmly thank my thesis committee, Eric Beaugnon, the president of the jury, Marco Breschi and Bernhard Holzapfel, the two examiners of my manuscript and Pierre Vedrine. I thank you for your interest in my work and for all the interesting questions we discussed.

I would like to thank the team from CEA, Saclay as I had the chance to work with Thibault Lecrevisse and Philippe Fazilleau. It has been very instructive to wind the coil with Thibault as well as the experiments under high field.

I am also grateful for Prof. Awaji and his team for the warm welcome and the help with the experiments in Sendai, Japan.

I also thank everyone for the useful discussions during all the seminars, conferences and summer schools I attended. It was always interesting to share experiences and knowledge.

Je tiens également à remercier plusieurs personnes qui ont contribué à la réussite de mon travail, au sein des différents laboratoires où j'étais rattachée.

Merci aux équipes de l'Institut Néel notamment à Julien et à Thibaut pour leur aide toujours apportée avec humour et merci à Anne, Elodie et Christiane.

Merci aux équipes du G2eLab, plus particulièrement à Blandine qui a rendu la fin de cette thèse tellement agréable sans oublier Quentin et Max. Merci aussi à Nico qui a été stagiaire dans notre équipe et d'une grande aide.

Merci aux équipes du LNCMI pour la bonne ambiance de travail. Merci à Claude pour avoir toujours pris le temps de me donner de nombreux conseils avisés. Merci à Rémi, Julien et Théo pour leur constante aide et bonne humeur et aussi à Manon, Julia et Xavier qui ont été stagiaires dans notre équipe. Merci à Benjamin pour m'avoir donné le goût de la recherche lors de mon stage précédent et d'avoir toujours pris le temps de suivre de près ou de loin mon travail. Merci chaleureusement à Natacha, Dominique, Alexandra et Amélie qui m'ont épaulée jusqu'au dernier moment. Merci à Isa et Cécile pour nos échanges et leur soutien.

Enfin, merci particulièrement à mes proches pour leur soutien inconditionnel.

CONTENTS

ACKNOWLEDGEMENT - REMERCIEMENTS	2
CONTENTS	3
LIST OF FIGURES	9
RESUME DE LA THESE EN FRANÇAIS	16
1.1 Introduction et contexte	16
1.1.1 Supraconductivité	16
1.1.2 Les matériaux supraconducteurs	16
1.1.3 Les conducteurs de type TRBCO	17
1.1.3.1 Composition générale	17
1.1.3.2 Comportement mécanique	17
1.1.3.3 Propriétés anisotropiques	18
1.1.3.4 Inhomogénéité du conducteur	18
1.1.3.5 Stabilité thermique	19
1.1.4 Utilisations des conducteurs TRBCO	20
1.1.5 Les aimants à champ magnétique intense	20
1.1.5.1 Les électro-aimants	20
1.1.5.2 Les technologies actuelles d'aimants	21
1.1.5.3 Aimants SHTC et projet NOUGAT	22
1.1.5.4 Différentes techniques de bobinage	22
1.1.6 Objectifs de la thèse	23
1.2 Caractérisation d'échantillons courts supraconducteurs	23
1.2.1 Objectifs de la caractérisation	23
1.2.2 Présentation du banc de mesure	24
1.2.3 Résultats expérimentaux	25
1.2.4 Relation $E(J)$	26
1.2.5 Interpolation des résultats	27
1.2.6 Conclusion intermédiaire	28
1.3 Modèle numérique de transition d'aimants SHTC	28
1.3.1 Objectifs du modèle	28
1.3.2 Description du modèle d'origine	29
1.3.3 Améliorations nécessaires pour simuler le comportement d'un aimant SHTC	29
1.3.4 Fonctionnement du modèle d'étude de transition d'aimant	30
1.3.5 Détails des modifications apportées au modèle de limiteur	31
1.3.5.1 Détails de la géométrie	31
1.3.5.2 Evaluation des composantes de champ	32
1.3.5.3 Introduction des échanges thermiques	33
1.3.6 Résultats d'une simulation type	34
1.3.7 Conclusion sur le modèle	36
1.4 Etudes expérimentales de bobines sous champ magnétique intense	36
1.4.1 Premiers tests d'aimant : double galette isolée	36

1.4.1.1	Objectifs : étudier des comportements mécanique et magnétique de la bobine -----	36
1.4.1.2	Description de la bobine -----	37
1.4.1.3	Protocole et résultats expérimentaux -----	38
1.4.2	Simple galette instrumentée -----	40
1.4.2.1	Objectifs : étudier le commencement de transition et sa propagation dans le bobinage -----	40
1.4.2.2	Description de la bobine -----	40
1.4.2.3	Protocole et résultats expérimentaux -----	42
1.5	Conclusion -----	45

1	INTRODUCTION AND CONTEXT -----	47
1.1	Superconductors: General knowledge -----	48
1.1.1	First steps in superconductivity -----	48
1.1.1.1	Discovery of superconductivity -----	48
1.1.1.2	Discovery of High Temperature Superconductors (HTS) -----	48
1.1.1.3	Critical surface -----	49
1.1.1.4	Two types of superconductors -----	50
1.1.2	First approach on HTS-specific properties -----	52
1.1.2.1	REBCO in details -----	52
1.1.2.2	Improvement in HTS tapes over the years -----	54
1.1.2.3	Inhomogeneity along the length -----	55
1.1.2.4	Thermal stability -----	56
1.1.3	Quick overview of large scale applications -----	57
1.2	Magnet technology -----	58
1.2.1	Electromagnet -----	58
1.2.2	DC field utility -----	59
1.2.3	Already existing technologies -----	59
1.2.3.1	Resistive magnets -----	59
1.2.3.2	LTS magnets -----	59
1.2.3.3	Hybrid magnets -----	60
1.2.4	Inductance and coupling -----	60
1.2.5	HTS magnets -----	61
1.3	NOUGAT project and other main HTS projects around the world -----	62
1.3.1	Quick overview of the projects around the world -----	62
1.3.1.1	Full HTS magnet -----	62
1.3.1.2	Hybrid magnet: HTS Insert in a LTS background -----	63
1.3.1.3	Hybrid magnet: HTS Insert in a resistive background -----	64
1.3.2	The NOUGAT project -----	64
1.3.2.1	Objectives -----	65
1.3.2.2	Main constraints -----	65
1.4	General knowledge about HTS coils -----	66
1.4.1	Winding techniques: layer wound and pancake wound coils -----	66
1.4.2	Conductor width -----	67
1.4.3	Manufacturers -----	67
1.4.4	Winding technique: insulated coil -----	67

1.4.4.1	Field stability	68
1.4.4.2	Quench and damages	68
1.4.4.3	Detection and protection	68
1.4.5	Winding technique: Non-insulated coil	70
1.4.5.1	Self-protection	70
1.4.5.2	Stability	70
1.4.5.3	Long-time constants	71
1.4.6	Winding technique: Metallic insulated coil	72
1.4.6.1	Intermediate solution	72
1.4.6.2	Self-protection	73
1.4.7	Mechanical behaviours of REBCO insert coils	73
1.4.8	Conclusion	74
1.5	Objectives of the thesis	74
1.5.1	Thesis orientation	74
1.5.2	Objectives of the thesis	74
2	YBCO TAPE CHARACTERIZATION UNDER HIGH FIELD WITH VARYING ORIENTATION	76
2.1	HTS coil: Design inputs, magnetic behaviour and limiting critical current evaluation	77
2.1.1	Outer field	77
2.1.1.1	Introduction of the field homogeneity	77
2.1.1.2	Calculation of the 20 T background field homogeneity	78
2.1.2	Field generated by the HTS insert	79
2.2	Geometry optimization of HTS insert coils	80
2.2.1	The tape thickness	80
2.2.2	Influence of the geometry on the operating current density	80
2.2.3	Homogeneity of the field: notch	82
2.2.4	Extrapolation of the I_c measured on short samples and insert	83
2.2.5	Geometry optimisation to reduce the transverse field	85
2.2.6	Conclusion: presentation of the selected model for the next paragraphs	88
2.3	Intermediate conclusion	88
2.4	The importance of a systematic characterization	89
2.4.1	Data on the conductor performance given by the providers	89
2.4.1.1	Critical current inhomogeneity along the conductor length	89
2.4.1.2	Critical current measurements extrapolation from 77 K to 4.2 K	91
2.4.2	Anisotropic property: angular dependency	92
2.5	Short sample experimental study description	94
2.5.1	Experimental measurement objectives	94
2.5.2	Experimental workbench for short sample characterization	94
2.5.2.1	Dedicated measurement probe	94
2.5.2.2	Details of the sample holder setup on the extremity of the measurement probe	96
2.5.3	Experiment specificity: full width conductor study	97
2.5.4	Main challenges and problems encountered during experiment	98
2.6	Experimental results	99
2.6.1	Quench model: power law	99
2.6.2	SuperOx short sample characterization	99

2.6.2.1	Tape composition and TapeStar	99
2.6.2.2	Experimental results: $J_c(B, \theta)$	100
2.6.2.3	n values	101
2.6.3	SuperPower short sample characterization	102
2.6.3.1	Tape composition	102
2.6.3.2	Experimental results	103
2.6.4	Performance comparison between SuperOx and SuperPower conductors	104
2.6.4.1	Lift factor and critical current quotient comparison	104
2.6.4.2	Critical current according to the temperature	105
2.7	Extrapolation of the missing data for numerical model implementation	105
2.7.1	Extrapolation using the Kim model using the B module	106
2.7.2	Extrapolation using the Kim model generalized formula	106
2.8	Conclusion	107
3	MAGNET COIL MODEL, FIRST SIMULATIONS	109
3.1.	Objectives of the model	110
3.2	An already existing model for fault current limiter	110
3.2.1	Main description and aims of the original FCL model	110
3.2.2	Necessary improvements to adapt the model to magnets	111
3.3	Electric circuit	111
3.3.1	Main modifications from the original FCL model	111
3.3.2	Calculation of the two operating phases	111
3.4	Definition of the wound coil geometry	112
3.4.1	Critical current measurements at 77 K, self-field	112
3.4.2	Definition in the winding of the block location along the length of the conductor	114
3.4.3	Discretization along the width	116
3.5	Definition of the magnetic behaviour	116
3.5.1	Background field	116
3.5.2	Field generated by the coil according to the current passing through it	116
3.5.3	Field components according to the position on the mesh	117
3.6	Current distribution between the superconductive layer and the resistive layers of the wound conductor	118
3.6.1	Critical current calculation on a block	118
3.6.2	Current sharing on a block	118
3.6.2.1	Details of the current distribution calculation	118
3.6.2.2	Original FCL model calculation for current distribution	119
3.6.2.3	Current distribution calculation in the magnet quench model	120
3.6.2.4	Proof a unique real positive solution in each case	121
3.6.2.5	Resolution and seek of the unique real positive solution	122
3.7	Implementation of the thermal behaviour study	122
3.7.1	1D thermic model: heat propagation along the length of the conductor	122
3.7.2	2D-thermic model: propagation along the length and the turns	124

3.8	Tests and sensitivity studies	126
3.8.1	Simulation example	126
3.8.1.1	General results presentation	126
3.8.1.2	Results comparison	128
3.8.2	Influence of the electric time step	129
3.8.3	Influence of the current ramp time rate	129
3.8.4	Constant performance of the conductor versus inhomogeneity	131
3.8.4.1	Different initial I_c at 77 K, self-field	131
3.8.4.2	Influence on the critical current	132
3.8.5	Influence of the number of blocks and the number of subdivisions of a block width	133
3.8.5.1	Influence of the number of blocks	133
3.8.5.2	Influence of the number of subdivisions in a block width	133
3.8.5.3	Conclusion	134
3.8.6	Influence of the n value	134
3.8.7	1D propagation versus 2D propagation	135
3.8.8	Conclusion	137
4	EXPERIMENTAL STUDY OF WOUND SAMPLES UNDER HIGH FIELD	139
4.1	Insulated coil: magnetic and mechanical behaviour and coupling issues	140
4.1.1	First coil objectives: study of a 4 mm DP insulated coil	140
4.1.2	Description of the insulated double pancake coil: fabrication and instrumentation	140
4.1.2.1	Double pancake coil fabrication	140
4.1.2.2	Instrumentation	142
4.1.2.3	Experimental protocol	142
4.1.3	Magnetic behaviour	143
4.1.4	Mechanical behaviour of the insulated double pancake coil	143
4.1.5	Coupling issues	144
4.1.6	Experimental results: electrical behaviour	146
4.1.6.1	Double pancake coil: calculation of the limiting critical current	146
4.1.6.2	Limiting critical current calculation and experimental coil performance	147
4.1.6.3	Another limiting critical current evaluation method while ramping the current inside the coil and taking into account the inhomogeneity along the conductor	148
4.1.7	Conclusion	149
4.2	Insulated coil: detailed study of the transition inside a wound sample in high field	149
4.2.1	Objective of the coil	149
4.2.2	Coil description: 6 mm SP insulated coil	150
4.2.2.1	Fabrication	150
4.2.2.2	Instrumentation	151
4.2.2.3	Experimental protocol	152
4.2.3	Noise level improvement	153
4.2.3.1	Experimental protocol	153
4.2.3.2	Comparison with and without NCC	153
4.2.4	Electrical behaviour	154
4.2.4.1	Definition of the coil working limitation	154
4.2.4.2	Extrapolation and comparison to calculation	155
4.2.4.3	Results: propagation along the turns	156
4.2.5	Comparison between experimental results and simulation	158
4.2.5.1	Comparison between model and experimental coil performance study: calculation of the critical current of the coil taken as the average value on the width of the conductor	158

4.2.5.2	Comparison between model and experimental coil performance study: calculation of the critical current of the coil taken as the minimum value of the width of the conductor	159
4.2.5.3	Comparison between model and experimental transition in a single pancake coil	160
4.2.6	Conclusion on the fully instrumented insulated single pancake	162
4.3	Intermediate conclusion on insulated coils	162
4.4	Comparison with a MI coil behaviour	163
4.4.1	6 mm SP MI coil	163
4.4.1.1	Objectives	163
4.4.1.2	Details of the coil	163
4.4.1.3	Instrumentation	165
4.4.2	Field coefficient	165
4.4.3	Coupling issues	167
4.4.4	MI coil behaviour	167
4.5	Conclusion	170
4.5.1	Summary	170
4.5.2	Assembly improvements	170
4.5.3	Chapter conclusion	171
5	CONCLUSION	172
6	APPENDIX	175
6.1	Proof of the unique real positive solution	175
6.1.1	Case with n is even	175
6.1.2	Case with n is odd	177
6.2	Material properties implemented in the model	178
6.2.1	Density	178
6.2.2	Specific heat capacity	178
6.2.3	Thermal conductivity	179
6.2.4	Resistivity	179
REFERENCES		180

LIST OF FIGURES

Fig. 1. Allure des résistances d'un métal ordinaire et d'un supraconducteur selon la température, ne respecte pas l'échelle.	16
Fig. 2. Illustration de la surface critique, ne respecte pas l'échelle.	16
Fig. 3. Schéma non à l'échelle d'une coupe de conducteur SuperOx, inspiré par [1].	17
Fig. 4. Angle d'incidence créée par la surface du conducteur en bleu et l'axe du champ magnétique extérieur en rouge.	18
Fig. 5. Résultats expérimentaux de SuperOx [8] : courant critique à 77 K sous 1 T pour trois différents conducteurs selon l'orientation du champ magnétique extérieur.	18
Fig. 6. Courant critique évalué à 77 K, en champ propre d'un ruban REBCO de 4 mm, fourni par SuperOx.	19
Fig. 7. Performance des conducteurs TRBCO en fonction du champ magnétique extérieur, données SuperOx [8].	20
Fig. 8. Schéma descriptif d'un électro-aimant.	21
Fig. 9. Distribution du champ magnétique (T) sur le quart en haut à droite de la coupe de l'aimant final. Elle prend en compte le champ magnétique généré par l'insert délimité par des traits noirs continues et celui généré par l'aimant extérieur résistif situé à droite de la ligne noire pointillée.	23
Fig. 10. Schéma d'une canne de mesure et son instrumentation.	24
Fig. 11. Support de l'échantillon. (a) : vue de côté. (b) : vue de haut. (c) Schéma d'explication.	25
Fig. 12. Mesure de tension sur un échantillon SuperOx de largeur 4 mm sous 8 T et un angle de 10° entre la surface du ruban et l'axe du champ magnétique extérieur.	25
Fig. 13. Courants critiques évalués selon l'orientation du champ magnétique extérieur pour différentes intensités de champ.	26
Fig. 14. Indice de la loi de puissance en fonction du champ magnétique extérieur, évalué pour différentes orientations de champ.	27
Fig. 15. Interpolation des valeurs de courants critiques mesurées expérimentalement, selon le champ magnétique extérieur et différentes orientations.	28
Fig. 16. Schéma explicatif avec détails des étapes de calcul lors d'un pas de temps t du modèle.	30
Fig. 17. Illustration de la découpe de la longueur de ruban utilisée pour le bobinage TRBCO étudié.	31
Fig. 18. Courant critique à 77 K en champ propre le long du ruban TRBCO. Les mesures fournies par le constructeur sont en bleu, les blocs du modèle sont délimités par les traits noirs pointillés et la valeur de I_c de chaque block est en rouge, il s'agit de la moyenne des valeurs du fournisseurs sur le même intervalle.	31
Fig. 19. Schéma d'un bobinage de galette simple avec en rouge la vue de dessus.	32
Fig. 20. Vue de dessus d'une galette simple avec les spires représentées par des cercles concentriques.	32
Fig. 21. Illustration de la géométrie en spirale.	32
Fig. 22. Résultat de la géométrie en spirale avec Matlab.	32
Fig. 23. Figure haute : Illustration de la vue de côté du bobinage d'une galette simple. Figure basse : Distribution de la composante parallèle du champ magnétique appliqué sur une simple galette, quart en haut à droite de la coupe de l'aimant TRBCO étudié.	33
Fig. 24. Illustration de la propagation 2D avec COMSOL.	34
Fig. 25. Courant et champ magnétique au centre de la galette en fonction du temps.	35
Fig. 26. Tension de la bobine entière ainsi que les tensions de chaque partie de la galette lorsqu'elle est divisée en six parties, selon le courant passant dans le conducteur.	35
Fig. 27. Propagation de la chaleur sur plusieurs blocs du bobinage, selon le temps.	36
Fig. 28. (a) Photographie de l'assemblage de la double galette isolée avant frettage. (b) Photographie prise pendant le bobinage avec une moitié du bobinage enroulée sur le satellite.	37
Fig. 29. Rampe de courant dans la double galette isolée avec un champ magnétique extérieur de 8 T.	39
Fig. 30. Mesures des sondes (bleu, mauve, noir) comparé aux valeurs de simulation (rouge pointillé) pour un courant atteignant 125 A sous 8 T.	40
Fig. 31. Photographie de la simple galette instrumentée avant frettage.	41
Fig. 32. Schéma explicatif de l'assemblage de la simple galette et son instrumentation.	41

Fig. 33. Position des prises de potentiel dans le bobinage de la simple galette TRBCO.	42
Fig. 34. Schéma explicatif de la simple galette isolée TRBCO donnant la position des sondes de température de type Cernox.	42
Fig. 35. Illustration du protocole expérimental pour une champ magnétique extérieur de 19 T, le courant à l'intérieur de l'aimant TRBCO atteint 300 A. La courbe noire est la mesure du champ magnétique au centre du conducteur bobiné. La courbe rouge envoie la valeur du courant passant dans le conducteur TRBCO. Le graphique encadré en bas à droite est un zoom de l'étape 2.	43
Fig. 36. Transition des premières spires sous un champ magnétique extérieur de 17 T, 250 A passant dans le conducteur.	43
Fig. 37. Températures obtenues lorsque les six premiers tours de la bobine TRBCO atteignent le seuil de tension arbitraire, selon le champ magnétique extérieur et le courant passant dans le conducteur bobiné.	44
Fig. 38. Résultats expérimentaux obtenus sur la simple galette TRBCO instrumentée. Il s'agit des températures obtenues lorsque le seuil de détection en tension est atteint sur les six premiers tours du bobinage pour un champ magnétique extérieur donné et un certain courant parcourant le conducteur.	44
Fig. 39. Courant critique limitant à 4,2 K de la simple galette évalué numériquement (traits continus en rouge et noir) comparé à l'extrapolation des résultats expérimentaux.	45

Fig. 40. Trend of the resistance behaviour for a non-superconductive metal compared to the resistance of a superconductor according to the temperature, not to scale.	48
Fig. 41. Superconductor critical temperature as a function of their year of discovery [2].	49
Fig. 42. Transition of a 4 mm tape provided by SuperOx, at 4.2 K under 8 T.	50
Fig. 43. HTS and LTS critical surface trends, not to scale.	50
Fig. 44. Temperature dependence of the critical fields for type-II superconductor, taken from [3].	51
Fig. 45. Irreversibility line for various type-II materials, from [4].	51
Fig. 46. Not to scale cut of a SuperOx layer according to [13].	52
Fig. 47. Delaminated conductor after experimental study.	53
Fig. 48. Incident angle created by the tape surface in blue and the background field axis in red.	53
Fig. 49. Experimental results from SuperOx [24] showing critical current according to the field intensity and its orientation.	54
Fig. 50. Advancements in REBCO technology according to the years taken from [25].	54
Fig. 51. Critical current improvement multiplied by the conductor length over the years from [26].	55
Fig. 52. I_c measurement data at 77 K, self-field for a 4 mm SuperOx coated conductor.	56
Fig. 53. SuperOx data: critical current factor according to background field and temperature [24].	58
Fig. 54. Sketch of an electromagnet, [45].	58
Fig. 55. Critical current density of commercialized superconductors at 4.2 K according to the magnetic field, taken from [56].	61
Fig. 56. (a) Picture of the completed magnet after final assembly. (b) to-scale drawing of the final DP coil assembly, [57].	63
Fig. 57. Cross section of the 20 T resistive magnet, the copper magnet is shown in red.	66
Fig. 58. Quarter of the cross section of the background field distribution. The inner diameter of the resistive magnet is shown by the dotted black line.	66
Fig. 59. Layer wound coil, taken from [67].	67
Fig. 60. Wound pancake coil.	67
Fig. 61. The two ways of pancake windings; (a) 'cross-over' from one pancake to the other and (b) which is soldered wire, taken from [70].	67
Fig. 62. Temperature and time limits for protection, taken from [79].	69
Fig. 63. Illustration of a hot spot in a non-insulated winding.	70
Fig. 64. Overcurrent test results of a REBCO coil up to 125 A. Black squares : power supply current; blue circles: axial field at the centre; red triangles: coil voltage, taken from [87].	71
Fig. 65. Deviation of the maximum magnetic field from linearity based on 20 A test results, taken from [74].	71

Fig. 66. Results of the sudden-discharge tests at 60 A, taken from [74].	72
Fig. 67. Illustration of a hot spot in case of a MI winding.	73
Fig. 68. Cross section quarter of the background field distribution. The inner diameter of the resistive magnet is shown by the dotted black line and the REBCO insert sketch is defined by the continuous black line.	75
Fig. 69. Trend of the magnetic field generated by the HTS insert; the green line underlines the shape of the insert and the tilled black line the cross-section, which is studied. For the calculation, the inner and outer radius are respectively taken as 60 mm and 110 mm. The height is 150 mm and the current density is 365 A/mm ² to generate 10 T in the centre of the solenoid.	77
Fig. 70. Magnetic field distribution generated by the outer resistive magnet at LNCMI; the outer magnet is defined by the black tilled line and the green tilled line underlines the space inside the magnet for experiment under high field.	78
Fig. 71. Deviation of the field in the centre of the magnet according to the height.	79
Fig. 72. Deviation of the field components on a sphere according to a given radius.	79
Fig. 73. Standard deviation of the parallel field B_z .	79
Fig. 74. Transverse field B_r .	79
Fig. 75. Magnetic field generated by the insert and the outer, the current density is 365 A/mm ² .	80
Fig. 76. Current density in A/mm ² necessary to reach 10 T according to the inner and outer diameter of the insert with a height of 120 mm.	81
Fig. 77. Nominal current density to reach 10 T in the centre of the insert according to the outer diameter and the inner diameter for a height of 150 mm.	81
Fig. 78. Nominal current density to reach 10 T in the centre of the insert according to the outer diameter and the inner diameter for a height of 150 mm.	81
Fig. 79. Notch configuration.	82
Fig. 80. Deviation of the magnetic field (T) on the height of the insert.	82
Fig. 81. Current density (A/mm ²) needed to generate 10 T in the coil centre according to the notch geometry.	83
Fig. 82. B module (T) generated by the insert. In standalone	85
Fig. 83. Transverse field (T) generated by the insert in standalone.	85
Fig. 84. Critical current (A) evaluated on the cross section in standalone.	85
Fig. 85. Module of the addition of the background field and field generated by the insert.	85
Fig. 86. Transverse field component when background field added to self-field.	85
Fig. 87. Critical current evaluated on the cross section according to the field components.	85
Fig. 88. Module of the magnetic field on a cross-section of the insert.	86
Fig. 89. Transverse component of the field on a cross-section of the insert.	86
Fig. 90. Transverse component of the field to underline the distance between the pancakes on the edges of the winding.	87
Fig. 91. Transverse field according to the total height and the edges geometry.	87
Fig. 92. Transverse component of the field (T) on the cross-section of the optimized insert, in self-field.	88
Fig. 93. Transverse component of the field (T) on the cross-section of the optimized insert, under 20 T background field.	88
Fig. 94. Critical current evaluated on the whole cross-section of the optimized insert in background field.	88
Fig. 95. Critical current distribution in a typical HTS tape produced at SuperOx [®] along the length measured by a TapeStar [™] device (the reference standard measurement machine fabricated and sold by THEVA) [13], at 77 K, self-field.	90
Fig. 96. Critical current as a function of position at 77 K in several (a) older (2010-2012) and (b) newer (2013-2014) 4-mm wide coated conductor tapes [111].	90
Fig. 97. (a) B dependence of I_c at 77 K for commercial conductors in perpendicular field. (b) B dependence of I_c at 4.2 K for commercial conductors in perpendicular field [116].	91
Fig. 98. J_c of the REBCO layers measured at 4.2 K, 19 T perpendicular field, versus J_c of the same layers measured at 77 K, self- field for six different manufactures. AMSC, BHTS stand respectively for American Superconductor, Brucker HTS [117].	92
Fig. 99. Angular dependency of a 4 mm SuperPower tape [118]. In this graph, 90° is used for parallel field and 0° for perpendicular field.	93

Fig. 100. Critical current measurements for three different 4-mm SuperPower conductors, [118].	93
Fig. 101. Voltage measurement for 1 cm on a short 4 mm SuperOx sample obtained under 8 T and an angle of 10°. E_c is the electric field defined as threshold in V/cm to evaluate the critical current of the conductor under these conditions.	94
Fig. 102. Cryostat draft and measurement probe photographs for high field experiment in helium bath. (a) is the whole measurement probe, (b) is its top part, (c) is its bottom part and (d) is a draft of the cryostat.	95
Fig. 103. Instrumentation set up along the measurement probe.	96
Fig. 104. (a) is the view from the side of the extremity of the probe, where the sample is placed, underlining the rotating part. (b) is a view from the top of the extremity of the probe. (c) is a draft to better understand how the sample is set up exactly on the workbench.	97
Fig. 105. Critical current measurements given by the provider at 77 K, self-field.	100
Fig. 106. Critical current value according to the intensity and the orientation of the background magnetic field applied on the tape.	101
Fig. 107. Power factor values according to the magnetic field intensity and orientation.	102
Fig. 108. n -value vs. B for commercial conductors in perpendicular fields at 4.2 K, taken from [116].	102
Fig. 109. Critical current measurement of a 6 mm SuperPower conductor at 4.2K, under magnetic field up to 23 T.	103
Fig. 110. Lift factors comparison of SuperPower and SuperOx experimental data.	104
Fig. 111. SuperPower tape difference from SuperOx tape.	105
Fig. 112. Critical current according to the temperature of two conductors provided by two different providers, self-field.	105
Fig. 113. Lift factor according to the temperature of two conductors provided by two different providers, self-field.	105
Fig. 114. Extrapolation of the critical current of a 4 mm SuperOx coated conductor according to the field intensity and orientation using the Kim model.	106
Fig. 115. Extrapolation of the critical current of a 4 mm SuperOx coated conductor according to the field intensity and orientation using the generalized Kim model.	107
Fig. 116. Illustration of the electric circuit.	111
Fig. 117. Illustration of the length study of the conductor for a single pancake coil.	113
Fig. 118. Critical current values given at 77 K, self-field along the length of the conductor provided by SuperOx, see section 1.5.2.3.	113
Fig. 119. Critical current measurement at 77 K, self-field according to the length of the conductor. The measurements provided by the manufacturers are in blue, the blocks are delimited by the dotted black lines and the average of the provider I_c value on the blocks are in red.	114
Fig. 120. View from the top of the magnet coil.	114
Fig. 121. When the winding is defined by concentric rings with the thickness of the conductor.	115
Fig. 122. Illustration of the creation of the geometry.	115
Fig. 123. Illustration of the block coordinates.	115
Fig. 124. Illustration of the definition of a block subdivision along the width.	116
Fig. 125. Evaluation of the component B_z of the magnetic field on each block according to their coordinates on the cross-section of the winding.	117
Fig. 126. Illustration of the cross-section for which the field components are studied on a single pancake winding.	118
Fig. 127. Example of an experimental measurement to determine I_c .	119
Fig. 128. Illustration of the subdivision of the length of the conductor into blocks underlining the layers of the tape.	119
Fig. 129. Electric circuit of the current sharing between the superconductive layers and the other layers.	120
Fig. 130. Illustration of $xn = a(1 - x)$. The dotted green lines underline the minimum and the maximum value of the solution.	122
Fig. 131. 1D heat propagation along the length of the conductor.	122
Fig. 132. Description of the model using the 1D heat propagation.	124
Fig. 133. Illustration of the 2D heat propagation model using COMSOL.	124

Fig. 134. Description of the model using COMSOL for a 2D heat propagation. _____	125
Fig. 135. Current and magnetic field inside recorded in the centre of the sample according to time. _____	127
Fig. 136. Voltage of the full coil and voltages of different part of the winding, according to the current. _____	127
Fig. 137. Heat propagation on some block of the winding, according to time. _____	128
Fig. 138. Limiting critical currents plotted according to the background field for two different voltage thresholds. _____	128
Fig. 139. Propagation of the transition inside the winding when the coil is studied in self-field. _____	129
Fig. 140. Propagation of the transition inside the winding when the coil is studied in a 20 T background field. _____	129
Fig. 141. Influence of the time step on the limiting critical of the coil for different voltage threshold. _____	129
Fig. 142. Full coil voltage measurement for different current ramp rate. _____	130
Fig. 143. Temperatures of the blocks when the voltage threshold is reached. _____	130
Fig. 144. Estimation of the critical current according to the current ramp rate. _____	131
Fig. 145. Critical current at 77K, self-field for each block of the length of the conductor, randomly calculated. _____	131
Fig. 146. Critical current at 77K, self-field for each block of the length of the conductor, given by the providers SuperOx. _____	131
Fig. 147. Critical currents according to the initial value of critical current at 77 K in self-field along the length of the conductor. _____	132
Fig. 148. Propagation of the transition inside the winding when the initial I_c is varying above the minimum studied I_c . _____	132
Fig. 149. Propagation of the transition inside the winding when the initial I_c is following the TapeStar value. _____	132
Fig. 150. Influence of the number of blocks along the length of the conductor on the limiting critical current evaluation. _____	133
Fig. 151. Influence of the number of subdivision along a block width on the limiting critical current evaluation. _____	133
Fig. 152. Propagation of the transition inside the winding when $n=30$, self-field. _____	134
Fig. 153. Propagation of the transition inside the winding when $n=60$. _____	134
Fig. 154. Temperature rise on the first blocks, when $n=30$, self-field. _____	135
Fig. 155. Temperature rise on the first blocks, when $n=60$, self-field. _____	135
Fig. 156. Spiral geometry of the studied wound sample with a focus on the beginning of the winding. _____	136
Fig. 157. Temperature of each block at different time using the 2D heat propagation model. _____	137
Fig. 158. Temperature of each block at different time using the 1D heat propagation model. _____	137
Fig. 159. Voltage of each block at different time using the 2D heat propagation model. _____	137
Fig. 160. Voltage of each block at different time using the 1D heat propagation model. _____	137
Fig. 161. (a) Double pancake assembly before wrapping. (b) Winding of the first pancake while the other half of the tape is set aside on a satellite. _____	141
Fig. 162. Illustration of the Hall sensor measurement. _____	142
Fig. 163. Illustration of the study protocol used for the DP-INS coil. The top graph is the magnetic field measured inside the wound sample, on the bottom graph, the blue line is the full coil voltage and in red the current inside the coil. _____	143
Fig. 164. Lorentz force JBr applied on the cross-section of the winding when 125 A are passing through the conductor under 8 T. _____	144
Fig. 165. Strain gauges measurements compared to simulation (red dotted line) under 8 T until 125 A. _____	144
Fig. 166. The red curve is the current passing through the coil while removing the current and during the outer magnet quench. The coil voltage is the blue curve and the top graph shows the magnetic field measured at the coil centre. The two field drops correspond to the current decrease in the insert and then to the emergency field removal in the outer LTS magnet. _____	145
Fig. 167. Parallel component of the field (T), when 200 A is inside the coil, in an 8 T background field. _____	146
Fig. 168. Transverse component of the field (T), when 200 A is inside the coil, in an 8 T background field. _____	146
Fig. 169. Critical current (A) evaluated on the cross section of the wound tape according to the intensity of the field and its orientation. _____	147
Fig. 170. Limiting critical current of the wound sample: the red curve is the minimum I_c , the blue one is when averaged on the conductor width. _____	148

Fig. 171. Limiting critical current according to the current passing through the coil in self-field. _____	149
Fig. 172. Limiting critical current according to the current passing through the coil under 8 T. _____	149
Fig. 173. Fully instrumented single pancake coil before wrapping. _____	151
Fig. 174. Draft of the fully instrumented insulated coil assembly. _____	151
Fig. 175. Voltage taps inside the SP-INS winding. _____	152
Fig. 176. Draft of the fully instrumented insulated coil assembly, details of the Cernox cryogenic temperature sensors position. _____	152
Fig. 177. Illustration of the experimental protocol for a background field fixed at 19 T and the current inside the coil reaching 300 A. The black curve is the magnetic field monitored by the Hall sensor in the middle of the wound sample SP-INS and the red line shows the current passing through the coil. The framed graph on the bottom right is a zoom of the second step. _____	152
Fig. 178. Onset of transition of the inner turns while the background field is 17 T and 250 A is passing through the coil. _____	153
Fig. 179. Current is ramped from 50 A to 200 A. _____	154
Fig. 180. Current plateau 200 A, self-field. _____	154
Fig. 181. 200 A circulating in the coil, the background field is ramped up to 3 T. _____	154
Fig. 182. Increase of the background field when 200 A is passing through the coil. _____	154
Fig. 183. Superconducting coil signal in red and compensated signal in blue when the background field is increased to 14 T, with 200 A passing through the coil. _____	154
Fig. 184. Temperature reached when the coil starts its transition to a resistive state and reach the voltage threshold, according to the background field and the current passing through the coil. _____	155
Fig. 185. Experimental results obtained on an instrumented insulated single pancake coil: set of temperatures when the voltage threshold is reached, for a given current and a given background field. The temperatures plotted vs the current for one magnetic field seem to follow a linear trend, which can be exploited to extrapolate currents at lower temperatures. _____	155
Fig. 186. (a) Limiting critical current evaluation: in green the data are evaluated according to the experiment presented in the paper; in black the curve is evaluated according to a short sample characterization applied on the field components while taking the lowest value and in red while taking the average on the width of the conductor. (b) Representation of the related errors. _____	156
Fig. 187. (a) Inner turn voltages according to the temperature with 250 A passing through the coil, self-field. (b) Evolution of the full coil compensated voltage signal with increasing temperature. _____	157
Fig. 188. (a) Inner turn voltages according to the temperature with 250 A passing through the coil, under 17 T. (b) is full coil compensated voltage signal. _____	157
Fig. 189. (a) Propagations along the turns for 17 T and 150 A passing through the coil. (b) Full coil compensated voltage signal. _____	158
Fig. 190. Temperature of the winding when the voltage threshold is reached according to the background field and the current inside the coil. _____	159
Fig. 191. Temperature of the winding when the voltage threshold is reached according to the background field and the current inside the coil. _____	160
Fig. 192. Numerical and experimental voltages of the full coil when 250 A are passing through the winding at 17 T. _____	160
Fig. 193. Temperature along the length of the conductor when the full coil voltage is 1 mV, with global heating. _____	161
Fig. 194. Voltage along the length of the conductor when the full coil voltage is 1 mV, with global heating. _____	161
Fig. 195. Temperature along the length of the conductor when the full coil voltage is 1 mV, without global heating. _____	161
Fig. 196. Voltage along the length of the conductor when the full coil voltage is 1 mV, without global heating. _____	161
Fig. 197. MI coil after wrapping. _____	164
Fig. 198. Photography of one of the three heaters placed inside the winding. _____	165
Fig. 199. MI coil measurements; full coil voltage, current and magnetic field at the centre of the coil are plotted. _____	166

Fig. 200. 2017 tests magnet constant. Black line, red dash and blue dot are respectively the calculated magnet constant, the constant reduced by 5 % and the constant with 5 % added.	166
Fig. 201. Voltage measurement and current inside the coil during the unexpected background discharge.	167
Fig. 202. Measured centre field and external field during unexpected discharged.	167
Fig. 203. Resistance of the damaged area of the winding before and after the outer discharges.	168
Fig. 204. Quench energy according to the magnetic field background and the current inside the coil.	168
Fig. 205. Quench energy according to the magnetic field background, giving also the heat pulse duration.	169
Fig. 206. Propagation of the transition after heat pulse for 250 A, self-field.	169
Fig. 207. Propagation of the transition after heat pulse for 250 A, 4 T.	169
Fig. 208. Propagation of the transition after heat pulse for 260A, 6 T.	170
Fig. 209. Propagation of the transition after heat pulse for 260 A, 16 T.	170
Fig. 210. Trend of the curve when n is even.	176
Fig. 211. Illustration of the trend of the curve according to the value of $y(0)$, when n is even.	176
Fig. 212. Illustration of the curve when n is odd.	177
Fig. 213. Heat capacity of the layer materials.	178
Fig. 214. Thermal conductivity of the silver and copper layers.	179
Fig. 215. Thermal conductivity of the Hastelloy and the superconductive layers.	179
Fig. 216. Resistivity of the silver and copper layers.	179
Fig. 217. Resistivity of the Hastelloy and the superconductive layers.	179

RESUME DE LA THESE EN FRANÇAIS

1.1 INTRODUCTION ET CONTEXTE

1.1.1 Supraconductivité

A très basse température, les supraconducteurs sont des matériaux qui n'opposent pas de résistance au passage du courant, c'est-à-dire qu'ils ne sont à l'origine d'aucune dissipation par effet Joule. Au-delà donc d'une certaine température dite température critique ou T_c , ces conducteurs retrouvent un état dissipatif. Ce phénomène est illustré dans Fig. 1 où il est comparé à la résistance d'un métal ordinaire non supraconducteur qui, à basse température, sature à une valeur supérieure à zéro.

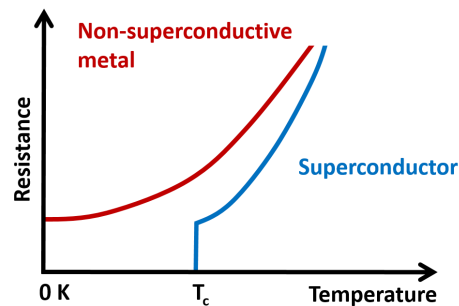


Fig. 1. Allure des résistances d'un métal ordinaire et d'un supraconducteur selon la température, ne respecte pas l'échelle.

1.1.2 Les matériaux supraconducteurs

Les supraconducteurs utilisés pour les applications dites de grande envergure, sont généralement divisés en deux catégories selon leur T_c ; on parle de Supraconducteurs à Basse Température Critique (SBTC) lorsque T_c est inférieur à 30 K. Dans le cas contraire, ces matériaux sont appelés Supraconducteurs à Haute Température Critique (SHTC).

T_c n'est pas la seule limite de l'état supraconducteur ; si le champ magnétique appliqué sur le matériau est trop élevé (B_c) ou bien si le courant traversant le conducteur est trop important (I_c), le matériau retrouve également un état dissipatif. Ces trois critères définissent une surface critique qui est spécifique à chaque supraconducteur. Elle est illustrée dans Fig. 2 : bien que non à l'échelle, le schéma met en avant la surface critique plus grande des SHTC.

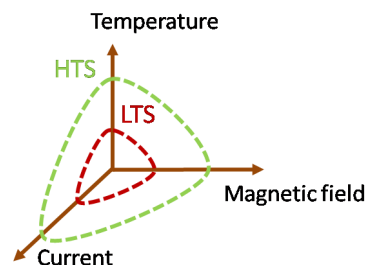


Fig. 2. Illustration de la surface critique, ne respecte pas l'échelle.

Cependant, les limites de l'état supraconducteur sont en général plus complexes car les supraconducteurs ont des propriétés fortement anisotropiques. La surface critique se voit également

modifiée lorsque le conducteur est mécaniquement déformé. Il est à noter que B_c et T_c sont intrinsèques au matériau alors que I_c peut être amélioré.

Lorsqu'une de ces limites est franchie et que la transition du matériau à un état dissipatif est irréversible, c'est-à-dire que le conducteur ne peut retrouver son état supraconducteur de lui-même, on parle alors de trempe ou *quench* en anglais.

1.1.3 Les conducteurs de type TRBCO

1.1.3.1 Composition générale

La suite du manuscrit se concentre sur les SHTC et plus particulièrement les matériaux dits TRBCO, il s'agit de céramiques dont la composition est $TRBa_2Cu_3O_{7-x}$, où TR désigne une Terre Rare généralement l'Yttrium (Y) ou le Gadolinium (Gd). Ces conducteurs sont un assemblage de couches minces dont l'épaisseur supraconductrice est de l'ordre de $1\ \mu m$, soit environ 1 % de la totalité. Cette couche supraconductrice est déposée sur un ruban métallique d'un alliage de nickel ou Hastelloy®. Cette dernière permet au conducteur de supporter des forces mécaniques élevées, jusqu'à 700 MPa.

A cause de leur processus de fabrication, ces conducteurs sont, à l'heure d'aujourd'hui, seulement fournis sous forme de ruban, dont un exemple de schéma de coupe est donné Fig. 3. Leur épaisseur varie entre $70\ \mu m$ et $170\ \mu m$ et leur largeur entre 2 mm et 12 mm.

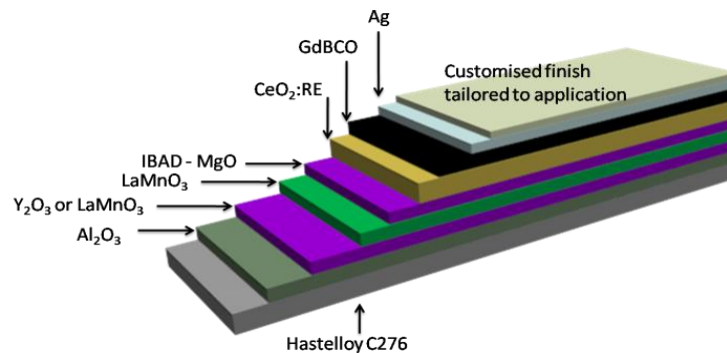


Fig. 3. Schéma non à l'échelle d'une coupe de conducteur SuperOx, inspiré par [1].

Le fait que ces conducteurs soient seulement fournis sous forme de ruban ne permet pas les mêmes bobinages qu'un conducteur rond. Dans cette étude, on préférera des bobinages dans le plan, c'est-à-dire des bobinages sous forme de *galette*.

1.1.3.2 Comportement mécanique

La fine composition céramique de ces conducteurs les rend très fragiles, menant rapidement à la délamination [2], lorsque les différentes couches ne sont plus en contact les unes avec les autres. En effet, même si ces conducteurs peuvent mécaniquement supporter d'importantes forces axiales, ce n'est pas le cas pour les autres directions de contraintes [3].

De plus, à cause de leur architecture, les conducteurs TRBCO ont un angle de courbure limité à $11\ mm$ [4]. En dessous de cet angle, les performances du conducteur seront réduites ou, dans le pire des cas, sa capacité à conduire du courant sera nulle. Si la contrainte de déformation est appliquée dans un sens ou dans l'autre du ruban, on parle alors de déformation « facile » (selon la longueur) ou « difficile » (selon sa largeur). Selon le cas, les détériorations du conducteur ne seront pas les mêmes,

voir [5]. Le paramètre déterminant reste néanmoins la contrainte d'élongation du matériau ϵ qui est de l'ordre de 0,4 % [6].

1.1.3.3 Propriétés anisotropes

La forte anisotropie de la structure cristalline du conducteur a des conséquences à l'échelle macroscopique [7]. L'axe du champ magnétique extérieur crée, avec la surface du conducteur, un angle dit angle d'incidence, illustré Fig. 4. Si l'angle est 0° , le champ magnétique extérieur appliqué sur le matériau est parallèle à la surface du conducteur et ce dernier présente alors généralement ses plus hautes performances. Si l'angle d'incidence vaut 90° , le champ magnétique est donc perpendiculaire au conducteur, ce dernier ne voit alors qu'une composante transverse et conduira un courant beaucoup moins élevé.

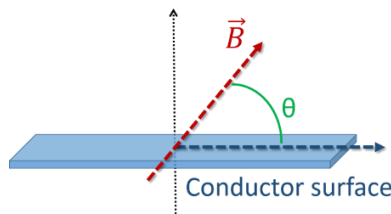


Fig. 4. Angle d'incidence créée par la surface du conducteur en bleu et l'axe du champ magnétique extérieur en rouge.

Ces propriétés anisotropes sont illustrées Fig. 5. Il s'agit du courant critique mesuré à 77 K et sous 1 T de trois conducteurs SuperOx [8] donné selon l'orientation du champ magnétique extérieur appliqué sur le ruban supraconducteur. L'anisotropie des performances d'un conducteur doit être prise en compte lors de son utilisation notamment pour définir les marges en courant du système étudié.

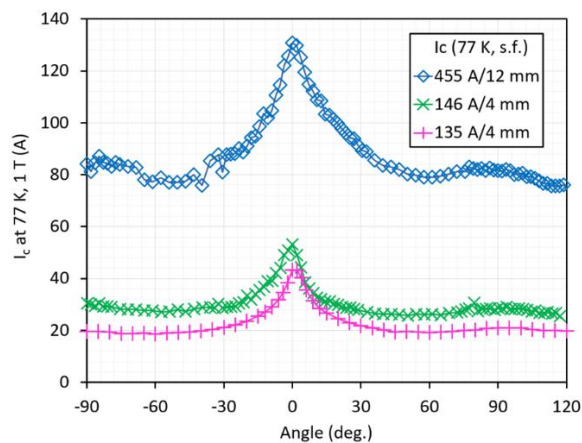


Fig. 5. Résultats expérimentaux de SuperOx [8] : courant critique à 77 K sous 1 T pour trois différents conducteurs selon l'orientation du champ magnétique extérieur.

1.1.3.4 Inhomogénéité du conducteur

Récemment, les conducteurs de type TRBCO sont produits dans des longueurs suffisantes pour permettre leur utilisation dans des applications à grande échelle. Néanmoins, bien que le phénomène ait été considérablement réduit au fil des années [9], ces conducteurs présentent toujours d'importantes inhomogénéités de performance sur leur longueur qui peuvent provoquer l'endommagement du ruban [10]. Les longueurs de conducteur TRBCO sont fournies avec la mesure de leur courant critique à 77 K, en champ propre le long du ruban comme celle présentée Fig. 6. Il s'agit

d'une mesure inductive et donc non intrusive du conducteur qui peut être effectuée en continu, avec des résultats moyennés sur 2 cm comme dans Fig. 6, mais parfois jusqu'à 5 m, selon le fournisseur.

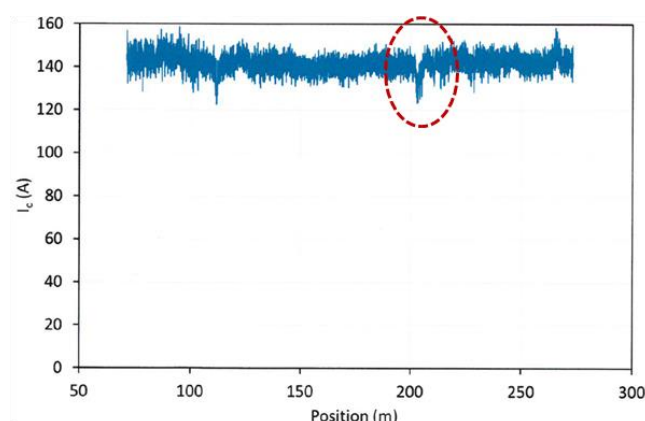


Fig. 6. Courant critique évalué à 77 K, en champ propre d'un ruban REBCO de 4 mm, fourni par SuperOx.

Cette longueur est définie par sa valeur minimum et dans le cas de Fig. 6, elle est de 120 A atteinte en seulement deux points du ruban. La valeur moyenne reste autour de 145 A avec une variation allant jusqu'à 20 % le long du conducteur.

Il semble néanmoins difficile de trouver une corrélation entre les valeurs à très basse température et en champs avec les valeurs à 77 K, sans champ extérieur en comparant les performances de conducteur venant de différents fournisseurs, voire même lorsque les rubans proviennent de la même ligne de production [11]. Cependant, les performances peuvent être approximées utilisant des lois dont les constantes varient d'un fournisseur à l'autre, voir section 1.2.5.

1.1.3.5 Stabilité thermique

Hormis leur T_c , une autre des principales propriétés distinguant les SHTC des SBTC est la vitesse de propagation du quench, qui est bien moins rapide pour les SHTC [12]. La vitesse de propagation de la zone normale (VPZN) est de 2 à 10 cm/s pour les SHTC [13] alors qu'elle peut atteindre les 7,5 km/s pour les SBTC [14] [15]. Cette propagation lente de la transition à un état dissipatif chez les SHTC ajoutée aux inhomogénéités de performance va se traduire par un échauffement très locale du conducteur qui peut irréversiblement endommager le ruban.

Plus spécifiquement, dans un assemblage de bobinages TRBCO plus grand, si le conducteur transite localement, la tension créée sera faible et donc difficile à détecter car le signal associé risque d'être noyé dans les bruits de mesure qui sont conséquents lors de tests sous champ intense. Le risque de destruction irréversible du bobinage avant que la transition soit détectée est donc important. Cette lente vitesse de propagation, notamment due à la chaleur spécifique du conducteur qui augmente très rapidement avec la température [16], est donc l'une des difficultés majeures à leur implémentation.

De plus, l'énergie minimum nécessaire pour déclencher un quench dans des conditions normales d'opération est supérieure à 1 Joule [17] pour les TRBCO, ce qui est approximativement trois fois plus important que pour les SBTC. Cela signifie qu'un bobinage TRBCO ne sera probablement pas endommagé par un évènement extérieur mais plutôt par un défaut du conducteur.

1.1.4 Utilisations des conducteurs TRBCO

Les conducteurs TRBCO ont vu très récemment leur coût de fabrication réduire en suivant les améliorations technologiques [18] et ils sont à présent au cœur de nombreux projets dans plusieurs domaines à travers le monde. Les performances en termes de courant n'ont eu de cesse d'augmenter en même temps que la longueur de conducteur proposée par les fournisseurs [19]. Ces récentes améliorations rendent donc les TRBCO très prometteurs pour les applications de grande échelle.

Les SBTC ont d'ores et déjà plusieurs applications industrielles telles que les IRM (Imagerie par Résonance Magnétique) et les aimants du Grand Collisionneur de Hadrons (LHC au Cern) mais ce n'est pas encore le cas pour les SHTC. Néanmoins, leurs incroyables performances promettent pour les systèmes étudiés, non seulement une réduction de la consommation énergétique mais aussi de poids et de taille.

Pour l'instant, les SHTC demeurent difficiles à implémenter et leur utilisation restent donc réduite à des applications de niche. Néanmoins, ils sont au cœur de nombreux projets de recherche dans le monde que ce soit pour les limiteurs de courant, le stockage d'énergie (SMES), les câbles électriques, les transformateurs, ou encore les moteurs et générateurs pour l'énergie éolienne, les avions électriques, les bateaux. Finalement, leur capacité à transporter un courant très élevé à 4,2 K rendent les conducteurs TRBCO très attrayants pour construire une nouvelle génération d'aimants à champ magnétique intense et à basse consommation énergétique. L'ensemble de ces applications est résumé dans Fig. 7.

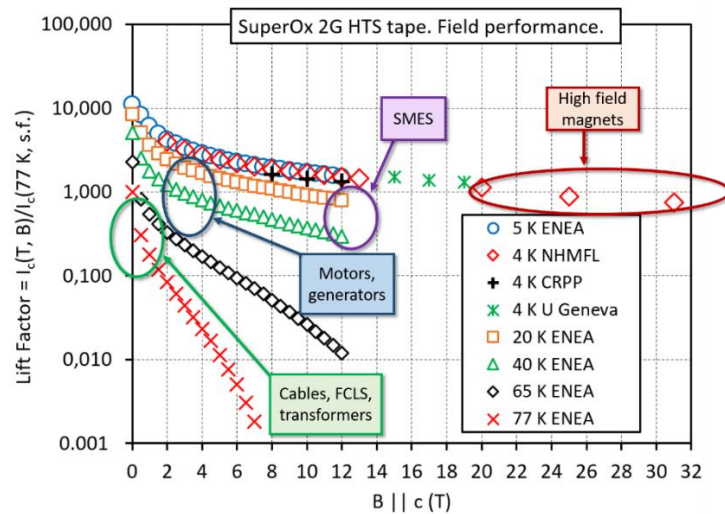


Fig. 7. Performance des conducteurs TRBCO en fonction du champ magnétique extérieur, données SuperOx [8].

1.1.5 Les aimants à champ magnétique intense

1.1.5.1 Les électro-aimants

Les aimants permanents peuvent générer un champ magnétique atteignant un maximum autour de 2 T (4 T en utilisant une configuration dite de Halbach [20]) et ne peuvent donc pas être envisagés pour générer des champs magnétiques intenses. Etant donné qu'un conducteur parcouru par un courant génère un champ magnétique proportionnel (expérience d'Oersted, 1820), si ce conducteur est bobiné, le champ qu'il génère est alors concentré au milieu du solénoïde, comme illustré dans Fig. 8. Ces conducteurs bobinés sont appelés électro-aimants.

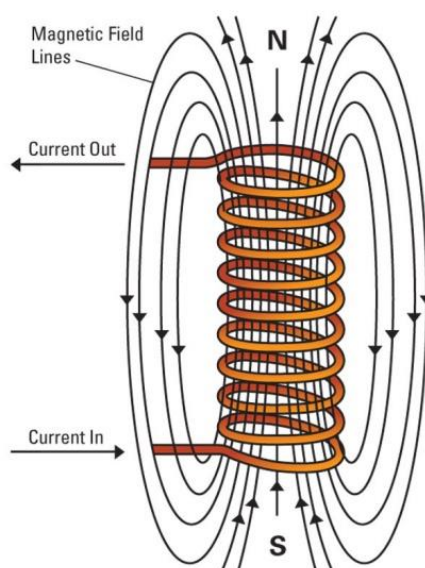


Fig. 8. Schéma descriptif d'un électro-aimant.

Le champ généré par un électro-aimant peut être soit continu soit pulsé, c'est-à-dire généré pendant un temps très court allant de centaines de microsecondes à des centaines de millisecondes [21]. Le Laboratoire National des Champs Magnétiques Intenses (LNCMI) en France fournit du champ magnétique intense à des chercheurs du monde entier, à la fois pulsé à Toulouse et continu à Grenoble. Aujourd'hui, le maximum atteint au LNCMI en champ continu est 36 T et 98,8 T en champ pulsé. Ce type de laboratoire est très rare car complexe et onéreux. Pour le LNCMI Grenoble par exemple, la consommation électrique est de 24 MW et les aimants sont refroidis par de l'eau sous pression à 300 L/s.

La suite se concentre sur les champs continus qui atteignent des champs moins élevés que les champs pulsés mais pendant un temps beaucoup plus long, jusqu'à plusieurs heures. Une importante source électrique et un système de refroidissement robuste sont donc nécessaires pendant le fonctionnement des aimants. Ainsi, les supraconducteurs sont très intéressants pour ce type d'application promettant à la fois une réduction de la consommation énergétique mais aussi une réduction en taille. Dans Tableau 1, un aimant résistif est comparé à un aimant supraconducteur pour souligner ses avantages.

	Bitter (résistif)	Supracon.	Ratio
Densité de flux magnétique (T)	10	11	1.1
Diamètre (mm)	500	500	1
Source (kW)	14 000	5	2 800
Refroidissement (kW)	200 (pompes)	100 (liquéfacteur)	2

Tableau 1. Comparaison d'un aimant résistif à un aimant supraconducteur.

1.1.5.2 Les technologies actuelles d'aimants

Les aimants SBTC sont d'ores et déjà commercialisés et semblent avoir atteint leur limite en termes de champ en 2009, avec l'installation de la bobine Bruker BioSpin au CRNM, à Lyon qui génère jusqu'à 23.5 T. Aujourd'hui, seuls les aimants résistifs permettent d'atteindre des champs magnétiques plus élevés mais à un coût énergétique très important. Le record est détenu par le MagLab à Tallahassee en Floride, qui a atteint 41,4 T en utilisant 32 MW, en Août 2017.

La limite en champ des SBTC est intrinsèque au matériau (B_c), ils demeurent néanmoins au cœur de projet d'aimants hybrides dont ils forment la partie extérieure, la partie intérieure de l'aimant étant résistive. L'autre possibilité pour générer des champs magnétiques intenses tout en réduisant la consommation énergétique est donc d'utiliser les SHTC.

1.1.5.3 Aimants SHTC et projet NOUGAT

Bien que la suite s'intéresse aux SHTC, ces derniers restent néanmoins étudiés à très basse température car c'est là qu'ils présentent leurs meilleures performances. Il existe à la fois des projets d'aimants entièrement SHTC comme décrit dans [22], mais aussi d'aimants supraconducteurs hybrides avec une partie intérieure SHTC et une partie extérieure SBTC comme dans [23], [24] et [25].

Cette thèse s'inscrit dans le cadre du projet NOUGAT dont l'objectif est le design et la réalisation d'un insert TRBCO générant 10 T sous un champ extérieur de 20 T. Pour les tests préliminaires, l'aimant extérieur est résistif notamment pour réduire les problèmes dus au couplage mais aussi parce qu'un tel aimant existe déjà au LNCMI. Dans un second temps, le champ extérieur sera généré par un aimant SBTC pour mener vers une génération d'aimants entièrement supraconducteurs. L'insert est donc géométriquement limité par l'aimant extérieur déjà existant pour son diamètre extérieur, par les standards déjà utilisés pour son diamètre intérieur et l'homogénéité du champ généré par l'aimant extérieur pour sa hauteur maximale. Les valeurs limites géométriques sont données dans le Tableau 2. Il est également à noter qu'un champ intense associé à un courant important dans le conducteur génère des forces de Laplace considérables qui doivent être prises en compte pendant l'élaboration de l'insert SHTC. L'objectif du projet NOUGAT n'est donc pas d'atteindre des champs magnétiques plus importants que ceux déjà existants mais plutôt de rendre compte des défis engendrés par l'utilisation des SHTC pour les applications haut champ.

Limitations géométriques de l'insert SHTC	
Diamètre extérieur maximum (mm)	120
Diamètre intérieur minimum (mm)	50
Hauteur maximale (mm)	200

Tableau 2. Limitations géométriques.

1.1.5.4 Différentes techniques de bobinage

A cause de la difficulté à détecter une transition dans un assemblage SHTC bobiné, il a été proposé par le MIT de retirer l'isolation électrique du conducteur [26]. Ainsi, toutes les spires sont en contact les unes avec les autres et dans le cas d'un défaut sur le conducteur, le courant va court-circuiter le tour en question en passant dans le suivant. On parle de bobine auto-protégée. Le revers de cette technique est une dynamique lente de l'aimant, c'est-à-dire que la bobine sera longue à charger et à décharger car le courant nécessitera de plus de temps pour trouver son chemin dans la spirale créée par la fine couche supraconductrice du ruban TRBCO bobiné. Le bobinage dit non-isolé provoque donc une détérioration de la linéarité et stabilité du champ magnétique généré. Pour pallier à cela, une solution intermédiaire a vu le jour : les bobines dites métalliquement isolées. Cette technique impose toujours d'enlever l'isolation électrique du conducteur mais de la remplacer par un ruban métallique afin de garder la capacité d'autoprotection de l'aimant mais de réduire ses temps de charges et décharges.

1.1.6 Objectifs de la thèse

Principalement pour sa capacité d'auto protection, le bobinage métalliquement isolé a été sélectionné pour construire le prototype de l'insert du projet NOUGAT. Néanmoins, certaines applications ne sont pas envisageables sans isolation électrique comme le stockage d'énergie ou les aimants d'accélérateurs de particules. Principalement pour cette raison, le présent travail se concentre sur les aimants isolés, c'est-à-dire que les spires d'un bobinage sont toutes électriquement isolées les unes des autres. La thèse va donc investiguer s'il est possible ou non de construire des aimants isolés et surtout s'ils peuvent être utilisés sans être détériorés.

1.2 CARACTERISATION D'ÉCHANTILLONS COURTS SUPRACONDUCTEURS

1.2.1 Objectifs de la caractérisation

Pour réaliser le design de l'insert, il est nécessaire d'étudier, dans les conditions de fonctionnement de l'aimant final, les performances du conducteur qui va être utilisé. Fig. 9 représente la distribution en coupe du champ magnétique généré par l'aimant final. Grâce aux symétries du champ, seulement un quart de la coupe est nécessaire pour évaluer les composantes du champ en tout point de l'aimant. Le champ magnétique est l'addition de celui généré par l'insert délimité par le trait noir continu et celui généré par l'aimant résistif extérieur à droite du trait noir pointillé. Ce dernier est à la fois calculé et mesuré par le LNCMI. L'insert est modélisé par un solénoïde en cuivre parcouru par une densité de courant homogène (365 A/mm^2) afin d'obtenir 10 T en son centre utilisant FLUX/CEDRAT [27] et respectant les limitations géométriques du projet. L'objectif est d'évaluer les composantes de champ appliquées sur l'insert pour identifier dans quelle zone de fonctionnement doit être caractérisé le conducteur SHTC. En effet, à cause de fortes propriétés anisotropiques, ce sont les composantes de champ transverses qui vont venir limiter le fonctionnement de l'insert. Fig. 9 montre qu'elles atteignent un maximum de 3,5 T sur les extrémités du bobinage, créant un angle d'incidence de 14° entre la surface du conducteur et l'axe du champ magnétique.

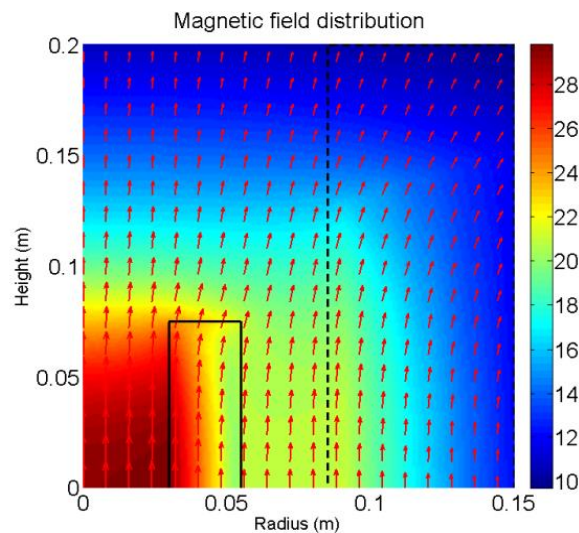


Fig. 9. Distribution du champ magnétique (T) sur le quart en haut à droite de la coupe de l'aimant final. Elle prend en compte le champ magnétique généré par l'insert délimité par des traits noirs continus et celui généré par l'aimant extérieur résistif situé à droite de la ligne noire pointillée.

Etant donnée la corrélation limitée entre les valeurs de courants critiques délivrées par le fournisseur à 77 K en champ propre avec les performances du conducteur à plus basse température

sous champ, il est primordial d'évaluer le ruban dans ces conditions. La littérature fournit des valeurs de performance de conducteurs SHTC dans ces conditions mais souvent il s'agit que de mesure en champ transverse [28] car un ruban d'une largeur de 4 mm peut à présent conduire jusqu'à plus de 1000 A à 4,2 K, [29]. Il faut donc que les bancs de test soient également capables de supporter cette charge de courant dans des trous de champ étroits. Lorsque dans la littérature, plus d'angles intermédiaires sont proposés, la largeur du conducteur est souvent réduite pour limiter la quantité de courant à passer dans la canne de mesure [30], [31] et cette découpe peut être à l'origine d'une diminution des performances du conducteur [32].

La spécificité de la caractérisation présentée ici est donc l'étude de la largeur complète du conducteur sous champ magnétique jusqu'à 23 T, à 4,2 K et pour plusieurs valeurs d'angle intermédiaires entre 0° et 90°.

1.2.2 Présentation du banc de mesure

Afin de tester un échantillon SHTC sous champ magnétique, il faut permettre au ruban d'être parcouru par un courant au centre de l'aimant extérieur. Pour cela, l'échantillon est placé à l'extrémité d'une canne de mesure comme celle du schéma Fig. 10 qui mesurent environ 1,7 m.

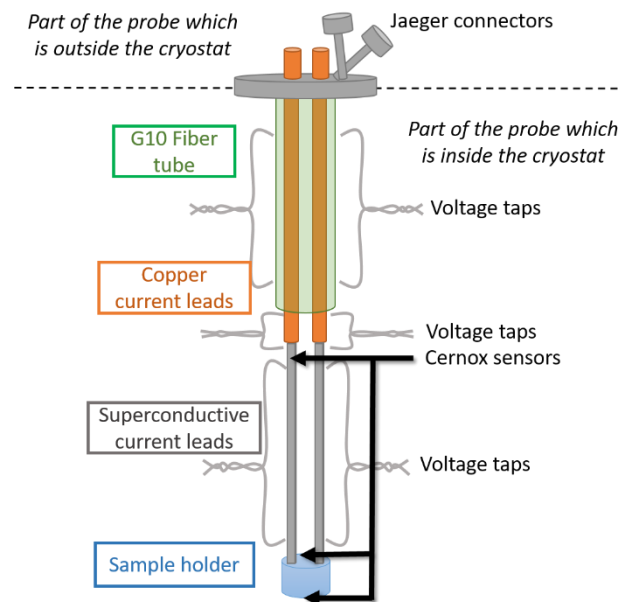


Fig. 10. Schéma d'une canne de mesure et son instrumentation.

Celle utilisée pour cette caractérisation permet de transporter jusqu'à 2000 A à 4,2 K dans un trou de champ de 50 cm. Elle permet donc de ne pas avoir à réduire la largeur des échantillons SHTC étudiés. Elle est entièrement instrumentée en termes de prises de potentiel pour surveiller les tensions le long de la canne mais aussi en sondes de température pour détecter les élévations anormales en température pendant les tests.

Le support de l'échantillon, illustré Fig. 11, est situé à l'extrémité de la canne de mesure et permet de faire tourner l'échantillon sur lui-même jusqu'à 360°, avec un pas de 2,5° et une précision de 1°. Fig. 11 (a) montre le support de l'échantillon de profil. La flèche pointillée noire représente l'axe du champ magnétique, le cercle rouge souligne la pièce en cuivre permettant la rotation de l'échantillon et finalement la flèche blanche, la surface du ruban testée. Ce ruban, visible sur Fig. 11. (b) a une longueur de 2,5 cm et sa largeur peut atteindre jusqu'à 6 mm. Deux prises de potentiel sont

soudées sur l'échantillon espacées de 1 cm pour enregistrer l'élévation de tension pendant la rampe de courant.

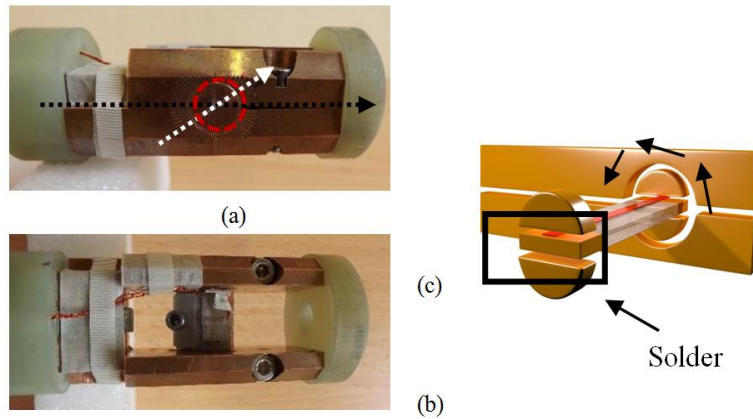


Fig. 11. Support de l'échantillon. (a) : vue de côté. (b) : vue de haut. (c) Schéma d'explication.

1.2.3 Résultats expérimentaux

Le ruban testé est un conducteur TRBCO d'une largeur de 4 mm fourni par la compagnie SuperOx dont les caractéristiques sont données dans le Tableau 3.

Caractéristiques	
Largeur	4 mm
Epaisseur totale	~ 120 μm
Substrat	60 μm
Couche d'argent	~ 2 μm
Couche de cuivre (x2)	20 μm
Polyimide déposé	10 μm
Couche supraconductrice	~1.5 μm
I_c min (77 K, champ propre)	120 A

Tableau 3. Caractéristiques du conducteur TRBCO étudié.

Un exemple de mesure de tension pendant une rampe de courant est donné Fig. 12 pour un test sous 8 T et un angle de 10° entre la surface du ruban et l'axe du champ magnétique extérieur.

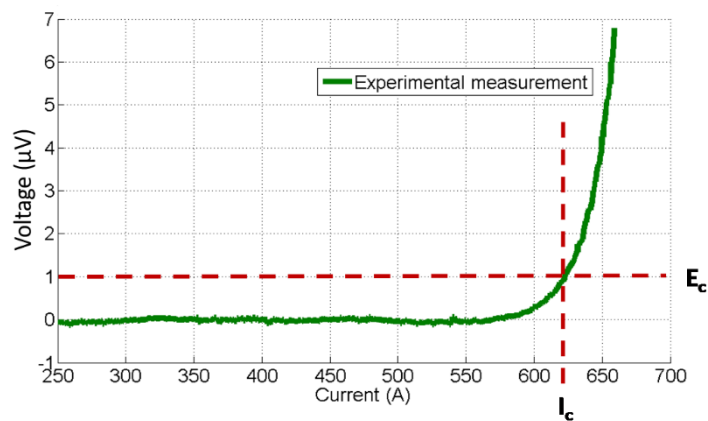


Fig. 12. Mesure de tension sur un échantillon SuperOx de largeur 4 mm sous 8 T et un angle de 10° entre la surface du ruban et l'axe du champ magnétique extérieur.

Un seuil de tension arbitraire pour déterminer la valeur du courant critique est donné à $1 \mu\text{V}/\text{cm}$. Etant donné l'espacement des prises de potentiel de 1 cm, la tension V est dans cette configuration confondue avec le champ électrique E . Dans cet exemple, le courant critique est donc de 620 A. Les performances ruban ont été mesurées en champ propre et jusqu'à un champ extérieur de 23 T pour les angles suivants : 0° , 5° , 10° , 15° , 20° , 30° , 60° et 90° . Les résultats expérimentaux sont donnés Fig. 13.

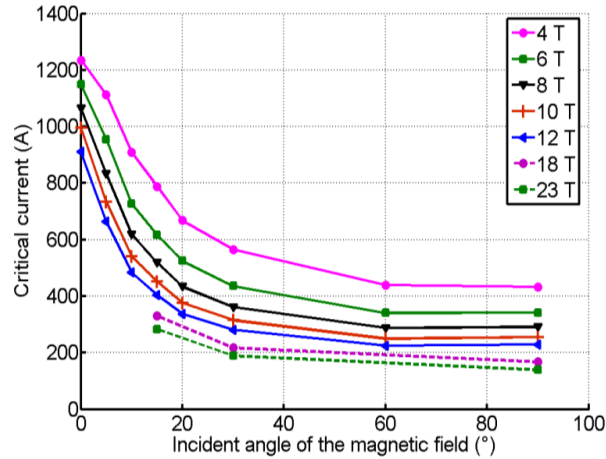


Fig. 13. Courants critiques évalués selon l'orientation du champ magnétique extérieur pour différentes intensités de champ.

La réduction de performance, selon l'orientation du champ, qui a été mentionnée précédemment section 1.1.3.3 est similaire sur Fig. 13. Elle est également plus prononcée pour des petits angles, soulignant l'importance de prendre en compte l'anisotropie des propriétés des rubans TRBCO lors de l'évaluation des marges en courant de l'insert car ce sont des petits angles auxquels sera soumis le ruban dans les conditions de fonctionnement finales, voir section 1.2.1.

On peut également noter que certaines valeurs sont absentes de Fig. 13, principalement les mesures faites à angle faible et sous un champ élevé. En effet, dans le cas où l'angle est faible le ruban nécessite un courant élevé pour pouvoir mesurer le courant critique. Or, associé à un champ magnétique élevé, il crée une force de Laplace considérable sur le ruban qui risque de l'endommager. Il faut aussi réussir à injecter un courant colossal depuis la canne de mesure dans l'échantillon TRBCO sans pour autant réduire ses performances.

De plus, à cause du petit diamètre du trou de champ et le besoin en courant élevé, la canne de mesure ne permet pas une rotation de l'échantillon depuis l'extérieur du cryostat. Cela signifie que pour étudier un nouvel angle, il faut donc réchauffer l'expérience, retirer la canne de mesure du cryostat pour délicatement changer l'inclinaison de l'échantillon TRBCO et remettre le banc de mesure en place pour refroidir à nouveau le ruban. Il faut considérer donc qu'une seule orientation peut être étudiée par jour et donc notamment par manque de temps certaines mesures n'ont pas été conduites et les valeurs manquantes doivent donc être interpolées.

1.2.4 Relation $E(J)$

L'allure du champ électrique pour un conducteur TRBCO, telle que celle illustrée Fig. 12, est communément modélisée par une loi de puissance (1).

$$E(J) = E_c \left(\frac{J}{J_c} \right)^n \quad 1$$

E est donc le champ électrique en V/m. E_c est le champ électrique seuil qui définit la densité de courant critique J_c souvent exprimée en A/mm². J est la densité de courant critique passant effectivement dans le conducteur également en A/mm² et n, appelé indice est sans unité et reflète de l'allure plus ou moins abrupt de la transition du conducteur à un état dissipatif. Ce type de mesure dite mesure de transport est notamment intéressante car elle permet d'évaluer ces facteurs de puissance qui seront ensuite implémentés dans le modèle décrit section 1.3. Les facteurs de puissance évalués lors de cette caractérisation sont donnés Fig. 14, les valeurs sont en accord avec celles qui peuvent être trouvées dans la littérature, [33]. Les facteurs de puissance ne semblent pas dépendre de l'orientation du champ magnétique mais seulement de son intensité. Les valeurs sont divisées par deux entre 0 T et 2 T alors qu'elles semblent réduire doucement pour des champs magnétiques extérieurs supérieurs.

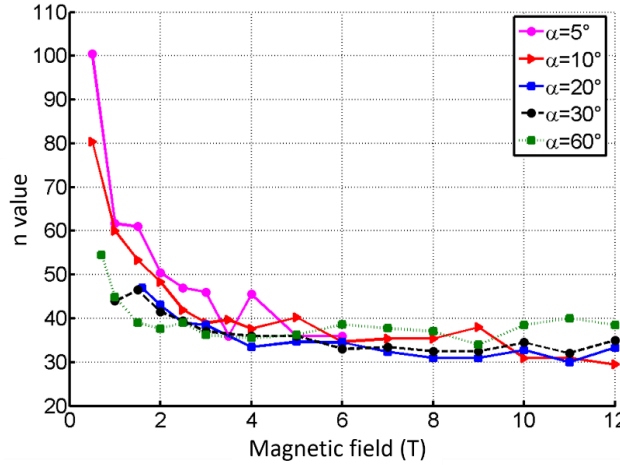


Fig. 14. Indice de la loi de puissance en fonction du champ magnétique extérieur, évalué pour différentes orientations de champ.

1.2.5 Interpolation des résultats

L'absence de certaines valeurs de courant critique sur le graphique Fig. 13 souligne la difficulté des mesures de transport sous champ magnétique intense. Les valeurs manquantes sont donc interpolées afin de compléter la caractérisation du conducteur. Dans un premier temps, les courants critiques évalués sont interpolés en utilisant le modèle de Kim [34] défini par la formule (2), où $J_c(0)$ est la valeur hypothétique de J_c en champ propre. En effet, quand le courant passant dans le conducteur est si élevé, le champ magnétique généré par le ruban ne peut plus être négligé. Le courant critique ici sans champ magnétique extérieur est ici de 1450 A. B_0 est le champ magnétique à partir duquel les valeurs de courant critiques commencent à lentement saturer [35].

$$J_c(B) = \frac{J_c(0)}{1 + \frac{|B|}{B_0}} \quad 2$$

En utilisant cette formule, l'erreur est de moins de 4 % pour les angles d'incidence inférieurs à 20°, mais supérieure à 10 % pour des angles plus grands. Afin de réduire l'erreur, les mesures expérimentales sont interpolées avec la formule (3) proposée dans [36], qui est une version généralisée de la formulation précédente (2).

$$J_c(H_i, T) = \frac{J_c(T)}{(1 + \frac{H_i}{H_0(T)})^\beta} \quad 3$$

Dans cette formule, β permet une interpolation plus fine mais pour chaque valeur d'angle, H_0 et β doivent être évalués. (3) permet de réduire l'erreur à moins de 10 % quel que soit l'orientation du champ magnétique extérieur. Une formule similaire est utilisée dans [11]. Le résultat de l'interpolation utilisant la formule de Kim généralisée (3) est donné Fig. 15 .

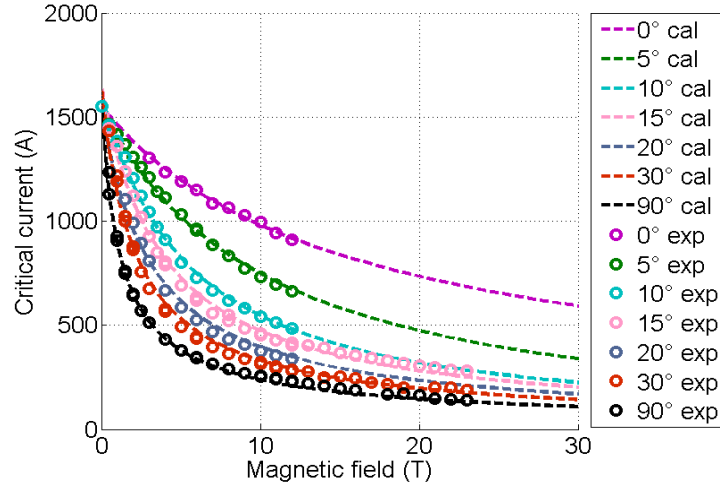


Fig. 15. Interpolation des valeurs de courants critiques mesurées expérimentalement, selon le champ magnétique extérieur et différentes orientations.

Afin de comparer les performances de plusieurs conducteurs et étant donné que les rubans TRBCO ne présentent pas le même courant critique à 77 K, champ propre ($I_{c,min}$ (77 K, champ propre)) fourni par les constructeurs, on préfère dans la suite travailler non pas directement avec les valeurs de I_c mesurées mais plutôt avec leur rapport avec leur $I_{c,min}$ (77 K, champ propre) respectif. Ce facteur permettant de confronter les performances des conducteurs - aussi appelé *lift factor* en anglais - est défini par (4).

$$Lift\ factor\ (B) = \frac{I_c(77\ K, \text{champ propre})}{I_c(4,2\ K, B)} \quad 4$$

1.2.6 Conclusion intermédiaire

Cette caractérisation souligne la difficulté des mesures de transport des rubans TRBCO notamment car elle atteint les limites du courant qui peut être injecté dans un si petit volume. Ces mesures sont non seulement très coûteuses en termes de temps et mais demandent aussi une grande précision. Par manque de disponibilité des aimants et de temps, cette étude n'a pas pu être conduite jusqu'à 30 T. Les résultats de valeurs de I_c mais aussi de facteurs de puissance concordent avec la littérature et les valeurs manquantes de I_c ont pu être extrapolées en utilisant la formule généralisée du modèle de Kim. Les résultats de performance du conducteur vont donc pouvoir être implémentés dans le modèle numérique mais vont également servir à évaluer les marges en termes de courant de l'insert TRBCO final.

1.3 MODELE NUMERIQUE DE TRANSITION D'AIMANTS SHTC

1.3.1 Objectifs du modèle

Le modèle a pour objectif d'approfondir les connaissances sur le comportement d'un conducteur TRBCO bobiné, notamment sous champ. Le but est de comprendre où va débiter la

transition du conducteur à un état dissipatif et comment cette zone va se propager dans le bobinage. L'une des principales spécificités du modèle est de prendre en compte les inhomogénéités de performance du ruban sur sa longueur en initialisant les valeurs de I_c avec les mesures à 77 K, champ propre fournies par le constructeur, en faisant l'hypothèse d'une corrélation avec les valeurs de I_c à basse température [37]. Le modèle permet d'étudier l'influence de ces inhomogénéités sur la propagation de la transition dans un bobinage TRBCO. Le problème majeur des bobinages isolés est de détecter la transition du conducteur avant que le conducteur ne soit détérioré. Améliorer notre compréhension du comportement de tels bobinages pourrait nous permettre de mettre en place des systèmes de protection à la fois plus adéquats et robustes.

Dans la suite, le modèle est explicité pour une simple galette mais il peut également être utilisé pour étudier une double galette. Le modèle permet alors de simuler soit une rampe de courant, une rampe du champ magnétique extérieur, une élévation de température du conducteur locale ou globale ou encore une combinaison des trois.

1.3.2 Description du modèle d'origine

Le modèle présenté est développé à partir d'un modèle de limiteur de courant mis au point antérieurement par l'équipe. Il utilise Matlab et sa « boîte à outils » Simulink. Le circuit électrique utilise une source de tension AC ou DC ainsi qu'une impédance de sortie qui représente le réseau dans lequel le limiteur de courant est inséré. Des simulations de défaut sont alors étudiées à l'aide d'un interrupteur parfait connectant une impédance choisie de défaut au réseau.

Le principal objectif du modèle est d'étudier l'influence des inhomogénéités du conducteur sur l'élévation en température pendant le fonctionnement du limiteur. Le modèle étudie le comportement du limiteur sur une gamme de températures allant de 77 K à 65 K et la longueur du conducteur bobiné est initialisée avec les valeurs de I_c à 77 K en champ propre fournies par le constructeur. Le ruban est donc découpé en plusieurs blocs avec des valeurs de I_c différentes et pour chacun des blocs, la proportion de courant passant effectivement dans la couche supraconductrice du conducteur est ensuite évaluée. En calculant la distribution de courant pour chaque bloc dans les couches résistives, l'élévation de température du conducteur est évaluée à chaque pas de temps.

Le limiteur est bobiné de manière à réduire son inductance et donc la création de champ magnétique, ce dernier est donc négligé pour évaluer les courants critiques le long du conducteur. De plus, afin de maximiser les échanges avec le bain d'azote dans lequel il est plongé, le bobinage d'un limiteur est lâche. Le modèle ne prend donc en compte que les échanges thermiques le long du conducteur et non les échanges d'une spire à l'autre du bobinage. Le modèle est développé plus en détails dans [38].

1.3.3 Améliorations nécessaires pour simuler le comportement d'un aimant SHTC

Afin de modéliser des bobinages d'aimant, plusieurs ajustements doivent être mis en place dans le modèle de limiteur. La première modification est relative au champ qui dans cette configuration n'est plus négligeable. Les composantes de champ doivent donc être calculées en tout point du bobinage, à la fois celui généré par le bobinage TRBCO étudié lui-même mais également par l'aimant extérieur. Ces composantes de champ vont modifier les valeurs de courant critique le long du conducteur. De plus, pour savoir quelle composante de champ va être appliquée sur quel bloc du conducteur, la position dans le bobinage de chaque bloc doit être évaluée avec précision.

La seconde modification est relative au comportement thermique du bobinage étudié. En effet, il ne fonctionne plus en bain d'azote mais en bain d'hélium et les spires sont en contact les unes avec les autres impliquant la nécessité d'implémenter des échanges thermiques entre les spires.

1.3.4 Fonctionnement du modèle d'étude de transition d'aimant

Le modèle n'utilise plus Simulink car dans l'étude d'un aimant, une source extérieure de tension n'est plus nécessaire étant donné le courant connu. L'étude se déroule en deux temps. L'aimant TRBCO est d'abord chargé et, lorsque le seuil de tension choisi est atteint, l'aimant se décharge. Pendant la période dite de charge, le courant peut également être choisi constant, laissant l'opportunité de faire varier d'autres paramètres, comme la température ou le champ magnétique extérieur.

Les étapes de calcul du modèle pas à pas sont détaillées dans Fig. 16. Après avoir initialisé la longueur de conducteur bobiné avec les I_c à 77 K, en champ propre, les valeurs locales de courant critique sont évaluées grâce à la caractérisation expérimentale sous champ selon les composantes de champ auxquelles est soumis le bloc en question, section 1.3.5.2. A partir du I_c local et du courant passant effectivement dans le conducteur, la distribution de courant dans les différentes couches du ruban est évaluée en chaque bloc. La dissipation de chaleur peut alors être estimée en chaque bloc, ce qui permet d'évaluer les échanges thermiques le long du conducteur et donc les nouvelles températures à la fin du pas de temps. Enfin, les nouveaux I_c locaux peuvent être estimés sur toute la longueur du ruban pour le pas de temps électrique suivant. Il est à noter que le pas de temps « thermique » peut être plus faible que le pas de temps « général » si besoin pour des raisons de convergence.

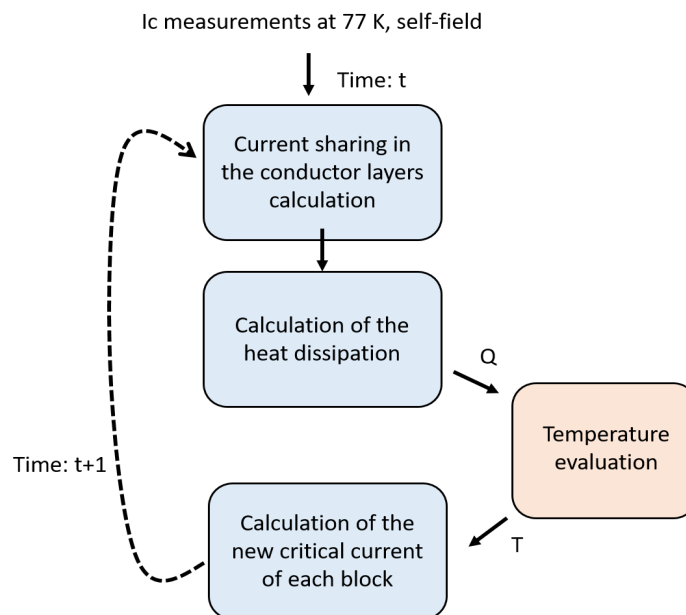


Fig. 16. Schéma explicatif avec détails des étapes de calcul lors d'un pas de temps t du modèle.

Les deux étapes modifiées du modèle original de limiteur sont expliqués plus en détails dans les paragraphes qui suivent.

1.3.5 Détails des modifications apportées au modèle de limiteur

1.3.5.1 Détails de la géométrie

Dans un premier temps, la longueur de ruban utilisée pour le bobinage de l'aimant modélisé est découpée en un nombre de blocs voulu, illustré Fig. 17. Les blocs ont tous une longueur identique pour faciliter par la suite les calculs sur les blocs, que ce soit pour l'évaluation des composantes de champ ou bien les échanges thermiques.

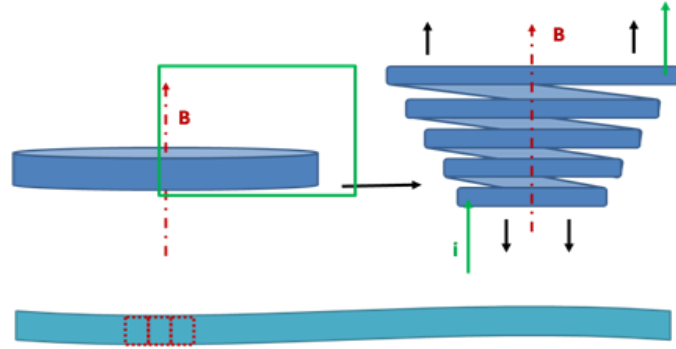


Fig. 17. Illustration de la découpe de la longueur de ruban utilisée pour le bobinage TRBCO étudié.

Chaque bloc est ensuite initialisé par la valeur de courant critique mesuré à 77 K en champ propre par le fournisseur, voir Fig. 6. Dans cet exemple, les I_c sont évalués sur tous les 2 cm. L'objectif de la découpe des blocs est d'obtenir un nombre assez conséquent pour que la valeur minimale de I_c utilisée dans le modèle soit la même que dans les mesures fournies par le constructeur. Pour chaque bloc, la valeur de I_c est définie comme étant la moyenne des valeurs sur cette intervalle comme illustré Fig. 18 où sont données les valeurs de I_c sur une portion de la longueur du ruban étudié. Les valeurs du fournisseur sont en bleu, les blocs utilisés dans le modèle sont délimités par les traits noirs en pointillé et chaque I_c de chaque bloc est donné par une croix rouge. Il s'agit de la valeur moyenne des mesures données sur le même intervalle.

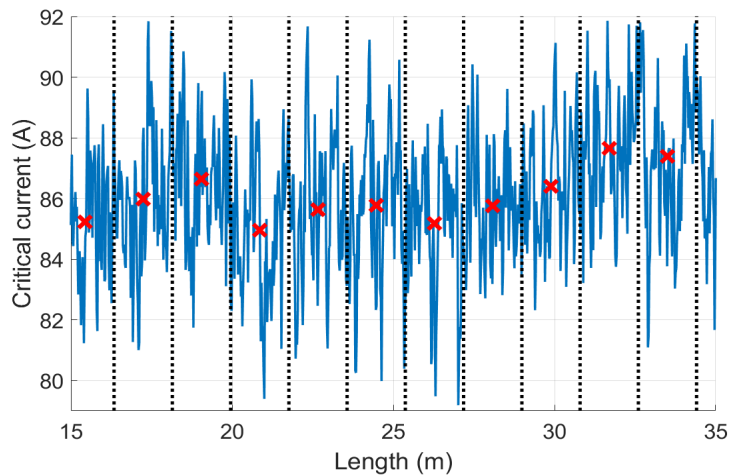


Fig. 18. Courant critique à 77 K en champ propre le long du ruban TRBCO. Les mesures fournies par le constructeur sont en bleu, les blocs du modèle sont délimités par les traits noirs pointillés et la valeur de I_c de chaque block est en rouge, il s'agit de la moyenne des valeurs du fournisseurs sur le même intervalle.

La longueur de ruban étant délimitée en un nombre de blocs fixé et initialisé avec les valeurs de I_c à 77 K, champ propre, il faut désormais évaluer la position de chacun de ces blocs dans l'espace

pour évaluer les composantes de champ qui seront appliquées sur chacune des subdivisions du conducteur. La vue de dessus du bobinage dans laquelle les coordonnées de chaque bloc doivent être définies est illustrée Fig. 19. Une manière simple de représenter un bobinage est de le représenter avec des cercles concentriques avec une épaisseur similaire à celle du conducteur, [39]. Dans cette configuration, il est difficile de garder la même taille pour chaque bloc notamment lors du passage d'une spire à l'autre comme souligné Fig. 20.

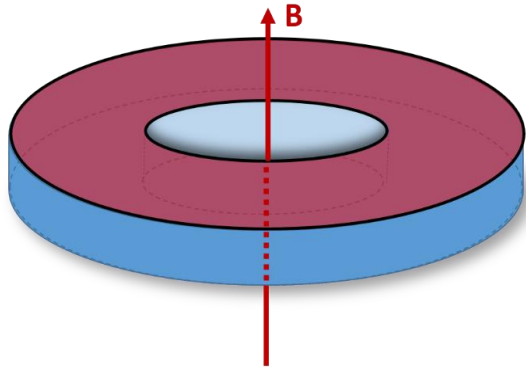


Fig. 19. Schéma d'un bobinage de galette simple avec en rouge la vue de dessus.

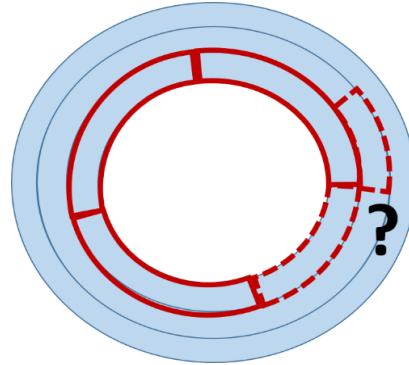


Fig. 20. Vue de dessus d'une galette simple avec les spires représentées par des cercles concentriques.

Notamment à cause de ce problème de saut de couche, le bobinage est assimilé, dans ce modèle, à une spirale, c'est-à-dire que chaque spire est formée de deux demi anneaux dont l'épaisseur est celle du conducteur et dont les centres sont légèrement déplacés l'un par rapport à l'autre selon x , illustré Fig. 21. Un exemple de la géométrie en spirale implémentée dans Matlab est montré Fig. 22 où chaque triangle bleu représente l'extrémité d'un bloc et le profil de la partie intérieure du ruban est la ligne noire.

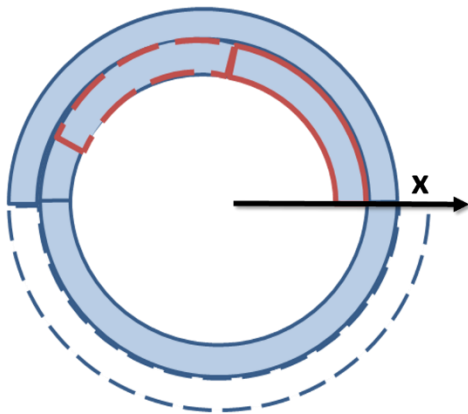


Fig. 21. Illustration de la géométrie en spirale.

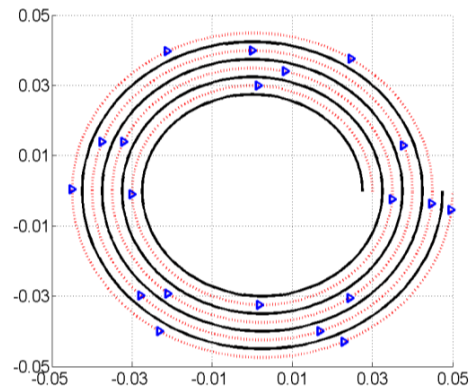


Fig. 22. Résultat de la géométrie en spirale avec Matlab.

1.3.5.2 Evaluation des composantes de champ

Les composantes de champ sont évaluées afin de calculer le courant critique local de chaque bloc. La distribution de champ magnétique est évaluée de la même manière que dans la section 1.2.1, toujours sur un quart de la coupe mais cette fois, les composantes de champ sont évaluées seulement sur l'élément bobiné TRBCO comme illustré Fig. 23.

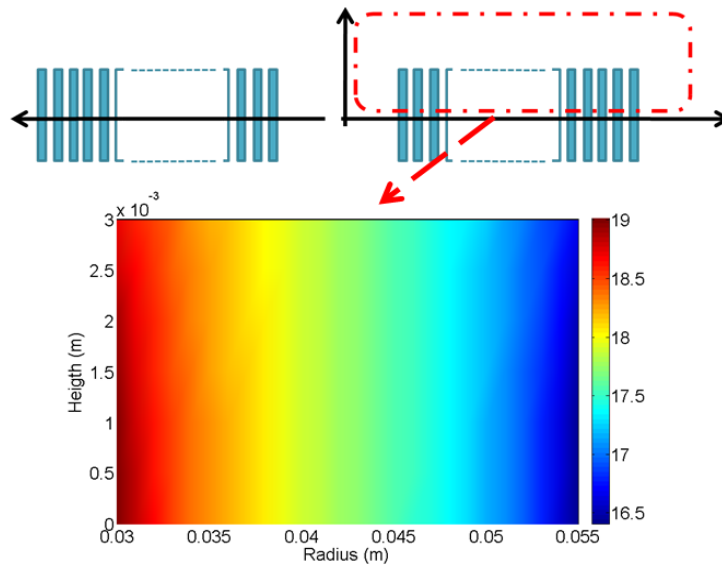


Fig. 23. Figure haute : Illustration de la vue de côté du bobinage d'une galette simple. Figure basse : Distribution de la composante parallèle du champ magnétique appliqué sur une simple galette, quart en haut à droite de la coupe de l'aimant TRBCO étudié.

En connaissant donc les composantes de champ sur la coupe de l'aimant et la position de chaque bloc du conducteur dans l'espace, il devient possible de savoir quelle intensité et orientation de champ seront appliquées sur chaque bloc. En utilisant les facteurs de performance du ruban TRBCO évalués lors de la caractérisation sous champ, voir 1.2, le courant critique local de chaque bloc est calculé à chaque pas de temps considéré. De plus, chaque bloc est également subdivisé dans sa largeur pour pouvoir réaliser le calcul voulu de I_c pour un bloc, par exemple le I_c évalué pour un bloc peut être la valeur moyenne des I_c sur la largeur ou bien la valeur minimum.

Une fois que le courant critique est évalué localement pour chaque bloc, la distribution de courant est calculée, c'est-à-dire que, connaissant le courant parcourant la bobine, la proportion de courant qui passe dans les couches résistives va être estimée pour chaque bloc. Les couches sont assimilées à un pont diviseur de tension entre la couche supraconductrice qui suit la loi de puissance et une couche résistive dont les propriétés sont les moyennes des propriétés de toutes les couches résistives.

1.3.5.3 Introduction des échanges thermiques

Sachant quelle quantité de courant passe effectivement dans la partie résistive du conducteur et dans la couche supraconductrice, la dissipation de chaque bloc est évaluée selon les propriétés des couches qui sont elles-mêmes dépendantes de la température.

Deux versions différentes sont alors proposées afin de calculer les échanges thermiques et donc les températures de chaque bloc à la fin du pas de temps étudié. La première possibilité est de travailler avec une propagation thermique 1D qui utilise la méthode des différences finies. Dans ce cas-ci, seulement la propagation le long du conducteur est prise en compte.

Etant donné l'isolant électrique entre chaque tour de bobinage et la couche de cuivre qui recouvre le conducteur, on pourrait s'attendre à ce que la propagation thermique d'une spire à l'autre soit négligeable devant celle qui a lieu le long du ruban. Cependant, la littérature montre que lorsqu'un bobinage isolé est sévèrement endommagé, une brûlure radiale peut être observée [40] et même dans

le cas d'un quench moins sévère, la transition se propage également radialement [41]. La deuxième version a donc pour objectif d'étudier une propagation thermique radiale et longitudinal. Cette fois, Matlab fait appel au logiciel COMSOL afin de calculer les nouvelles températures à la fin du pas de temps mais en travaillant avec une propagation thermique 2D, illustrée Fig. 24. La création de la géométrie des blocs le long de la spirale dans Matlab a été réfléchi en amont de telle sorte que la création de la géométrie avec COMSOL est immédiate.

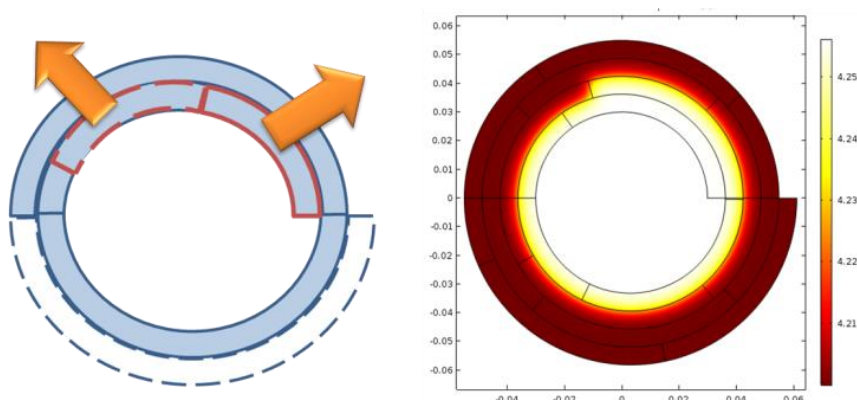


Fig. 24. Illustration de la propagation 2D avec COMSOL.

1.3.6 Résultats d'une simulation type

Cette partie a pour objectif de détailler un exemple de résultats dans un cas précis de simulation pour illustrer ce qui peut être réalisé avec le modèle. Les caractéristiques de la bobine étudiée dans cette simulation sont données dans le Tableau 4.

Caractéristiques de la bobine modélisée	
Diamètre intérieur (mm)	60
Diamètre extérieur (mm)	110
Epaisseur du conducteur (μm)	145
Largeur du conducteur (mm)	6
Nombre de tours	170
Nombre de pancake	1
Coefficient de champ (mT/A)	3.04

Tableau 4. Description de la bobine TRBCO étudiée dans le model.

Dans cette simulation, le champ extérieur est maintenu constant à 0 T, la galette est initialement à 4,2 K et la rampe de courant est de 5 A/s. Dans le cas présenté dans cette partie, la longueur de conducteur est divisée en 500 blocs et la largeur en 4. Le champ magnétique est calculé au centre de la galette et tracé Fig. 25.

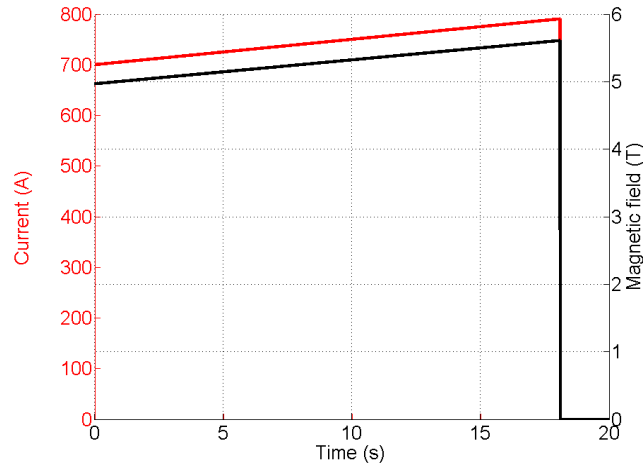


Fig. 25. Courant et champ magnétique au centre de la galette en fonction du temps.

Comme attendu, le champ magnétique ici seulement généré par l'aimant TRBCO est proportionnel au courant. La tension est évaluée pour chaque bloc à chaque pas de temps. Il est donc possible de visualiser le début de la transition dans chaque bloc mais pour une meilleure visibilité, la galette est divisée en six parties dont les tensions, avec celle de la bobine entière sont tracées Fig. 26. On peut observer que la transition commence dans les tours intérieurs du bobinage.

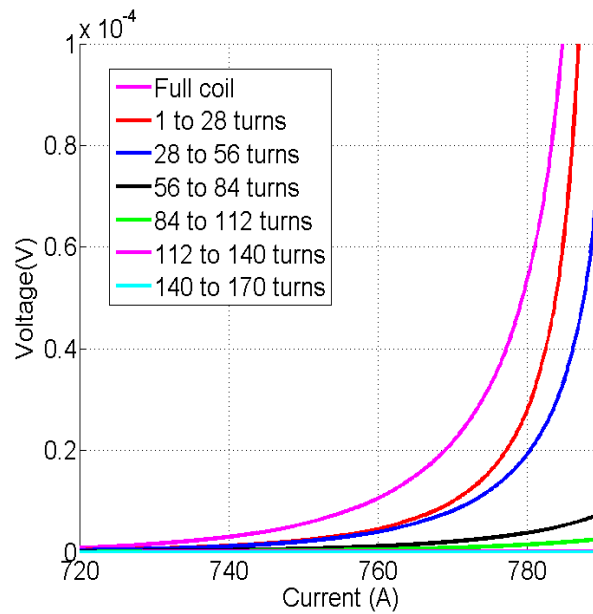


Fig. 26. Tension de la bobine entière ainsi que les tensions de chaque partie de la galette lorsqu'elle est divisée en six parties, selon le courant passant dans le conducteur.

Connaissant désormais l'évolution de la tension dans la bobine, on peut également observer la température, Fig. 27. Dans ce cas-ci, seulement la propagation 1D est utilisée.

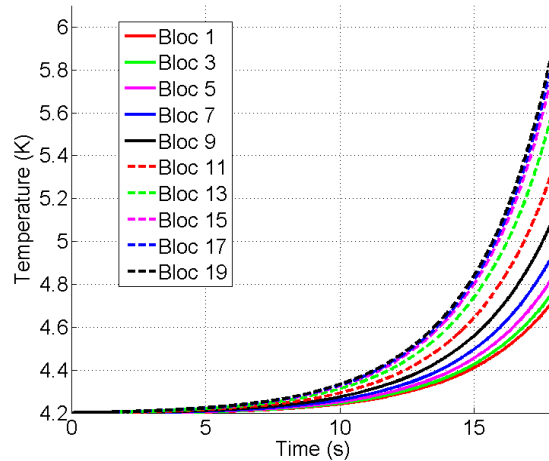


Fig. 27. Propagation de la chaleur sur plusieurs blocs du bobinage, selon le temps.

Il s'agit d'un court exemple pour donner un aperçu de l'utilisation du modèle et de quelle manière il peut améliorer notre compréhension des aimants TRBCO isolés. Les résultats sont présentés pour un courant critique initial constant, on peut imaginer comparer ces résultats à des valeurs initiales de courant critique très inhomogènes le long du conducteur pour voir comment se déplace le début de la transition par exemple.

1.3.7 Conclusion sur le modèle

Le modèle présenté dans ce chapitre est un outil pour améliorer notre compréhension du comportement des bobinages TRBCO isolés notamment lorsqu'une partie du conducteur commence à dissiper. Il permet de comprendre comment les différents paramètres tels que le champ extérieur, la température, le courant passant dans le conducteur influent sur le comportement de la bobine, mais également l'influence des inhomogénéités du courant critique le long du ruban.

Les spécificités du modèle sont donc non seulement la considération des inhomogénéités le long du conducteur mais également la simulation de la galette entière afin de localiser l'initialisation de la transition dans le bobinage et d'observer sa propagation.

L'étape suivante est donc l'étude expérimentale d'éléments bobinés avec un conducteur TRBCO pour compléter l'étude numérique.

1.4 ETUDES EXPERIMENTALES DE BOBINES SOUS CHAMP MAGNETIQUE INTENSE

1.4.1 Premiers tests d'aimant : double galette isolée

1.4.1.1 Objectifs : étudier des comportements mécanique et magnétique de la bobine

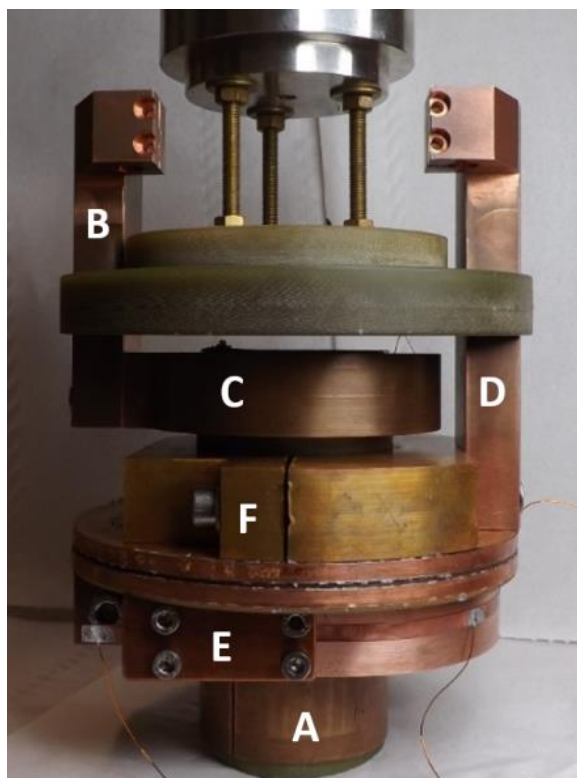
Deux bobines électriquement isolées ont été fabriquées afin d'améliorer la compréhension de leur comportement, notamment sous champ et à très basse température, qui sont les conditions de fonctionnement de l'insert final. La première bobine est une double galette dont le but est d'étudier son comportement magnétique, thermique et les problèmes dus au couplage. Sa principale spécificité est l'absence d'instrumentation intrusive dans le bobinage pour étudier son comportement au plus près des conditions de fonctionnement de l'insert final, en réduisant au maximum les risques d'endommagement pendant la fabrication de la bobine.

1.4.1.2 Description de la bobine

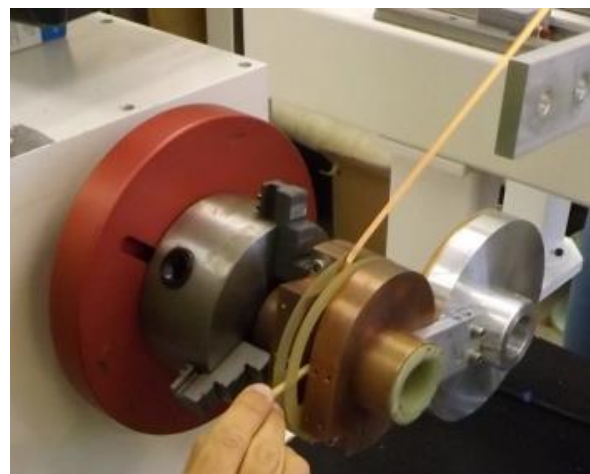
L'allure finale de l'assemblage de la double galette est présentée Fig. 28 (a), avant frettage. Après que le bobinage soit recouvert de ruban adhésif armé (fibre de verre) pour réduire les effets des contraintes mécaniques, il va ensuite être monté à l'extrémité basse de la canne de mesure dédiée. Dans cette configuration, le courant est injecté dans l'assemblage par la pièce en cuivre B qui est vissée sur le cylindre C. Ce dernier est lui-même serré sur le mandrin intérieur en cuivre A sur lequel est serré le cylindre E. A cet endroit, l'une des extrémités du conducteur TRBCO est pincée sous la pièce où est inscrit le E. Le conducteur est entièrement désisolé sur toute la partie où il est en contact avec la pièce en cuivre jusqu'au début du bobinage. L'autre extrémité du bobinage est pincée sur la pièce F, sur le côté non visible de la photo. Le courant peut donc rejoindre la pièce en cuivre D qui est vissée sur F afin de retrouver la source de courant.

La double galette a été bobinée avec une seule longueur de conducteur, c'est-à-dire qu'il n'y a pas de soudure à l'intérieur du bobinage. Afin de réaliser la double galette, le milieu du conducteur est installé sur le mandrin, une moitié du conducteur est enroulée sur la bobineuse pendant que l'autre moitié est sur une pièce satellite qui va venir tourner en même temps que la première galette. Une photographie prise pendant le bobinage est montrée Fig. 28 (b) afin d'illustrer le processus de fabrication.

Dans le but de réduire la déformation mécanique, les deux derniers tours de bobinage sont soudés l'un sur l'autre.



(a)



(b)

Fig. 28. (a) Photographie de l'assemblage de la double galette isolée avant frettage. (b) Photographie prise pendant le bobinage avec une moitié du bobinage enroulée sur le satellite.

Les caractéristiques de la double galette sont données dans le Tableau 5. Il s'agit de la géométrie finale qui correspond aux résultats expérimentaux présentés ci-dessous : à cause d'endommagement pendant certains tests, la bobine a dû plusieurs fois être réparée et donc sa

géométrie modifiée. La bobine a une inductance de l'ordre de la dizaine de milli Henri et un coefficient de champ autour de 6 mT/A. La géométrie de la bobine respecte les limitations géométriques données précédemment. Le ruban TRBCO utilisé pour le bobinage est le même que celui caractérisé en échantillon court sous haut champ magnétique et à basse température.

Caractéristiques de la bobine	
Diamètre intérieur (mm)	58
Diamètre extérieur (mm)	108
Galette supérieure (tours)	170

Tableau 5. Caractéristiques de la double galette isolée.

L'instrumentation de cette galette est non intrusive afin de ne pas altérer le comportement naturel du bobinage, notamment de prévenir les risques d'endommagement pendant la fabrication qui vont impacter les performances de l'aimant en fonctionnement. Le champ magnétique est enregistré par une sonde à effet Hall de type Arepoc (LHP-MU, [42]), placée au centre du bobinage. Des sondes de température de type Cernox sont installées au-dessus et en dessous du conducteur pour surveiller les élévations de température pendant l'expérience. La tension globale du conducteur bobiné est mesurée grâce à des prises de potentiel soudées sur les extrémités du ruban, donc en dehors du bobinage. Enfin, le comportement mécanique de l'aimant est surveillé grâce à plusieurs sondes Kyowa de type KFL-5-120-C1-16 recommandées pour les études à 4,2 K ([43]), utilisées notamment pour étudier les effets dans [44]. Elles sont collées avec du M-Bond 600 ([45]), quatre sur l'extérieur du ruban sur les deux galettes et deux sur les extrémités du conducteur qui servent d'amenées de courant et rejoignent les pinces en cuivre.

1.4.1.3 Protocole et résultats expérimentaux

Le protocole expérimental est illustré Fig. 29. Le graphique du haut montre l'allure du champ magnétique pendant l'expérience. Au début de celle-ci, le champ mesuré est de 8 T, il s'agit du champ fourni par l'aimant extérieur. Ensuite, le courant est progressivement augmenté dans le bobinage TRBCO jusqu'à 125 A, son évolution est tracée en rouge dans le graphique du bas, Fig. 29. L'effet inductif de la bobine est ensuite visible sur la mesure de tension, tracée en bleu dans le graphique du bas. Jusqu'à atteindre le plateau de courant, la tension est constante autour de 3,5 V, il est donc possible de vérifier l'état supraconducteur du ruban TRBCO, la tension n'étant qu'une composante inductive due à l'élévation du courant dans le bobinage, voir formule (5).

$$V = L \cdot \frac{dI}{dt} \quad 5$$

Le plateau de courant permet de vérifier que la tension précédemment enregistrée est bien seulement due à l'inductance, c'est-à-dire que le conducteur est toujours dans un état entièrement supraconductif. Ce dernier est bien confirmé par l'absence de tension lors du plateau de courant.

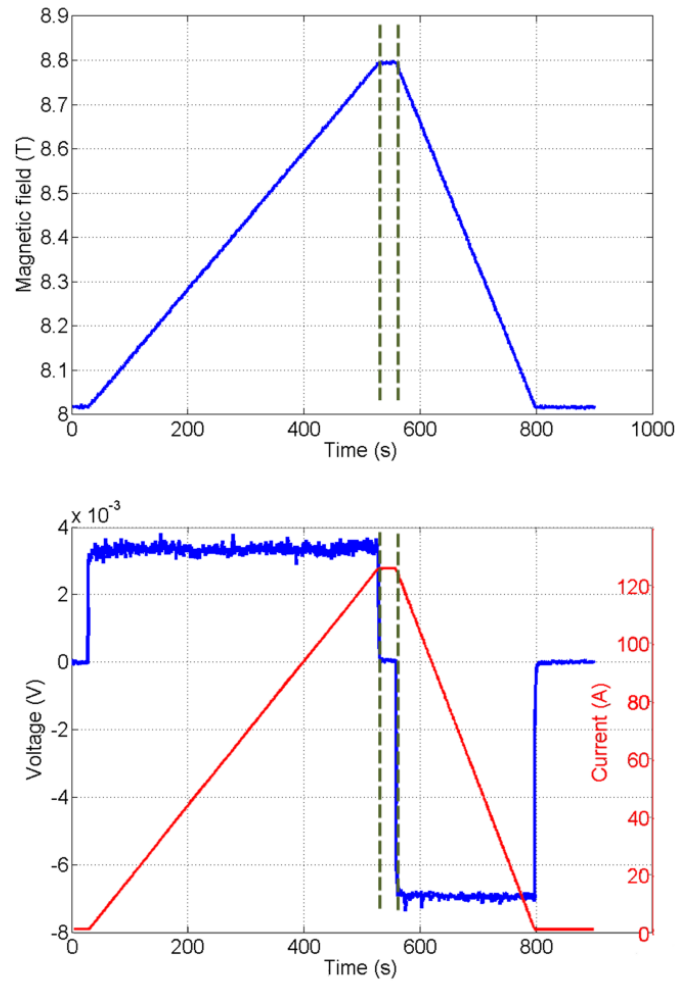


Fig. 29. Rampe de courant dans la double galette isolée avec un champ magnétique extérieur de 8 T.

Ce test confirme également la linéarité et stabilité du champ magnétique généré par l'aimant isolé TRBCO comme attendu.

Concernant le comportement mécanique de la double galette, trois sondes ont cessé de fonctionner dès le début des tests. Les mesures des trois sondes restantes sont rapportées dans Fig. 30 en mauve, bleu et noir en utilisant un module de Young moyen pour le conducteur qui est de 205 GPa ([46]). Ces valeurs expérimentales sont comparées au calcul (trait rouge pointillé) en faisant l'hypothèse que les tours du bobinage se comportent indépendamment les uns des autres ([47]). L'effort mécanique est calculé en tout point du bobinage en utilisant la formule de Laplace (6) mais seule la valeur maximale est tracée Fig. 30 en fonction du courant, soit la valeur calculée sur le tour externe. Les valeurs expérimentales et obtenues par calcul correspondent, confirmant ainsi l'hypothèse de départ.

$$\sigma = J \cdot B_r \cdot r$$

6

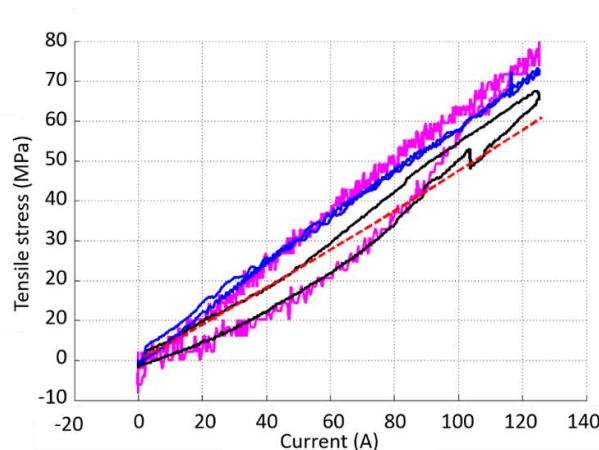


Fig. 30. Mesures des sondes (bleu, mauve, noir) comparé aux valeurs de simulation (rouge pointillé) pour un courant atteignant 125 A sous 8 T.

En conclusion, ce premier aimant TRBCO a permis de confirmer les hypothèses de calcul concernant les comportement mécaniques et magnétiques de la bobine. Néanmoins, à cause à la fois du bruit de mesure de ce type de tests et la volonté de ne pas avoir d'instrumentation intrusive, il n'a pas été possible de mesurer le courant critique limitant de la double galette. Les valeurs maximales atteintes sont 370 A, en champ propre et 280 A sous 8 T, respectivement à 22 % et 30 % du courant critique limitant calculé à partir de la caractérisation en échantillon court du conducteur et des composantes de champ appliquées sur le conducteur bobiné.

1.4.2 Simple galette instrumentée

1.4.2.1 Objectifs : étudier le commencement de transition et sa propagation dans le bobinage

L'objectif principal de la seconde galette est de compléter l'étude précédente et par conséquent de rendre possible la surveillance de la transition locale du conducteur et donc de parvenir à protéger l'aimant avant qu'il ne soit endommagé.

1.4.2.2 Description de la bobine

La bobine étudiée dans cette partie est une simple galette isolée mais cette fois entièrement instrumentée. Les caractéristiques de la bobine sont données Tableau 6. Le conducteur est de composition similaire à celui caractérisé sous champ magnétique intense, sa largeur est cette fois de 6 mm et non plus de 4. La géométrie reste également proche de celle des galettes qui viendront construire le prototype d'aimant final du projet NOUGAT.

Caractéristiques de la simple galette	
Largeur du conducteur (mm)	6
Epaisseur du conducteur (mm)	~0.145
Nombre de tours	170
Diamètre intérieur (mm)	60
Diamètre extérieur (mm)	110
Inductance (mH)	1.16
Coefficient de champ (mT/A)	3.04

Tableau 6. Caractéristiques de la galette simple TRBCO isolée.

L'assemblage final de la galette simple est présenté sur la photographie Fig. 31. De manière similaire à la bobine précédente, il s'agit du montage qui s'insère en bas de la canne de mesure pour permettre à l'échantillon bobiné TRBCO d'être étudié dans le centre du champ magnétique généré par l'aimant extérieur. Le courant arrive par le cylindre laiton E qui est le mandrin sur lequel est soudée une des extrémités du conducteur TRBCO. La tranche du bobinage est alors visible, il s'agit de la surface brillante orange qui se termine en D. Des morceaux courts de conducteur sont ensuite soudés à la fois sur la deuxième extrémité du conducteur bobiné et le disque de laiton C. Les disques C et B sont vissés l'un à l'autre et B étant soudé au cylindre cuivre A, le courant peut retourner à la source de courant. Un schéma explicatif en coupe de l'assemblage est donné Fig. 32.

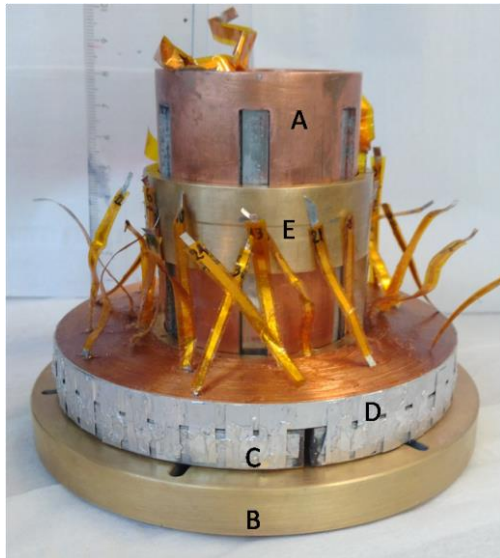


Fig. 31. Photographie de la galette simple instrumentée avant frettage.

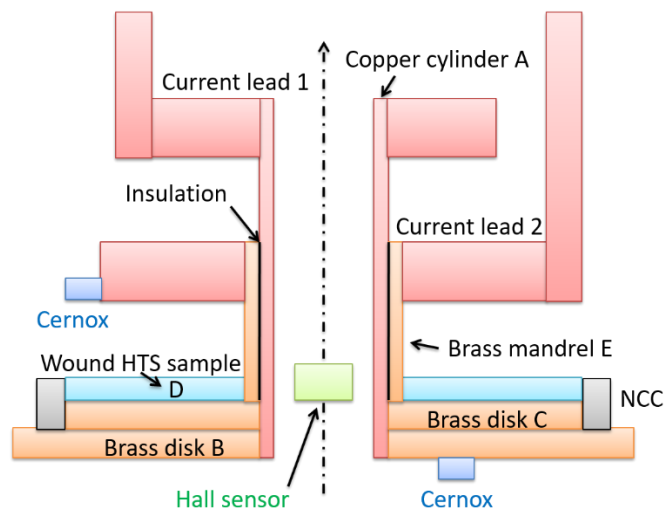


Fig. 32. Schéma explicatif de l'assemblage de la simple galette et son instrumentation.

Une sonde à effet Hall est à nouveau installée au centre de l'aimant pour enregistrer le champ magnétique pendant les tests, voir Fig. 32. Afin de réduire le bruit lu sur les mesures de tension, une bobine de compensation est utilisée, ou NCC en anglais pour *noise compensation coil* (142). Il s'agit d'un conducteur fin de cuivre bobiné autour de la bobine TRBCO étudiée de telle sorte que les inductances soient similaires. Ainsi, la NCC enregistrera seulement le bruit extérieur notamment dû à l'aimant extérieur et permettra en étant soustrait aux signaux de tension de l'aimant TRBCO d'en diminuer les bruits de mesure.

Des sondes de température sont fixées au-dessus et en dessous de l'échantillon bobiné TRBCO pour surveiller la température lors des tests, voir Fig. 34. La différence majeure avec la bobine précédente est la position des prises de potentiel. La galette simple présentée ici possède 33 prises de potentiel soudées à l'intérieur de son bobinage. Il s'agit d'un ruban fin de cuivre béryllium et elles sont positionnées tous les six tours. Afin d'éviter une déformation géométrique du bobinage notamment due à la surépaisseur créée par les rubans CuBe, les prises de potentiel sont légèrement déplacées le long du bobinage comme illustré Fig. 33.

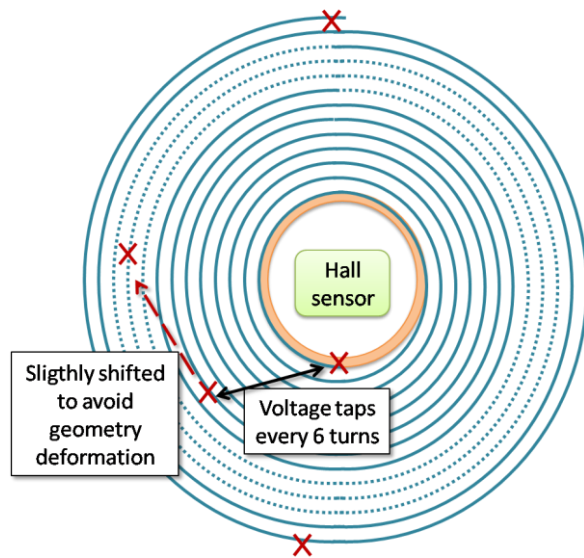


Fig. 33. Position des prises de potentiel dans le bobinage de la galette simple TRBCO.

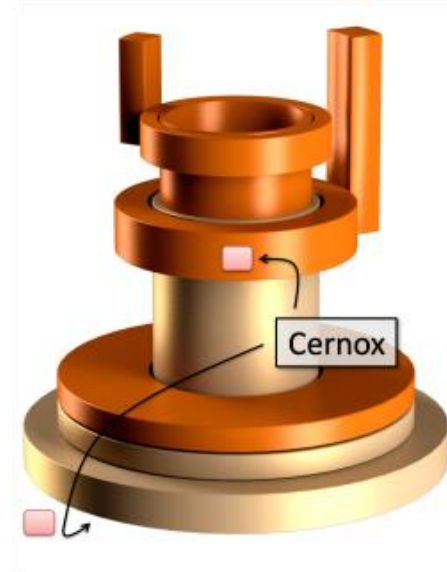


Fig. 34. Schéma explicatif de la galette simple isolée TRBCO donnant la position des sondes de température de type Cernox.

Le but de ces nombreuses prises de potentiel est de localiser le début de la transition dans le bobinage et de pouvoir suivre sa propagation mais avec un risque d'endommagement du conducteur à cause des nombreuses soudures et surépaisseurs dans le bobinage.

1.4.2.3 Protocole et résultats expérimentaux

Le protocole expérimental répond également à l'objectif principal qui est de réduire au maximum le bruit de mesure afin de détecter une transition locale du conducteur. Pour cela, tous les tests seront effectués à la fois avec un champ magnétique extérieur constant mais également un courant traversant le conducteur constant. Le protocole expérimental est illustré Fig. 35. La première étape est l'augmentation du champ magnétique extérieur jusqu'à la valeur cible, dans l'exemple elle est de 19 T. Lorsque cette valeur est atteinte, le courant est augmenté jusqu'à une valeur de courant cible qui est, ici, de 300 A. Il s'agit de la deuxième étape qui est mise en avant par le zoom encadré de Fig. 35. Lorsqu'à la fois le champ magnétique et le courant ont atteint leur plateau respectif, l'assemblage va s'échauffer doucement grâce aux pièces résistives de l'assemblage tout en modifiant la quantité d'arrivée d'hélium du cryostat. L'élévation de température du bain est voulue très lente de telle manière que les deux sondes de température mesurent la même valeur.

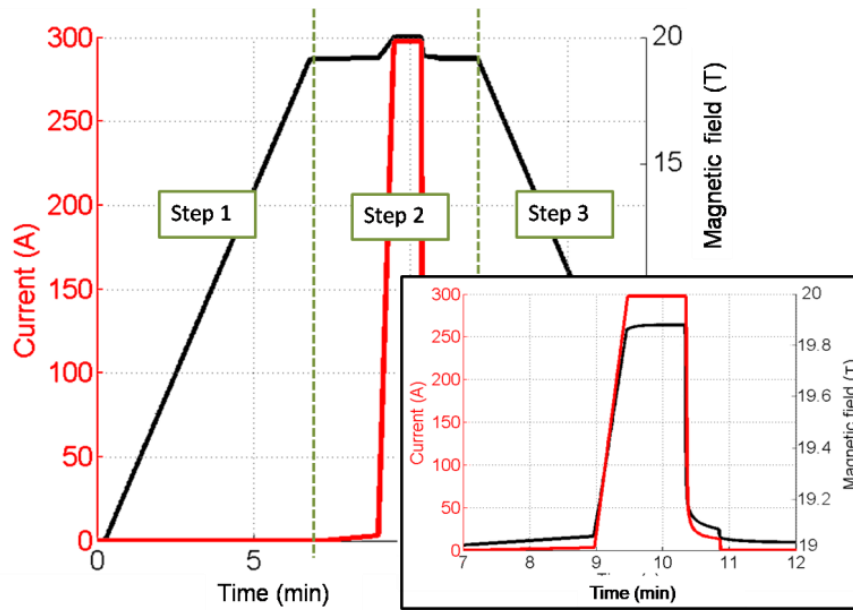


Fig. 35. Illustration du protocole expérimental pour un champ magnétique extérieur de 19 T, le courant à l'intérieur de l'aimant TRBCO atteint 300 A. La courbe noire est la mesure du champ magnétique au centre du conducteur bobiné. La courbe rouge envoie la valeur du courant passant dans le conducteur TRBCO. Le graphique encadré en bas à droite est un zoom de l'étape 2.

L'élévation en température venant notamment du mandrin sur lequel est soudé le conducteur TRBCO, les spires intérieures commencent à transiter lorsque la température se rapproche de $T_c(B)$. Le seuil de détection en tension est choisi à 0,13 mV sur les six premiers tours qui mesurent environ 1,146 m afin de garder le seuil arbitraire de 1 $\mu\text{V}/\text{cm}$ ([48]). Un exemple de transition est présenté Fig. 36, où sont tracées les mesures de tension des premières spires de bobinage et la tension globale de la galette simple TRBCO.

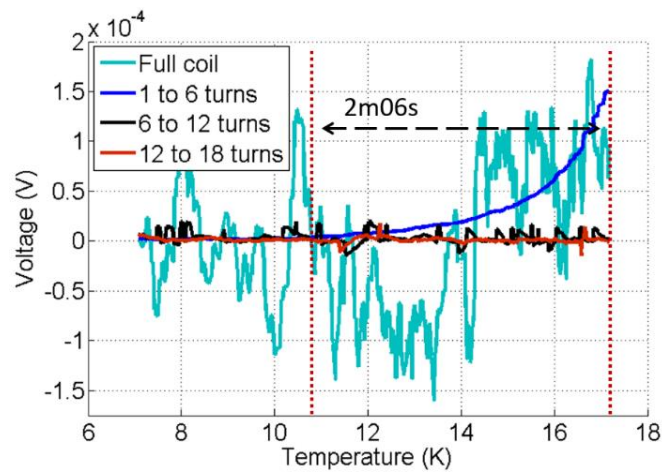


Fig. 36. Transition des premières spires sous un champ magnétique extérieur de 17 T, 250 A passant dans le conducteur.

Les résultats globaux sont présentés Fig. 37. Sur le graphique, chaque anneau est un test de l'aimant sous un champ particulier et un courant passant dans le conducteur. Il s'agit de la valeur obtenue en température lorsque les six premiers tours de bobinage atteignent la tension seuil de détection. La galette simple a été testée de 4,2 K à environ 60 K, pour des courants allant de 150 A à 450 A, à la fois en champ propre et sous un champ extérieur atteignant 19 T.

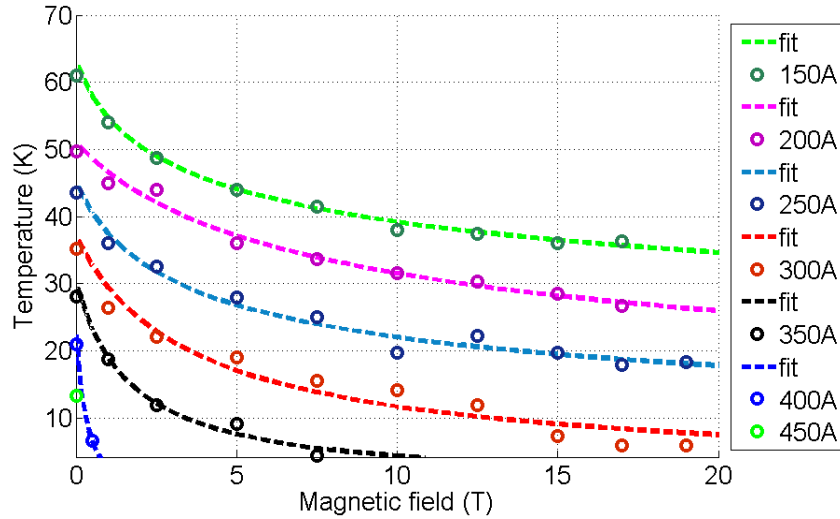


Fig. 37. Températures obtenues lorsque les six premiers tours de la bobine TRBCO atteignent le seuil de tension arbitraire, selon le champ magnétique extérieur et le courant passant dans le conducteur bobiné.

Pour un courant donné, les courbes ont une allure similaire. Les lignes pointillées sont seulement des aides visuelles et ont été tracées en utilisant le modèle de Kim.

Ce protocole expérimental a permis de protéger l'aimant plusieurs fois sans l'endommager. Plusieurs tests témoins ont été réalisés de nombreuses fois pour vérifier que des valeurs identiques en température étaient trouvées. Cependant, l'un des inconvénients majeurs de cette méthode est que l'échantillon bobiné étant chauffé, il n'y a pas de valeur mesurée à 4,2 K. Néanmoins, Fig. 38 montrent la globalité des résultats expérimentaux tracés autrement, il s'agit cette fois des températures atteintes selon le courant dans le conducteur pour différentes valeurs de champ magnétique extérieur. Dans cette configuration, les droites semblent cette fois linéaires et parce que les valeurs mesurées sont nombreuses et proches de 4,2 K, il est possible d'extrapoler les valeurs à 4,2 K.

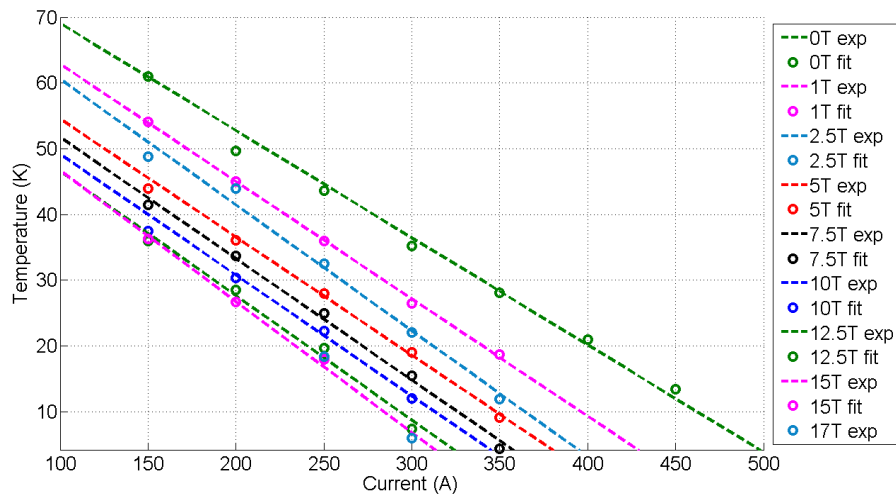


Fig. 38. Résultats expérimentaux obtenus sur la galette simple TRBCO instrumentée. Il s'agit des températures obtenues lorsque le seuil de détection en tension est atteint sur les six premiers tours du bobinage pour un champ magnétique extérieur donné et un certain courant parcourant le conducteur.

En utilisant la caractérisation d'échantillons courts sous champ et en évaluant les composantes de champ appliquées sur le bobinage de la galette simple TRBCO, il est possible d'estimer son courant critique limitant à 4,2 K selon le champ magnétique extérieur. Fig. 39 compare l'extrapolation des

résultats expérimentaux à 4,2 K avec deux méthodes de calcul du courant critique limitant de la bobine étudiée.

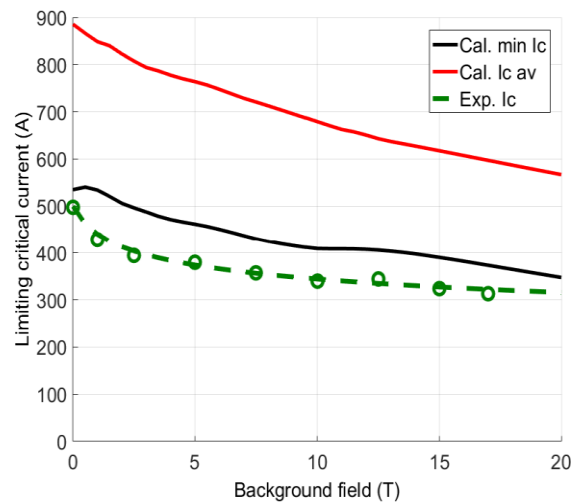


Fig. 39. Courant critique limitant à 4,2 K de la galette simple évalué numériquement (traits continus en rouge et noir) comparé à l'extrapolation des résultats expérimentaux.

Fig. 39 montre que l'extrapolation des résultats expérimentaux n'est qu'à seulement 20 % de la courbe noire, malgré une instrumentation très invasive du bobinage. Ceci est prometteur pour les bobinages TRBCO. Ces résultats expérimentaux servent également à comprendre le comportement du conducteur bobiné sous champ ou en champ propre selon le courant passant dans le conducteur car toutes les transitions mesurées peuvent être comparées les unes avec les autres comme celle présentée Fig. 36.

1.5 CONCLUSION

Le travail présenté s'inscrit dans le projet NOUGAT dont l'objectif est la réalisation d'un insert TRBCO 10 T qui fonctionne sous 20 T produit par un aimant extérieur. Le prototype final d'insert sera un empilement de bobinages métalliquement isolés, principalement pour leur capacité d'autoprotection. Néanmoins, ce type de bobinage ne peut être utilisé pour toutes les applications et même dans le cadre d'un aimant haut champ, leur linéarité et stabilité de champ ainsi que leur dynamique peuvent poser problèmes. Il est donc pertinent à plus long terme d'étudier la faisabilité d'aimants TRBCO isolés fiables, et c'est dans cette logique que s'inscrit le présent travail.

Dans le cas d'un bobinage isolé, la capacité calorifique élevée et les inhomogénéités du conducteur sont à l'origine de points chauds locaux qui peuvent endommager irréversiblement le ruban TRBCO. De plus, à cause d'une vitesse faible de propagation de la zone normale, le signal en tension à détecter risque d'être noyé dans le bruit de mesure intrinsèque à un environnement de champ intense. Ceci rend donc difficile la mise en place d'un système de détection et de protection pour les bobinages isolés de même que l'évaluation de leur performance sans risque d'endommagement.

Le travail présenté ici se déroule autour de trois axes principaux. Dans un premier temps, le conducteur est caractérisé sous haut champ magnétique, jusqu'à 23 T sous différentes orientations et une température allant de 4,2 K à 77 K. L'objectif de cette caractérisation est double. Il a pour but d'obtenir des données de performance récentes car les rubans TRBCO sont continuellement améliorés

mais aussi de prendre en main le conducteur qui reste très délicat à manipuler, plus particulièrement lorsque leurs limites sont testées (haut champ, basse température). Un protocole de mesure expérimental sous haut champ, élaboré en utilisant les installations du laboratoire, a permis de caractériser un conducteur SuperOx pour lesquels les performances n'étaient pas encore disponibles au moment des tests.

Le deuxième axe est l'étude d'un modèle de transition de galette simple et double afin de prédire l'initialisation de la transition et comment cette dernière va se propager le long du conducteur bobiné. La précédente caractérisation sous champ y est implémentée afin de prendre en compte les plus récentes performances du conducteur. Ce modèle est le premier à notre connaissance à prendre en compte les inhomogénéités du conducteur pour étudier les phénomènes de transition. Il est encore en développement mais les premiers résultats sont encourageants, permettant également la comparaison avec des tests expérimentaux d'aimant sous champ.

Finalement, le troisième axe de ce travail est le test de bobines TRBCO sous champ. La première double galette a permis de confirmer les hypothèses de calcul sur les comportements magnétiques et mécaniques des bobinages TRBCO. Elle a aussi permis d'étudier les problèmes de couplage avec l'aimant extérieur bien qu'ils ne soient pas présentés ici. La seconde bobine a permis d'étudier le phénomène de transition et sa propagation en champ propre mais également sous champ jusqu'à 19 T, de 4,2 K à 60 K. Ces résultats ont été rendus possible grâce notamment à sa forte instrumentation en termes de prises de potentiel. Malgré cette méthode de mesure intrusive, la bobine montrait des performances à seulement 20 % des valeurs calculées avec la caractérisation d'échantillons courts. La bobine a survécu plus de 50 débuts de transition, confirmant la procédure de test expérimentale mise en place, à savoir travailler avec une élévation globale de température et un champ et courant constants. Dans certain cas, la transition était même détectable sur le signal de tension du bobinage entier. Ces résultats expérimentaux sont très encourageants et prometteurs pour les bobinages TRBCO isolés.

En conclusion, ce travail étudie l'initialisation d'une transition du conducteur dans un bobinage et sa propagation. L'objectif est double, le premier étant d'évaluer le comportement d'un bobinage isolé afin d'établir des marges de fonctionnement appropriées. Le deuxième but est d'utiliser ces connaissances pour mettre en place des systèmes de détection et de protection robustes. Les premières comparaisons des résultats expérimentaux et numériques sont prometteuses. Même si le modèle montre, pour le moment, des résultats différents, le début de la transition peut être localisé, ainsi que la façon dont elle se propage et l'élévation de la température. L'échauffement durant l'expérience étant difficile à quantifier, plus de simulations mais aussi plus d'expériences sous champ sont nécessaires afin de confirmer ces premiers tests encourageants.

1 INTRODUCTION AND CONTEXT

This first chapter is an introduction of the necessary general knowledge to understand the context of the present work. Section 1.1 details information about superconductivity in general and more specifically on high temperature superconductors (HTS). Section 1.2 is dedicated to magnet technologies, which leads to a presentation of the different ongoing projects around the world in section 1.3. In this latter, the framework of the present work, the NOUGAT project is also detailed. All the first sections up to section 1.4, which presents general knowledge on HTS coils are bibliographic work.

Section 1.5 presents the most important issues that the present work intends to answer.

1.1 SUPERCONDUCTORS: GENERAL KNOWLEDGE

The aim of section 1.1 is to quickly summarize the superconductivity history from their discovery to their applications and to provide the necessary knowledge about superconductors in order to easily understand the following chapters. However, some of the information is general knowledge about superconductivity.

1.1.1 First steps in superconductivity

1.1.1.1 Discovery of superconductivity

In 1911, Heike Kamerlingh Onnes discovered superconductivity in mercury at 4.2 K; it was only made possible thanks to the achievement of the helium liquefaction, couple of years earlier. He measured that under a given temperature, mercury has no more measurable resistance meaning mercury reaches a non-dissipative state under this specific temperature, called critical temperature or T_c , which is discussed in more details in 1.1.1.3.

In ordinary metallic conductors, the electrical resistance decreases with the temperature and then shows a plateau (residual resistance) even at very low temperature, hence they still have a resistance against the current passing through them. On the contrary, for superconductors, the resistance abruptly decreases to zero (resistivity $\rho < 10^{-25} \Omega m$ [49]) under their critical temperature, T_c . The trend of the resistance behaviours according to the temperature for both non-superconductive metals and superconductors are compared in Fig. 40.

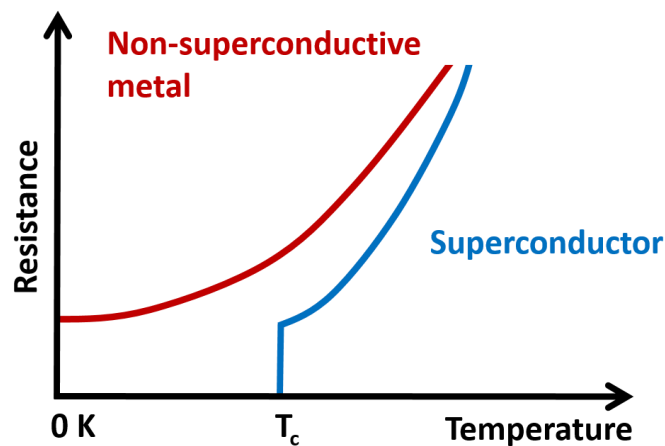


Fig. 40. Trend of the resistance behaviour for a non-superconductive metal compared to the resistance of a superconductor according to the temperature, not to scale.

The other main property of the superconductor is the Meissner effect but it is not developed here as it is not used in the present work.

1.1.1.2 Discovery of High Temperature Superconductors (HTS)

The first superconductors that have been discovered are called Low Temperature Superconductors or more commonly LTS. As indicated by their name, their critical temperature is very low, under 30 K.

High Temperature Superconductors (HTS) have only been found later, in 1986 when cuprate-perovskite ceramic materials were discovered to be superconducting above 30 K. Soon after, further compounds such as YBaCuO were shown to have a T_c above 90 K. At this time, it was the promise of low cost and more practical applications operating in liquid nitrogen. Nitrogen boils at 77 K and is cheaper and easier to setup than liquid helium (4.2 K), which is required for LTS applications. In order to classify superconducting materials, the most common criterion is their critical temperature, T_c . They are considered HTS if their T_c is above 30 K and LTS if their T_c is lower.

However, superconductors can also be classified according to their composition. Most of the superconductors are summarized in the graph below, Fig. 41, according to their year of discovery. In the present work, we focus on cuprate oxides HTS and the most famous are the BSCCO (bismuth strontium calcium copper oxide) and REBCO (rare earth barium copper oxide) families, both in blue in the graph. Also, some iron-based compounds were found to be HTS; they are more commonly called iron pnictides, shown in yellow, and the last one to be mentioned is MgB_2 with a bit lower T_c , around 40 K, plotted in green. Eventually, H_2S has the highest T_c but only under high pressure.

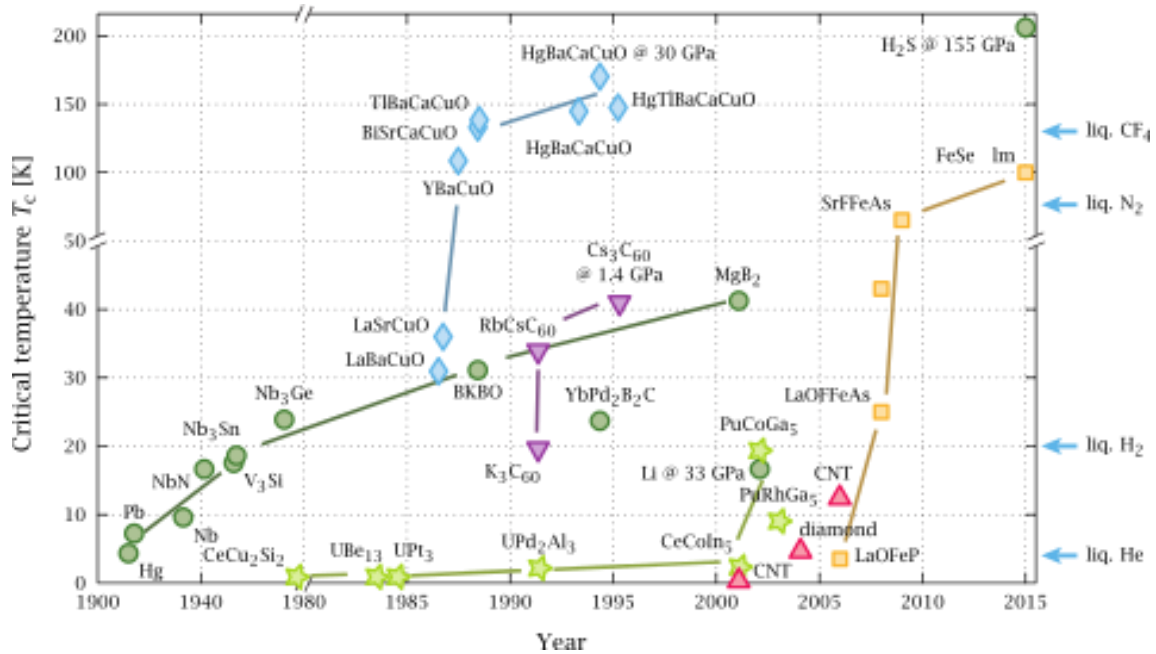


Fig. 41. Superconductor critical temperature as a function of their year of discovery [50].

1.1.1.3 Critical surface

As previously explained, superconductors can be classified according to their T_c , above which the conductor leaves its superconducting state to a dissipative one. This transition is called quench if the conductor is not able to come back to its superconductive state by itself, i.e. an irreversible loss of the superconducting state.

Moreover, the superconducting state of these materials is not only restricted by the temperature but also by the magnetic field applied on the conductor and the maximal current that can pass through it while remaining superconductive. These are referred to as critical magnetic field, B_c and critical current density, J_c , respectively. If one of these limits is exceeded, the material starts to be in a dissipative state. Each superconducting material is defined by its own specific limiting values; T_c and B_c are intrinsic properties of the material whereas J_c can be improved by engineering. Fig. 42,

shows a critical current measurement: the current is ramped in a short straight YBCO conductor. The increase of voltage underlines the change of state of the superconductor from its superconductive state to its resistive state. The J_c is defined as the current density when reaching a defined electrical field, generally $1 \mu\text{V}/\text{cm}$ for HTS.

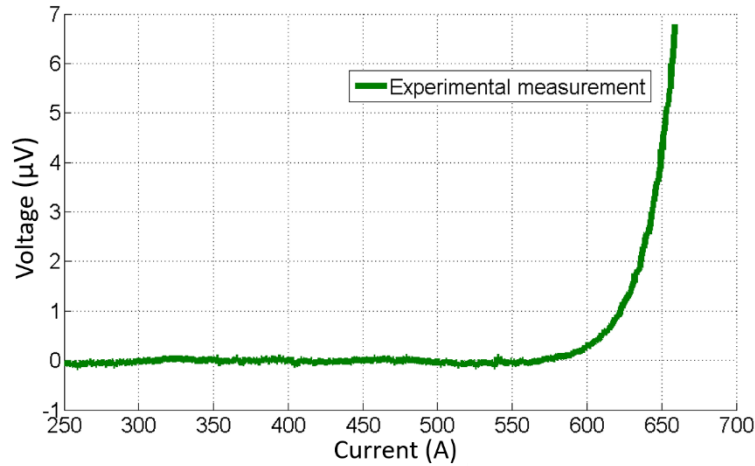


Fig. 42. Transition of a 4 mm tape provided by SuperOx, at 4.2 K under 8 T.

These limiting values of current, field and temperature define a critical surface, which is specific for each superconducting material. As expected the critical surface of HTS is bigger than that of the LTS mainly because they stay superconductive under higher temperatures. In Fig. 43, although not to scale, the sketch gives an idea of the trend of the critical surface of these materials.

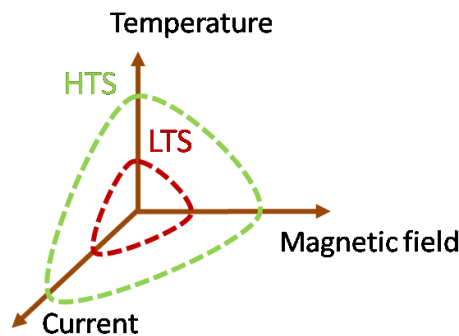


Fig. 43. HTS and LTS critical surface trends, not to scale.

However, in practice, the limits of the superconductive state are more complex because of the anisotropy of the conductor properties as explained later in 2.4.2. Moreover, the critical surface is also influenced by the superconductor's mechanical deformation, see section 1.1.2.1.

1.1.1.4 Two types of superconductors

Even if superconductors are popularly classified according to their critical temperature, they are also divided in two categories according to their intrinsic properties. The two main types are known as type-I and type-II superconductors. The first one includes all the pure elemental superconductors with the exception of niobium, vanadium and technetium. This work focuses only on type-II superconductors.

In a type-II superconductor, for a certain critical field, known as the lower critical field or B_{c1} , the magnetic field is excluded from the bulk of the material. Nevertheless, above B_{c1} , there is no sudden transition to the normal state, but very thin elliptic normal regions appear also referred to as flux lines, passing through the specimen parallel to its axis. As the applied field is increased, they become more and more closely packed together. Only then a second critical field is reached, called upper critical field or B_{c2} , above which the material is entirely in a normal state. The state between B_{c1} and B_{c2} is known as the mixed state. Both B_{c1} and B_{c2} depend on the temperature and are intrinsic properties of the material. This type-II behaviour is illustrated in Fig. 44.

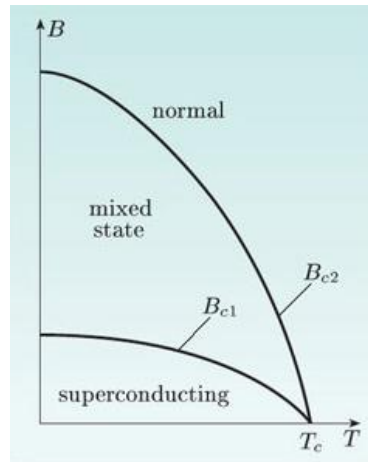


Fig. 44. Temperature dependence of the critical fields for type-II superconductor, taken from [51].

Nevertheless, while studying type-II superconductors there is a magnetic field value that is more used than B_{c1} or B_{c2} for practical works known as the irreversibility field, B_{irr} . This is the field above which flux lines are no longer pinned and start moving, causing dissipation. This behaviour also depends on the temperature. The irreversibility line, which describes the variation of B_{irr} with temperature depends not only on the level of pinning, but more importantly on the degree of coupling between the CuO_2 planes. For poorly coupled materials such as BSCCO, the irreversibility line is much lower than for materials such as YBCO, as underlined in Fig. 45, taken from [52]. The irreversibility lines of talium lines are higher than those of BSCCO but this material is not really good for applications.

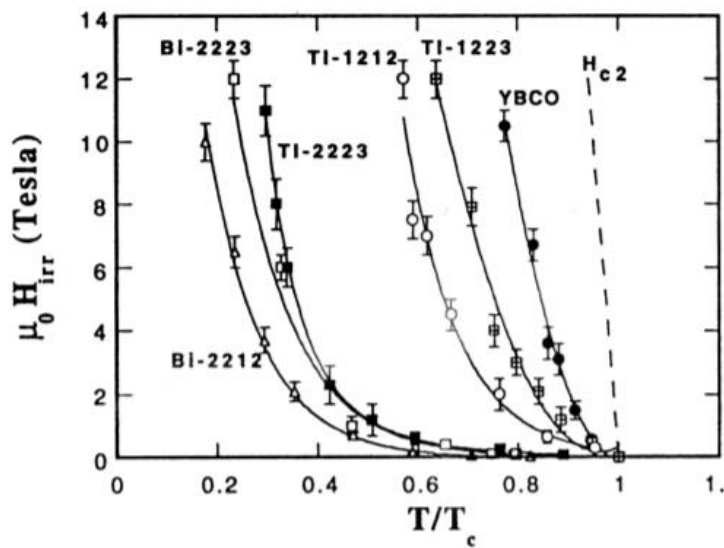


Fig. 45. Irreversibility line for various type-II materials, from [52].

The very high value of B_{c2} of many type-II superconductors [53] (estimated to be higher than 200 T for YBCO [54] at 4.2 K) makes them really attractive for many applications especially for high field magnets. The rest of the manuscript focuses on HTS, more precisely on REBCO coated conductors previously introduced, which belong to the type-II group.

1.1.2 First approach on HTS-specific properties

1.1.2.1 REBCO in details

For now, REBCO are only provided in the shape of a tape for large scale applications because of their fabrication process. This is the result of a complicated strategy for turning a brittle ceramic into a flexible conductor with outstanding properties.

They are built as a stack of thin films, where the superconducting layer is only about 1 μm thick that makes about 1 % or less of the total thickness. This superconducting layer is deposited on a buffer layer itself setup on a flat metal like a nickel alloy or Hastelloy® that allows the conductor to bear strong mechanical stresses (up to 700 MPa). The buffer layer is made in such way that it offers a textured template that induces the biaxial texturing of the superconducting layer essential to the current transport through the deposited grains of REBCO. Providers are mainly using one of the two following methods: either by rolling-assisted, bi-axially textured substrate method, RaBiTs ([55], [56], [57]) or by using an ion-beam-assisted deposition called IBAD ([58], [59], [60]).

REBCO tapes are called coated conductors due to their layers structure illustrated in Fig. 46. One cross-section of a superconducting conductor is drawn according to the SuperOx® data, the layers are not to scale [1]. REBCO tapes are mainly produced with a thickness between 70 μm and 170 μm according to their composition and fabrication process, and a width from 2 mm to 12 mm.

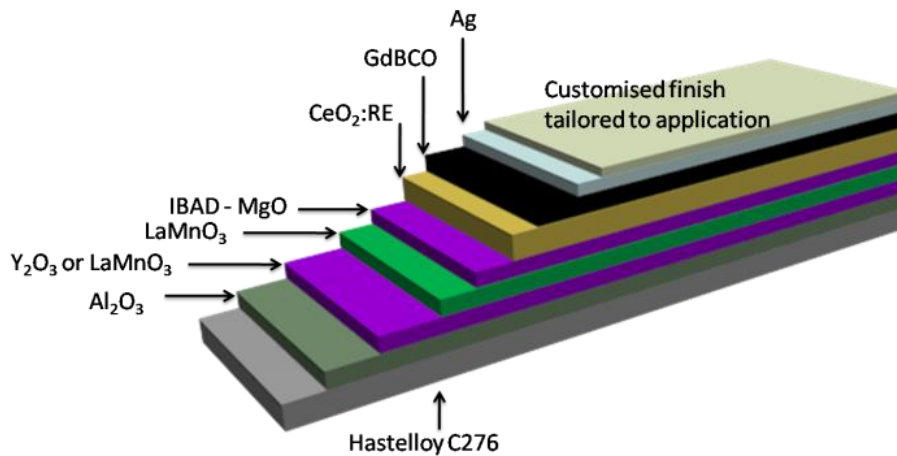


Fig. 46. Not to scale cut of a SuperOx layer according to [1].

Since REBCO conductors are only provided in the shape of a tape, the winding process is slightly different than when using round wires. The different winding techniques are discussed later in section 1.4.1.

Their thin layer ceramic composition makes them brittle and can easily lead to delamination [2], when layers are not in contact with each other anymore. This can be caused by five common

stresses: tensile, shear, compressive, cleavage and peel [61]. Although REBCO coated conductors can handle strong axial tensile stresses, up to 700 MPa thanks to Hastelloy® substrates, this is not the case for other kinds of stresses [3]. In Fig. 47, tape delamination is illustrated, that led at this time to severe damage. One can see for example how the copper layer is removed on the right part of the conductor and other layers are also visible on the left part as the area between the layers is black, probably Hastelloy® or even the superconductive layer. The sensitivity of coated conductors to delamination strongly depends on the interface quality. Specific strategies are employed during winding to mitigate this effect, such as a dry winding or Teflon coating. Epoxy impregnation has been shown to promote this detrimental effect [62]. However, some groups have succeeded with some similar impregnation techniques [63], [64].



Fig. 47. Delaminated conductor after experimental study.

Due to their architecture, REBCO coated conductors have a very low critical curvature limit, about 11 mm [4]. Below this critical bend diameter, the conductor is likely to show severe damage, decreasing its performance and in a worse case it will not be able to transport current anymore. The bending strains are defined according to two principal directions, either it occurs along the conductor axis and it is called easy bending or it is normal to the conductor axis and it is called difficult bending or hard bending. Their influence on the performance of the conductor are investigated in [5]. Moreover, one of the relevant parameters to be considered is the strain limit ϵ which is around 0.4 % [6].

The large anisotropy of the crystal structure has macroscopic consequences as it also yields a strong anisotropy of the material properties [7]. It needs to be taken into account while working with these conductors as their performance can be strongly influenced. For instance, the application of a magnetic field has a severe effect depending on its orientation with regard to the tape. The angle between the background magnetic field axis and the surface of the tape is called incident angle, as illustrated in Fig. 48.

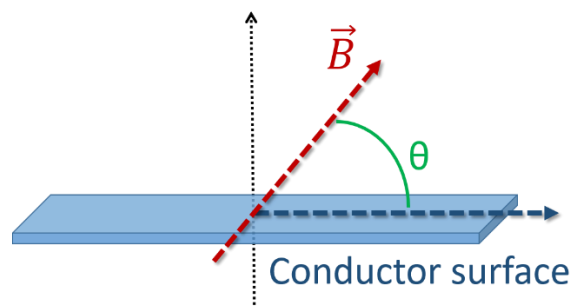


Fig. 48. Incident angle created by the tape surface in blue and the background field axis in red.

When this angle is 0° , which means that the magnetic field axis and the surface of the tape are parallel to each other, the component of the field is then longitudinal. In this case, the tape is able to carry much more current than if the value of this angle is higher. If the angle is 90° , meaning that the tape surface is perpendicular to the background magnetic field axis, i.e. the field only has a transverse component, the conductor can carry much less current as shown in Fig. 49. The critical current can be almost two times lower in perpendicular field than in parallel field. For example, in Fig. 49, for 0° the critical current under 1 T is 55 A and around 30 A under the same field when the incident angle is 90° .

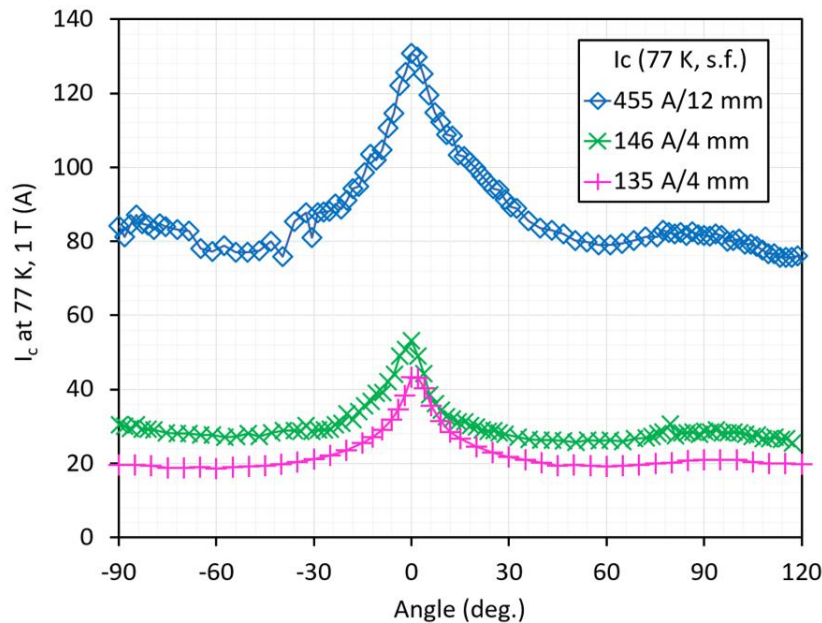


Fig. 49. Experimental results from SuperOx [8] showing critical current according to the field intensity and its orientation.

1.1.2.2 Improvement in HTS tapes over the years

REBCO are nowadays in the heart of many projects around the world in a lot of different application fields, developed hereafter. This was only made possible recently as the price of the coated conductors has rapidly decreased following the fast technology advancements shown in Fig. 50.

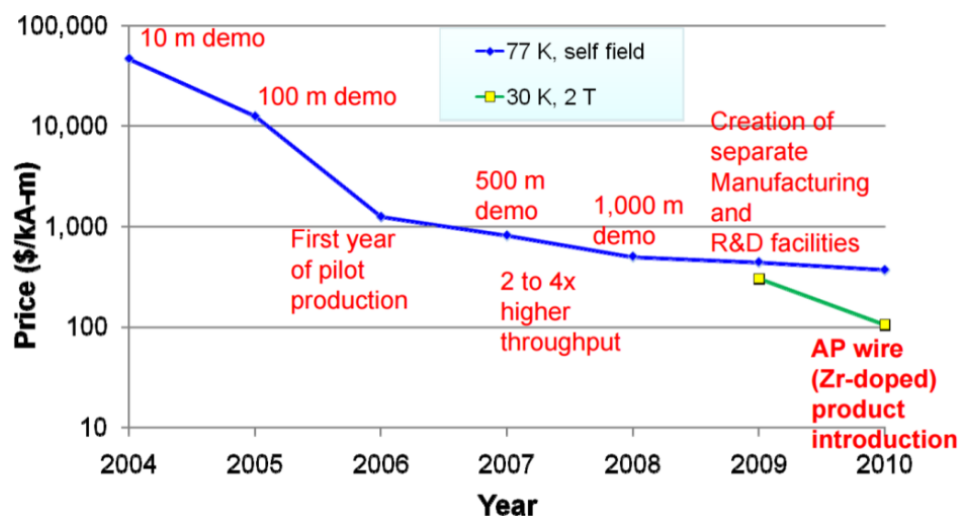


Fig. 50. Advancements in REBCO technology according to the years taken from [18].

In the meanwhile, thanks to this technology improvement, both the critical current as well as the available length kept increasing, as shown in Fig. 51, taken from [19]. Only T_c and B_c are intrinsic properties of the material while J_c depends on impurities and defects introduced purposely during fabrication. This enhancement recently allows providers to sell conductors in long length with high critical current making REBCO large scale applications really promising.

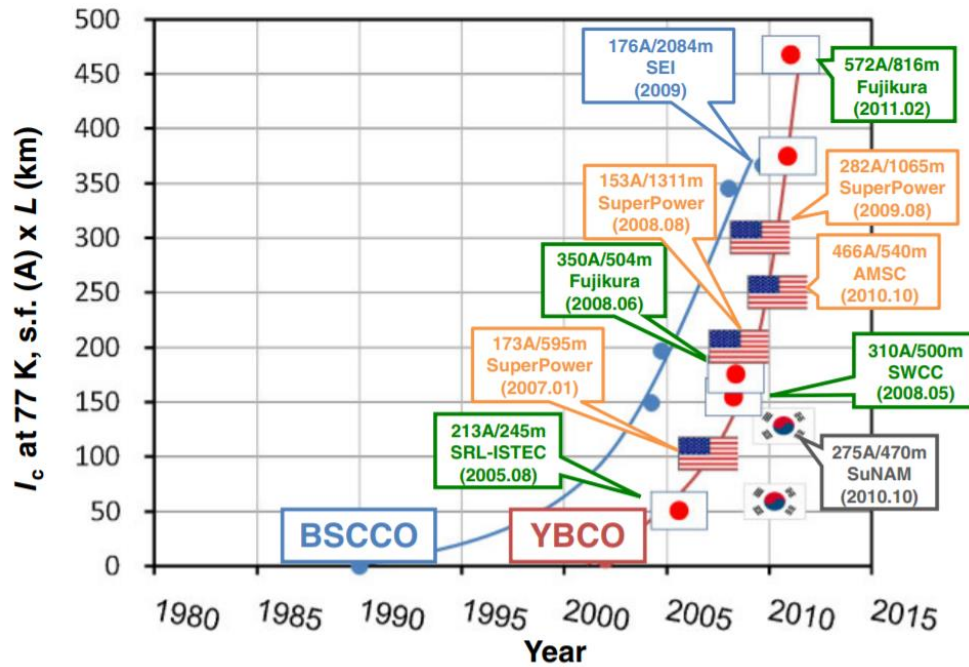


Fig. 51. Critical current improvement multiplied by the conductor length over the years from [19].

1.1.2.3 Inhomogeneity along the length

Despite the available long length REBCO conductors, they remain challenging as they still show inhomogeneities along their length that can lead to severe damages [10]. Each length of conductor is sold with its measurement data at 77 K in self-field, meaning with no background field, conducted with a non-intrusive inductive process. An example of a 77 K measurement along the length provided by SuperOx[®] is shown in Fig. 52. In this data set, measurements are shown every 2 cm, but other manufacturers may only provide this data every 5 m. In Fig. 52, two major drops are present along the length, one at about 120 m and the second at 210 m, circled in dotted red. As a consequence, the tape is defined by its lowest critical current, here about 120 A even if the average is mostly around 145 A, with between 10 % and 20 % variations along the length.

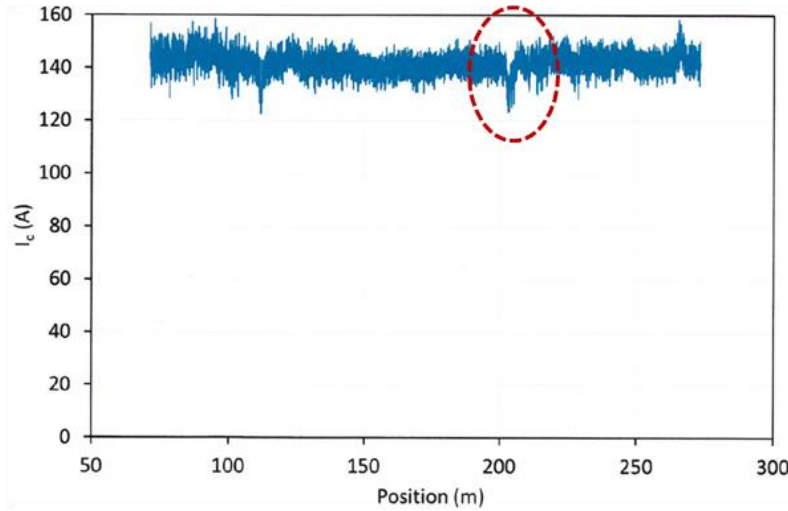


Fig. 52. I_c measurement data at 77 K, self-field for a 4 mm SuperOx coated conductor.

It does not seem possible to find a correlation between critical current values at low temperature/high field and at 77 K/self-field when comparing the performance of conductors from various providers or even from different production batches of the same manufacturer [11]. This is developed in section 2.4.1 and section 2.4.1.2 shows that even if there is no correlation from one tape to another, the performance follows some laws in which constants are varying according to the conductor.

1.1.2.4 Thermal stability

One of the major properties that distinguish HTS from LTS is the quench propagation velocity, which is much lower for HTS [12]. The Normal Zone Propagation Velocity (NZPV) for HTS is between 2 to 10 cm/s [13] and up to 7.5 km/s for LTS [14][15]. This slow propagation means that the transition will not spread along the length quickly enough to prevent the conductor from local heating. Inhomogeneities along the length added to this low propagation can create local hot spots that can irreversibly damage a conductor. More specifically, in a large REBCO assembly, a local transition of the conductor will be hard to monitor as the associated voltage is likely to be buried in the total voltage. The risk is for the conductor to burn before the transition could be detected; voltage and temperature measurements remain problematic for quench detection in large magnets because of this slow propagation velocity. The NZPV is a significant parameter for the protection of superconducting devices and the HTS low NZPV values remain one of the main obstacles to the use of REBCO coated conductors. This low NZPV is mainly due to the very high specific heat of the material [16]. Furthermore, high NZPV values would also allow limiting the maximum temperature attained during a quench so the transverse component of NZPV is crucial in the quench process [65].

Also the minimum energy required to trigger a quench in operating conditions (MQE), is higher than 1 Joule [17] for REBCO conductors, which is approximately three orders of magnitude greater than that of LTS conductors. It means that a REBCO winding is unlikely to be damaged by an outside event but rather by a local defect of the conductor. The protection strategies are discussed in section 1.4.4.3.

1.1.3 Quick overview of large scale applications

Even if LTS have been studied for a long time and have already industrial applications like MRI (Magnetic Resonance Imaging) and LHC (Large Hadrons Collider at Cern), it is still not the case for HTS. During the past few years, the technology has rapidly evolved, not only the properties increased but also the price decreased making coated conductors available and more affordable for large scale applications.

HTS are expected to bring many improvements to electrical engineering such as energy storage and transport as they can carry high currents even under high fields. They promise a decrease in energy consumption, as well as application weight and size, forecasting a bright future for HTS embedded applications.

For now, HTS conductors remain challenging and expensive to use so they are only exploited in niche applications, i.e. when they are the last possible option. Nevertheless, they are at the heart of several projects around the world. Already operating applications and ongoing projects will be quickly exposed in the following to illustrate the already and near future breakthrough technologies. Some applications are summarized in Fig. 53 according to the operating temperature and field.

A few applications using HTS are already operating like in power line setups such as the one settled in the city of Essen in Germany (2014) in the framework of the AmpaCity Project [66]. The project used BSCCO cables. The LIPA II cable can also be mentioned for Long Island Network [67] made of REBCO.

Still in the framework of electric grids, HTS are used for Fault Current Limiters (FCL). They aim at reducing the fault current in case of defect in the grid. Several are setup in Essen, for the AmpaCity project. Other projects around the world are studied in Italy [68], the ASSiSt project for FCL for public 10 kV grid of Stadtwerke Augsburg, Bavaria in Germany or the European FastGrid project, leading to FCL industrialization as some of them are already sold such as WPD in Birmingham and AMAT in Thailand.

REBCO are also used for superconductive transformers in order to reduce the weight and the size and a lot of demonstrators are already working, most of them with BSCCO but also with YBCO like the KIT demonstrator in 2010, Germany (60 kVA), the American Waukesha prototype still in 2010 (28 MVA/69 kV) [69] or a Japanese demonstrator in 2009 (2 MVA/22 kV/6.9 kV) [70].

In conclusion, HTS implementation for motors and generators could allow a reduction of 50 % both in losses and size compared to conventional machines with same specification. That is why they are studied for motors and generators for wind energy applications [71], for electric planes [72] and also to be implemented in ships [73].

Eventually, the spectacular current carrying capacity ratio of REBCO tapes at 4.2 K, illustrated in Fig. 53 makes them promising to fabricate a new high field magnets generation at low cost and we focus now only on high field magnets in the following sections.

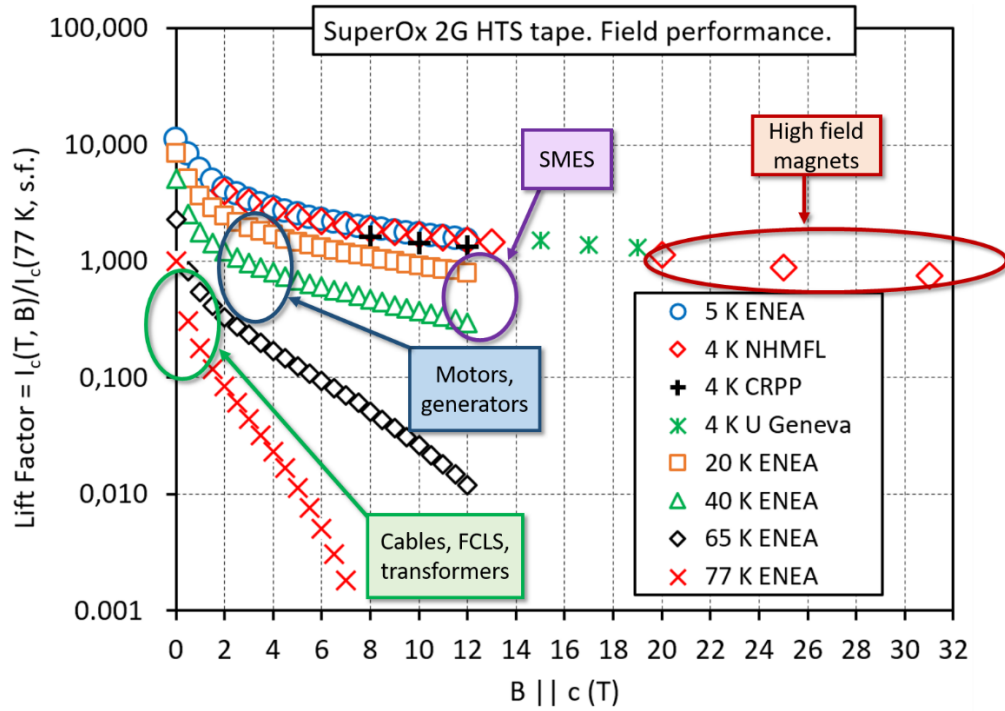


Fig. 53. SuperOx data: critical current factor according to background field and temperature [8].

1.2 MAGNET TECHNOLOGY

1.2.1 Electromagnet

To generate high fields, permanent magnets cannot be used anymore as the maximum field for neodymium material is around 2 T (higher when Halbach type magnet configuration is used [20]). Therefore, electromagnets are fabricated based on the fact that a conductive cable carrying current generates a proportional magnetic field (Oersted experiment, in 1820). Based on this property, electromagnets are made of wound conductors generating in this solenoid configuration a more focused field in their centre and as we will see, many different conductors can be used.

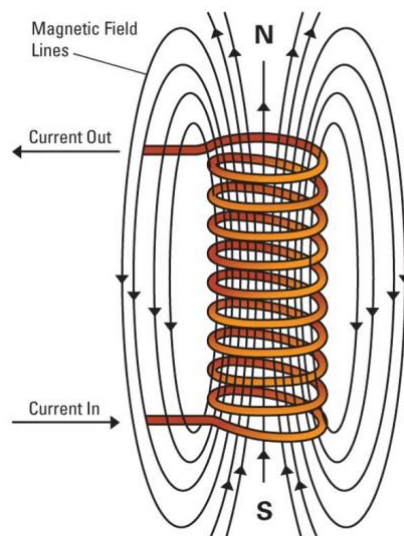


Fig. 54. Sketch of an electromagnet, [74].

First, one should know that this very high magnetic field provided by dedicated laboratories can be either continuous or pulsed. The National High Magnetic Field Laboratory in France or LNCMI (Laboratoire National des Champs Magnétiques Intenses) provides high field to researchers from all around the world, both pulsed in Toulouse and continuous in Grenoble. For now, the LNCMI can reach 36 T in continuous field and 98.8 T in pulsed field. This kind of laboratory is rare as it needs complex and expensive technologies, requiring a high energy consumption, 24 MW for LNCMI and using a substantial cooling system of 300 L of water per second. Pulsed and continuous field are used for different purposes. Pulsed fields allow reaching higher field but only during a really short time (from hundreds of microseconds to hundreds of milliseconds [21]). On the contrary, continuous fields allow reaching rather lower field but during a long time making high power and reliable cooling during operations necessary. For these reasons, superconductors are interesting for continuous fields and the following sections focus on these. One comparison is made in Table 1 between one resistive and one superconducting magnet to underline the possible gain in size and energy consumption.

	Bitter (resistive)	Supercon.	Ratio
Magnetic flux density (T)	10	11	1.1
Core (mm)	500	500	1
Supply (kW)	14 000	5	2 800
Cooling (kW)	200 (pumps)	100 (liquefier)	2

Table 1. Comparison of a resistive and a superconductive magnet.

1.2.2 DC field utility

Continuous field magnets or DC magnets are mainly used for NMR (Nuclear Magnetic Resonance) but also for studying semiconductors and nanophysics, strongly correlated systems, molecular magnetism, mesoscopic physics, magneto-science and applied superconductivity. First, technologies already used to generate high fields are presented, after which several ongoing projects are introduced to show setups all around the world expected to reach higher fields in the near future.

1.2.3 Already existing technologies

1.2.3.1 Resistive magnets

The first high field magnets are made of copper, they form the resistive generation and their technologies are described in [75]; they can be either made with Bitter or polyhelix coils or a combination of both of them. The record has been recently reached by MagLab in Tallahassee, FL, USA when it reached 41.4 T using 32 MW DC power source, in August 2017 as explained in [76]. Not only the field value is important for record but also the inner diameter of the magnet as the smaller is the diameter, the higher can be the field.

1.2.3.2 LTS magnets

Nevertheless, resistive magnets have high energy consumption implying high cost. From 1913, H. K. Onnes imagined superconducting magnet [77] and LTS materials are a next logical step to build high field magnets as they have no heat dissipation at 4.2 K so it promises energy consumption reduction especially during long experiments. According to the current that can pass through LTS materials under high field, they might have reached their limit of 23.5 T with the Bruker BioSpin setup at the CRNM, in Lyon, France in 2009. It is the world's first commercial 1 GHz NMR system [78]. The field generation limit is explained by the materials properties illustrated in Fig. 55.

1.2.3.3 Hybrid magnets

LTS magnets are highly limited by their critical field as explained in section 1.2.5 so the next logical step in magnet development is to fabricate hybrid magnets working both with resistive and LTS conductors. In this configuration, and for LTS not to face too high magnetic field, they are used as the outer part of the hybrid magnet to provide the background field, but then, it has to withstand severe mechanical stresses. The record is still retained by the National High Magnetic Field Laboratory (NHMFL) in Tallahassee, Florida, USA. They built a 45 T hybrid magnet in a 32-mm room temperature bore [79]. This field is reached using a resistive insert that generates 31 T and a 14 T superconducting outsert. Other ongoing projects are being built around the world like the hybrid magnet at LNCMI [80]. In this project, the superconducting part generates 8.5 T and the resistive one 33.5 T in a 34-mm warm aperture. However, when two magnets are working inside one another, they interact with each other and for this reason, in this project, an eddy-current shield is set up between the resistive and the superconducting magnets [81]. Other solutions are investigated such as connecting the magnets in series such as in [82]. The next paragraph explains this interaction.

1.2.4 Inductance and coupling

One of the main properties of a solenoid in electromagnetism is its inductance by which a change in current through it induces an electromotive force in, first, the conductor itself but also in any nearby conductor by mutual inductance.

L is the self-inductance of the coil in Henri, which is linked to the magnetic energy E_m via the following formula:

$$E_m = \frac{1}{2}LI^2 \quad 1$$

In the case of a solenoid [83],

$$L = \mu_0 \frac{\pi D^2}{4h} \cdot \frac{N^2}{1 + 0.45 \frac{D}{h}} \quad 2$$

where N is the number of turns, h is the height of the coil and D its diameter, underlining the influence of the shape of the geometry on the inductance value. This definition is used when Noise Compensation Coil (NCC) is defined to improve the voltage measurement clarity.

When two coils are coupled together, the coupling is defined by the mutual inductance M. The total magnetic energy becomes the formula below.

$$E_m = \frac{1}{2}L_1I_1^2 + \frac{1}{2}L_2I_2^2 + MI_1I_2 \quad 3$$

The mutual inductance M is related to L1 and L2 by the following relation:

$$M = k \sqrt{L_1L_2} \quad 4$$

k is called the coupling coefficient; it is equal to 0 when the coils are not coupled and 1 when they are fully coupled. For thin-walled solenoids, k is simply approximated by the ratio of diameters.

The main objective is here to understand that anything happening in the outer part of the magnet impacts the inner part behaviour and the contrary remains true, meaning that if the insert quenches, it has consequences on the voltage inside the outer coil as well. One has to be aware of these coupling issues as most of the magnets presented in this section are an assembly of several coils. This difficulty is also illustrated in the chapter dedicated to the wound samples as the samples actually experience outsert discharges, see section 4.1.5.

1.2.5 HTS magnets

The next step for reaching high fields and at the same time considerably reducing the energy consumption is to use HTS as they are the only superconductors now sold in length long enough for this kind of application. First discovered, BSCCO materials were first considered for this kind of applications and now both BSCCO and YBCO are used in many ongoing projects. Fig. 55 taken from [84], shows that very high engineering current can still be transported by YBCO tape even at fields higher than 25 T as their critical field is very high [53].

The magnetic field at the centre of a solenoid is proportional to the current passing through the electromagnet. By deriving the Biot and Savart equation, the field produced by a current density J carried by an infinite solenoid is given by the following equation (5). So, the higher is the current, the higher is the magnetic field. However, the produced field not only depends on the current passing through the conductor but also on the geometry of the solenoid as n is the number of turns divided by the length.

$$B_z = \mu_0 \cdot I \cdot n$$

5

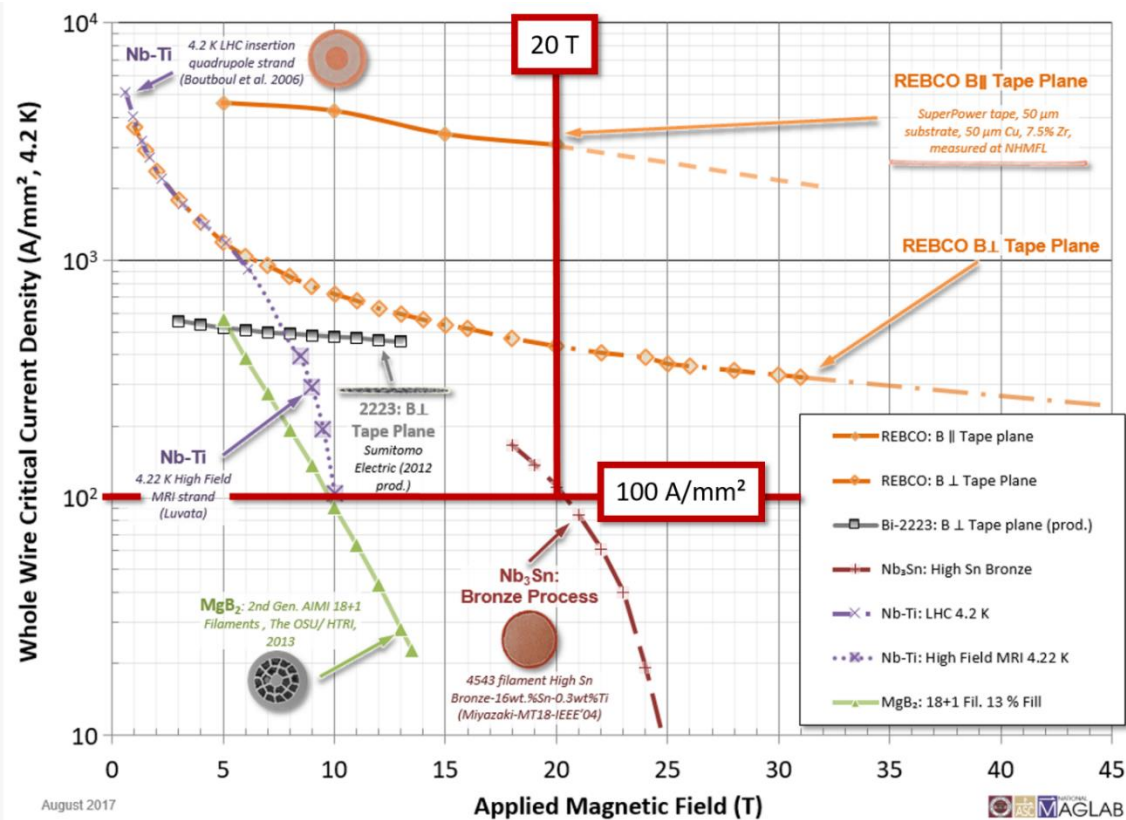


Fig. 55. Critical current density of commercialized superconductors at 4.2 K according to the magnetic field, taken from [84].

1.3 NOUGAT PROJECT AND OTHER MAIN HTS PROJECTS AROUND THE WORLD

This section presents both HTS and HTS hybrid magnet projects around the world to put the framework of the present work in context; the NOUGAT project is then introduced in detail. In a second part, general knowledge about magnets are given in order to fully understand the challenges of this new magnet generation and more particularly, when possible and relevant, applied on the NOUGAT project insert. Eventually, focusing on the NOUGAT project, some design inputs and calculation made during the PhD are presented in order to underline the main challenges and to define the present work problematics.

1.3.1 Quick overview of the projects around the world

There are two kinds of magnets using HTS, it can be either only fabricated with HTS or designed as a hybrid magnet, i.e. an HTS insert working inside a bigger LTS magnet. This kind of project is presented below underlining the main laboratories decisions especially about design; all design terms are more precisely defined and discussed in the section 2.2.

1.3.1.1 Full HTS magnet

The full HTS magnet record is retained by a 26 T 35 mm winding diameter all-GdBaCuO tape magnet designed by the MIT Francis Bitter Magnet Laboratory, constructed and tested by the SuNAM Co. It is a non-insulated magnet using the multi-width winding technique and operating in liquid helium bath [22]. No-insulation and multi-width techniques are respectively developed in more details in 1.4.5 and 2.2.5. The magnet is built with five different types of pancake coil, for which specifications are given in Table 2 to give an idea of the geometry and conductor needs. A photograph of the final assembled magnet and a sketch are shown in Fig. 56, all data are taken from [22].

Parameters	M1	M2	M3	M4	M5
Average tape width (mm)	4.1	5.1	6.1	7.1	8.1
Average tape thickness (mm)	146	145	135	138	135
Stainless steel substrate (mm)	0.11				
Copper stabilizer (μm)	30 (15 per side)				
I_c at 77K, self-field (A/mm^2)	>150/4.1				
Coil Inner diameter ; Outer diameter (mm)	35.0 ; 171.9				
Overall height (mm)	327				
Number of double pancake (DP)	10	4	4	4	4
Turns by DP	914	916	996	968	984
Conductor per DP (m)	297	298	324	315	320
Total conductor (km)	3.0	1.2	1.3	1.3	1.3
Magnet constant (mT/A)	109.2				
Inductance (H)	12.79				
Current density at 26.4 T (A/mm^2)	404	327	293	247	221
Peak hoop stress t 26.4 T (MPa)	286				

Table 2. Specifications of the different coils used in the full HTS magnet, [22].

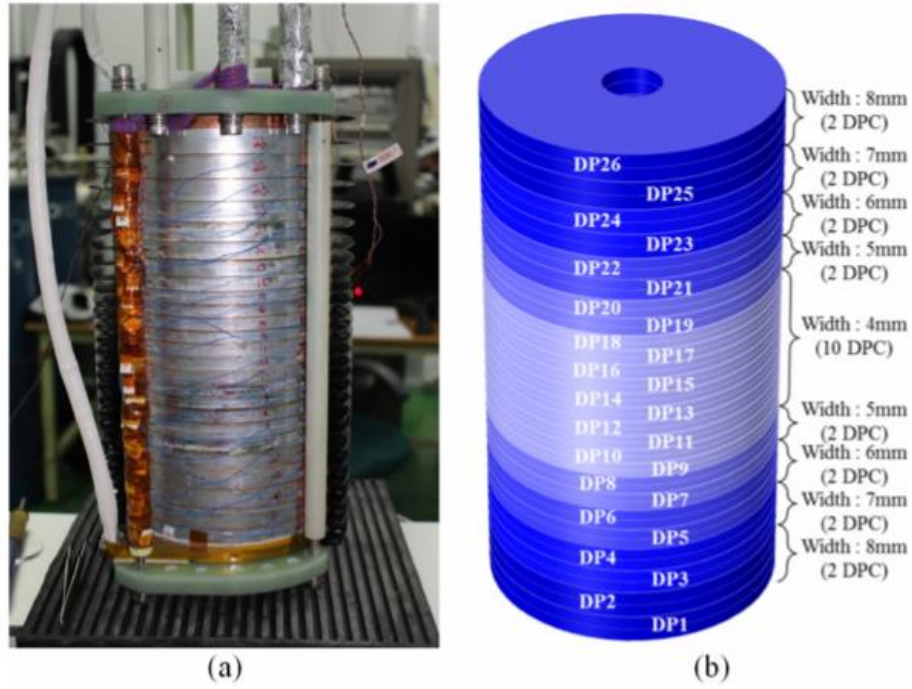


Fig. 56. (a) Picture of the completed magnet after final assembly. (b) to-scale drawing of the final DP coil assembly, [22].

1.3.1.2 Hybrid magnet: HTS Insert in a LTS background

The National High Magnetic Field Laboratory of Tallahassee has designed and built a full-superconducting magnet to provide 32 T in its centre. It is composed of an outer LTS magnet generating 15 T with a separately powered HTS insert made of two concentric REBCO coils that generates 17 T [85], [86]. It has been decided that the insert coil fabrication method is pancake wind, dry wind coils with sol-gel insulation on a stainless steel tape co-wound for mechanical reinforcement. The insert conductor is provided by SuperPower and is protected by heaters. They are calculated to drive enough of the coil in a dissipative state so that the stored energy in this part of the winding does not damage the coil, it is explained in more details in [87].

A second magnet project at Tohoku University, HFLSM in Sendai, Japan aims at delivering a full-superconducting magnet, expected to generate 25 T [88] with an 11.5 T HTS insert [23]. The conductor is provided by Fujikura, a Japanese HTS provider. Two inserts have been tested, one built with BISCCO reached 25 T and one in GBCO which faced a destructive quench while at 24 T.

A third superconducting magnet is under study at the Chinese Academy of Sciences [89]. It is designed to be 25 T full superconducting magnet with a HTS insert expected to generate 5 T in its centre. The superconductor provided by SuperPower [24] is co-wound with a Kapton insulating film.

The Francis Bitter Magnet Laboratory (FBML) in Boston is working on an HTS insert of 18.8 T expected to work inside a NMR LTS 11.7 T magnet already existing at the FBML [25]. This insert uses the notch technology meaning that the pancakes at the centre have a higher inner diameter in order to generate a more homogenous field in its centre. This is explained in more details in the dedicated section 2.2.3.

The four HTS insert characteristics are given in Table 3. Numbers can slightly change according to the design evolution following the ongoing projects development. Nevertheless, they easily give an idea on the size and the properties of each project.

	NHMFL, 32 T		HFLSM, 25 T	CAS, 25 T	FBML, 30.5 T		
Cold inner bore (mm)	34		48	24	91		
Inner coil field (T)	17		11.5	5	18.8		
Outer coil field (T)	15		14	20	211.15		
Number of coil for insert	2		1	2	3		
Operating current (A)	177		135	134.5	250		
Uniformity 1 cm DSV	<5.10 ⁻⁴		NC	1.10 ⁻³	NC		
	Coil 1	Coil 2	Coil 1	Coil 1	Coil 1	Coil 2	Coil 3
Conductor size (mm)	4.1	4.1	5	4		6.1	
Inner diameter (mm)	20	82	48	24	91	150.75	196.90
Outer diameter (mm)	70	116	140	68.9	118.75	168.90	211.15
Height (mm)	53.4	53.4	394.4	253.4	318.60	392.13	465.65
Wire/DP (m)	178	318	NC	NC	120.7	120.7	120.7
Number of disks	40	72	68	44	26	32	38
Turns per disk	255	150	438	NC	185	121	95
Field increment (T)	10.7	6.3	10	5	8.72	5.65	4.42
Current density average (A/mm ²)	193	170	110.8	225.26		544.04	
Peak stress on conductor (MPa)	363	378	461	226		NC	
Self-inductance (H)	2.6	9.9	NC	NC		20.82	

Table 3. HTS inserts specificities given for four different projects.

1.3.1.3 Hybrid magnet: HTS Insert in a resistive background

Most of the all superconductive hybrid magnets are first tested in a resistive background or at least some parts of the windings are tested separately due to coupling issues as resistive magnets are more robust than LTS magnet. This is explained in detail in the next paragraphs. Nevertheless, the final objective is always to build an all-superconductive magnet.

1.3.2 The NOUGAT project

The NOUGAT project has been started in October 2014 and it is expected to finish at the end of 2018; it is a collaboration between CEA, Saclay, and CNRS, Grenoble, founded by ANR (Agence Nationale de la Recherche). The aim of this project is to design and build a DC 10 T REBCO insert working inside a DC 20 T outer magnet; 30 T are expected to be reached in the centre of the final magnet. The first step is to investigate the insert behaviour inside an already existing 20 T resistive magnet in LNCMI to pave the way for a future all-superconducting magnet. The NOUGAT insert is defined to work first inside a resistive magnet mostly because only resistive magnets of this capacity are available in the laboratory. Also, experimental quench studies on winding inside an LTS magnet can be challenging because of coupling issues as explained in sections 1.2.4 and 4.1.5.

1.3.2.1 Objectives

We have seen earlier, in section 1.2.3.1 that resistive DC magnets are already able to generate more than 30 T. One can understand that the aim of this project is obviously not to reach higher fields than the magnetic fields already available worldwide but rather to show the possibility of full superconducting high field magnets allowing a reduction in both cost and energy consumption. This project is aimed at underlining the main challenges and to develop appropriate solutions. Only on a longer term, the next objective would be to reach higher magnetic fields at low cost with full superconducting magnets.

This project is at the heart of YBCO magnets developments allowing at the same time a cost reduction and a decrease of the facility size which could be also used for slightly different applications requiring field generation such as ILL, ESRF, ESS or even CERN. It also participates at increasing the global knowledge about high temperature superconductivity which can lead to major advancements in many topics in a near future. For example, using HTS for motors and generators could allow a reduction of 50 % both in losses and sizes compared to conventional machines with the same specifications.

1.3.2.2 Main constraints

In this project, one of the main constraints is about the geometry as the REBCO insert has to fit inside the already existing resistive magnet in operation at LNCMI. Its cold temperature bore is 170 mm meaning that the maximum diameter for the final insert prototype is about 125 mm. A cross section of the resistive magnet is shown in Fig. 57, where the copper magnets are in red.

The final hybrid magnet prototype is designed as a user magnet, meant to be used by researchers. It implies that the inner cold bore of the insert has to fit the already existing standards allowing users to work with their own equipment. The room temperature inner diameter has been chosen as 50 mm. Therefore, the insert has to be wound on a mandrel with a larger diameter and it has a strong influence on the central magnetic field generated by a solenoid.

Fig. 58 shows the field distribution generated by the resistive magnet evaluated on only a quarter of the cross-section thanks to the field symmetries. The values were calculated by LNCMI from the geometrical details of the magnet; measurements are done systematically along the z-axis for confirmation. Eventually, the magnetic field distribution is drawn using the Matlab software. It is important to already mention the background field distribution to define the insert geometry especially for its height limitation. As we want the insert to work in the most homogenous field as possible, the height of the final prototype has to be around 200 mm maximum.

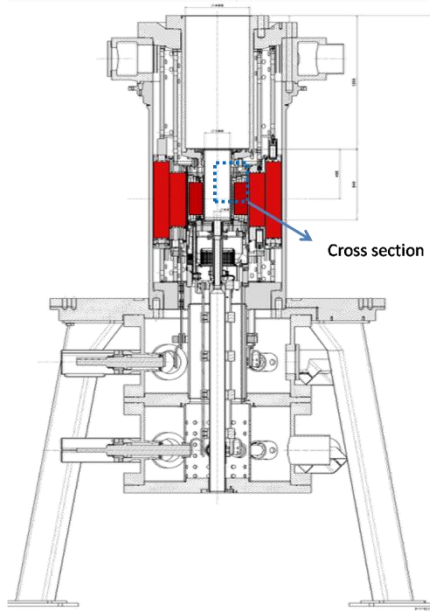


Fig. 57. Cross section of the 20 T resistive magnet, the copper magnet is shown in red.

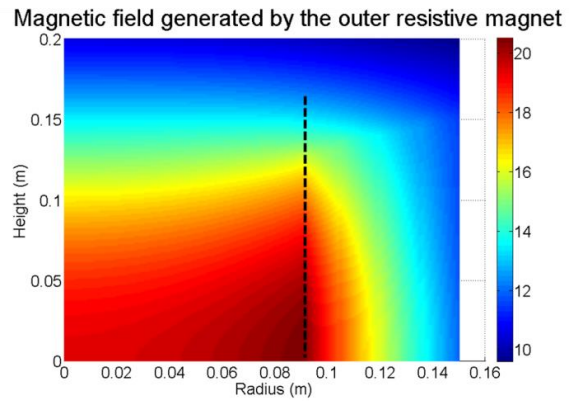


Fig. 58. Quarter of the cross section of the background field distribution. The inner diameter of the resistive magnet is shown by the dotted black line.

1.4 GENERAL KNOWLEDGE ABOUT HTS COILS

1.4.1 Winding techniques: layer wound and pancake wound coils

The particular shape of coated conductors allows two different winding techniques; solenoids can either be layer-wound (LW) or pancake-wound (PW) [61], [90]. In the first technique, the conductor is wound as a helix, layer by layer, meaning from the inner turns to the outer turns. For this kind of winding it is better to use only one conductor for each layer so joints are only on the extremities of the coil. If one layer is made of several conductors, lap joints inside the winding would create extra thickness inside the helix and could provoke local weak point. An example of LW coil is shown in Fig. 59, taken from [91]. With this technique, the transition of different layers is difficult to set up, it is also difficult to optimise the design of the winding by only using LW, for example multi-width design is impossible, see section 2.2.5. Eventually, if there is any issue in the winding, the whole coil has to be rebuilt.

In the second technique, the conductor is radially wound from the inner diameter to the outer diameter as REBCO conductors are tapes. PW looks like a pancake; it is illustrated in Fig. 60. This geometry also allows winding two pancakes at the same time from the inner turn with only one continuous length of the conductor; it is then called double pancake (DP) illustrated in Fig. 61 (a). If two different lengths are used, they are soldered on the mandrel as shown in Fig. 61 (b). Using PW technique allows in a case of a bad event for one pancake to change only the damaged one instead of rewinding the whole coil. PW should also require a smaller length than LW especially for a large magnet; for a DP, a continuous length of conductor less than 1 km should be sufficient whereas it can exceed 10 km for a LW [61]. REBCO fabrication is still challenging and manufacturing lengths longer than 200 m remains difficult. For this reason and also to reduce the number of joints in the windings, a stack of PW is chosen for the design of the NOUGAT project prototype. Nevertheless, both winding techniques are used, [86], [92], [93].

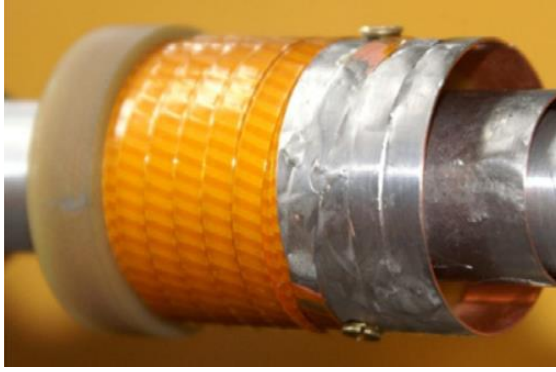


Fig. 59. Layer wound coil, taken from [91].

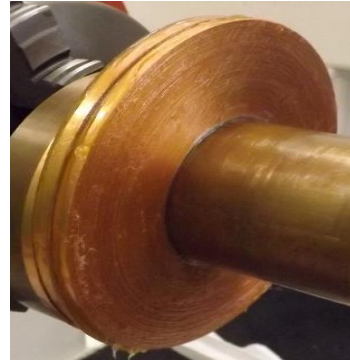


Fig. 60. Wound pancake coil.

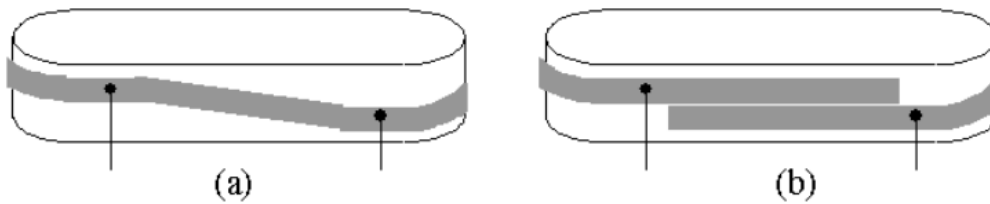


Fig. 61. The two ways of pancake windings; (a) 'cross-over' form one pancake to the other and (b) which is soldered wire, taken from [94].

1.4.2 Conductor width

The width of the conductor has been chosen to be a compromise of the main objectives. First, it aims at taking the higher possible width in order to reduce the impact of the inhomogeneities of the conductor and also minimize the impact of the degradation of critical current density on the edges of the conductor [32]. Moreover, increasing the current inside the conductor leads to a decrease of the inductance, which allows in the end faster charge and discharge time. Another goal is to select the smallest width possible, firstly to reduce the screening effect [95] when the current is passing through the conductor and secondly, to have sufficient margins to optimise the edges of the coil where the transverse field is the highest [96]. This last point is developed in the next paragraphs, see section 2.2.5. To answer these issues, a 6 mm wide tape was found to be a good compromise to wind the pancakes in the middle of the final insert.

1.4.3 Manufacturers

The choice of the manufacturers is developed in chapter 2, dedicated to short sample characterization but the final insert is expected to be fabricated using SuperPower conductors. Pancake and double pancake samples studied in the present paper are wound both with SuperOx and SuperPower conductors.

1.4.4 Winding technique: insulated coil

From an electrical engineering point of view, the expected way to wind a conductor in order to generate magnetic field is to have an electric insulation between every turn of each pancake, not to

create shortcut in the winding which could reduce or suppress the magnetic field generation. When speaking about REBCO tapes, this kind of winding is called Insulated coil or INS coil.

1.4.4.1 Field stability

Electric insulation between every layer induces a linear and stable field [97] meaning that the magnetic field follows the trend of the current passing through the coil with no time delay [98]. Nevertheless, according to the width of the conductor, current creates shielding, which slightly reduces the magnetic field generated by the insert. The consequence of this phenomenon is illustrated in section 1.4.5.2, in Fig. 65. It is also discussed in [95].

1.4.4.2 Quench and damages

In a superconductive winding, in the case of an inhomogeneity or a defect along the length of the conductor, the current will not be able to pass through the superconducting layer anymore. Instead, it will pass through the resistive layers, dissipate energy and cause a voltage increase.

One could have considered that REBCO coated conductors coils are hard to be quenched because of their high quench energy and specific heat, but during operation, presence of defects in the conductor can lead to transition and imply severe damages. For LTS conductors, the thermal stability is small, as well as the heat capacity while the quench velocity and normal zone are large, making the quench detection easy to setup. If a quench occurs in a LTS material, the phenomenon will spread rapidly along the conductor length at a speed from 10 to 1000 m/s. The winding can either self-dissipate its energy leading to a small homogeneous increase of temperature or it can be actively discharged for bigger systems.

On the contrary, for YBCO, the high temperature margin and the low quench velocity make the quench difficult to detect. The transition will spread slowly, from a few cm/s to dozens of cm/s [17], along the tape and it will be difficult to monitor it before it starts damaging the conductor due to the very low measured voltage. This minimum voltage detection is non-trivial as the low voltage value has to be discerned in the presence of extraneous voltage signals while in operating conditions [99]. The key factors affecting permanent damages of REBCO coated conductors are still investigated to be better understood [10].

1.4.4.3 Detection and protection

A magnet quench is often initiated over a small winding volume, the so-called hot spot, which can lead to irreversible damage.

The protection can be either active or passive, which for HTS seems unreachable. Nevertheless, the behaviour during quench can be improved by working on the intrinsic winding properties or by improving the detection sensitivity. It would for example mean spreading the quench heat faster by, for instance modifying the conductor materials; the adequate stabilizer thickness can be determined for REBCO so that the temperature of hot spot does not exceed the permissible temperature [100]. Only the active protection is discussed.

An active protection starts by detecting the presence of an increasing dissipative power and has to be triggered only in a case of a real quench and not on some noise measurement to prevent unnecessary system shutdown. This requires the detection of a small normal zone and its time scale

has to be discussed. The conductor is supposed to stay under a specific temperature during a specific time [99] in order not to be permanently damaged or see its performance reduced [101]. Fig. 62 gives an idea of the degradations that the conductor faces when the temperature and the delay are not respected.

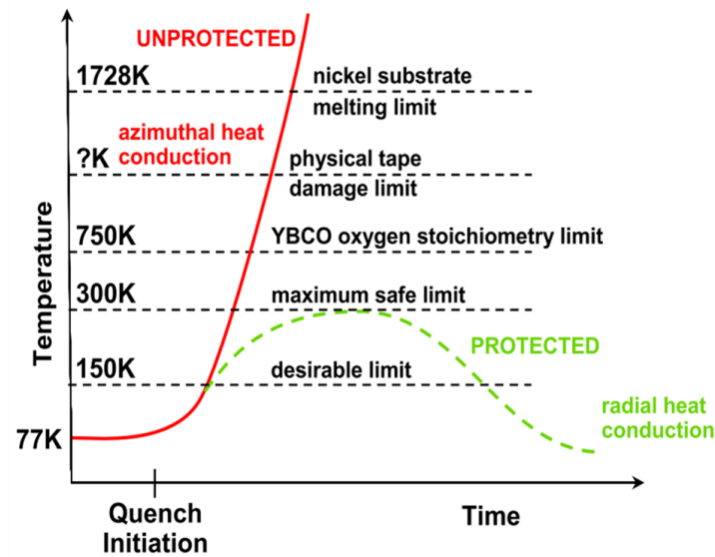


Fig. 62. Temperature and time limits for protection, taken from [102].

However, as recording the transition remains challenging, one of the solutions is to improve the detection for example, by working directly on the conductor. Some techniques are developed to enlarge the normal zone or to propagate the quench faster, i.e. increasing the NZPV to facilitate the quench detection [103].

More specifically about detection, noise compensation coils (NCC) [104] can be used to reduce the noise in the voltage measurements or the magnet recording can also be subdivided in order to detect more locally.

Once the transition is detected, the magnet's protection can be triggered; the magnet can either be discharged in a dump resistance [23] or heaters can be actuated in order to spread the quench faster in the coil assembly [87]. Nevertheless, recording a slow voltage in the presence of real-world signals remains challenging so non-voltage-based detection techniques are being developed (Acoustic Emission –AE– technique) [105] or by using optic fibres [106].

An alternative option is, for example to increase the current margin i.e. the quotient of the operating current (I_{op}) on the critical current (I_c) of the coil to be sure to never cross the limits of the conductor. In the following, the critical current when defined for a coil stands for the limiting critical current during operation, i.e. the current value that limits the coil operation. This value is calculated using only the conductor performance and does not take anything else into account. More information about this calculation is given in section 2.2.4.

1.4.5 Winding technique: Non-insulated coil

1.4.5.1 Self-protection

As suggested by its name, in non-insulated coils or NI coils, the insulation is removed from the winding to build a self-protected coil [26]. If the current cannot pass through the superconducting layer it may bypass the dissipative region by passing through the next turn as illustrated in Fig. 63. Moreover, a voltage would be monitored as the resistance between turns is rather high.

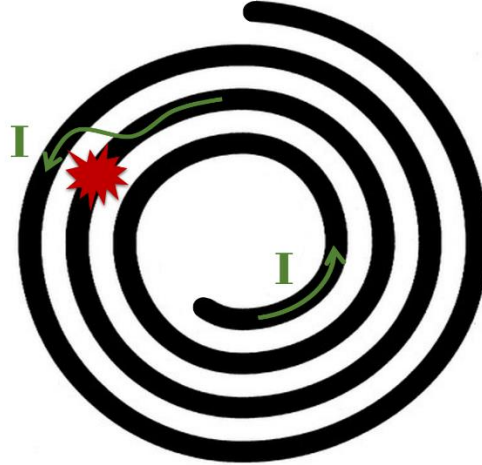


Fig. 63. Illustration of a hot spot in a non-insulated winding.

NI coils have been studied much recently and their behaviour is described in the literature. It is interesting to see the comparison between INS and NI coils to better understand the NI coils' behaviour. In [107], two coils with similar geometry, one with no insulation (coil 1) and one with insulation (coil 3) are studied and compared. During over-current testing, coil 3 burns at about 88 A, which is 1.13 times its I_c ($I_c=78$ A), while coil 1 remains undamaged after being tested at about 1.5 I_c . In this configuration, coil 1 is self-protected and allows working stably with higher current than its critical current without burning the coil but at a cost of a field decrease.

1.4.5.2 Stability

Two stabilities are discussed here, first the thermal stability and then the field stability. In a NI coil the heat propagates more through the winding even if the quench propagates slower which could lead to higher hot spot temperature [108].

An example of the field behaviour is shown below in Fig. 64, which illustrate this field decrease, mentioned in section 1.4.4.1. The field at the centre is not proportional to the current during the whole experiment. As soon as the wound sample starts transiting, i.e. increase of the voltage, the curve of the magnetic field curve changes.

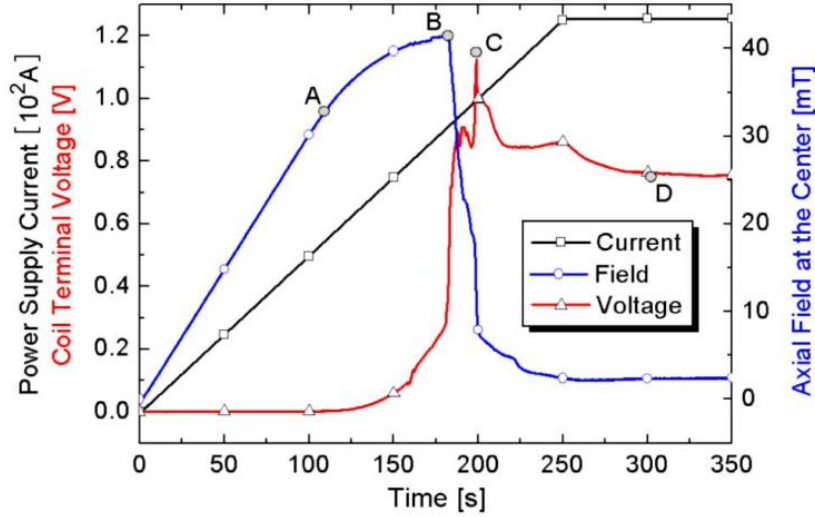


Fig. 64. Overcurrent test results of a REBCO coil up to 125 A. Black squares : power supply current; blue circles: axial field at the centre; red triangles: coil voltage, taken from [109].

This remains true even at lower current than the expected limiting critical current of the coil as the conductor is inhomogeneous along his length or it can be slightly damaged while winding. Fig. 65 shows seven coils' behaviour taken from [97]: we will focus here on coil 1 and coil 7 as they are respectively INS and NI coils. Coil 1 also has a magnetic field deviation ($\sim 1\%$) due to screening currents on the conductor.

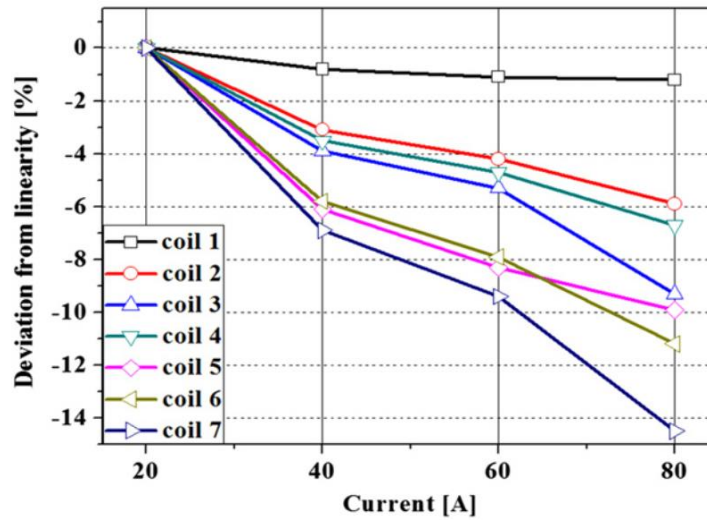


Fig. 65. Deviation of the maximum magnetic field from linearity based on 20 A test results, taken from [97].

1.4.5.3 Long-time constants

The other main drawback of NI coils is related to time constants. During charge (or discharge), the inductive tension due to the current increase (or decrease), can become higher than the turn-to-turn resistance making the current by-pass the turn-to-turn contact from its original spiral path. First, this phenomenon generates losses because of the radial current [110] but also creates strong delay [111] by increasing the required time to reach a stable field. The magnetic field can also be lower than the expected one. This has to be taken into account especially for user magnets. The long time

expected for discharge is illustrated in Fig. 66. The coils are the same as detailed in the previous paragraph; one can see the difference in the discharge speed of coil 1 (INS coil) and coil 7 (NI coil), taken from [97].

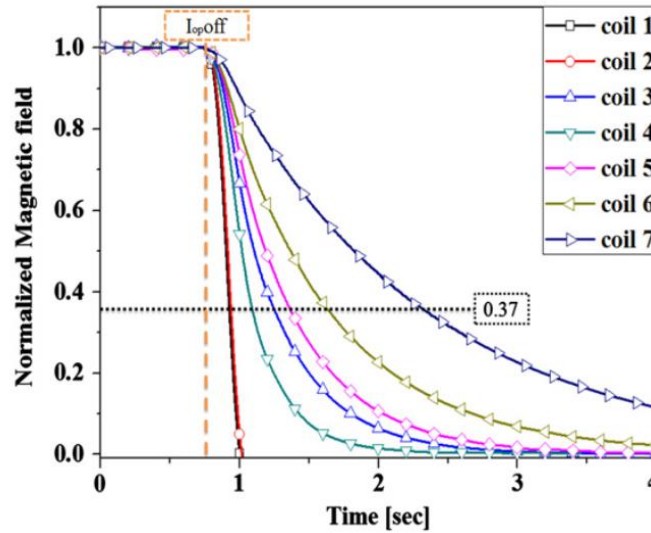


Fig. 66. Results of the sudden-discharge tests at 60 A, taken from [97].

NI coils behaviours are also hard to model as they strongly depend on the conductor itself (inhomogeneities) but also the winding; it is difficult to evaluate how the current distributes between the turns especially during charge and discharge of the magnet. Not being able to predict one coil's behaviour can be critical for the magnet; for example, a voltage pulse at the beginning of a fast discharge has been observed in [112]. Although fast discharge is expected to be used only for insulated coils, unexpected one can occur on a no-insulated coil if this latter is coupled with another magnet for example. This can lead to permanent damages of the NI insert; its behaviour has to be known with accuracy in order to setup a reliable self-protection. The resistance of the turn-to-turn contact must be investigated in order to give a precise estimation of the time constants [113]. However, some solutions have been proposed to reduce these time decays such as a current regulation for example, detailed in [114].

This time constants can be increased by inserting electric insulations only between some turns of the winding. In Fig. 66, coil 4 is partially co-wound with Kapton, every fourth turn, leading to a decrease of the time constants. The impact of the partial insulation winding has also been studied here [115]. Nevertheless, most of the time, the experimental work is conducted in nitrogen bath (77 K) without high background field. In this configuration, mechanical stresses would be huge on the winding and this extra thickness could create a step between the turns and damage the conductor in a local area. For these reasons, and in order to reduce the time constants, an intermediate solution has been studied: replacing the electric insulation and co-winding the conductor with a metallic layer. Coils wound with such a technique are called metallic insulated coils or MI coils [116].

1.4.6 Winding technique: Metallic insulated coil

1.4.6.1 Intermediate solution

As suggested by their name, MI coils are co-wound with a metallic layer in order to increase the contact resistance between the turns and hence decrease the time constants. By increasing the

metal thickness, change the material and the winding strength, the turn-to-turn contact resistance can be modified [117]. In the last two previous figures (Fig. 65 and Fig. 66), coil 2 and coil 3 are respectively co-wound with stainless steel and copper every turn [97]. The behaviour of coil 2 is closer to that of an insulated coil than the one of coil 3, as stainless steel has a higher resistance than copper.

1.4.6.2 Self-protection

MI coils have been shown to remain self-protected such as NI coils [116] as illustrated in Fig. 67.

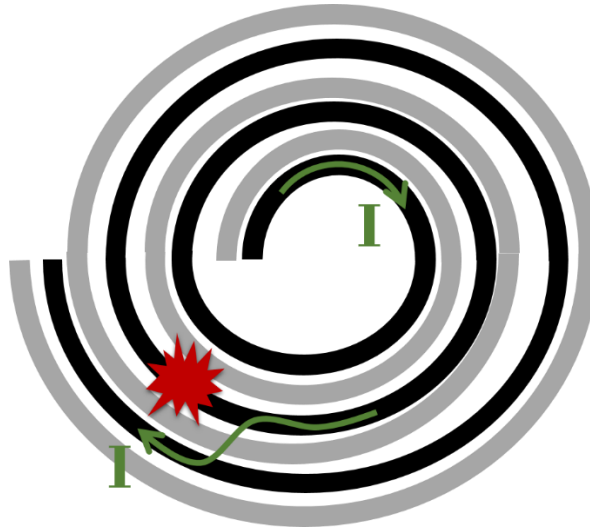


Fig. 67. Illustration of a hot spot in case of a MI winding.

1.4.7 Mechanical behaviours of REBCO insert coils

HTS insert implies both high magnetic field and high current, which lead to severe mechanical stress such as the Lorentz force [90]. Winding tension may be used in some cases to reduce the radial stress applied on the insert; when a coil is wound with a conductor in tension, this latter generates radial stresses in the opposite direction within the winding like in [118]. In the present work, this is used for MI coil winding but not for insulated coils as the impact of this preload on the insulation is not clear and could damage the conductor. The winding also faces significant axial contraction due to axial forces but also thermal shrinkage, which has to be accommodated by mechanical structures to avoid deterioration. Two solutions are possible; either the final assembly allows the winding to move in a controlled manner to avoid the terminals and soldered to be damaged [119], or the assembly is fully constrained to reduce at its maximum the movement when in operation, preload is used in [120].

For a conductor element carrying current density \vec{j} in the presence of \vec{B} , the Lorentz force density, \vec{f}_L is given by (6).

$$\vec{f}_L = \vec{j} \times \vec{B} \quad 6$$

1.4.8 Conclusion

A MI winding has been chosen to build the NOUGAT final prototype, as it shows a good compromise between self-protection and time constants. Nevertheless, as some user applications need a more reliable field linearity and stability and since MI coils cannot be considered for every application, INS coils are still investigated, for SMES for example.

Moreover, both MI and INS coils are interesting to be studied together as MI coils allow investigating the quench phenomenon without damaging the coil. It can be seen as a first step in the fabrication of a reliable insulated wound magnet. The following focuses on an electric insulated design for the 10 T insert prototype.

1.5 OBJECTIVES OF THE THESIS

1.5.1 Thesis orientation

Section 1.4.7 shows that metal insulation windings do not answer to all issues of REBCO insert for user magnets especially in terms of field linearity and stability, charge and discharge reliability but also the accuracy of MI coil simulation to know exactly how the current distributes inside the winding. Moreover, MI coils cannot be considered for every application. Even if this kind of winding can be used for user magnet fabrication, others applications still require electrical insulation such as SMES (Superconducting Magnetic Energy Storage) that needs to allow fast discharges for example [121] or even racetrack coils, which have a large surface contact between each turn that would probably dangerously decrease the contact resistance.

For these discussed reasons, I decided to orient my PhD work on electrically insulated coils and their protection. However, working in parallel with insulated coils and MI coils is relevant as these latter can be seen as a first step for insulated coil applications, allowing the study of the quench phenomenon and current margins without any risk of permanent damage.

1.5.2 Objectives of the thesis

The main objective of my thesis is to improve the knowledge about insulated coils in order to better understand their behaviour especially during quench. NI and MI coils have so far show good results and seem to work but most INS coils have been damaged while being tested. We believe that a better understanding of insulated coil behaviours would lead to a better prevention of the quench phenomenon and would allow implementing appropriate detection and protection systems.

The magnetic field distribution, shown in Fig. 68 is the addition of the background field and the magnetic field generated by the REBCO insert evaluated on FLUX/CEDRAT [27] to reach 10 T in the centre of the magnet.

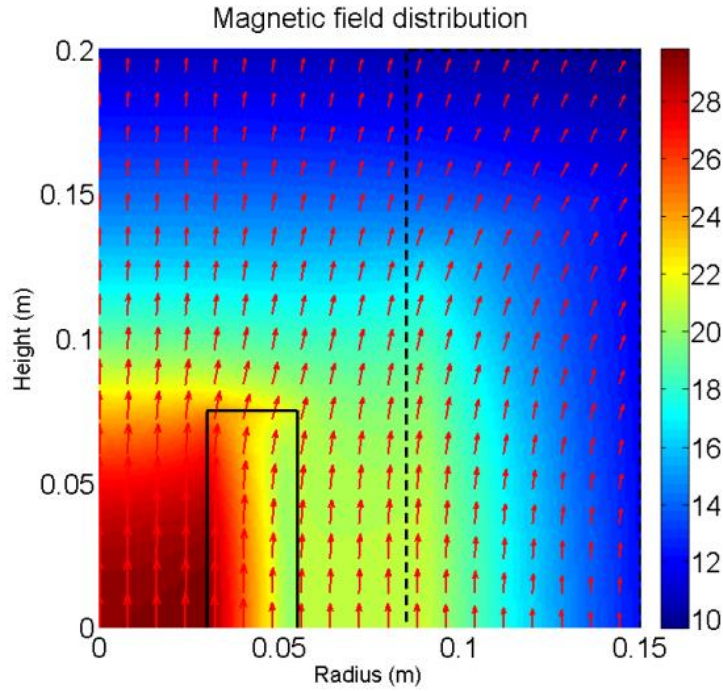


Fig. 68. Cross section quarter of the background field distribution. The inner diameter of the resistive magnet is shown by the dotted black line and the REBCO insert sketch is defined by the continuous black line.

In Fig. 68, the magnetic field is mainly vertical on the cross section of the REBCO insert but its orientation and intensity vary strongly, especially on the edges of the winding. Since REBCO conductors have strong anisotropic properties, this area of the final prototype will limit its performance while in operation. Understanding deeper the behaviour of the conductor under these specific conditions would help to define the working limits of a wound sample, which would then work with appropriate margins.

My objective is to study in detail REBCO conductors both experimentally and numerically, both straight short samples and wound samples in order to evaluate their performance limitations and how a reliable protection can be set up.

Moreover, MI coil studies can be seen as a first step for understanding insulated coils. MI coils can be used to better understand insulated coils, which are more difficult to study close to their limits, especially under high magnetic field where the noise measurement is important, and the mechanical stresses are huge.

In this present work, I focus my work on giving answers to the following questions. In what extent can increasing the knowledge about REBCO coils behaviour facilitate appropriate protection setup or at least prevent coils from permanent damages by using confident margins? How can the operating limits can be safely defined?

The experimental and simulation studies on insulated conductors constitute my own work; I studied the short straight samples under high magnetic field and two wound insulated samples presented later. I will also compare the experimental works and models on insulated coils to a metal insulation wound sample, which is a work in collaboration with Thibault Lecrevisse from CEA, Saclay.

2 YBCO TAPE CHARACTERIZATION UNDER HIGH FIELD WITH VARYING ORIENTATION

In the previous chapter, necessary knowledge to understand the following have been introduced in terms of both superconductivity and magnet technologies. It has been underlined how conductor performance can influence a coil's behaviour and how a better understanding of the HTS properties would allow the final demonstrator to work more safely with precise and appropriate margins. In the following, HTS only stands for REBCO coated conductors. This chapter focuses on short sample characterisation, first in liquid nitrogen bath (77 K) and thereafter, in liquid helium bath (4.2 K) at high magnetic field, up to 23 T, where the sample can be rotated up to 360° to study its properties.

First, the design of the final insert prototype is studied in more details to underline the necessity of a precise knowledge of the selected conductor performance. Then, the variation of the REBCO performance according to its provider and its fabrication process is discussed, as well as how one conductor length may differ from another one, elaborated in the same conditions. This makes short sample characterization mandatory for the current margin evaluation in the final insert conditions, especially as the conductor performance is continuously improved. Thereafter, the experimental setup is introduced, underlining the main differences to other laboratories and the main challenges of these kinds of experiment. In a third part, experimental results are shown; they are modelled with a power law to evaluate the critical current for each test. This allows comparing different provider tapes and highlighting the HTS improvement over the past few years. Eventually, missing points are extrapolated using the Kim model for a further implementation in a numerical model, see section 2.7.

2.1 HTS COIL: DESIGN INPUTS, MAGNETIC BEHAVIOUR AND LIMITING CRITICAL CURRENT EVALUATION

In the following sections, the assumption is made that the current is homogeneously carried by the conductor i.e. the current density distribution in the tape cross section does not depend either on the background field or the self-generated field, as shown in [122].

Fig. 69 shows the full cross-section of the field distribution generated by the HTS insert. In the rest of the manuscript, only one quarter of the cross-section is studied thanks to the field symmetries: the top right one as underlined below by the dotted back rectangle.

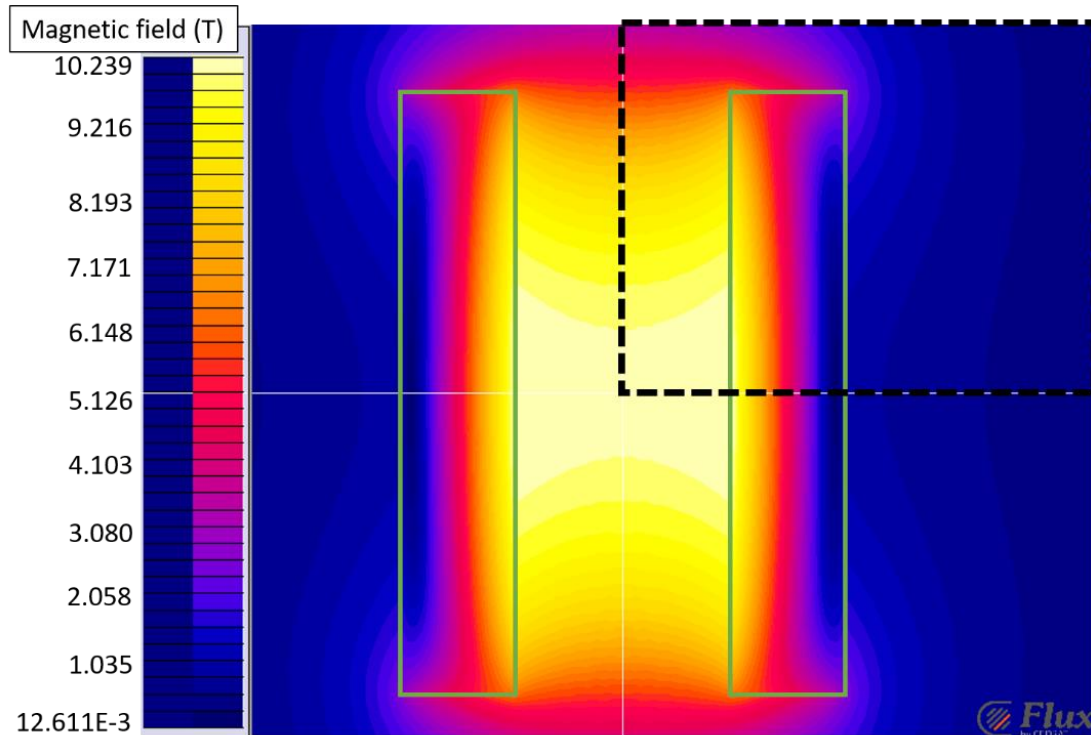


Fig. 69. Trend of the magnetic field generated by the HTS insert; the green line underlines the shape of the insert and the tilted black line the cross-section, which is studied. For the calculation, the inner and outer radius are respectively taken as 60 mm and 110 mm. The height is 150 mm and the current density is 365 A/mm² to generate 10 T in the centre of the solenoid.

2.1.1 Outer field

2.1.1.1 Introduction of the field homogeneity

The insert is expected to work inside an already existing resistive magnet. A quarter of the cross-section is shown in Fig. 70, both calculated and measured at LNCMI. In section 2.4.2, the decrease of performance due to the magnetic field orientation and intensity is mentioned and is detailed in 2.4.2. For this specific reason the background field, in which the insert is expected to work, has to be studied carefully. The background field homogeneity is investigated to know how it would limit the insert geometry.

In the following parts, the standard deviation is evaluated according to the magnetic field in the centre of the magnet $B(0,0)$, i.e. the amount of variation from this specific value is calculated to compare the homogeneity for different studied cases.

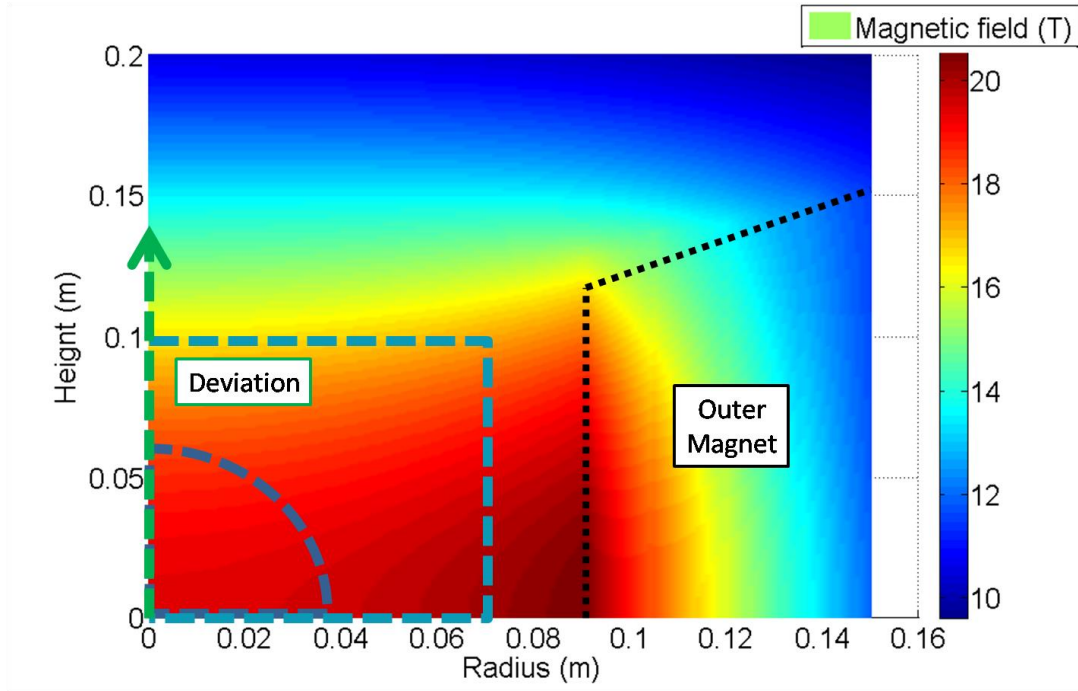


Fig. 70. Magnetic field distribution generated by the outer resistive magnet at LNCMI; the outer magnet is defined by the black tilted line and the green tilted line underlines the space inside the magnet for experiment under high field.

2.1.1.2 Calculation of the 20 T background field homogeneity

Fig. 71 shows the B_z standard deviation in the centre of the magnet, calculated according to the considered height. As expected, the smaller is the height used for evaluation, the lower is the deviation. The contrary is also true, i.e. the bigger is the height, the higher is the deviation, as illustrated in Fig. 70. As a reminder, the standard deviation formula is given in (7). In Fig. 71, only B_z is calculated as B_r is equal to zero on this axis.

$$s = \sqrt{\frac{\sum_{i=1}^N (x_i - x_0)^2}{N}} \quad 7$$

Fig. 72 shows the standard deviation calculated no longer on a line but on a sphere, the radius of which is given as the horizontal axis. B_r and B_z are both evaluated. As $B_r(0,0)=0$, the standard deviation is directly B_r . B_z tends to increase quickly as soon as the radius reaches 20 mm.

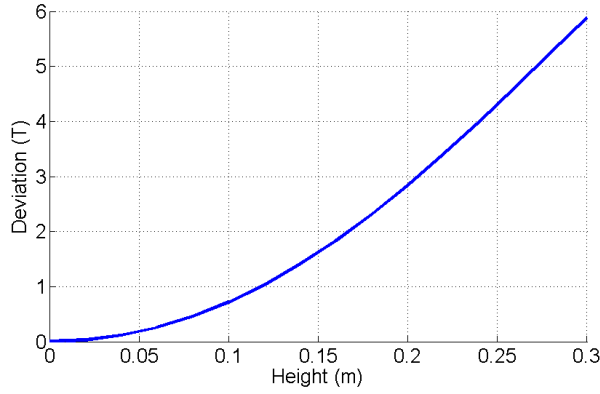


Fig. 71. Deviation of the field in the centre of the magnet according to the height.

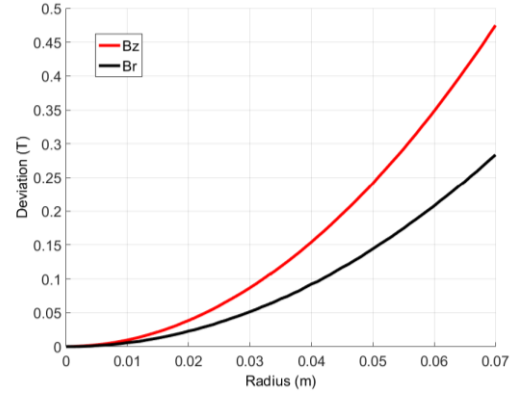


Fig. 72. Deviation of the field components on a sphere according to a given radius.

Fig. 73 and Fig. 74 respectively show the deviation of B_z and B_r of the background field according to the geometry of the final insert: according to both its height and its outer radius. Here the results are shown on the upper-right quarter of the cross-section, as allowed by the field symmetry previously explained. It means that for these two graphs, each point defines a specific insert geometry, the height of which would be equal to twice the height of the ordinate on the graph. For example, in Fig. 74, the dotted red line defines the studied zone for the insert, so the maximum B_r value is defined by the position of the red cross, i.e. between 0.4 and 0.5 T. To keep B_r and B_z as homogeneous as possible the height should be limited to 200 mm and the outer radius should be as small as possible.

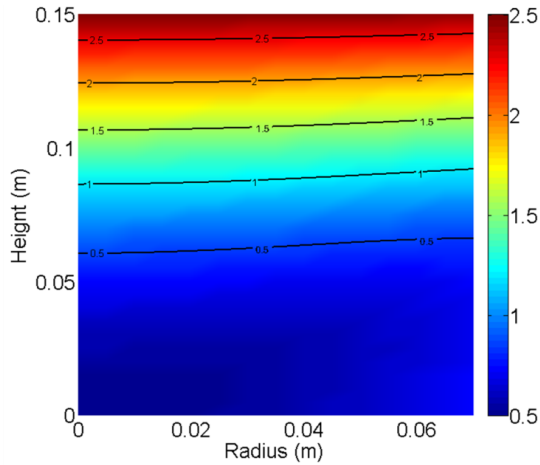


Fig. 73. Standard deviation of the parallel field B_z .

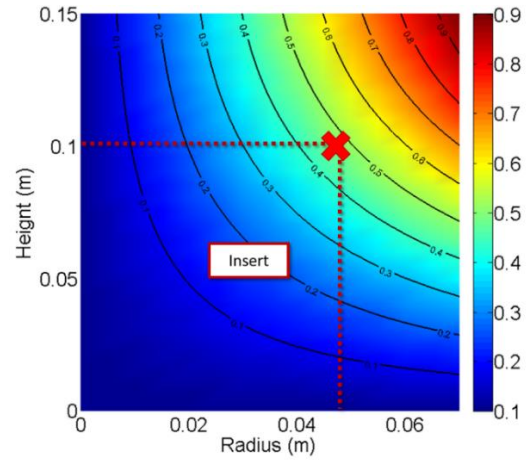


Fig. 74. Transverse field B_r .

2.1.2 Field generated by the HTS insert

The outer field gives the limits for the geometry of the insert. First, the insert has to fit inside the resistive magnet but also since the insert is expected to work under the lowest transverse component of the field as possible. The following focuses on the insert itself.

The field module calculation is interesting to evaluate what current density needs to go through the conductor to reach 10 T in the centre of the magnet. However, the performance of this latter will be mainly restricted by the transverse component of the field applied on the insert while working under the final operating conditions. Fig. 75 shows the module of the magnetic field generated

by both the outsert and the insert. The inner limit of the outsert bore is represented by the black dotted line on the right of the figure and the insert is shown by the black dotted line that draws a rectangle in the middle of the figure.

Fig. 75 underlines the orientation of the field according to the area of the cross-section; the field orientation is given by the red arrows. As expected, the field is longitudinal on the inside of the insert but slightly disoriented on the edges of the winding, circled in red.

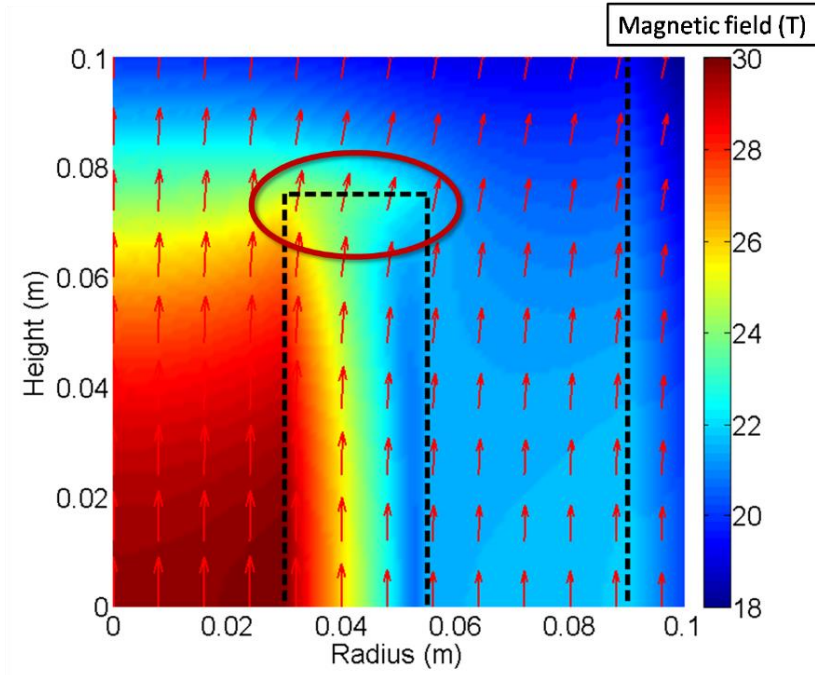


Fig. 75. Magnetic field generated by the insert and the outer, the current density is 365 A/mm^2 .

In the following, the geometry impact on the required current to reach 10 T in the centre of the insert is first investigated. In a second step, the optimization of the insert's edges is discussed in order to reduce the value of the transverse field on this area.

2.2 GEOMETRY OPTIMIZATION OF HTS INSERT COILS

2.2.1 The tape thickness

Most of the following results are given according to the overall current density but the tape thickness also has an impact on the insert and some points have to be taken into consideration. First, a thick copper layer on the conductor can give a better stabilization, [123] as it would improve the protection of the tape itself against over-current or inhomogeneity by lowering the resistance by unit length [124]. However, in equal conditions, the operating current density in the superconducting layer is higher as less turns can be placed in the same cross-section.

2.2.2 Influence of the geometry on the operating current density

In order to achieve the highest current margin, both the transverse field and the current density have to be decreased as much as possible. The impact of the geometry on the current density is discussed here. Fig. 76 shows the necessary current density to reach 10 T according to the inner and outer diameters, calculated for a height equal to 120 mm. For example, following the red dotted lines

added in Fig. 76, if the inner diameter is taken at 50 mm and the outer diameter is 105 mm, the current needed inside the coil to generate 10 T is found where the lines cross (see red cross), i.e. about 450 A are needed. As expected, as the inner diameter increases and the outer diameter decreases, the required current density to generate 10 T in the centre of the insert gets higher.

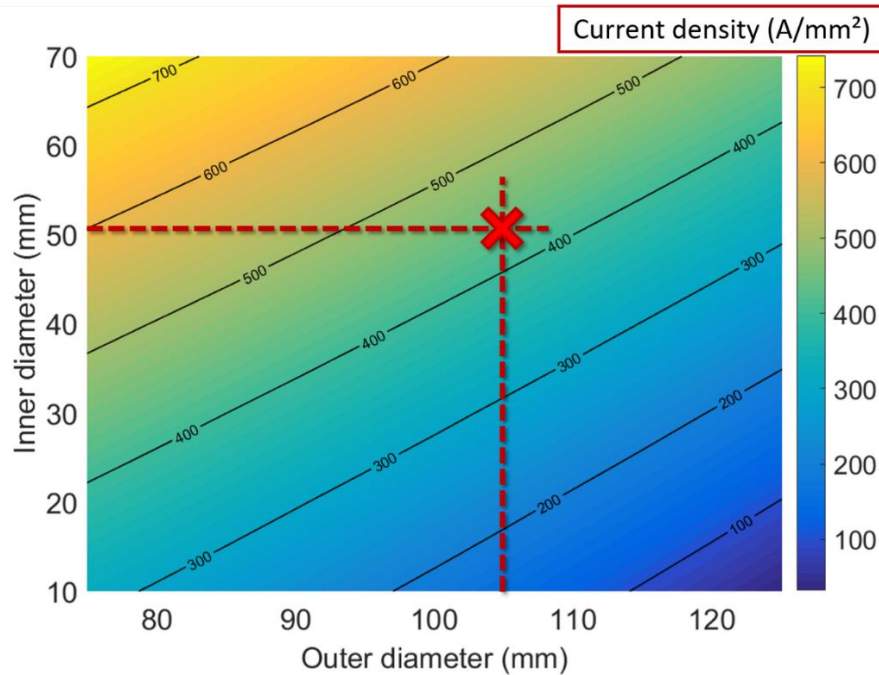


Fig. 76. Current density in A/mm^2 necessary to reach 10 T according to the inner and outer diameter of the insert with a height of 120 mm.

The height of the magnet has a low influence on the nominal current density compared to the inner and outer diameters. In Fig. 77 and Fig. 78, where the height is 150 mm, the influence of the outer and the inner diameter is underlined. For an inner diameter higher than 50 mm the current density starts to increase at a greater rate.

The outer diameter is in any case limited to 120 mm by the outsert inner bore and the cryostat.

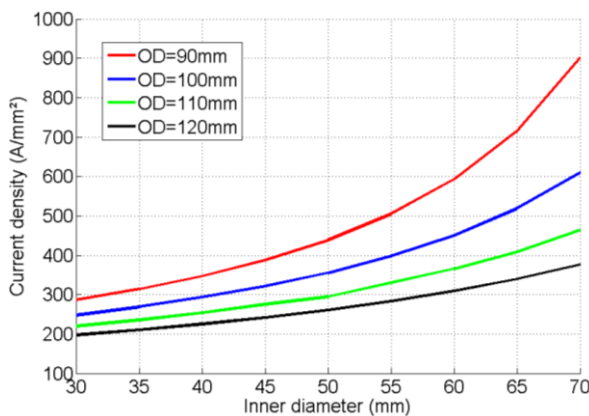


Fig. 77. Nominal current density to reach 10 T in the centre of the insert according to the outer diameter and the inner diameter for a height of 150 mm.

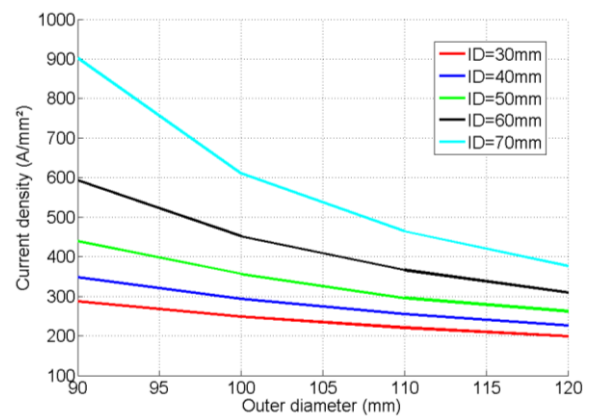


Fig. 78. Nominal current density to reach 10 T in the centre of the insert according to the outer diameter and the inner diameter for a height of 150 mm.

2.2.3 Homogeneity of the field: notch

Once the geometry is optimised to reduce the current inside the coil, it can be improved to generate a more homogeneous field using a notch, i.e. an increase of the inner diameter of the pancakes at the centre of the insert as illustrated in Fig. 79. D_N is the diameter of the pancakes situated in the notch area and H_N is the height of the total notch.

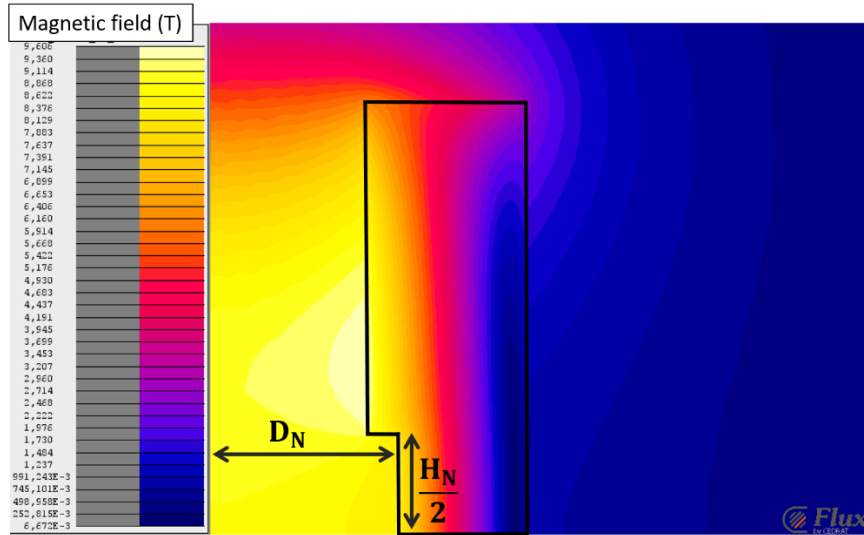


Fig. 79. Notch configuration.

The deviation of the parallel field is evaluated on the full height of the insert and shown in Fig. 80 according to the total height of the notch and the inner diameter of the pancakes in the notch area. For H_N and D_N , respectively, equal to 45 mm and 75 mm (red dotted lines in the figure), the deviation is between 1 T and 1.1 T highlighted by the red cross.

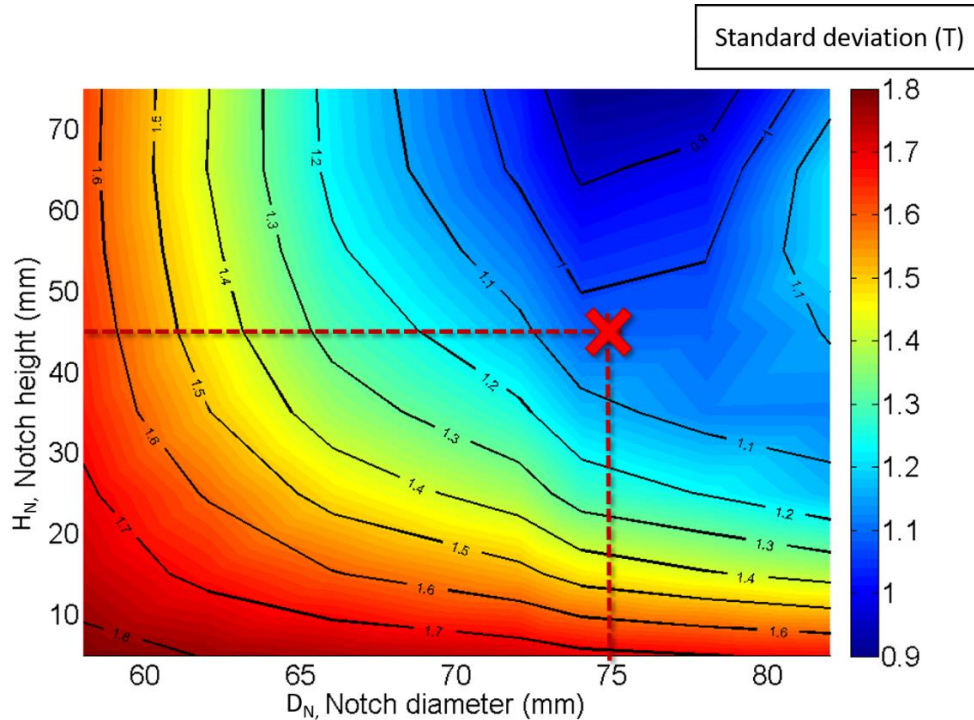


Fig. 80. Deviation of the magnetic field (T) on the height of the insert.

The deviation can be easily divided by two but by reducing the conductor area, it increases the nominal current necessary to reach 10 T as shown in Fig. 81. The evolution of the current density according to the geometry of the notch is shown in Fig. 81. For the previous example, which considers an inner and outer diameter of respectively 45 mm and 75 mm, the necessary current density is approximately 450 A/mm². A compromise between the deviation of the field and the necessary nominal current density has to be found.

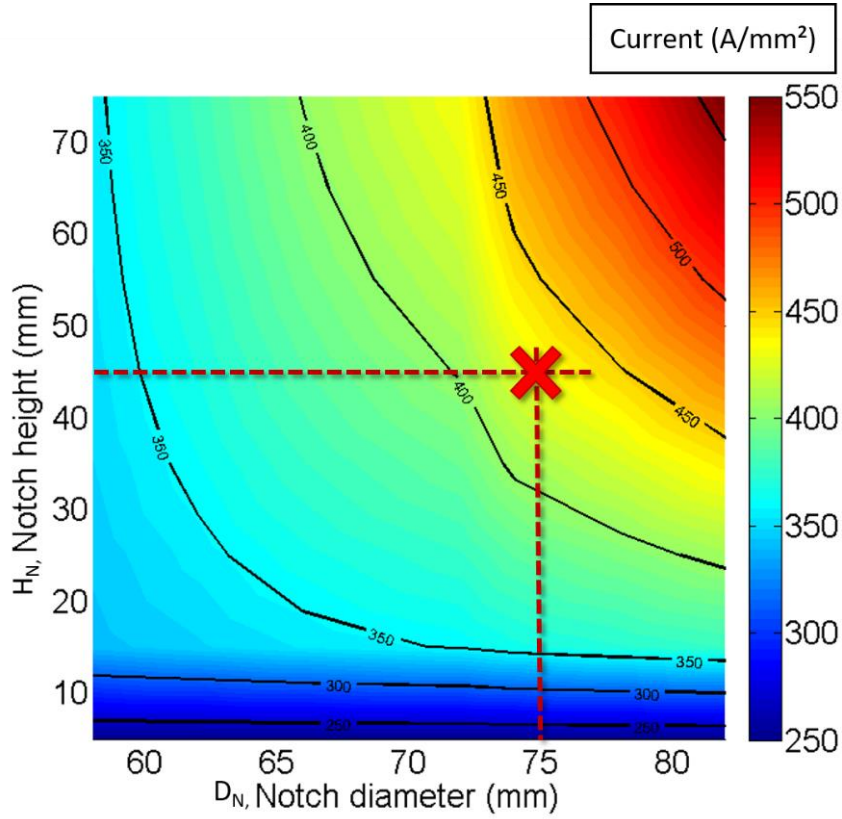


Fig. 81. Current density (A/mm²) needed to generate 10 T in the coil centre according to the notch geometry.

In this section, the opportunity of improving the homogeneity of the magnetic field generated by the insert has been detailed. It seems obvious that acceptable margins on the operating current should be defined first even before working on the homogeneity of the field. On the previous graphs, no field minimum variation is found as the operating current is rapidly too high. For further work, this notch preoccupation can be pertinent (even if screening currents also have to be considered to assert the field homogeneity) but so far, the main project hurdles are the geometric constraints, hence the operating current should be as low as possible to increase the current margins. Nevertheless, it is interesting to see how the magnetic field is impacted by the geometry and how fast it leads to an abrupt increase of the required current. Moreover, as there is no request in the project for specific field homogeneity, the next paragraph will focus on a geometry without a notch.

2.2.4 Extrapolation of the I_c measured on short samples and insert

According to the components of the magnetic field, the critical current can be evaluated on the whole cross-section of the insert; the geometry of the model is presented in Table 4. The calculation of the limiting critical current is made using the short sample characterization, which will be presented in section 2.5. For a better accuracy, each conductor of every pancake could be characterized under high field with different orientations but this would require an impractically long

time to predict the whole insert behaviour and so far, it seems unrealistic as all lengths are shown to have slightly different performance and even on the same length, the conductor performance shows high variations. Nevertheless, as variations are expected from a statistical point of view, it has to be taken into account especially when calculating the current margins by adding extra margins due to this inhomogeneity.

Therefore, the calculation of the critical current also has to take into account the inhomogeneity along the length that has been briefly described in section 1.1.2.3 and which can reduce by about 10 % the performance of the insert [125]. This is developed in more detail in 2.4.1.1.

Insert model information	
Inner diameter (mm)	54
Outer diameter (mm)	110
Height (mm)	170
Nominal current density (A/mm ²)	365
Pancake number	26
Conductor width (mm)	6
Thickness between pancakes (mm)	1

Table 4. Details of the insert model.

The components of the magnetic field generated by the insert model presented above are evaluated using the software FLUX/ALTER. All the following figures show the top-right quarter of the cross-section of the insert. Knowing the components of the field, the critical current on each point of the winding can be extrapolated using the short sample experimental characterization detailed in 2.5.

To generate 10 T with the geometry previously presented, 365 A/mm² are required inside the conductor. If a 6-mm wide tape is considered, the required operating current would be approximately 318 A. In this case and considering only the insert self-generated field, the maximum transverse field is 3.75 T and the lowest critical current value on the winding is 634 A.

However, this limiting value for the insert performance is made with a pessimistic assumption: the critical current is evaluated on the whole section of the coil according to the magnetic field components and the lowest value of this critical current distribution is taken as the limiting critical current of the winding. It is the lowest value evaluated on the cross section on the whole insert and not the critical current of the conductor. Another calculation can be done with the assumption that the critical current is the average of the local critical current densities on the whole width of the conductor. In that case, a limiting critical current is defined for each pancake and the lowest value is taken as the limiting critical current of the whole insert. In self-field and with about 7000 points on each pancake (around 13 in the conductor width and 561 in the winding thickness), the limiting critical current is found to be 690 A.

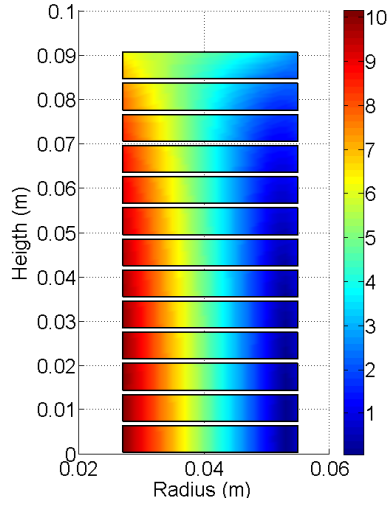


Fig. 82. B module (T) generated by the insert. In standalone

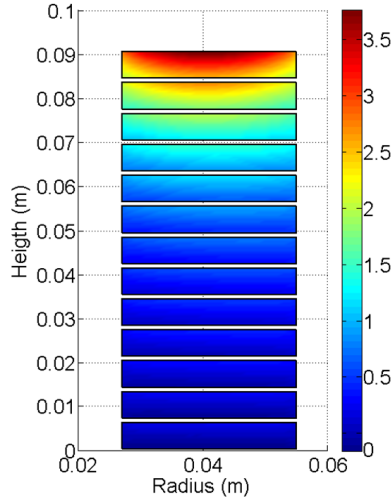


Fig. 83. Transverse field (T) generated by the insert in standalone.

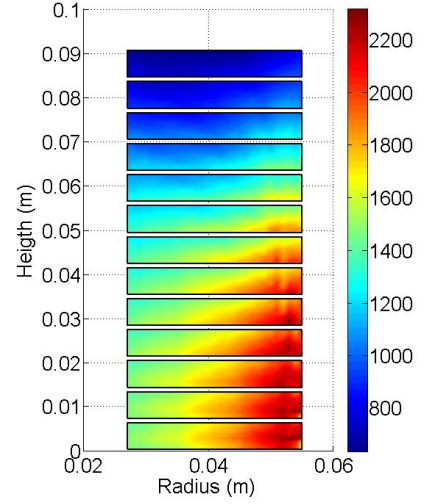


Fig. 84. Critical current (A) evaluated on the cross section in standalone.

In a second step, the background field measured and calculated by the LNCMI is added on the cross section of the model, shown in Fig. 85, Fig. 86 and Fig. 87 to generate a total of 30 T in the centre of the assembly. The maximum transverse field is now 4.89 T and the maximum I_c is 503 A on the cross section. While doing the same hypothesis as in the previous paragraph, the limiting critical current averaged on the cross-section of the tapes under background field is 592 A, which makes the I_{nom} about 54 % of the limiting critical current.

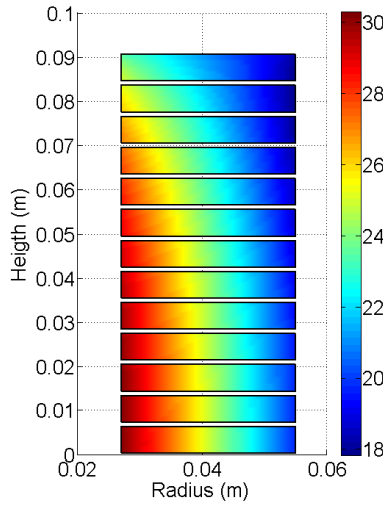


Fig. 85. Module of the addition of the background field and field generated by the insert.

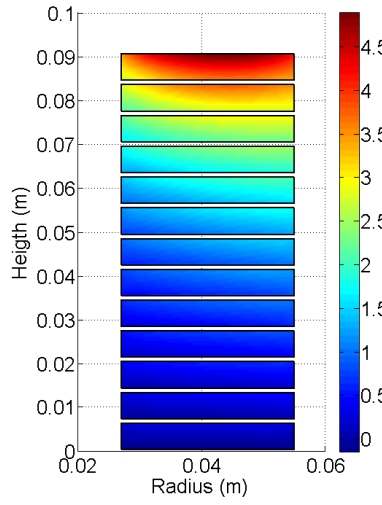


Fig. 86. Transverse field component when background field added to self-field.

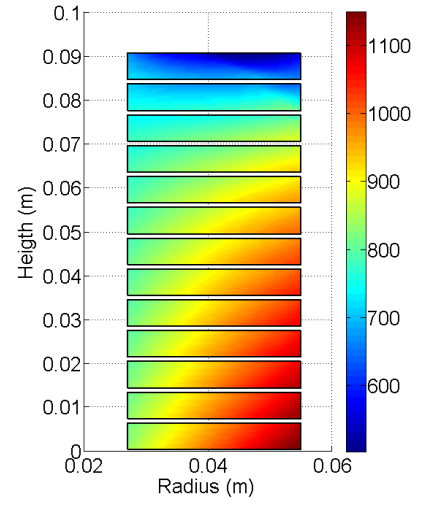


Fig. 87. Critical current evaluated on the cross section according to the field components.

2.2.5 Geometry optimisation to reduce the transverse field

The limiting critical current is defined on the edges of the winding, as expected [126], this area of the insert geometry can be optimised in order to reduce the transverse component of the field. The field mapping is shown on the cross-section of the insert in Fig. 88 and in Fig. 89, respectively the

module of the field and its transverse component, to highlight the transverse component of the field that has to be reduced.

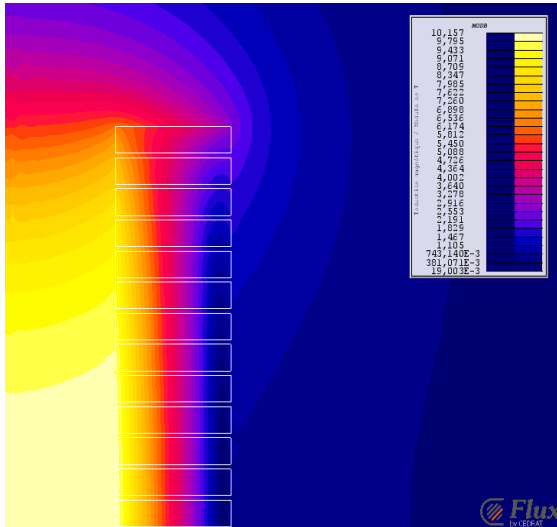


Fig. 88. Module of the magnetic field on a cross-section of the insert.

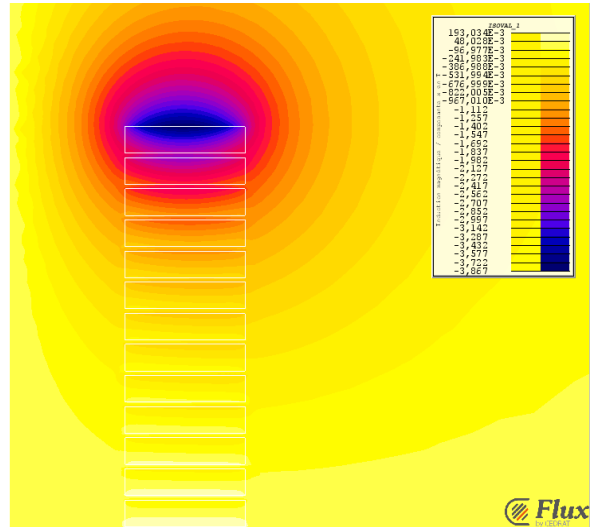


Fig. 89. Transverse component of the field on a cross-section of the insert.

Several methods can be used to decrease the transverse field and the influence of some of them on the geometry of the studied insert will be discussed, respecting the geometry limitations.

First, the space between the pancakes on the edges of the coil can be increased. These pancakes can also be chosen with higher performance than the pancakes setup in the middle of the insert. Only the first method is studied for the insert, other methods are illustrated based on literature.

To increase the performance of the insert, the width of the top and bottom pancakes can also be increased, as explained in [127] to reduce the impact of the transverse component on the wound conductor which has been used for [22], [120].

Another solution is to test all the pancakes and choose to setup the ones with the highest limiting critical current on the bottom and on the top of the insert as explained in [128], [129] in order to increase the performance of the final assembly.

The first method is studied in this paragraph, i.e. the space between the top and bottom pancakes is increased to investigate the influence on the transverse field on the edges of the winding and the evolution of the limiting critical current of the insert. Fig. 90 highlights which heights are increased in the following; H1 H2 and H3 are slightly increased to influence the performance of the coil.

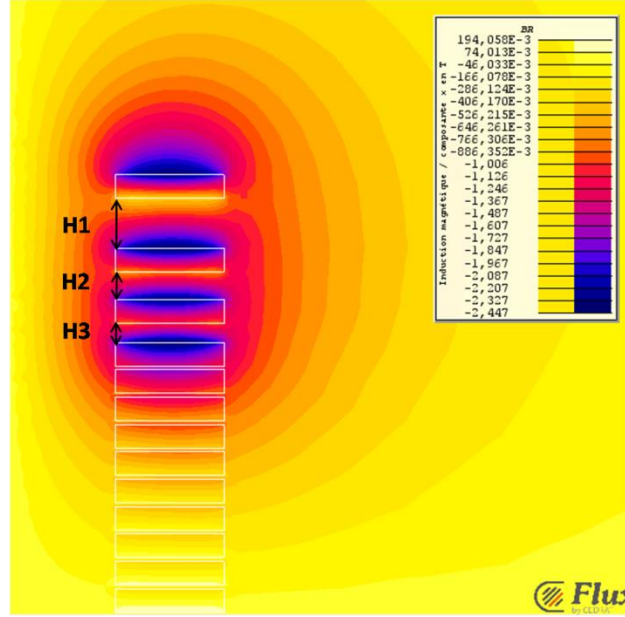


Fig. 90. Transverse component of the field to underline the distance between the pancakes on the edges of the winding.

In Fig. 91, H1, H2 and H3 are modified and the highest transverse field is plotted according to the total height of the insert, only the variation of H1 is specified in the legend even if H2 and H3 are also modified: they are increased from 0 mm to the value of H1 every 1 mm. No optimization software is used for this study as the main objective is to evaluate the trend of the solutions rather than finding the best one. The insert is studied in self-field but more precise studies could be done under background field. However, a compromise has to be found between the total height and the reduction of the transverse field for the insert to respect the geometry limitation. Solutions that seem appropriate are circled in dotted red.

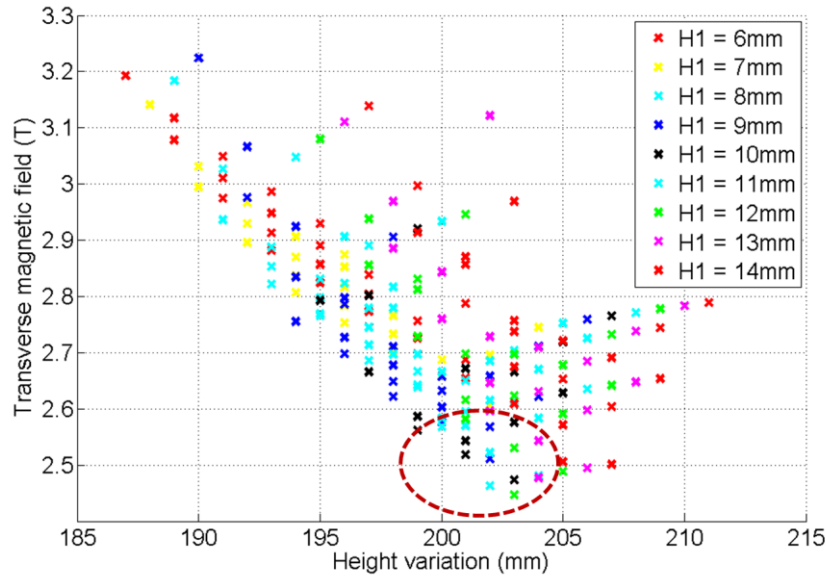


Fig. 91. Transverse field according to the total height and the edges geometry.

One of the compromise solutions is shown in Fig. 92, Fig. 93 and Fig. 94; H1 is 12 mm, H2 is 6 mm and H3 is 4 mm. Under 20 T, the lowest critical current is 611 A and when averaged on the width of the conductor is 718 A, which means the performance has been increased by 18 %. However, the

homogeneity of B_z on the centre of the insert, calculated on a height of 100 mm, is slightly reduced as it is 0.68 T with the previous design and 0.82 T with the optimized one. When the final design will be decided, all these characteristics will have to be considered, knowing all the advantages and drawbacks of each possible design to find a good compromise.

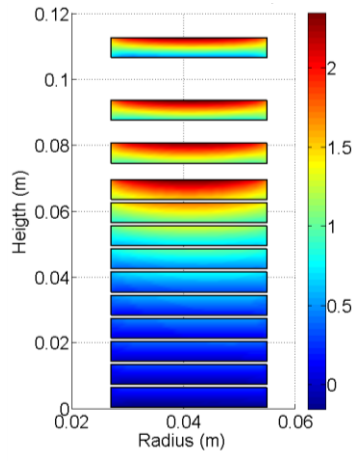


Fig. 92. Transverse component of the field (T) on the cross-section of the optimized insert, in self-field.

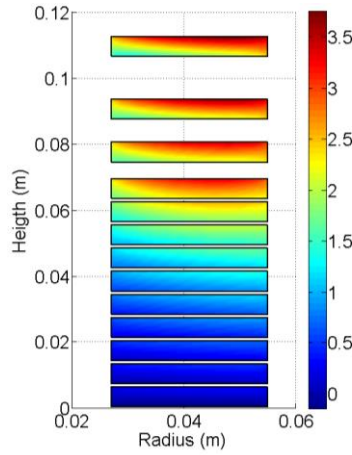


Fig. 93. Transverse component of the field (T) on the cross-section of the optimized insert, under 20 T background field.

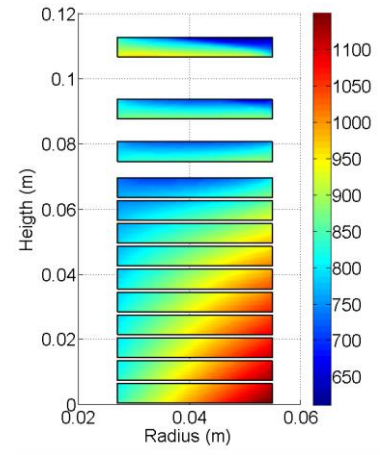


Fig. 94. Critical current evaluated on the whole cross-section of the optimized insert in background field.

2.2.6 Conclusion: presentation of the selected model for the next paragraphs

Although the final insert has been chosen to be built using MI windings, the final geometry studied here is supposed to be wound with insulated conductors. The geometry, which is used for the following studies of the insert behaviours is the one presented in 2.2.4. As a reminder, the main parameters are given in Table 5.

Insert characteristics	
Inner diameter (mm)	54
Outer diameter (mm)	110
Number of pancakes	26
Number of turns/pancake	193
I_{nom} (A)	318
Limiting critical current, self-field (A)	690
Limiting critical current, 20 T background (A)	592
Current density (A/mm ²)	365
Field coefficient (mT/A)	31.45

Table 5. Parameters of the insert model.

2.3 INTERMEDIATE CONCLUSION

The aim of this chapter is mainly to underline the challenges of using REBCO for user magnets which are mostly about the difficulties to setup a reliable protection to prevent the insert from irreversible damages. Only when detection and protection would be both mastered, could tailored

solutions be introduced to better face high hoop stresses, to increase the current margins, to evaluate the limiting critical current with more accuracy, etc.

However, it has been previously shown how the insert design can be improved to reduce the transverse component of the field, allowing to increase the current margin by improving the limiting critical current. It was also seen how a slight modification of the insert geometry can help generate a more homogeneous field in the magnet bore. All this is shown theoretically and should be confirmed experimentally.

The limiting critical current is calculated according to the results from the conductor characterization under high field with different orientations. In the next sections, these results are shown to be different for every conductor and for this main reason, we decide to study in detail the conductor used for the wound samples to be able to model it with a better accuracy.

Even if the present main objective of the NOUGAT project is not to reach higher field than the already existing ones, this kind of application remains challenging. As mentioned above, one of the main difficulties is to setup a reliable and robust protection as it can be rather difficult due to thermal stability, slow propagation velocity and the inhomogeneities along the length of the REBCO conductors. Only then, could other parameters be improved. Nevertheless, to ease this problem, it has been decided that the final prototype will be built using co-wound metallic tapes instead of insulated windings mostly for its self-protection ability.

2.4 THE IMPORTANCE OF A SYSTEMATIC CHARACTERIZATION

This section develops in what extent precise tape characterization may lead to a more accurate evaluation of wound samples and the insert current margins.

2.4.1 Data on the conductor performance given by the providers

2.4.1.1 Critical current inhomogeneity along the conductor length

HTS conductors provided by the industry also come with their critical current measurements over the whole length in liquid nitrogen bath. Providers use a non-intrusive method in order not to damage the conductor; it is a non-contact magnetic measurement method, see the example of TapeStar [1]. Such a protocol cannot be setup in liquid helium bath mostly because of the high cost it would induce (helium price, difficult process, more qualified employees required, etc) but also for the lack of an interesting market when seen by the industry. For similar reasons, conductors are not studied under high magnetic field with varying orientation. The correlation between the I_c values at 77 K, self-field and those under high field at lower temperature are still discussed, see section 2.4.1.2.

The inhomogeneity of REBCO conductors has been mentioned in section 2.4.1.1. An example of the critical current uniformity at 77 K along the length measured by THEVA on a typical 12 mm HTS tape produced at SuperOx[®] is given in Fig. 95 ; the machine that allows this measurement is called TapeStar[™], fabricated and sold by Theva [1]. The I_c value is measured every 2 cm, whereas measurements from other manufacturers may only be provided every 5 metres. However, even if this technique prevails in industry, other techniques are used in research and are the promise of measurement accuracy improvement, leading to the detection of new inhomogeneities on the conductor, such as two dimensional imaging of critical current density developed in [130], which is based on a scanning Hall-probe microscopy (SHPM). Unfortunately, this kind of new measurement also

allows the detection of other critical current drops along the length of the conductor that were not recorded with more common techniques [131], hence it makes the TapeStar measurement not entirely reliable.

On the TapeStar™ measurement shown in Fig. 95, the average I_c value is not the same on the whole length and this value also varies locally considerably, leading to a minimum I_c value under 300 A whereas the average value along the length would rather be around 350 A.

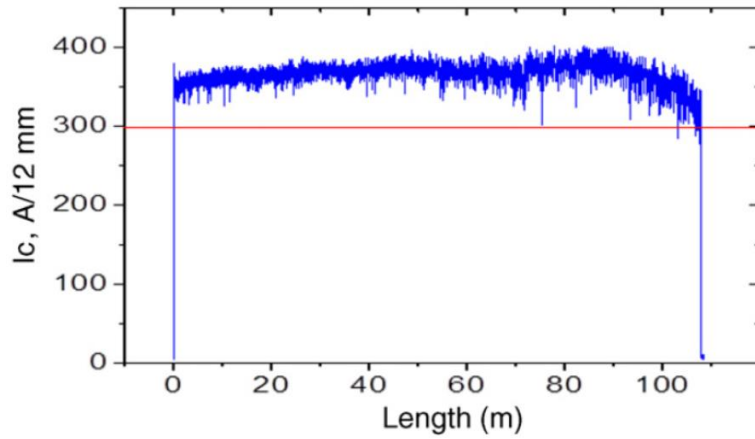


Fig. 95. Critical current distribution in a typical HTS tape produced at SuperOx® along the length measured by a TapeStar™ device (the reference standard measurement machine fabricated and sold by THEVA) [1], at 77 K, self-field.

In spite of the recent elaboration process improvements, as shown in the comparison of I_c variations in older tapes (Fig. 96. a) and in newer tapes (Fig. 96. b) taken from [2], this elaboration process remains challenging. Fig. 96 underlines the fast speed of these technology improvements in these REBCO coated conductors.

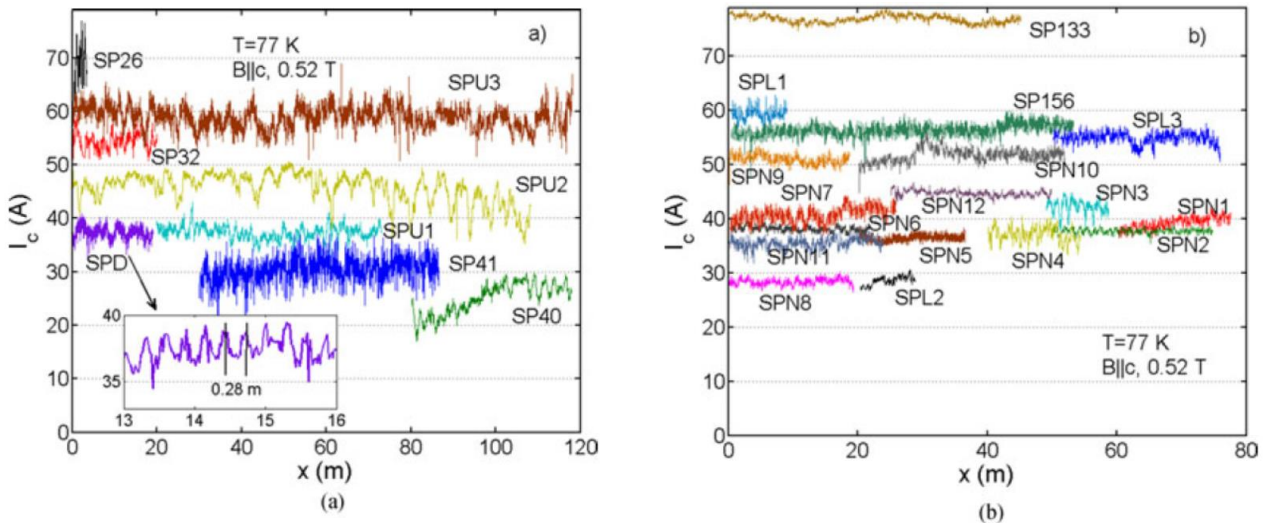


Fig. 96. Critical current as a function of position at 77 K in several (a) older (2010-2012) and (b) newer (2013-2014) 4-mm wide coated conductor tapes [9].

However, high performance variations along the length of the conductor still need to be taken into consideration. For example, the influence of HTS tape inhomogeneity on self AC loss has been

studied: the inhomogeneity coefficient of critical current variation is discussed in [132]. It implies that this standard deviation of the critical current value along the length has to be taken into account while modeling and designing a coil [38].

2.4.1.2 Critical current measurements extrapolation from 77 K to 4.2 K

In spite of the common evaluation of the current margins using the lowest critical current given by the providers at 77 K, self-field, it is not certain that the area of the length which has the lowest I_c value at 77 K, self-field, remains the lowest value at 4 K and even more, under high field. Performance at 77 K and 4.2 K do not correlate in certain cases, mainly when adding artificial pinning [30]. However, correlations are investigated and a more valuable prediction of the 4.2 K, high field critical current measurement has been found while studying the 77 K performance under a low background field (0.5 T) [133].

In Fig. 97, the I_c of five different manufacturer's tapes are investigated for several background field values. For instance, under 1 T and at 77 K, the SuNAM tape has a higher critical current than the SuperOx tape and when the background field is higher than 1 T, their performance seems to be similar. On the contrary, when they are studied at 4.2 K, a higher performance is reached by the SuperOx tape no matter the background field [33]. This means that it is difficult to extrapolate the 77 K, self-field I_c values of a conductor to 4.2 K under high field conditions. This change of performance from one provider to another underlines the necessity to characterize a conductor under similar conditions to its final operating environment.

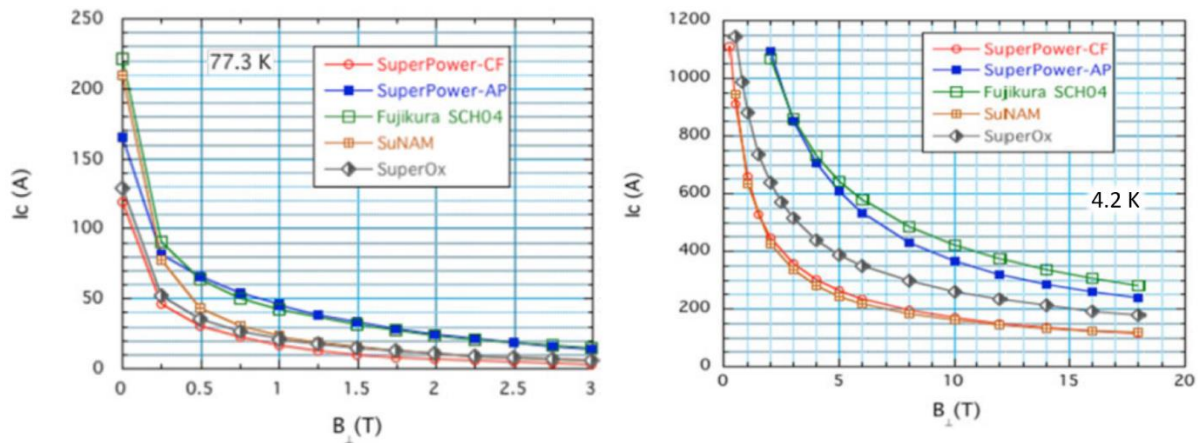


Fig. 97. (a) B dependence of I_c at 77 K for commercial conductors in perpendicular field. (b) B dependence of I_c at 4.2 K for commercial conductors in perpendicular field [33].

The comparison of the different tapes in Fig. 97 clearly highlights the fact that each tape has a different behaviour depending on the manufacturer. The Fujikura wire is clearly optimized for high field applications at low temperatures, whereas SuNAM is optimized for 77 K operation.

Moreover, it has also been shown that even a batch can be different from another, sold by the same provider [134]. This is illustrated in Fig. 98, where several conductors' performance are compared, provided by six different manufacturers.

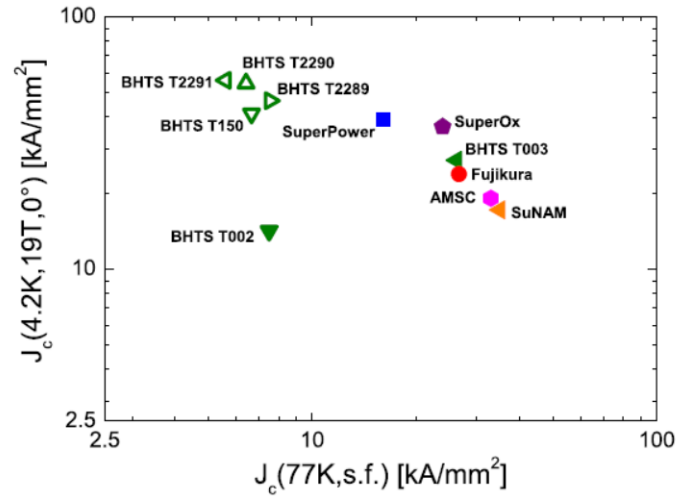


Fig. 98. J_c of the REBCO layers measured at 4.2 K, 19 T perpendicular field, versus J_c of the same layers measured at 77 K, self-field for six different manufactures. AMSC, BHTS stand respectively for American Superconductor, Brucker HTS [134].

Knowing this absence of correlation in the performance of one conductor operating under different conditions, it is difficult to estimate how severe the lowest I_c value at 77 K will be at 4.2 K or even under high field. To this extent, it is not possible to evaluate which area of the conductor length will have the lowest performance. Therefore, it is challenging to predict what the lowest I_c value of the conductor is in the operating conditions of the final insert of the NOUGAT project.

As the measurement at 77 K does not allow extrapolating with accuracy the performance at 4.2 K and under high field [134], the critical current of the studied tape in this present paper is characterized at 4.2 K under high field with various orientations but also at a higher temperature up to 77 K, in self-field. In the following work, it is assumed that the whole length of the conductor has similar performance at 77 K, as similar results were found in liquid nitrogen bath, i.e. each of the samples studied under high field are characterized under the same conditions, no matter where they are taken on the length of the conductor.

In the following paragraph, we will see in more detail what other reasons make it so important for us to study carefully the conductor in the same conditions as the final ones, i.e. those encountered in the insert working inside the resistive magnet.

2.4.2 Anisotropic property: angular dependency

The performance of HTS strongly decreases with high field but also according to its orientation, see section 1.1.2.1. In term of field dependency and in order to reach the objectives of the project, the HTS insert winding is expected to be subjected to a field of approximately 30 T. In terms of orientation dependency, the insert design has been careful studied at the first part of this chapter, section 2.2.4, to evaluate the components of the field applied on each area of the windings, especially the transverse component.

Knowing the final insert operating conditions, it is now possible to focus the investigation on the conductor performance under these specific conditions. The angle of the field applied on the winding has to be known accurately as the conductor performance drastically decreases when the field is oriented from 90° to 60°, as illustrated in Fig. 99. In this latter, 90° is used for a conductor parallel to the background field whereas 0° stands for a conductor studied perpendicularly to the background

field. The critical current is equal to around 600 A at 30 T and 90° but decreases to around 200 A at 30 T and 60°; its performance is decreased by a factor of three when the field orientation changes by only 30°. It is particularly required to evaluate the conductor performance with accuracy in this precise area as it will give the performance of the final insert. It has been seen in section 2.1.2 that the performance of the final insert is limited by the extremities of the windings, which face these specific conditions where the conductor performance abruptly decreases.

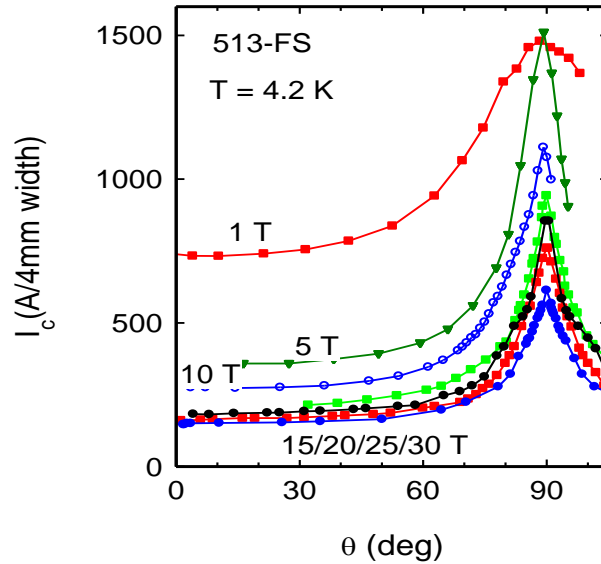


Fig. 99. Angular dependency of a 4 mm SuperPower tape [135]. In this graph, 90° is used for parallel field and 0° for perpendicular field.

In Fig. 100, the performance of a 4 mm SuperPower conductor is shown under high field with various orientations taken from [135]; here, 90° is also taken for parallel field and 0° for perpendicular field. Although these three different conductors belong to the same provider, their performances are slightly different. It underlines the necessity to include some margins when calculating a winding performance even if one similar conductor length has been previously characterized.

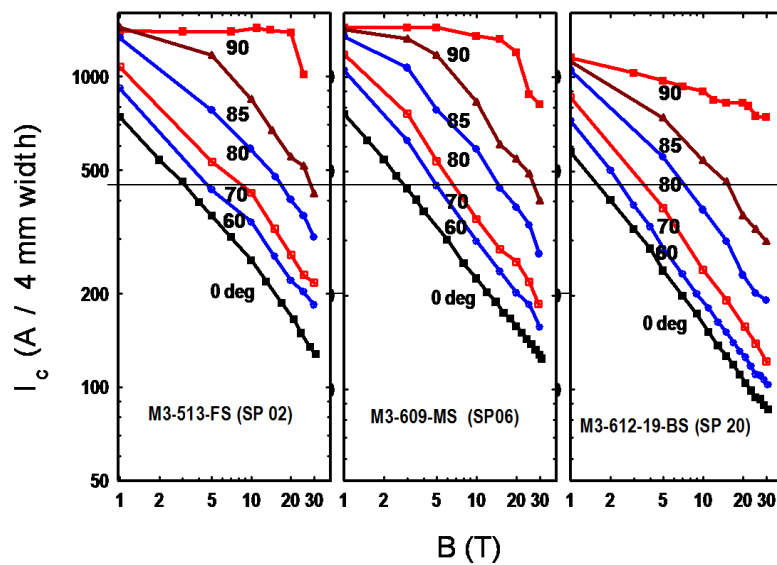


Fig. 100. Critical current measurements for three different 4-mm SuperPower conductors, [135].

The method used to measure the critical current of short HTS samples in the present work is detailed in the following sections.

2.5 SHORT SAMPLE EXPERIMENTAL STUDY DESCRIPTION

In this section, the experimental short sample characterization is detailed. In a first part, the objectives and the experimental protocol are developed and in a second part, the experimental setup allowing this study is presented.

2.5.1 Experimental measurement objectives

This section gives the outline of the experimental conductor characterization, the main objective of which is to evaluate its performance at different temperatures and different background fields, i.e. its critical current. This latter has been defined in section 2.2.4 in a theoretical way. However, a more practical definition is introduced in this section, allowing its experimental evaluation.

Several methods have been quickly presented previously to determine I_c values. In the present study, the conductor performance is evaluated using transport measurements. It means that under a specific temperature and background field conditions, some current is ramped in a superconducting conductor while recording its voltage. The critical current is then defined as the current for which the voltage reaches a defined electric field threshold, here equal to $1 \mu\text{V}/\text{cm}$ and set for comparison purpose between conductors and measurements. Such a voltage measurement according to the current passing through the superconducting sample is illustrated by the example given in Fig. 101, for an 8 T background field, at 4.2 K.

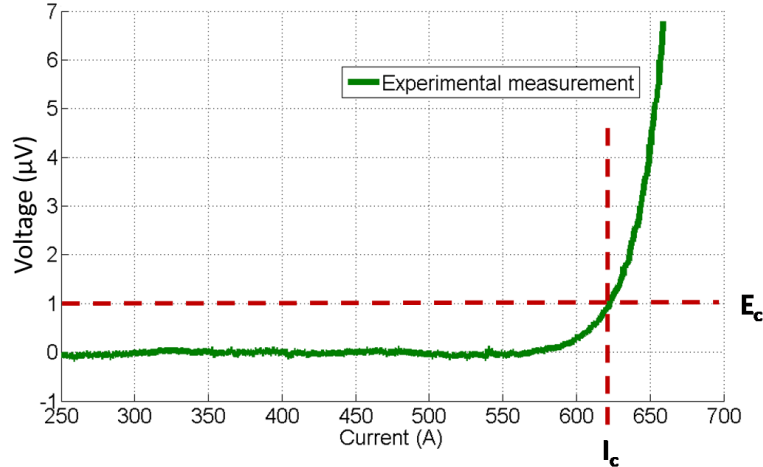


Fig. 101. Voltage measurement for 1 cm on a short 4 mm SuperOx sample obtained under 8 T and an angle of 10° . E_c is the electric field defined as threshold in V/cm to evaluate the critical current of the conductor under these conditions.

The experimental setup used here for this kind of study is detailed in the next section.

2.5.2 Experimental workbench for short sample characterization

2.5.2.1 Dedicated measurement probe

The device used to study straight samples is shown in Fig. 102. The sample has to be set up on the extremity (see description of the sample holder in section 2.5.2.2) of a measurement probe (Fig. 102, (a), (b) and (c)) to reach the centre of the magnetic field and this measurement probe has to fit

inside a cryostat (Fig. 102, (d)), designed to fit in the inner room temperature bore of the resistive magnet in order to study the sample at low temperature under high magnetic fields. The other extremity allows retrieving the experimental data of the inside instrumentation using two Jaeger connectors of 12 inputs each.

The measurement probe available at LNCMI allows working under high field in a 38 mm cold bore, which limits the length of the conductor sample to 30 mm. It is designed to carry up to 2000 A in liquid helium bath, under high field.

The current leads are made of copper on the top part, hidden by the G10 cylinder (Fig. 102 (b)). This G10 tube makes the probe extremity helium-tight and so allows it to be slightly outside the cryostat while using a sealing gland. Thanks to this particularity the probe can fit different resistive magnets as it can reach different heights still allowing its sample to be studied in the centre of the magnetic field produced by the outer magnet.

The second part of the current leads shown in Fig. 102 both (a) and (c), is made of brass, where the bottom part is soldered with REBCO tapes to reduce the heat dissipation during experiment. In the same figure, several G10 rings are set up along these current leads for mechanical reinforcement. The sample holder is only seen in Fig. 102 (a), at the extremity of the probe (bottom part of the photograph) but it is developed in the following, in section 2.5.2.2.

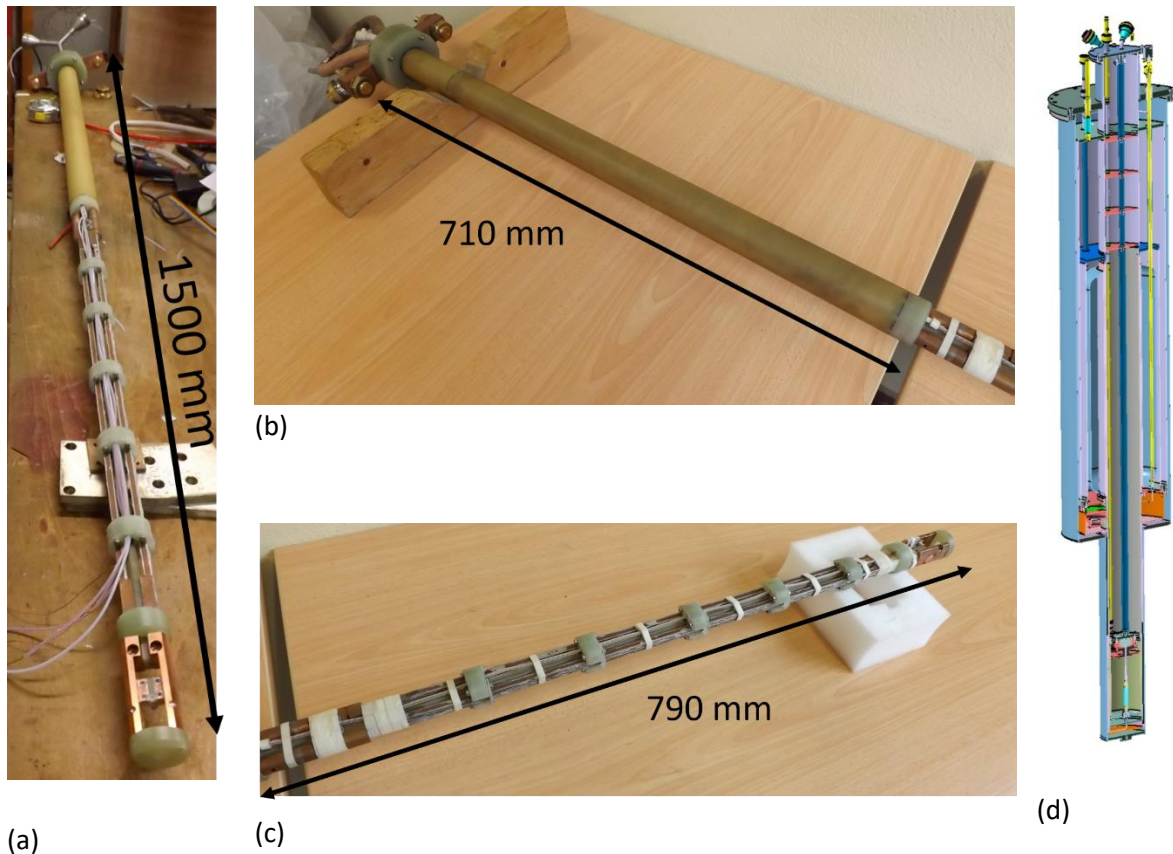


Fig. 102. Cryostat draft and measurement probe photographs for high field experiment in helium bath. (a) is the whole measurement probe, (b) is its top part, (c) is its bottom part and (d) is a draft of the cryostat.

The probe is also fully instrumented for a good monitoring of the whole experiment. First, it is equipped with six voltage taps set up along the height to monitor its behaviour; Fig. 103 shows the voltage taps setup along the probe according to their location. This voltage surveillance is expected to prevent thermal runaway as a high current may cause severe damages, but it also serves to identify bad contacts.

The measurement probe also enables working at different, higher temperatures achieved by a heater plate that can be added at the extremity of the probe. Its temperature is evaluated by Cernox sensors set up at different places on the measurement probe, i.e. on the heating plate below the sample, on the sample holder and at the top of the brass current leads doubled with HTS tapes, see Fig. 103. While working at a constant temperature, these sensors allows monitoring any change of value that could distort the results, especially close to the sample; most of the following results are given in liquid helium bath.

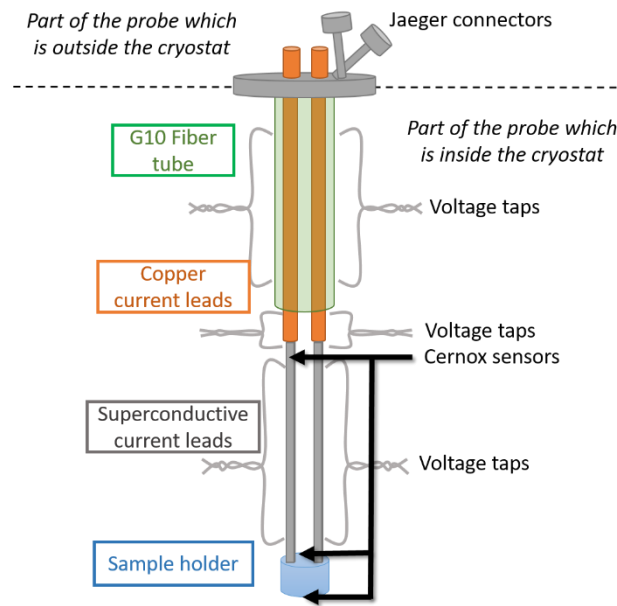


Fig. 103. Instrumentation set up along the measurement probe.

2.5.2.2 Details of the sample holder setup on the extremity of the measurement probe

The sample holder is set up at the extremity of the measurement probe. It allows rotating the sample in order to study the angular dependency of short straight HTS conductors. The sample is located at the extremity of the measurement probe shown in photographs (a) and (b) in Fig. 104. In Fig. 104 (a), the white arrow shows the direction of the conductor surface and the black one the background field axis. The red circle underlines the rotating part of the sample holder. The draft (c) shows how the REBCO sample is set up (red tape) on the rotating part of the measurement probe; the copper pieces are opaque orange and the glass fibre is transparent white.

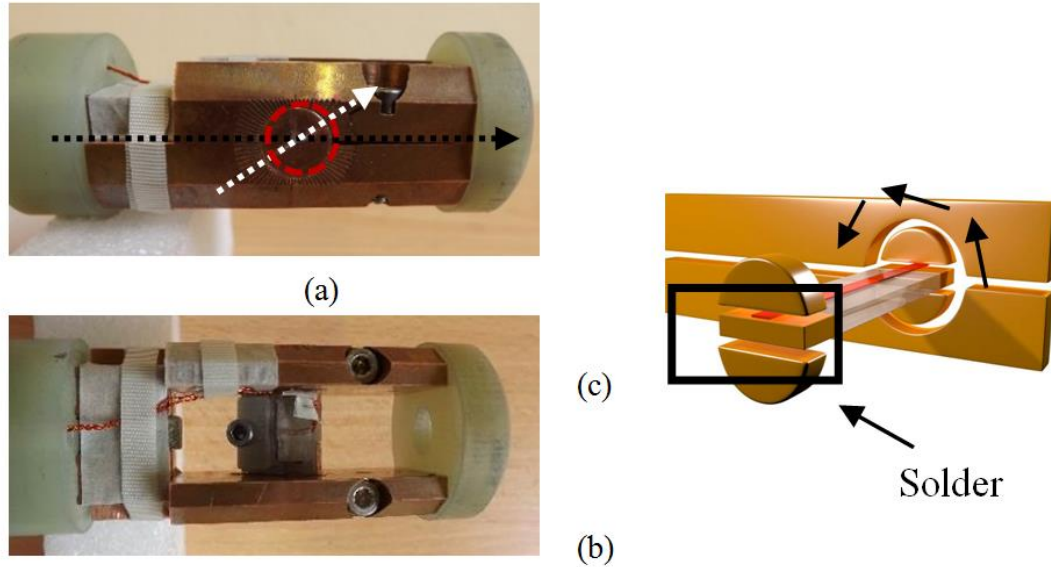


Fig. 104. (a) is the view from the side of the extremity of the probe, where the sample is placed, underlining the rotating part. (b) is a view from the top of the extremity of the probe. (c) is a draft to better understand how the sample is set up exactly on the workbench.

The straight samples are prepared to measure about 25 mm in length, their width can be up to 6 mm, and their thickness about 100 μm . A schematic view of the workbench is shown in Fig. 104, (c), illustrating the very extremity of the probe to better understand the rotating part. The tape can either be clamped between the two half copper cylinder or soldered in it for a better contact depending on the thickness of the conductor.

The sample setup allows studying the sample from 0° to 360° with an angular step of 2.5° under magnetic field, and an accuracy of 1° . It is made possible thanks to the scale which is engraved in the copper piece. The voltage measurement is in the middle of the tape with voltage taps made of copper wires soldered on the tape, 1 cm far from each other. The critical current I_c is defined as the critical current value achieved when the voltage corresponds to an electric field threshold E_c of $1 \mu\text{V}/\text{cm}$ as already illustrated by Fig. 101, this measurement requires to inject a current above 600 A.

2.5.3 Experiment specificity: full width conductor study

One of the main specificities of this workbench is its high current capacity. First, large inner diameter for high field magnets is rare: for a given power, the larger the inner bore, the lower the field generated. However, even for this size (30 mm cold bore of the cryostat), it is not easy to design a probe able to carry 2 kA.

As a result of their steady improvement, REBCO conductors can carry more and more current; at 4.2 K (liquid helium bath), more than 1000 A can pass through a 4-mm tape in parallel magnetic field [29]. Therefore, measurement probes also have to carry more and more current. The free area under magnetic field is narrow, so measurement probes cannot easily carry enough current even at low temperature because of the need of a minimum section for the resistive interfaces.

Critical current measurements of several different tapes under various high magnetic fields can be found in the literature but they are mostly measured under specific magnetic field orientation, especially under parallel and perpendicular fields [28]. Some other orientations between these two

specific cases can be also found but most of the time, the width of the tape is reduced in order to accommodate the measurement probe limitations [30], [31]. Generally, it also enables to fit a remote rotating stage, avoiding ex-situ manipulation. However, the fact that the tape is cut in order to reduce its width can be responsible of some defects in the conductor leading to a decrease in performance [32]. For design purpose, the characterization of the sample in its full width is preferred as it may also happen that the local J_c varies from edges to centre [32].

To conclude, the will to study full width conductors requires to work with very high currents, i.e working at the very limit of what can be done with our means. This has for direct consequences many resistive interfaces that can create temperature increase but it also makes it impossible to change the orientation of the sample from outside the cryostat. Moreover, the fast improvement of REBCO technologies make it necessary for these kinds of measurement probes to face higher and higher currents to allow measuring new HTS tapes.

2.5.4 Main challenges and problems encountered during experiment

This kind of measurement is tedious and repetitive, because of the requirement to work with full a width conductor. First, when the orientation of the sample needs to be changed, the probe has to be warmed up to room temperature to be removed from the cryostat. Only then can the sample be rotated according to the expected angle without damaging the sample and the already setup instrumentation. Eventually, the probe is inserted back into the cryostat and cooled down again. No more than one angle can be studied during a day because of this long process.

Moreover, given that the conductor limits are studied, they are easily damaged during experiment and it can be so for a range of reasons. First, because of the high current and the high background field, the sample faces strong mechanical stresses created by the Lorentz force 1.4.7. The current is then set up to pass through the sample so that this stress is oriented in a way which presses the conductor on the sample holder, expected to be flat enough not to damage the tape. If the current is set up the other way, the conductor would deform and could be damaged by the edges of the current leads, or even delaminate. Secondly, the interface between the superconducting sample and the copper current leads is rather small and can create elevated heating. However, since there is no space for Cernox sensor here, this increase of temperature cannot be monitored properly.

The samples are studied in liquid helium bath as the final wound prototype is supposed to work in the same conditions. Since the high current carried by the probe implies heat generation the assumption was made that the current is ramped fast enough to prevent the heating and keep the bath in adiabatic conditions, at 4.2 K. Current ramps are above 30 A/s, in order not to heat up the probe, and according to how much current needs to be passed into the sample to see the transition. The experiment is also cooled down between each current ramp.

One last issue that needs to be mentioned is the fact that above 20 T, the field gradients are so important that they create bubbles in the liquid helium [136], [137], [138] so the cooling process is less efficient and the sample is more likely to burn. This means that after one measurement above 20 T, the background field has to be set up again under 19 T to let the experiment cool down before the next current ramp. This has also to be kept in mind for the final insert, which is expected to work at approximately 30 T.

2.6 EXPERIMENTAL RESULTS

This section first gives the formula to model the experimental voltage curves monitored during experiments. Only then, the experimental results of two different short sample characterizations under high field with varying orientation are given.

2.6.1 Quench model: power law

The power law (8) is commonly used to model the $E(J)$ behaviour in superconductors.

$$E(J) = E_c \left(\frac{J}{J_c} \right)^n \quad 8$$

E is the electric field in V/m. E_c is the electric field set as a criterion, usually it is assumed to be 1 $\mu\text{V}/\text{cm}$ for REBCO current transport measurement [139]. J is the current density and J_c is the critical current density, i.e. the value of J when E_c is reached: both of them are in A/mm^2 . n has no unit and is the exponent of the law, called the power factor; it reflects the sharpness of the transition. It may help to estimate the quality of the conductor and can be a marker in a case of some degradation [140]. Its value varies mostly with field intensity, but is in the order of 30 or 40 for REBCO [33]. The power law constants, J_c and n are determined with the help of the experimental curve while trying to minimize the error, see Fig. 101 for the trend of the curves that is fitted with the power-law.

In the following, the critical current and the n factor are evaluated from the experimental $V(I)$ curve using the power-law formula.

2.6.2 SuperOx short sample characterization

2.6.2.1 Tape composition and TapeStar

The first conductor to be studied is a 4 mm REBCO coated conductor provided by SuperOx whose details are given in Table 2. The copper layers (top and bottom) are used as a shunt in order to stabilize the conductor when quenching and to propagate at the same time the produced heat. It also helps to handle local defects and so to reduce the consequences of the inhomogeneities along the length of the conductor.

Its substrate is made of Hastelloy®, a high performance nickel tungsten alloy enabling HTS tapes to face severe mechanical stresses; its yield strength reaches about 900 MPa at 4 K [46].

The geometry of the insert is one of the main constraints. In order to reach the project goal, the insulation has to be chosen as thin as possible. Deposited polyimide was then selected rather than insulating tape wound around the superconducting tape. In the first case, the layer has a thickness of about 10 μm as compared to between 25 μm to 50 μm for the second case [141]. However, for this short sample study, this insulation has to be removed. It can be either gently scraped with sandpaper or by using a chemical solution. This latter is a preparation of alkali water solution (8 g NaOH /100 g water or 11 g KOH /100 g H_2O) to which 50 % of diethylenetriamine is added by volume but other amines can be used as well. The solution is then heated to about 80 °C. The part of the conductor whose coating has to be removed is dipped into this solution for 2-5 minutes. When removed, the solution residue is wiped off from the tape with a tissue and the conductor is rinsed with water, wiped with a tissue again, and then rinsed with acetone. The same results are achieved with both methods.

Characteristics	
Width (mm)	4
Total thickness (μm)	~ 120
Substrate (μm)	60
Silver layer (μm)	~ 2
Copper (x2) layer (μm)	20
Deposited polyimide (μm)	10
Superconducting layer (μm)	~ 1.5
$I_{c,\text{min}}$ (77 K, self-field) (A)	120

Table 6. REBCO tape details.

The critical current measurements at 77 K given by the provider are shown in Fig. 105 with a minimum I_c value of 120 A ($I_{c,\text{min}}(77 \text{ K, self-field})$). The maximum I_c value reaches 160 A and the average value is about 145 A which makes around 17 % variations along the length of the conductor. For several samples, around 145 A was measured experimentally in liquid nitrogen bath, self-field so this value has been chosen to be the critical current at 77 K, self-field for further calculations, as in section 2.6.4.

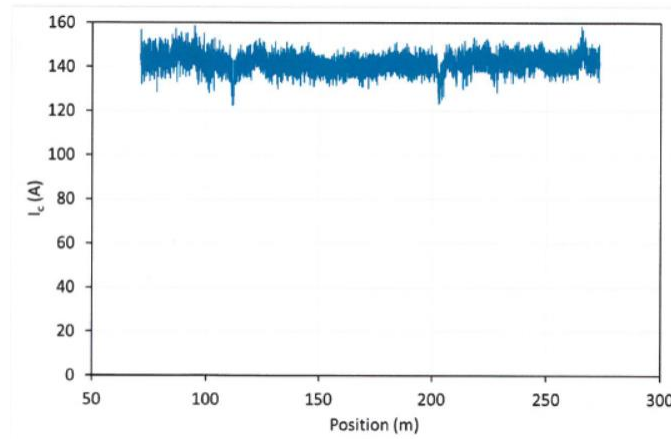


Fig. 105. Critical current measurements given by the provider at 77 K, self-field.

2.6.2.2 Experimental results: $J_c(B, \theta)$

Initially, the critical current of the conductor is measured at 77 K, self-field to give an idea of the values that can be expected at 4.2 K using already existing data on similar conductors [8]. In the present work, the critical current is first evaluated in fields up to 12 T and only then until 23 T, according to the availability of the magnetic fields at LNCMI during the period of the tests.

In both cases, the conductor is studied from 0° (parallel field) to 90° (perpendicular field) on the following specific intermediate values: 5° , 10° , 15° , 30° and 60° . Results are presented on the following graph, in Fig. 106. The critical current measurements are given according to the incident angle for several magnetic field values.

It has been seen above that these measurements are difficult to perform, and this is especially true at low angles for which the current is very high as well as the mechanical stresses applied on the sample. Some points are missing on the graph Fig. 106 for incident angles lower than 15° and magnetic field higher than 12 T. In this configuration, the strong mechanical stresses can easily damage the

conductor and so the samples have to be changed for every few measurements. The data shown in Fig. 106 represents the average of all the measurements obtained for same test conditions.

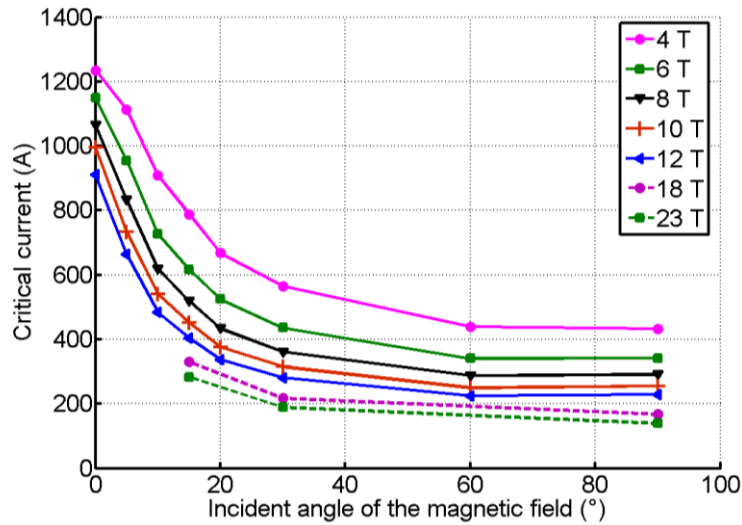


Fig. 106. Critical current value according to the intensity and the orientation of the background magnetic field applied on the tape.

In Fig. 106, the critical current values decrease by 30 % for a sample rotated from 0° to 15°. On the opposite, current performance does not really decrease anymore for incident angles higher than 50°. However, according to section 2.1.2, only small angles are interesting for the HTS inserts. Hence, the decrease of 30 % is a major concern to evaluate the critical current that will limit the performance of the coil. Later, it has been decided to compare this conductor to one from the SuperPower company as this latter could provide the lengths to build the whole insert according to the industry availability to meet the project deadlines.

2.6.2.3 *n* values

The *n* values, presented in Fig. 107, are also evaluated according to the *V(I)* curve in order to use them later in models, see section 3.8.6. The obtained results are conformed with what is found in the literature [33], shown in Fig. 108. The trend is similar between the two graphs; the *n* values start to slightly saturate when the background field is higher than 4 T or 5 T. Nevertheless, in Fig. 107, the *n* values seem to be between 30 and 40 above 5 T and in Fig. 108, SuperOx values are almost always higher than 40. The orientation of the field does not seem to have an important impact on the *n* value. The performance highly depends on the providers, as for instance, the results from Fujikura tapes are mostly around 60 when the background field is higher than 5 T.

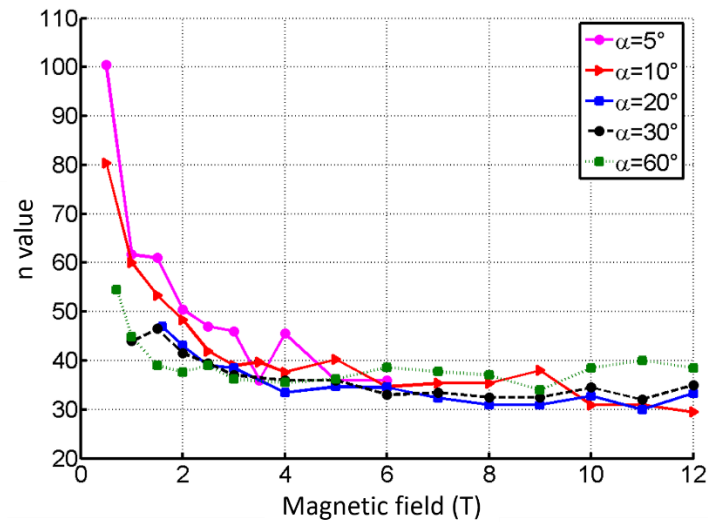


Fig. 107. Power factor values according to the magnetic field intensity and orientation.

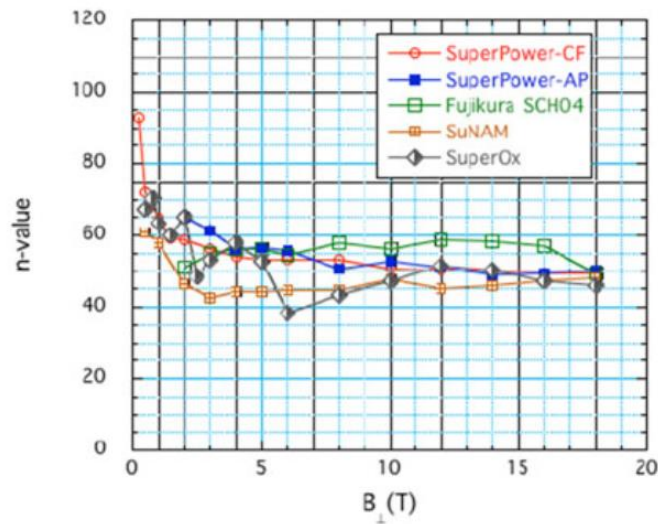


Fig. 108. n-value vs. B for commercial conductors in perpendicular fields at 4.2 K, taken from [33].

2.6.3 SuperPower short sample characterization

2.6.3.1 Tape composition

We intend to evaluate the performance of most of the conductors that will be used for winding the coils of the insert. I did the 4 mm SuperOx conductor characterization, but I believe it is interesting to compare the results with the 6 mm SuperPower conductor that is currently studied in our team. I could only participate in the first experiments but as this kind of study is time demanding, I cannot be part of the tests that will be done later. In this paragraph, only the beginning of the critical current measurement under high field with different orientation is presented; the SuperPower conductor characteristics are detailed in

Characteristics	
Width (mm)	6
Total thickness (μm)	~ 75
Substrate (μm)	50
Silver layer (μm)	~ 3
Copper (x2) layer (μm)	10

Superconducting layer (μm)	~ 2
$I_{c\text{min}}$ (77 K, self-field) (A)	196

Table 7.

Characteristics	
Width (mm)	6
Total thickness (μm)	~ 75
Substrate (μm)	50
Silver layer (μm)	~ 3
Copper (x2) layer (μm)	10
Superconducting layer (μm)	~ 2
$I_{c\text{min}}$ (77 K, self-field) (A)	196

Table 7. SuperPower conductor details.

2.6.3.2 Experimental results

The first results from the characterization of the SuperPower tape under high field with different orientation at 4.2 K are given in Fig. 109.

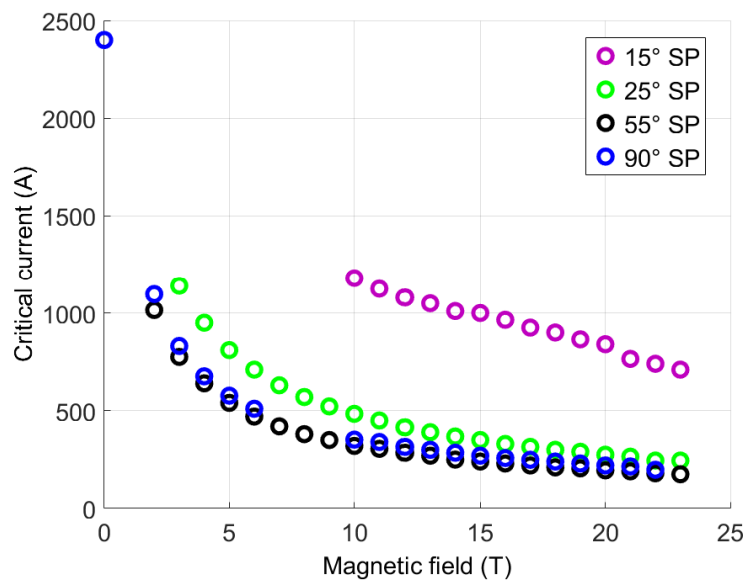


Fig. 109. Critical current measurement of a 6 mm SuperPower conductor at 4.2K, under magnetic field up to 23 T.

Only the critical current in self-field in liquid helium bath was evaluated with currents higher than 1200 A, up to 2400 A. At the time of the experiment with a background field, a higher power source was no longer available, so tests were only performed up to 1200 A.

As the minimum critical current at 77 K, self-field and the width of the conductor are different from the tape previously studied, it is hard to compare their performance by only watching their critical current values. With only these few curves, it is difficult to compare several conductor performances

and to know which one has the expected properties, especially when measured on different conductor widths. That is why a lift factor is used thereafter.

2.6.4 Performance comparison between SuperOx and SuperPower conductors

2.6.4.1 Lift factor and critical current quotient comparison

In order to compare conductor capacities, the lift factor is used; it means the critical currents evaluated during experiments are not directly used anymore but their ratio on the conductor minimum critical current given by the provider at 77 K, self-field.

$$\text{Lift factor } (B) = \frac{I_c(77 \text{ K, self-field})}{I_c(4.2 \text{ K, } B)} \quad 9$$

The comparison between the two tapes is shown in Fig. 110; comparing conductor properties will help choosing the provider to build the final insert. It is noticeable in Fig. 110 that for high incident angles above 20°, the lift factors are similar, but below, as for the 15° angle for example, the performances are quite different.

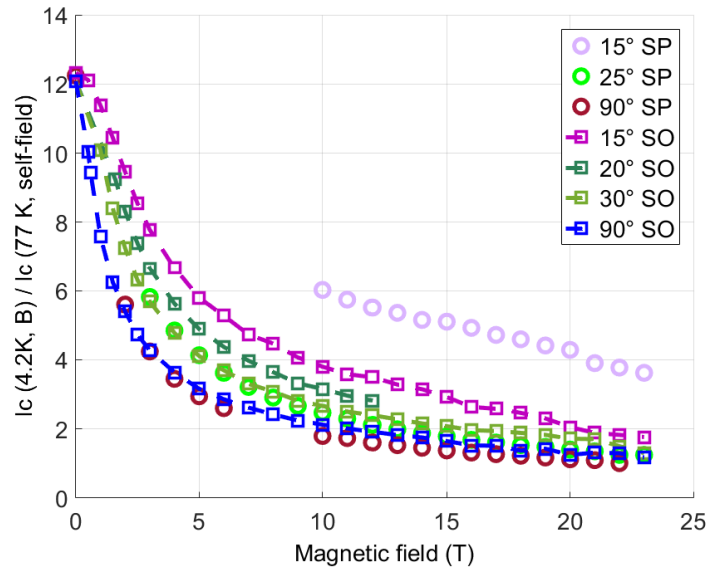


Fig. 110. Lift factors comparison of SuperPower and SuperOx experimental data.

Fig. 111 shows the differences from the SuperOx and SuperPower experimental measurements evaluated in percentages according to the experimental SuperOx data; this allows underlining the pronounced increase of performance for low angles in the studied SuperPower tape compared to the SuperOx one. Comparing lift factors is crucial as it is seen in the previous paragraphs that the final windings will be subjected to high fields with an orientation up to 15°. Fig. 111 shows that this is the specific area where the largest difference between the two conductors is observed. For 15°, the difference in lift factors between SuperOx and SuperPower is higher than 2. Moreover, this performance mismatch is also underlined with the comparison of the 25° from SuperPower and 30° SuperOx which is lower than 0.5. However, the lift factors are similar for the same field orientation of 90°.

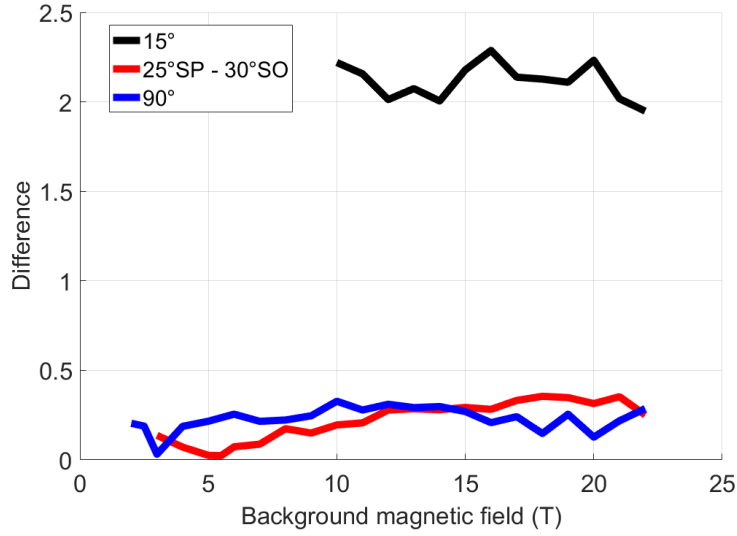


Fig. 111. SuperPower tape difference from SuperOx tape.

2.6.4.2 Critical current according to the temperature

The characterization under high field has been studied but also according to the temperature in order to extrapolate the conductor behaviour when they heat up, in self-field.

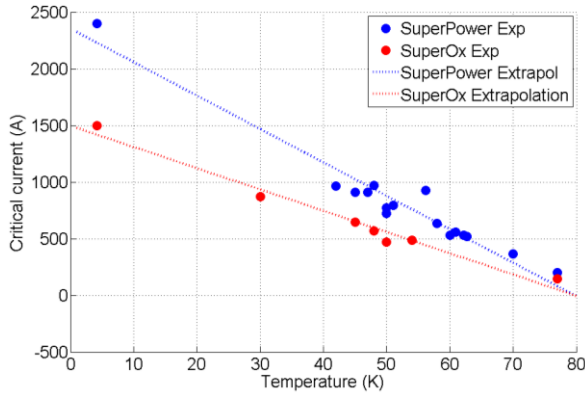


Fig. 112. Critical current according to the temperature of two conductors provided by two different providers, self-field.

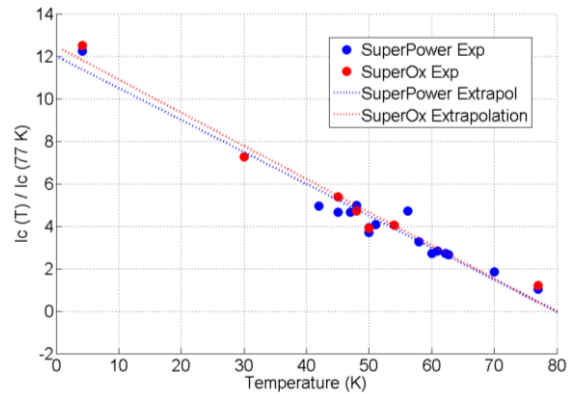


Fig. 113. Lift factor according to the temperature of two conductors provided by two different providers, self-field.

In term of temperature, both conductors have similar behaviour. The observation is also used in the model developed in section 3.6.1.

2.7 EXTRAPOLATION OF THE MISSING DATA FOR NUMERICAL MODEL IMPLEMENTATION

This kind of study is time demanding and difficult to conduct, especially when the current passing through the sample is high (small angles) under field. Therefore, missing points need to be numerically extrapolated to be implemented in the dedicated model. First, the common Kim model is used according to the B module and in a second part, its generalized formula is applied on the experimental results.

2.7.1 Extrapolation using the Kim model using the B module

Kim's model [34] was introduced to account for the effect of the magnetic field on the J_c value. It is here used to extrapolate the previous results, using the following formula (10).

$$J_c(B) = \frac{J_c(0)}{1 + \frac{|B|}{B_0}} \quad 10$$

$J_c(0)$ is the hypothetic value of J_c in self-field. As the critical current is huge for low fields, it is not possible anymore to neglect the magnetic field generated by the tape itself. The critical current without any background field is about 1450 A for the tape studied here. J_c is then numerically approximated and this number is designated as $J_c(0)$. Above the B_0 value, the critical current starts to slightly saturate [35]. The results obtained by fitting Kim's model on the experimental results are shown in Fig. 114. Constants are derived from experimental results. The error is less than 4 % for incident angles lower than 20° but above 10 % for the incident angles higher than 20°.

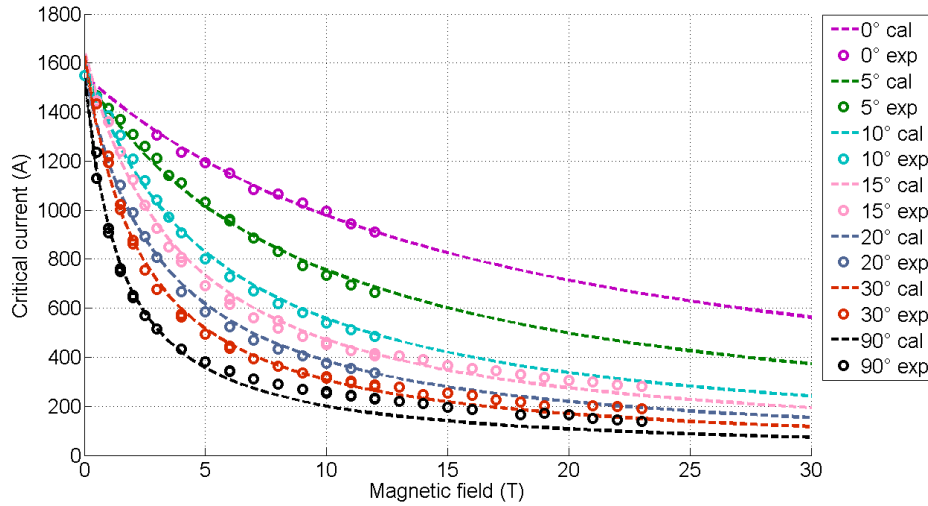


Fig. 114. Extrapolation of the critical current of a 4 mm SuperOx coated conductor according to the field intensity and orientation using the Kim model.

The numerical model only uses the B module, it does not fit the experimental curves trend for magnetic field lower than 10 T with incident angles higher than 20°. Nevertheless, the model is sufficient for the present work as the insert only faces small incident angles of the magnetic field, lower than 20°: in this range the model fits the experimental results with an error lower than 10 %. Moreover, it has also been seen that the transverse field component can be easily decreased thanks to the geometry. Using this formula, the error is up to 35 % for some conditions especially when background field is high, for example when the angle is 90°.

2.7.2 Extrapolation using the Kim model generalized formula

Even if the previous model could be used further, another formula is now considered taking into account the change of performance with respect to the field orientation; it was proposed in [36].

$$J_c(H_i, T) = \frac{J_c(T)}{(1 + \frac{H_i}{H_0(T)})^\beta} \quad 11$$

In this formula, β allows fitting more accurately the trend of the experimental curves; a similar formula is used in [11]. The results using this formula are shown in Fig. 115 and it yields a reduction of the error down to around 10 %. This interpolation is used in the next parts of this work, especially for modelling. Other more complete formula are also investigated like in [5].

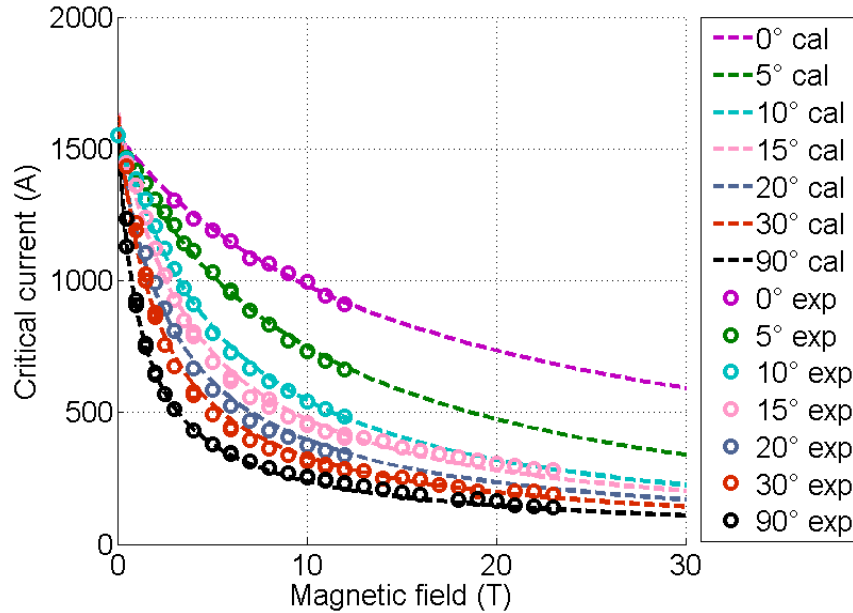


Fig. 115. Extrapolation of the critical current of a 4 mm SuperOx coated conductor according to the field intensity and orientation using the generalized Kim model.

2.8 CONCLUSION

In this part, I_c measurements of short straight samples of HTS tape are presented. The difficulties of these measurements are no negligible as the limits are tested of what current can be reached in a small volume.

As well, because of technical constraints (changes of samples and sample angles), these measurements are time consuming and the required magnetic fields to do so are rare, especially for very high fields. Due to lack of availability, measurements have not been conducted up to 30 T.

The power-law is used to model the measurement data and evaluate the critical current of the conductor as well as the n values. The results are compared to what is found in the literature and show good similarity. Several models are introduced that help to fit the experimental data for interpolation as well as extrapolation and good results are found using the generalized Kim model.

The characterization of these tapes is a continuous task as they improve regularly or may differ from one batch to another. Further measurement campaigns are continued. The set of data already obtained, focusing on two main suppliers, will be used to model our winding as explained next.

This study has two main objectives; the first one is to compare conductors, especially their performances under the same conditions as the final insert, in order to choose, which one could be best for the project. We mainly focus on two companies, SuperOx and SuperPower. The second goal is

to evaluate the conductor performance in detail to use the data when modelling wound samples and the final insert behaviours. A better understanding of the conductor will help create a more accurate model; this is more developed in the next chapter.

All measurements on short straight samples is used to create single and double pancake models; the main objective is still to find out whether a better knowledge of the conductor behaviour as characterized by short straight samples can lead to a better protection.

3 MAGNET COIL MODEL, FIRST SIMULATIONS

The experimental short sample characterization presented in chapter 2 aims at investigating the conductor behaviour while working under similar conditions as the final insert. A numerical model is then necessary to evaluate how precisely the behaviour of longer lengths of the same conductor in a winding can be predicted and eventually the behaviour of a full insert made of a stack of several pancakes.

In the first part of this chapter, the main objectives of the numerical model are explained followed by the details of an already existing model, which is used as a base for the magnet quench model. In the second part, the necessary improvements on the original model are developed as well as how the modifications are implemented. The magnet quench model is then used in several test cases to evaluate the influences of its inputs.

3.1. OBJECTIVES OF THE MODEL

A model was previously developed in our team to simulate the behaviour of a FCL, presented in [38]. This model is called the original FCL model in the whole chapter. A new model is developed on this basis but modified and expanded to simulate the quench propagation in pancake coils for magnet applications. The model explained in the following and based on the original FCL model is called the magnet model.

The main objective of this magnet model is to better understand the wound sample behaviours, i.e. how and where a quench starts and propagates inside the winding. This model is wanted to be as accurate as possible taking into account the inhomogeneity along the length of the conductor. Hence, the model is expected to give the location of the start of the transition in the winding as well as how the transition propagates according to the initial local critical current density values of the conductor given by the provider at 77 K, self-field, assuming that there is a correlation with the data at lower temperature, under field [37].

The model is developed below for a single pancake but can also similarly simulate double pancakes. The model can be applied to simulate a current ramp in the coil, a background field ramp or a local or general increase of temperature. The magnet quench model is also expected to be compared to the results of the wound sample experiments. Section 3.2.1 below presents the original FCL model operate in order to underline what can be kept and what parts need to be added or modified to develop a coil quench model.

3.2 AN ALREADY EXISTING MODEL FOR FAULT CURRENT LIMITER

3.2.1 Main description and aims of the original FCL model

The original FCL model uses Matlab and its toolbox Simulink. The electric circuit implemented in the model can be either an AC or DC voltage source, with a given output impedance, which represents the grid in which the FCL is inserted. Fault scenarios can be simulated by a perfect switch connecting the grid to various fault impedances.

The main objective of the original FCL model is to evaluate the influence of the inhomogeneities along the length of the conductor on the temperature rise during operation.

The original FCL model studies operation from 77 K to 65 K only and the length of coated conductor used for the winding is divided into blocks so that the TapeStar values can be applied along the length of the FCL. In each block the current sharing between the normal layers and the superconducting layer is evaluated, which follows the power law. As FCL windings are made so that their inductance (and thus the field) is almost zero, there is no need to calculate in detail the local field value to estimate the local critical current density. This model is detailed in [38].

The original FCL model includes the calculation of the thermal propagation along the length of the tape used for the FCL and exchanges from the tape faces to the cooling bath, but no thermal exchange from one turn to the other as in the FCL case the turns are wound very loosely to maximize heat exchange with the bath. The new model and its main features are described with more details in the following sections.

3.2.2 Necessary improvements to adapt the model to magnets

In order to enable pancake coil simulations, several adjustments have to be made. First, the magnetic behaviour of the coil itself has to be added to the model as well as the field generated by the background field, as these will impact the local critical current density.

Moreover, to know what components of the field are applied on each point of the winding, the geometric coordinates of the wound conductor have to be known precisely.

One more adjustment is about the thermal behaviour of coil, which does not work anymore in nitrogen bath but in liquid helium, and with closely wound turns allowing heat exchanges between turns. The original FCL model 1-D thermo-electric approach is therefore not sufficient. 2D heat propagation must be considered in the new coil quench model. These necessary updates are developed below.

3.3 ELECTRIC CIRCUIT

3.3.1 Main modifications from the original FCL model

The model does not use Simulink toolbox as it is not required anymore: in the original FCL model, an external voltage source is used whereas for a magnet coil, the current is known. Also, the two operating phases are well defined for the magnet coil model as detailed in the next paragraph.

3.3.2 Calculation of the two operating phases

The model is a transient simulation coded in two parts: charge and discharge of the coil. The electric circuit is illustrated in Fig. 116. In a first part, from $t=0$ s, the coil is charged with the current source. When the voltage of the coil reaches the chosen threshold, at t_d , K closes, leading to the discharge of the superconducting coil in the resistance R until t_f defined in the model initialization. The switch is assumed to be perfect so the state changes are instantaneous and there is no time delay between the protection trigger and the switch changes.

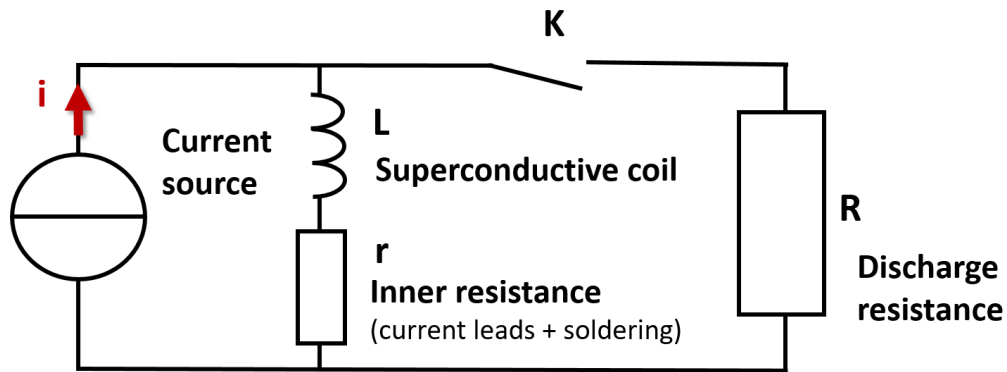


Fig. 116. Illustration of the electric circuit.

From $t=0$ s to $t=t_1$, the current in the coil is equal to the current generated by the source; it can be either a ramp or a constant depending on the simulation.

$$I_{winding}(t) = I_{Power\ Source}(t)$$

12

From $t=t_d$ to $t=t_f$, the coil discharges in the resistance so the current follows the next equation, assuming that the resistance of the coil while it is dissipating is negligible compared to the other resistances in the circuit.

$$I_{winding}(t) = I_{winding}(t_d) \cdot e^{-\frac{(t-t_d) \cdot (R+r)}{L}} \quad 13$$

According to the electric circuit, when K_1 is open and K_2 is closed, the following equation is obtained.

$$U_L = U_R + U_r \quad 14$$

Which leads to:

$$L \frac{di}{dt} + Ri + ri = 0 \quad 15$$

Also written:

$$\frac{di}{dt} + i \frac{R+r}{L} = 0 \quad 16$$

With all considered constants, the solution of this equation is

$$i(t) = A \cdot e^{-\frac{t}{\tau}} \quad 17$$

As the integration starts at t_d so the solution is

$$i(t) = A \cdot e^{-\frac{t-t_d}{\tau}} \quad 18$$

Moreover, the current is constant for an inductance meaning

$$i(t_d) = i_d \quad 19$$

So, the value of A is

$$A = i_d \quad 20$$

The two equations (12) and (18) define the two phases of the model: the charge and the discharge of the wound sample coil. The first phase of the model is always called 'charge' in the following even if, as mentioned above, the current can also be considered as a constant.

3.4 DEFINITION OF THE WOUND COIL GEOMETRY

3.4.1 Critical current measurements at 77 K, self-field

The length of the conductor is divided into a given number of blocks whose position is evaluated in order to initialise each part of the winding with its I_c value at 77 K, self-field. These blocks are expected to have the same length. Fig. 117 illustrates the conductor when wound and unwound. On the unwound conductor, couples of blocks are drawn in dotted red rectangles on the length, not to scale, to give an idea of the subdivisions.

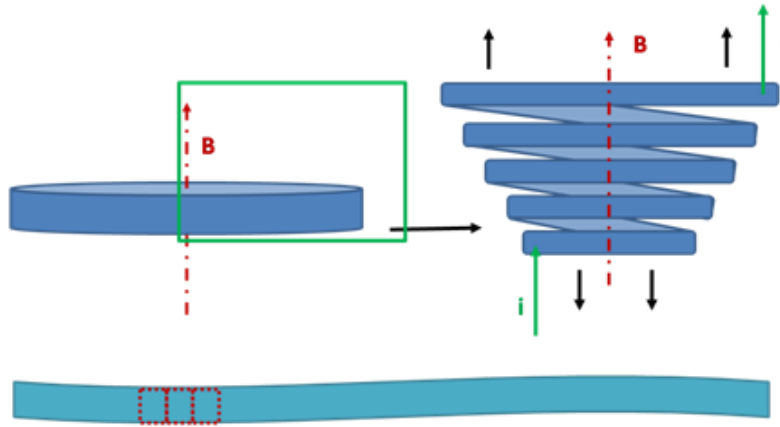


Fig. 117. Illustration of the length study of the conductor for a single pancake coil.

For the present model, these I_c values are either defined constant or following the trend of the measurement data at 77 K, self-field, according to the length of the conductor, given by the providers. An example of these measurement data is shown in Fig. 118.

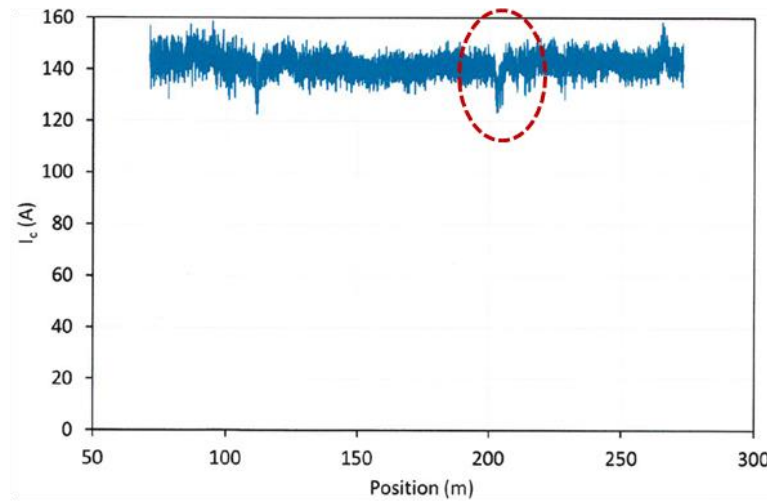


Fig. 118. Critical current values given at 77 K, self-field along the length of the conductor provided by SuperOx, see section 1.1.2.3.

In Fig. 118, the critical current value is given for every 2 cm but in the model the blocks along the length are expected to be bigger so when the manufacturer values are used, the I_c of one block is the average of the I_c values measured on the length of the block. It means that as many blocks as possible have to be defined along the length to stay accurate: this is illustrated in Fig. 119. In Fig. 119, the critical current measurements given by the providers at 77 K, self-field are in blue, according to the part of the conductor length. The blocks are delimited by the dotted black lines and the average value of the I_c is in red.

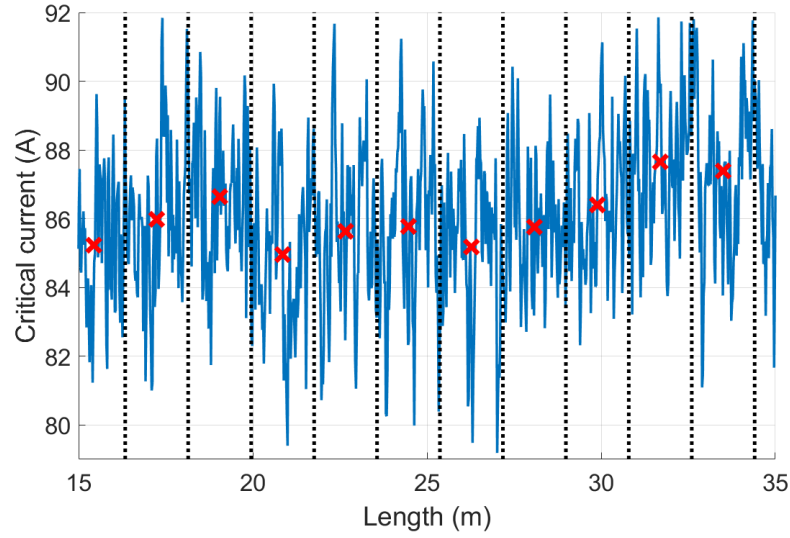


Fig. 119. Critical current measurement at 77 K, self-field according to the length of the conductor. The measurements provided by the manufacturers are in blue, the blocks are delimited by the dotted black lines and the average of the provider I_c value on the blocks are in red.

The objective is to have enough blocks to obtain at least the same minimum I_c value in the averaged I_c along the length of the conductor in the model as in the initial I_c measurement at 77 K, self-field. In section 3.8.5.1, the influence of the number of blocks is investigated for different initial I_c .

3.4.2 Definition in the winding of the block location along the length of the conductor

The superconducting tape used to wind the sample coil is divided into a given number of blocks, which is illustrated in Fig. 117 for a single pancake. All the blocks are expected to have the same length as the I_c (77 K, self-field) measurement is given with a constant definition: as observed in Fig. 118, the initial I_c measurement at 77 K is discretised on blocks of identical lengths. Each block's coordinates are used first to know what components of the field are applied on it, which is explained in section 3.5. Moreover, these coordinates are also used to implement a 2D thermal propagation; the geometry building in COMSOL is detailed in section 3.7, dedicated to the thermal study.

In this section, the evaluation of the space coordinates for each block is explained, i.e. how each block is defined in space when the coil is viewed from the top as shown by the red surface in Fig. 120.

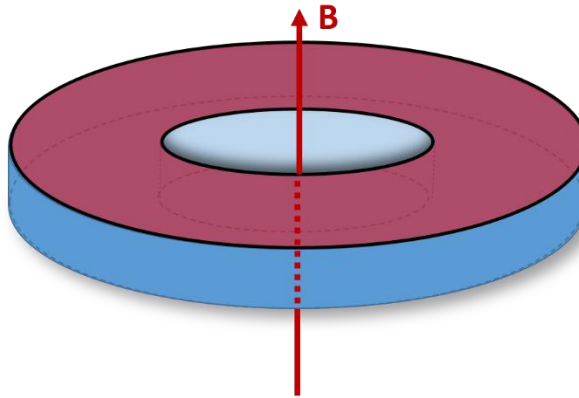


Fig. 120. View from the top of the magnet coil.

The method is similar for both a single pancake and a double pancake and in each case, the coordinates of each block are defined according to the winding. An obvious choice to model the winding geometry would be to see it as several concentric rings with a similar thickness to that of the conductor [39]. However, it is then difficult to discretise the wound conductor into blocks of the same length for blocks which are straddling two contiguous rings, as illustrated in Fig. 121.

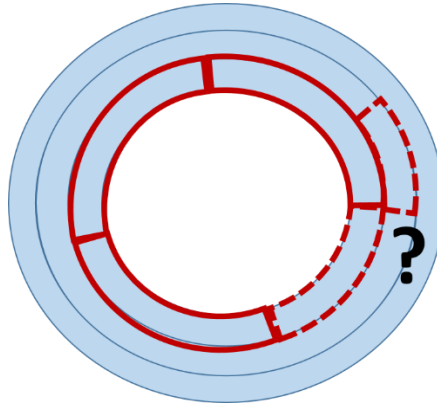


Fig. 121. When the winding is defined by concentric rings with the thickness of the conductor.

For this reason, in this model, the winding is seen as a spiral: i.e. each turn is built with two half rings of the conductor's thickness, and whose centres are slightly shifted in the x direction, see Fig. 122. Using this method, the whole winding is defined so all the blocks have the same length as illustrated in Fig. 122.

This method also gives a more precise evaluation of the magnetic field generated by the pancakes compared to the concentric ring hypothesis. Even if such refine field distribution evaluation is not necessary from the quench modelling point of view, it is interesting to point that such model approach could be usefully integrated in high field homogeneity coil design.

The result using Matlab is shown in Fig. 123 for a very large conductor in order to see how the blocks are defined; the blue triangles show the extremities of the blocks.

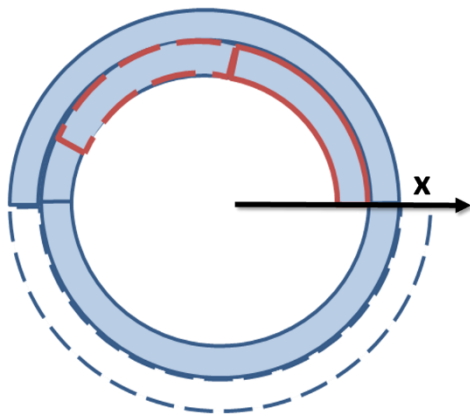


Fig. 122. Illustration of the creation of the geometry.

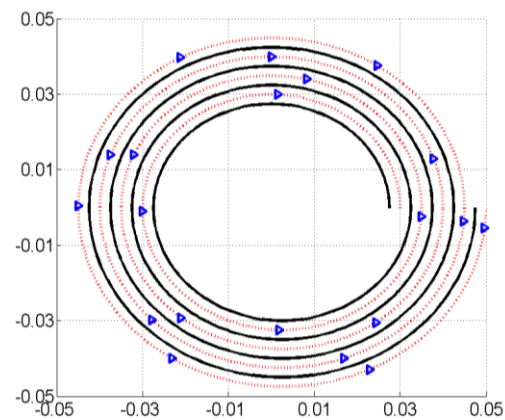


Fig. 123. Illustration of the block coordinates.

3.4.3 Discretization along the width

Each block along the length is also discretized along its width as illustrated in Fig. 124 in order to allow several limiting critical current calculations (see section 3.6.1) but also with higher accuracy for evaluating the components of the field on the winding.

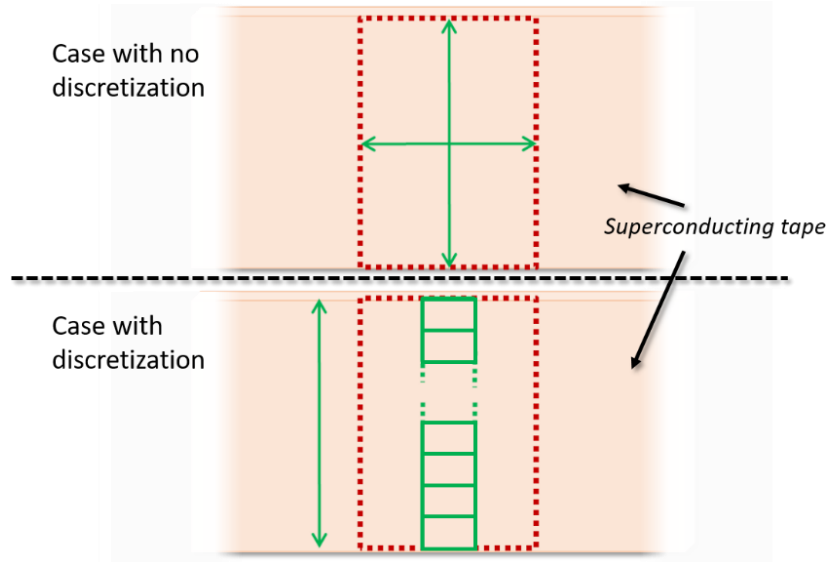


Fig. 124. Illustration of the definition of a block subdivision along the width.

3.5 DEFINITION OF THE MAGNETIC BEHAVIOUR

As mentioned in the introduction of this chapter, one major update of the model is the implementation of a magnetostatic study of the coil to obtain the local lift factor, previously evaluated in section 2.6.4.1 during the experimental short sample characterisation.

In this section, the calculations of the magnetic field generated by the outer magnet and by the sample coil itself are first explained. Then, the implementation of the correlation between these magnetic field distributions and the block coordinates is detailed. Eventually, this allows the evaluation of the I_c evolution on each block during the simulation.

3.5.1 Background field

The background field is integrated into the model using the field distribution generated by the outer magnet, both measured and calculated at LNCMI, see section 2.1.1.2. The magnetic field distribution is only evaluated on the cross-section of the sample coil, see section 2.1.2. A coefficient is added to the field distribution according to the centre background field required in the experiment.

3.5.2 Field generated by the coil according to the current passing through it

The magnetic field generated by the wound pancake is first evaluated using the software FLUX®/Alter [27] for an arbitrary current density, and used as an input in the magnet quench model. As there is no magnetic material in the coil, this field map can be used to obtain the actual field map at any given current using the following procedure.

The field distribution is evaluated using FLUX® for one current value passing through the coil, assuming the current is homogeneous in the conductor. With this hypothesis, the magnetic field distribution can be adapted to any amount of current as the field generated by the coil is proportional to the current. Hence, the magnetic field distribution on the cross section of the coil is evaluated using the initial FLUX® map multiplied by the ratio of the current passing through the winding by the current value used for the initial FLUX® calculation.

Fig. 125 shows both the cross-section of a single pancake winding, not to scale, on the top of the figure and the magnetic field distribution evaluated on a quarter of this cross-section. Only a quarter of the section is necessary as explained in section 2.1.

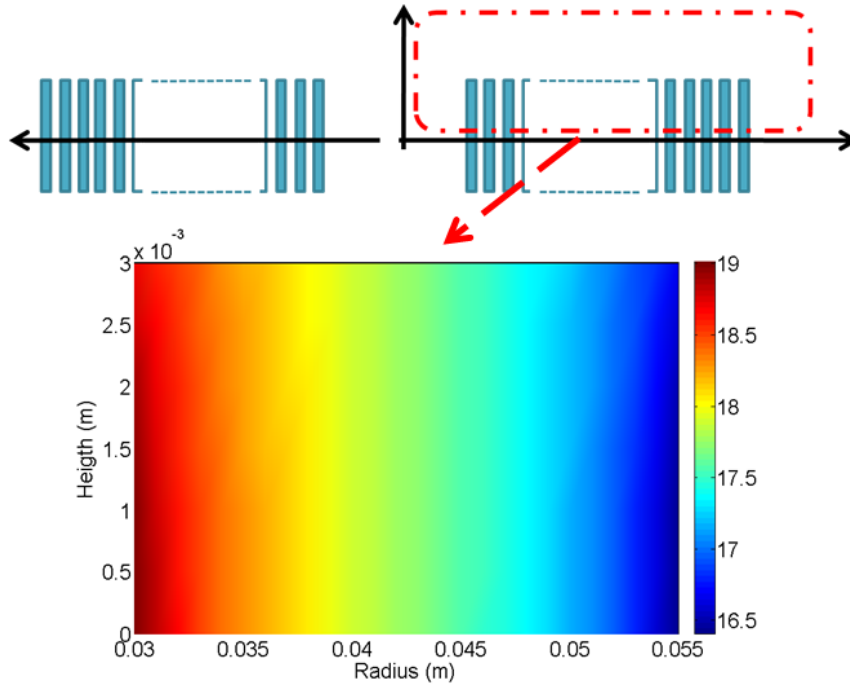


Fig. 125. Evaluation of the component B_z of the magnetic field on each block according to their coordinates on the cross-section of the winding.

3.5.3 Field components according to the position on the mesh

Once the components of the field are evaluated on the cross-section of the coil as illustrated by Fig. 125, the field components have to be extrapolated on each block. Each block is defined by its coordinates inside the winding as explained in 3.4. It means that the coordinates of each block's centre are known and for a single pancake, only the radius is different from one block to another. The radius of each block's centre is reported on the cross-section (illustrated in Fig. 126), for which the magnetic field distribution is calculated. The field distribution on the cross-section, in red in Fig. 126, allows determining the field components applied on each block using the cylindrical symmetry of a solenoid's field.

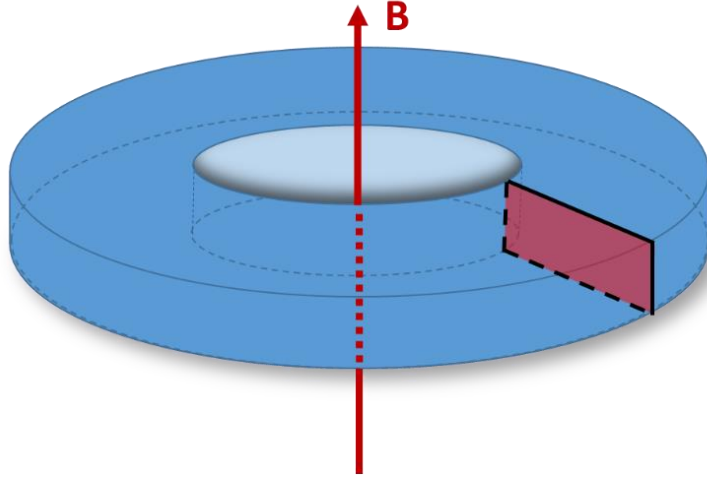


Fig. 126. Illustration of the cross-section for which the field components are studied on a single pancake winding.

Finally, for each time step of the simulation, the critical current of each block is evaluated using its initial I_c value at 77 K, self-field according to the length of the conduction and, on this value, is applied the lift factor extrapolated from the experimental characterisation (see section 2.6.4.1) according to the field components applied on the studied block.

3.6 CURRENT DISTRIBUTION BETWEEN THE SUPERCONDUCTIVE LAYER AND THE RESISTIVE LAYERS OF THE WOUND CONDUCTOR

3.6.1 Critical current calculation on a block

Before being calculated on a block, the critical current at a given time is first calculated for each subdivision of a block, see section 3.4.3. A lift factor is also used according to the temperature of the block using the short sample experimental characterization detailed in section 2.6.4.2. Only then, several methods are used to calculate the critical current of a block; it is either the minimum of the I_c calculated on each subdivision of a block or the average of it according to what assumptions are made. Both measurements are conducted, and the results are compared in section 0.

3.6.2 Current sharing on a block

3.6.2.1 Details of the current distribution calculation

At each time step, the critical current is evaluated on each block according to its temperature and the field intensity and orientation applied on it. At the same time, the current passing through the coil, i.e. in each block is also known as it is an input of the model.

When the current is passing through the conductor, the conductor voltage follows the power law, given below and illustrated in Fig. 127, see section 2.6.2.2.

$$E(J) = E_c \left(\frac{J}{J_c} \right)^n \quad 21$$

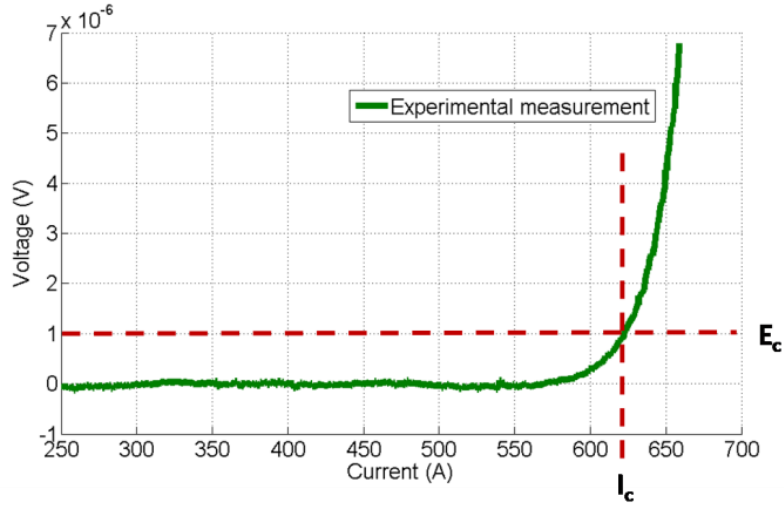


Fig. 127. Example of an experimental measurement to determine I_c .

For a given block, when the voltage inside the superconductive layer starts to increase, the current is expected at some point to also pass through the other (normal) resistive layers, which are illustrated in Fig. 128. These resistive layers are considered as only one equivalent layer whose properties are the average of the all materials properties that form this layer (properties are given in appendix 6.2) as illustrated in the following equation giving the equivalent resistivity of the normal layers as a function of the resistivity of each layer and their thicknesses.

$$\rho_{eq} = \frac{\rho_1 \cdot Th_1 + \rho_2 \cdot Th_2 + \dots + \rho_n \cdot Th_n}{Th_{tot}} \quad 22$$

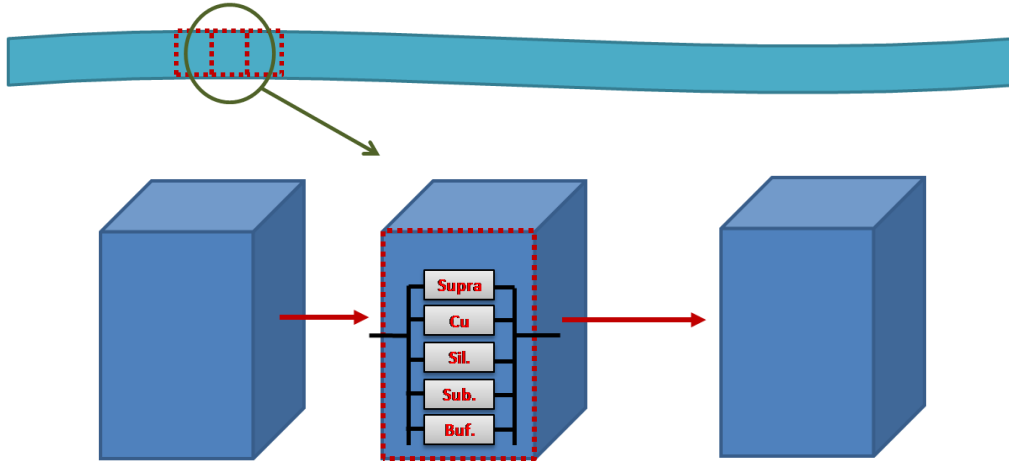


Fig. 128. Illustration of the subdivision of the length of the conductor into blocks underlining the layers of the tape.

3.6.2.2 Original FCL model calculation for current distribution

In the original FCL model, the calculation is iterative meaning that in a first step, the assumption is done that all the current is going through the superconductive layer, so the voltage of the superconductive layer is known using the power law. Knowing this voltage, the current going through the other layers can be assumed and thanks to this current proportion, the second step can start; knowing what proportion of current goes into the resistive layers, the voltage on the

superconductive layer can be evaluated. It stops only when the last current values calculated are close enough to the previous ones, at which point the correctness of the solution is assumed [142].

3.6.2.3 Current distribution calculation in the magnet quench model

In this part, the current sharing problem is studied to prove the existence and unicity of the solution whose existence was only assumed previously, which enable the use of an efficient root finding algorithm. First, according to the hypotheses explained in the previous section, the current distribution is seen as a voltage divider bridge, illustrated in Fig. 129, between the superconducting layer and the other resistive layers, seen as one resistive layer whose properties are the average of the several layers it represents.

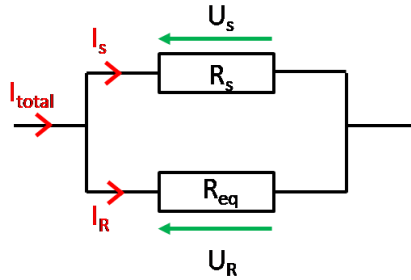


Fig. 129. Electric circuit of the current sharing between the superconductive layers and the other layers.

In the following, R stands for R_{eq} . The total current (I_{tot}) is the current passing through the superconductive layer (I_s) and through the other layers (I_R), leading to (23).

$$I_{tot} = I_R + I_S \quad 23$$

And for the case of a voltage bridge diverter both voltages are equal to each other, meaning:

$$U_R = U_S \quad 24$$

Also:

$$U_R = RI_R = R(I_{tot} - I_S) \quad 25$$

And using the Power Law:

$$R(I_{tot} - I_S) = E_c L g_u \frac{I_S^n}{I_c^n} \quad 26$$

Where $L g_u$ is the unit length of one block.

So, the final equation that needs to be resolved is the following.

$$I_S^n \frac{E_c L g_u}{I_c^n} + I_S R = R I_{tot} \quad 27$$

The unknown is the current passing through the superconductive layer. To simplify, the equation is divided by I_{tot} so the unknown is now the proportion β of the total current going through the superconductive layer, i.e. it has to be between 1 and 0. Finally the equation becomes the following.

$$\beta^n \frac{E_c L g_u I_{tot}^{n-1}}{I_c^n} + \beta R = R \quad 28$$

With

$$\beta = \frac{I_S}{I_{tot}} \quad 29$$

Nevertheless, this equation is an n degree equation; it means that the equation has n solutions that can be either real or complex. In the case of the present study, a real positive value is wanted and expected to be unique. Before looking for the solution, the existence of this unique real positive solution has to be proven to be sure not to find only local result while using any resolution method. Moreover, in the present model, the n influence is also expected to be studied so n cannot be fixed, it means that the existence of the unique real positive solution of this equation has to be proven for any n value.

3.6.2.4 Proof a unique real positive solution in each case

As n is expected to change in the model, it is not possible to investigate on the existence of a literal value for the solution. In this section, the existence of one positive real solution for all n values is discussed so the solution can be numerically assessed later in Matlab. The equation is now the following.

$$\beta^n + \beta \cdot R_{eq} \cdot \frac{I_C^n}{E_C \cdot Lg_u I_{tot}^{n-1}} = R_{eq} \cdot \frac{I_C^n}{E_C \cdot Lg_u I_{tot}^{n-1}} \quad 30$$

So, the studied function becomes (31):

$$y \rightarrow x^n + ax - a \quad 31$$

Where

$$a = R_{eq} \cdot \frac{I_C^n}{E_C Lg_u I_{tot}^{n-1}} > 0 \quad 32$$

It means that x is wanted such as $x^n = a(1 - x)$. Graphically, the existence of one positive real solution for all n value is defined by the intersection of the two curves x^n and $a(1 - x)$, which is illustrated in Fig. 130. The yellow square underlines the area of the possible intersection.

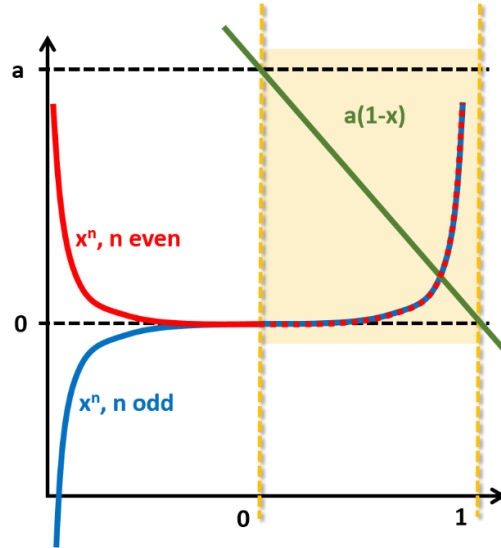


Fig. 130. Illustration of $x^n = a(1-x)$. The dotted green lines underline the minimum and the maximum value of the solution.

The proof of the existence of a unique real positive solution, presented in appendix 6.1, enables the use of any kind of root finding algorithm to solve the equation.

3.6.2.5 Resolution and seek of the unique real positive solution

However, the position of the solution is well-known, i.e between 0 and 1. As the solution is the proportion of current passing through the superconductive layer, it is expected to be between 0 (none of the current is passing through the superconductive layer) and 1 (all the current is passing through the layer). Resolving an n degree equation appears then not to be required and a method to approximate the zero is used to save time. As the existence of a unique real positive solution has been proven, these kinds of method cannot converge towards incorrect roots. Different root-finding methods can be used such as the bisection method or the Newton-Raphson method which allows fast resolution especially when knowing the trend of curve and the fact that the real positive solution is unique: Newton Raphson allows faster resolution and cannot possibly diverge in this specific case.

3.7 IMPLEMENTATION OF THE THERMAL BEHAVIOUR STUDY

Knowing what proportion of current goes through the resistive layers and the dissipation in the superconducting layer, the heat dissipation is evaluated on each block according to the resistive layers' properties, which are also temperature dependent, see appendix 6.2.

3.7.1 1D thermic model: heat propagation along the length of the conductor

The thermal propagation used in the model is a 1D heat propagation using Finite Difference Method. The propagation is only calculated along the length of the conductor as illustrated in Fig. 131.



Fig. 131. 1D heat propagation along the length of the conductor.

The 1D model uses the heat equation which is the following.

$$c_p \cdot \frac{\partial T}{\partial t} = \text{div} \left(\lambda \cdot \overrightarrow{\text{grad}}(T) \right) + Q \quad 33$$

Where c_p is the volumetric heat capacity in $\text{J.K}^{-1}.\text{m}^{-3}$, λ is the thermal conductivity $\text{W.m}^{-1}.\text{K}^{-1}$ and Q the heat source W.m^{-3} . The heat sharing only happens along one space component, x and so the equation becomes the next one.

$$c_p \cdot \frac{\partial T(x, t)}{\partial t} = \lambda \cdot \frac{\partial^2 T(x, t)}{\partial^2 x} + Q \quad 34$$

' λ ' can be defined for each block at each t time so it is supposed to be constant for one time step. The equation is now discretized according to both x and t .

$$\frac{T(x, l) - T(x, t - 1)}{\Delta t} = \frac{\lambda}{c_p} \cdot \frac{\partial^2 T(x, t)}{\partial^2 x} + Q \quad 35$$

And

$$a = \frac{\lambda}{c_p} \quad 36$$

For the second part of the equation, a centred explicit model has been chosen following the next equation.

$$\left(\frac{\partial^2 u}{\partial x^2} \right)_i = \frac{u_{i+1} - 2 \cdot u_i + u_{i-1}}{\Delta x^2} + \sigma(\Delta x^2) \quad 37$$

It leads to the following equation for each block, excepted for the two extremities of the length.

$$\frac{\partial^2 T(x, t)}{\partial x^2} = \frac{T(x + 1, t - 1) - 2 \cdot T(x, t - 1) + T(x - 1, t - 1)}{\Delta x^2} \quad 38$$

So, the final equation of the 1D model of the heat propagation is ruled by the equation below.

$$\frac{T(x, l) - T(x, t - 1)}{\Delta t} = a \cdot \frac{T(x + 1, t - 1) - 2 \cdot T(x, t - 1) + T(x - 1, t - 1)}{\Delta x^2} + Q \quad 39$$

Using this resolution technique for the heat propagation, the model is resumed in the draft presented in Fig. 132.

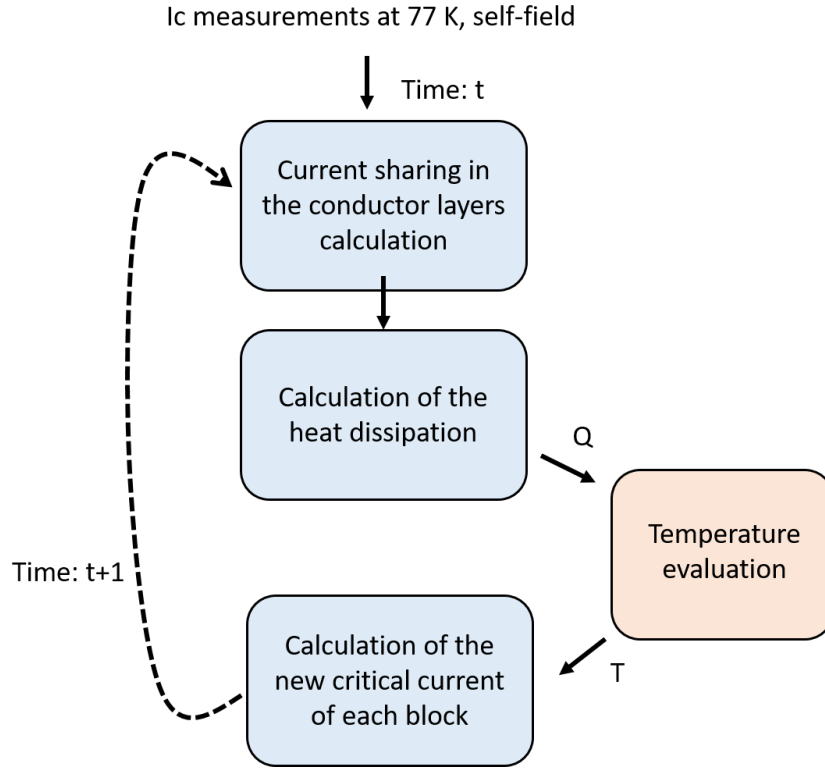


Fig. 132. Description of the model using the 1D heat propagation.

3.7.2 2D-thermic model: propagation along the length and the turns

As the conductor stabilizer is made of copper and the turns are insulated from each other, it could have been expected that the heat propagation along the turns was negligible compared to the heat propagation along the length of the conductor. However, in the case of a severe damage in insulated pancake coils, winding can show damaged turns following a radial direction, as experimentally illustrated in [40]. Even in the case of a less severe quench, a transverse quench propagation has been observed [41]. Hence, the present magnet model intends to compare the simulation results while using the two thermal models.

For the 2D model, Matlab is coupled with COMSOL which is used only for the heat propagation. The generation of the geometry as well as the change of method is straightforward as the coordinates of the blocks are already calculated as illustrated in Fig. 133.

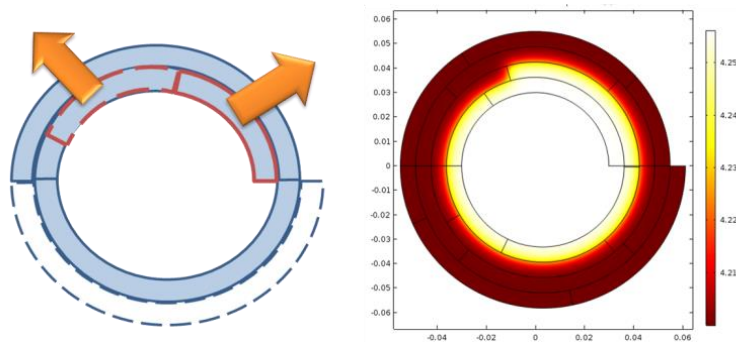


Fig. 133. Illustration of the 2D heat propagation model using COMSOL.

Most of the model follows the same logic as the 1D model except that the thermal study is now conducted in COMSOL. The 2D-model is still mainly written in Matlab which only calls COMSOL to perform the thermal calculations.

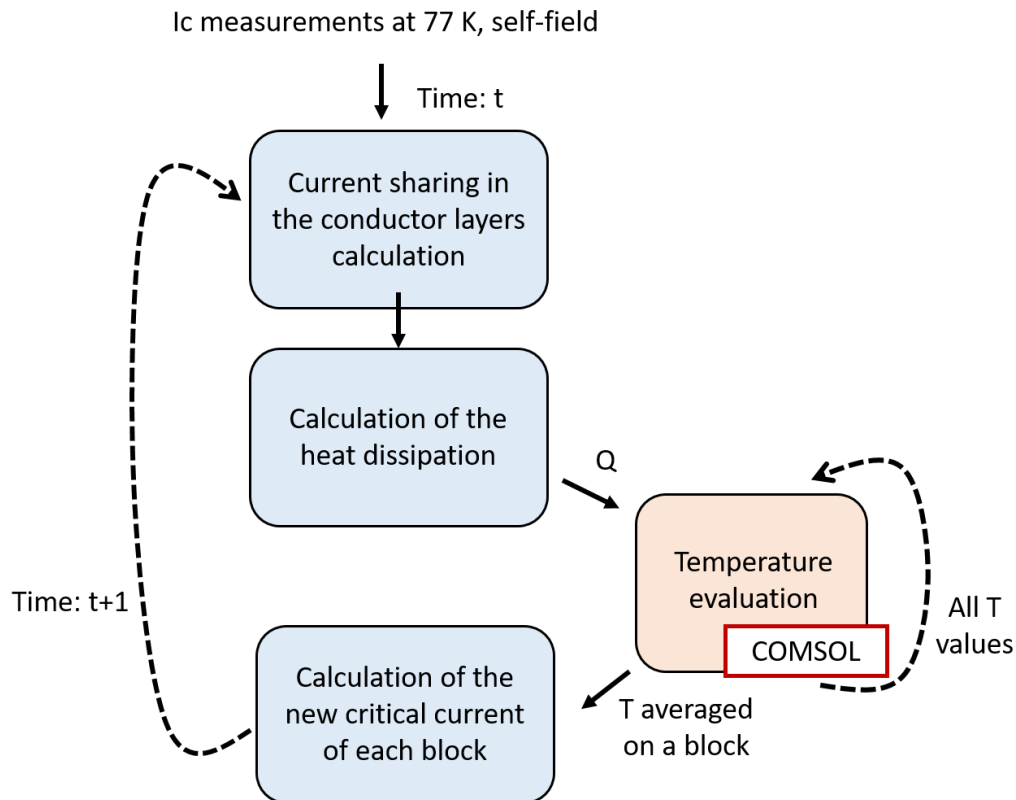


Fig. 134. Description of the model using COMSOL for a 2D heat propagation.

The geometry is created in COMSOL at the beginning of the study based on a Matlab script. Following the block subdivisions explained in 3.4.2, COMSOL also creates the mesh, which is only built one time during the initialisation of the model and is reused each time COMSOL is called by Matlab.

The Matlab program computes the transient study of the electrical problem in an explicit scheme using either constant or adaptive time-steps. For each of these so-called “electrical time-steps”, the Matlab program outputs the heat dissipated in each block according to the current distribution between the conductor layers (see 3.6.2.3) taking the average temperature of the blocks and the total current as inputs.

The heat dissipated in each block is then given to COMSOL, in which a transient FEM study computes the new temperature distribution in the whole winding based on the temperatures at the previous “electrical” step. The COMSOL study can create several intermediate “thermal” time-steps to solve the thermal transient problem. It outputs the average of the temperature in each block.

In Matlab, the new average temperature in each block is then used to evaluate the I_c for the next “electrical” time step, and so on.

It is thus possible in this 2D-model to work with two different time-steps, one for the electrical and one for the thermal phenomenon, which may take place in a different time-scale.

3.8 TESTS AND SENSITIVITY STUDIES

This section intends to show what can be calculated with this model and how the model can be adapted to obtain the desired information. In the following results, the pancake, which is modelled, is detailed in Table 8; it follows the geometry of the final design of the NOUGAT insert pancakes.

Model pancake characteristics	
Inner diameter (mm)	60
Outer diameter (mm)	110
Conductor thickness (μm)	145
Conductor width (mm)	6
Number of turns	170
Number of pancakes	1
Field coef. (mT/A)	3.04

Table 8. Characteristics of the coil which is studied in the model.

In these simulations, the background field is constant, and the pancake is initially at 4.2 K; the current is ramped at different rates to make the coil quench. If it is not specified, the conductor is divided into 500 blocks along its length and in 4 along its width.

3.8.1 Simulation example

3.8.1.1 General results presentation

In this section, an example of the results obtained on one simulation is shown for a better understanding of what can be investigated using this model. While studying a real coil, it is better to slowly ramp the current inside the coil in order to avoid huge voltage peaks due to the coil inductance. Hence, in this model the single pancake described above is studied, in self-field, and the current is ramped at a rate of 5 A/s.

First, the current as well as the magnetic field can be monitored in the centre of the coil, both generated by the background field and the field generated by the coil itself, see Fig. 135; i.e. here it is only the field produced by the studied sample. There is no time delay and the magnetic field is directly proportional to the current.

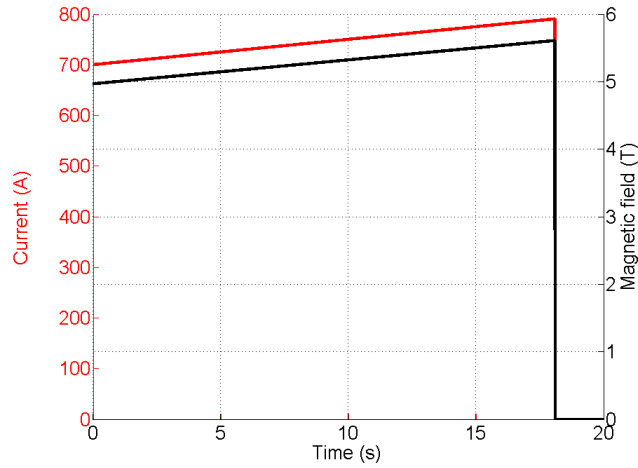


Fig. 135. Current and magnetic field inside recorded in the centre of the sample according to time.

Each voltage of each block is evaluated for every time step so that the voltage of the whole coil can be studied as shown in Fig. 136, where the coil monitoring is divided in six parts for a better visualization. The inner part of the coil starts the transition whereas the external turns do not show any voltage.

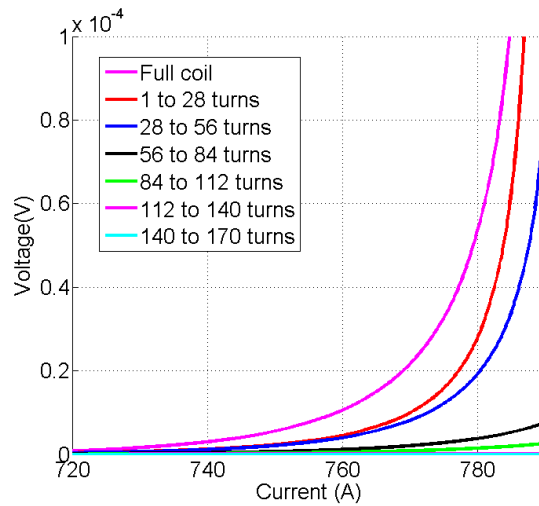


Fig. 136. Voltage of the full coil and voltages of different part of the winding, according to the current.

At the same time as the voltage inside the winding increases, the temperature on each block increases as well as illustrated in Fig. 137. As expected, the model gives back the critical current of the coil but also shows how the transition propagates inside the winding and where it starts.

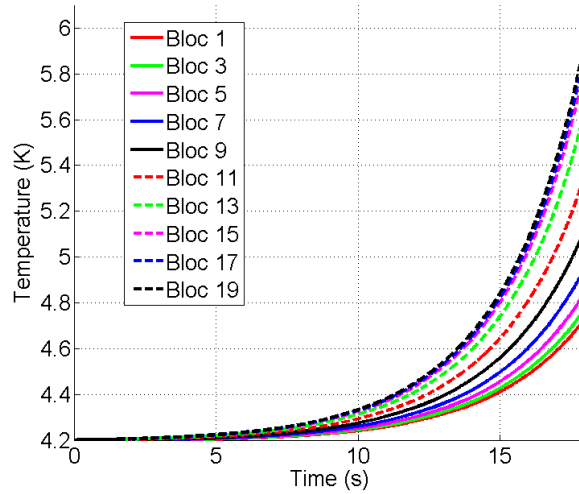


Fig. 137. Heat propagation on some block of the winding, according to time.

3.8.1.2 Results comparison

The transition is now recorded for every background field to allow plotting the limiting critical current of the studied wound sample. It is plotted in Fig. 138 for the single 6-mm pancake coil previously detailed according to the background field. The thick curve is calculated with a threshold of 1 mV on the whole coil and the thinner curve is drawn for a threshold of 0.1 mV. In this case, the critical current at 77 K, in self-field is initialized by 180 A on the whole length of the conductor.

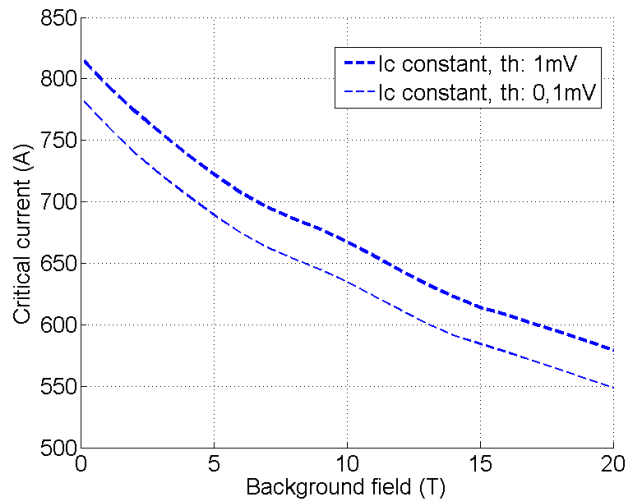


Fig. 138. Limiting critical currents plotted according to the background field for two different voltage thresholds.

For each point of the curves, the transition is recorded inside the winding, so the beginning of the transition can be localized, and its propagation can be monitored. For instance, the behaviours of the coil is compared for different background fields as illustrated in Fig. 139 and in Fig. 140, which respectively show the transition propagation in self-field and under 20 T. The propagation is slightly different in these two cases. In self-field, the transition starts on the inner part of the winding, whereas under 20 T, the transition begins in the middle of the winding. In the two different examples, not the same length of the conductor is transiting, which can be interesting when discussing about detection to prevent the coil from being damaged by a quench.

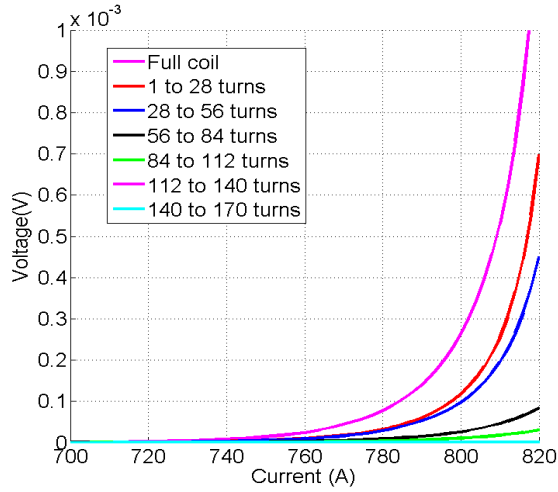


Fig. 139. Propagation of the transition inside the winding when the coil is studied in self-field.

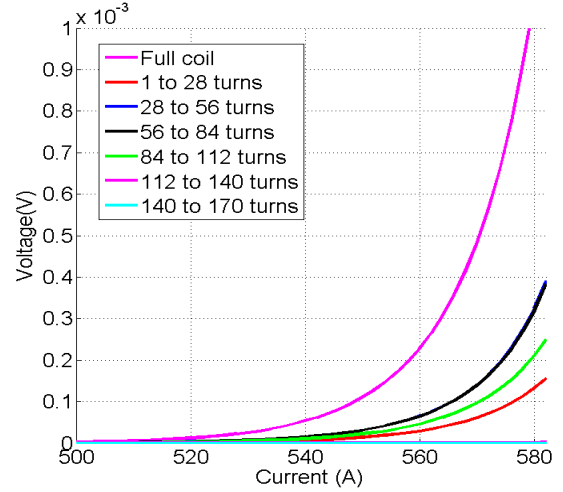


Fig. 140. Propagation of the transition inside the winding when the coil is studied in a 20 T background field.

3.8.2 Influence of the electric time step

First, it is important to investigate the influence of the time step to evaluate the appropriate speed to run simulations. The limiting critical current of the coil for different threshold values is computed for varying time steps and drawn in Fig. 141. For a time step lower than 0.01 second, the I_c values start be constant.

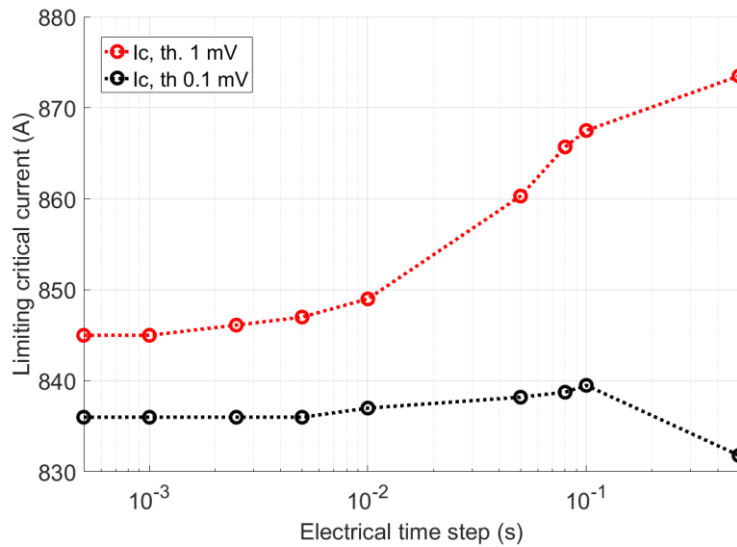


Fig. 141. Influence of the time step on the limiting critical of the coil for different voltage threshold.

3.8.3 Influence of the current ramp time rate

The influence of the time rate of the current ramp is then studied in order to investigate how fast the simulations can be run. In this section, the initial I_c at 77 K, self-field is taken as constant equal to 180 A as well as the 'n' factor which is also taken as a constant equal to 30. The limiting critical current is calculated as the minimum of the averages of the critical currents on the width of each block.

In Fig. 142, the full coil voltage is shown for different current ramp rates according to the current inside the coil.

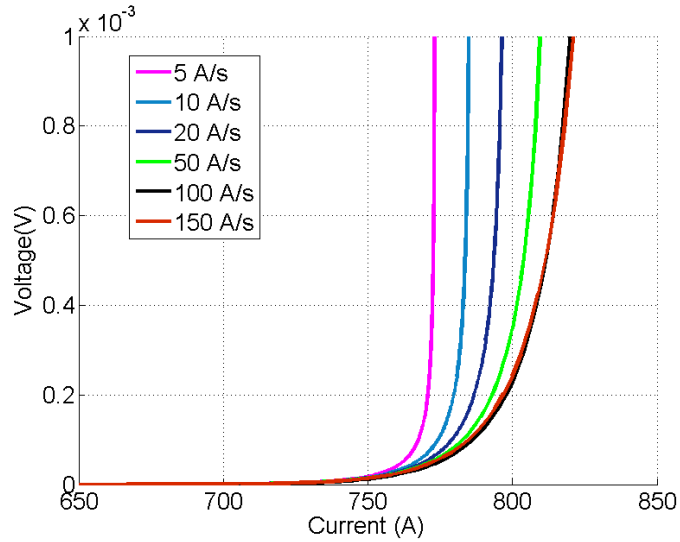


Fig. 142. Full coil voltage measurement for different current ramp rate.

The voltage change of trend can be due to the heat propagation as if the current is slowly increased inside the winding, the conductor has time to heat locally before some other parts of the winding start transiting because of the current. It means that, in this condition, only one local area is transiting, which explains the sharp transition when the ramp rate is 5 A/s. If the model only uses the heat propagation along the length of the conductor, this phenomenon is kind of obvious as illustrated in Fig. 143; it shows the temperature on each block when the voltage threshold is reached.

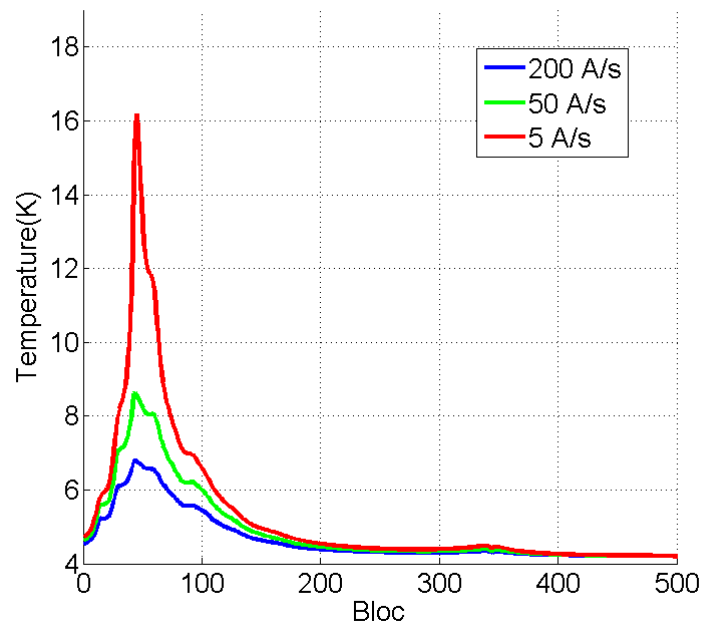


Fig. 143. Temperatures of the blocks when the voltage threshold is reached.

If the voltage threshold is setup at 1 mV and at 0.1 mV on the full coil voltage measurement, the critical current according to the current ramp rate can be plotted such as in Fig. 144.

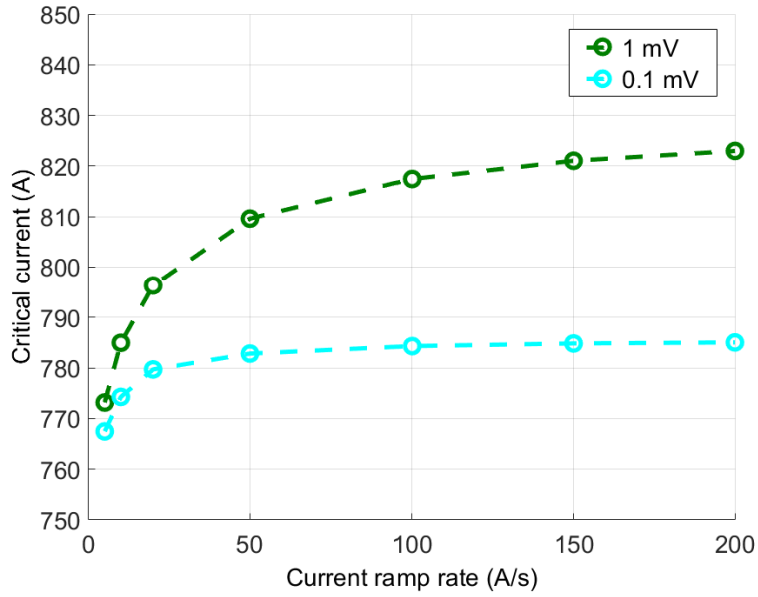


Fig. 144. Estimation of the critical current according to the current ramp rate.

3.8.4 Constant performance of the conductor versus inhomogeneity

3.8.4.1 Different initial I_c at 77 K, self-field

In this section, the influence of the I_c initialization is studied; three different cases are compared. First, the I_c at 77 K in self-field is taken as a constant equal to 180 A. The results are compared with a varying I_c , and also, to a real Tapestar which in both cases has a minimum I_c of 180 A. For each initialization, in the model, the I_c has to be averaged on each block as illustrated in Fig. 145 and in Fig. 146, respectively when the I_c is randomly setup and when a Tapestar is used. In the second case, the lowest values of I_c are all localized in one extremity of the length of the conductor.

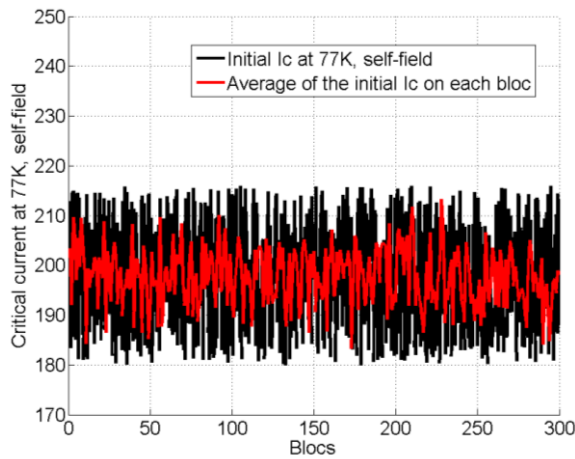


Fig. 145. Critical current at 77K, self-field for each block of the length of the conductor, randomly calculated.

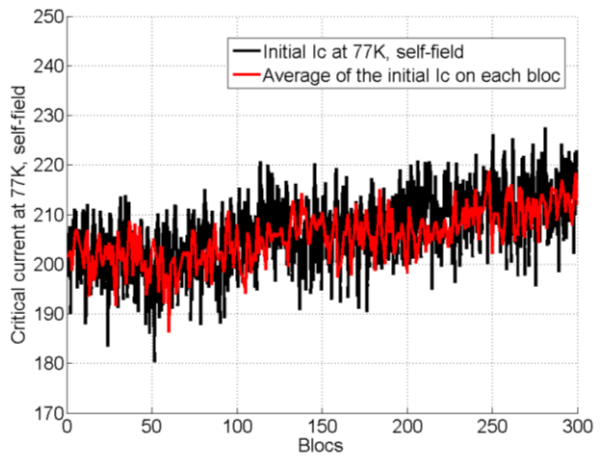


Fig. 146. Critical current at 77K, self-field for each block of the length of the conductor, given by the providers SuperOx.

3.8.4.2 Influence on the critical current

We will now see how the limiting critical current values are impacted by these changes, illustrated in Fig. 147. The curves are plotted for a constant I_c equal to 180 A in a dotted blue line, for an I_c varying above this minimum I_c in a dotted black line and for an I_c similar to a Tapestar, which minimum is also 180 A in a dotted red line. The specific initial I_c are shown in Fig. 145 and in Fig. 146, presented in the previous section. As expected the black and red curves show higher limiting critical current for the winding than when the initial I_c is constant.

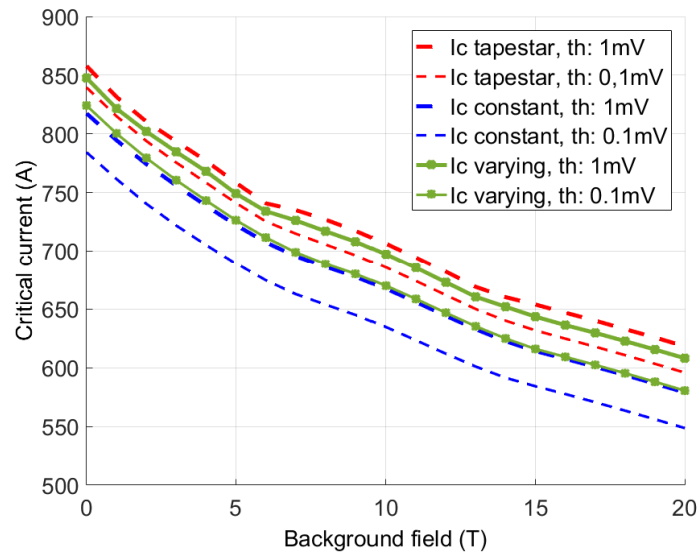


Fig. 147. Critical currents according to the initial value of critical current at 77 K in self-field along the length of the conductor.

The propagation of the transition inside the winding can also be compared as in Fig. 148 and in Fig. 149, which respectively show the propagation in self-field with different initial I_c at 77 K, self-field. The trends of the curves are slightly different, which underlines the importance of initializing the length of the conductor with appropriate data.

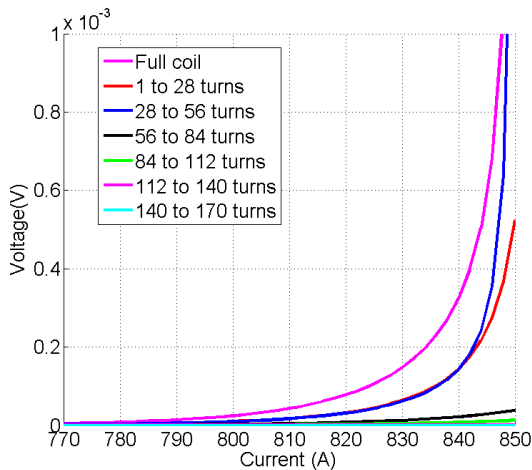


Fig. 148. Propagation of the transition inside the winding when the initial I_c is varying above the minimum studied I_c .

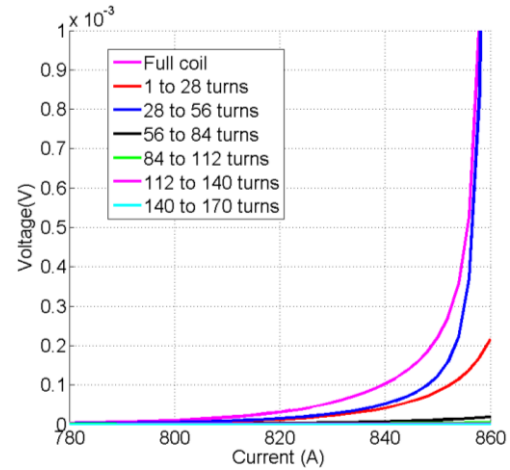


Fig. 149. Propagation of the transition inside the winding when the initial I_c is following the Tapestar value.

3.8.5 Influence of the number of blocks and the number of subdivisions of a block width

The influence of the number of blocks along the length of the conductor and the number of subdivisions along the width of the conductor is studied. The impacts on the model results are detailed.

3.8.5.1 Influence of the number of blocks

It is crucial to know how many blocks are needed along the length of the conductor for each studied configuration to reach a satisfactory accuracy. The influence of the number of blocks on the calculation of the limiting critical current is shown in Fig. 150 for the three different I_c initializations at 77 K, self-field. In Fig. 150, independent of the number of blocks along the length of the conductor, the calculated critical current for the winding does not evolve much. Furthermore, when the number of blocks is higher than 600, the limiting critical current starts to converge.

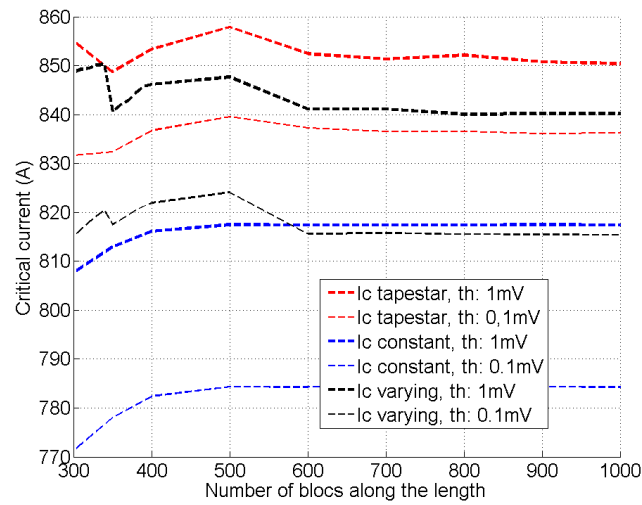


Fig. 150. Influence of the number of blocks along the length of the conductor on the limiting critical current evaluation.

3.8.5.2 Influence of the number of subdivisions in a block width

Fig. 151 shows the influence of the number of subdivisions along the width of each block. This time, the limiting critical current quickly saturates especially when there are more than 6 subdivisions.

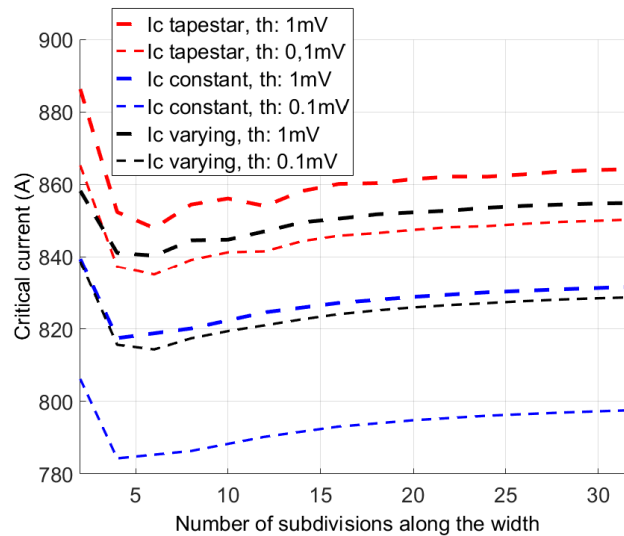


Fig. 151. Influence of the number of subdivision along a block width on the limiting critical current evaluation.

3.8.5.3 Conclusion

The influence of the number of subdivisions along the length of the conductor is important especially when the initial I_c at 77 K, self-field is not a constant. When comparing the model to the study of wound samples, the I_c data given by the providers is measured every couple of metres and sometimes less. When it is used in model, the I_c values are average on the length of a block. Hence, the model is expected to have enough subdivisions to allow for a high enough resolution to work with the lowest measured I_c of the data given by the providers.

3.8.6 Influence of the n value

It could also be interesting to study the same coil but with an inhomogeneity in the 'n' factor along the length of the conductor to compare the model results with the already existing literature about these kinds of inhomogeneity and their impact in a winding.

For $n=30$, the I_c when the full coil voltage measurement reaches respectively 1 mV and 0.1 mV are 858 A and 840 A. For $n=60$, the currents are respectively 851 A and 849 A. Fig. 152 and Fig. 153 show the propagation of the transition inside the winding respectively when n is 30 and n is 60. As expected, the voltage measurements are sharper in the case of $n=60$ and only one part of the winding is transiting.

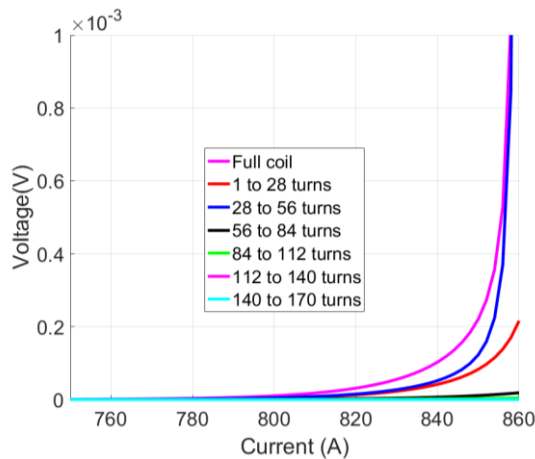


Fig. 152. Propagation of the transition inside the winding when $n=30$, self-field.

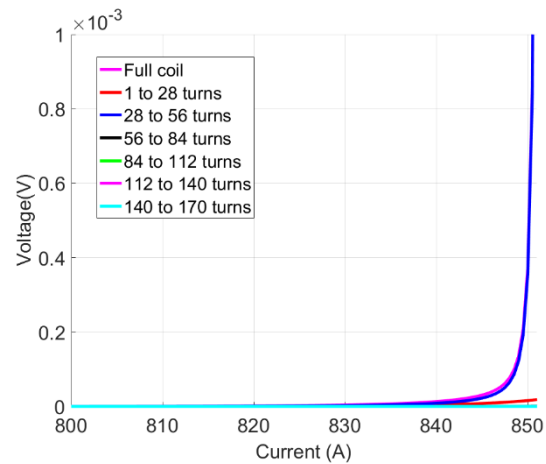


Fig. 153. Propagation of the transition inside the winding when $n=60$.

Fig. 154 and Fig. 155 show the temperature rises in the first blocks of the conductor when n is 30 and 60, respectively. It has been observed that the transition is abrupt in the second case so the blocks have less time to heat up compared to the case when n is 30. Hence, for $n=30$, the maximal temperature is higher than 5 K when for $n=60$, all the temperatures seem to stay close to 4.2 K.

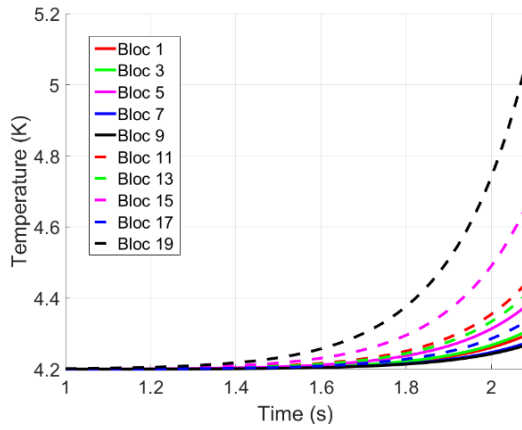


Fig. 154. Temperature rise on the first blocks, when $n=30$, self-field.

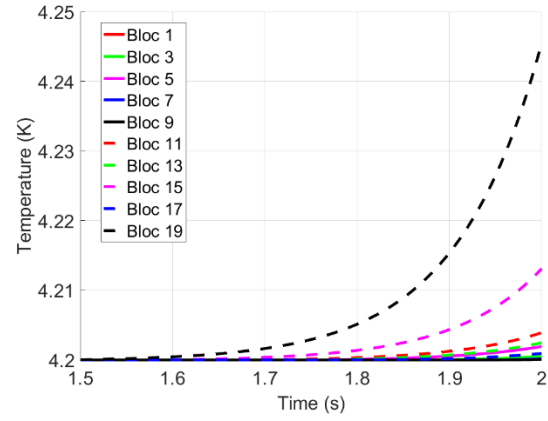


Fig. 155. Temperature rise on the first blocks, when $n=60$, self-field.

Knowing the n value with accuracy is important as it both changes the value of the limiting critical current of the coil and the way the winding is heating during its transition to a dissipative state.

3.8.7 1D propagation versus 2D propagation

In this section, to provide a better comparison of the heat propagations, both models are studied with a constant current passing through the coil and a constant background field, at a temperature for which some part of the winding is already dissipating. 500 A are passing through the coil with a 17 T background field. Fig. 156 shows the COMSOL geometry of the wound sample drawn as a spiral with a focus on the beginning of the winding in its centre to observe the conductor turns as well as the definition of the blocks and the half rings.

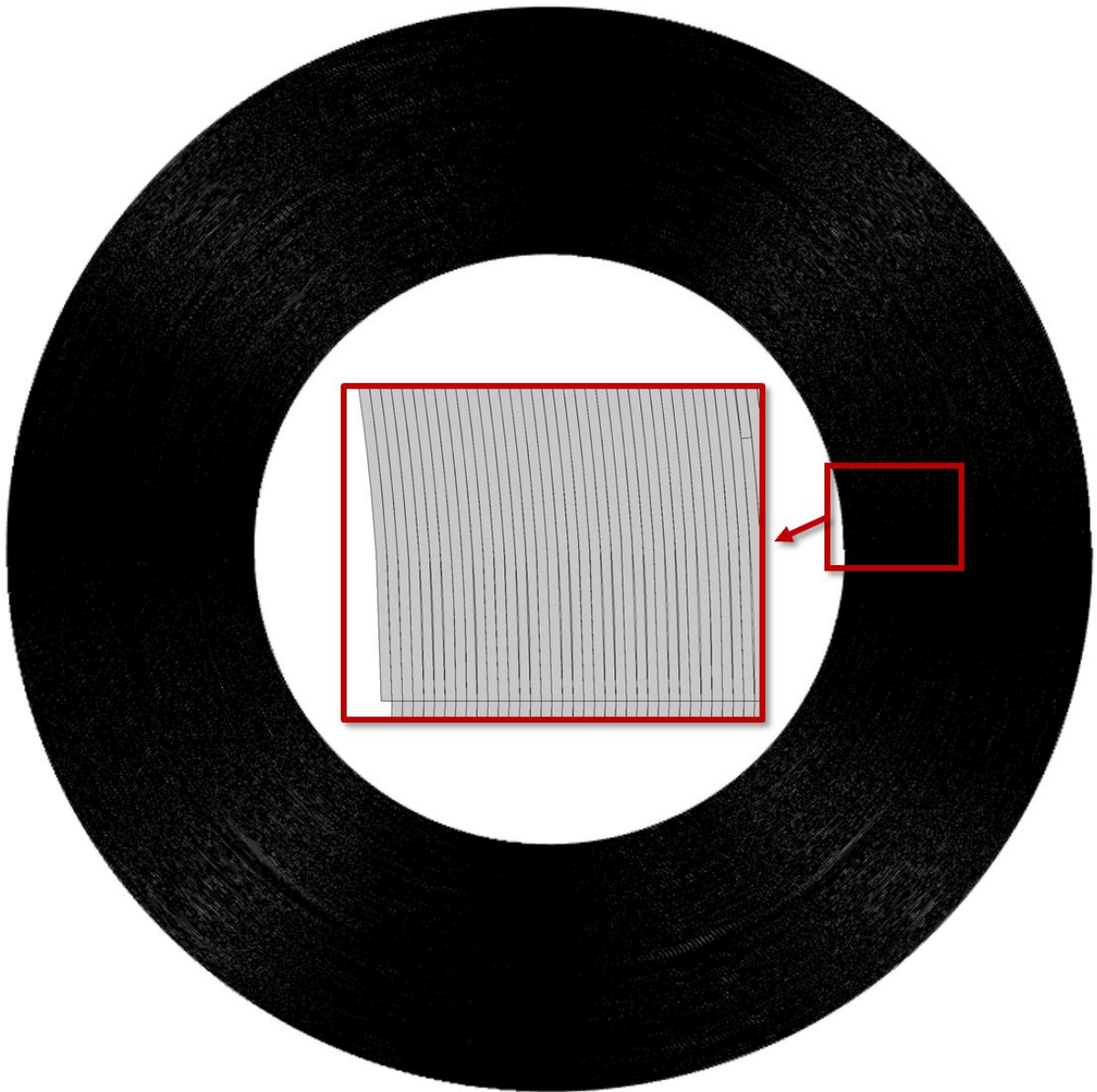


Fig. 156. Spiral geometry of the studied wound sample with a focus on the beginning of the winding.

When the 2D heat propagation is used, the temperature rises in the whole winding as illustrated in Fig. 157, the temperature along the length of the conductor is homogeneous. On the contrary, when only using the 1D model, the heating is localized on the area where the I_c is the lowest as shown in Fig. 158. In this second configuration, the temperature reached is also higher as the I_c is reduced according to the increase of the temperature.

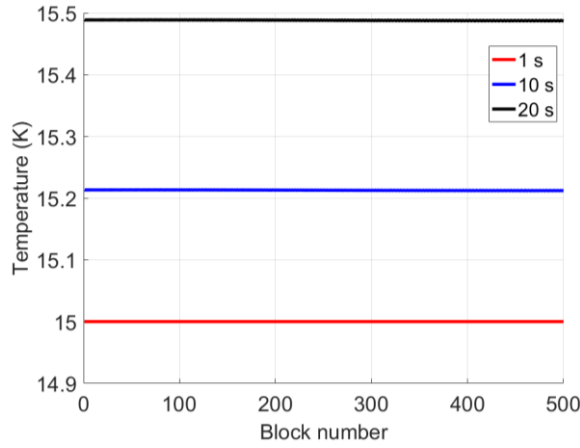


Fig. 157. Temperature of each block at different time using the 2D heat propagation model.

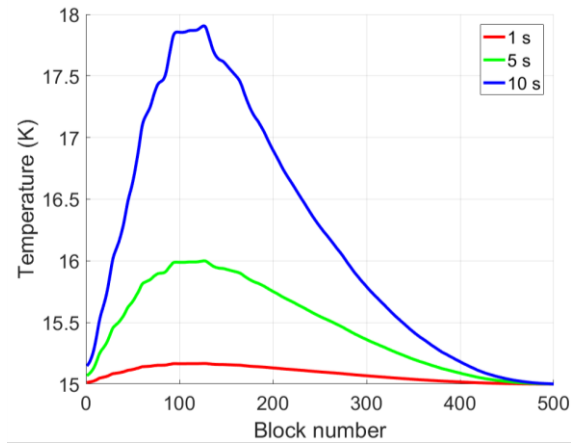


Fig. 158. Temperature of each block at different time using the 1D heat propagation model.

Voltages can also be compared along the length of the conductor. These are plotted in Fig. 159 and in Fig. 160, respectively using the 2D and the 1D heat propagation model. In the case of the 1D model, the voltage increase along the length is sharper than when using the 2D model.

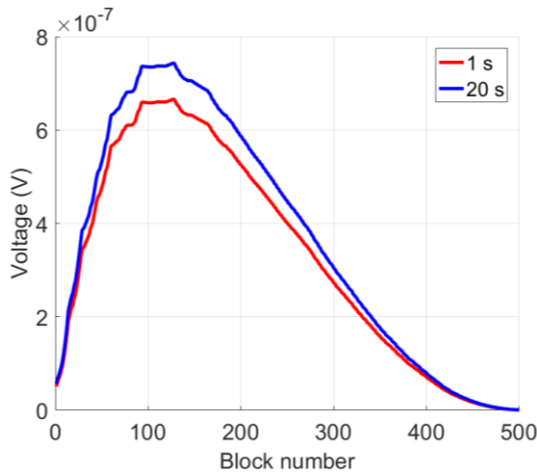


Fig. 159. Voltage of each block at different time using the 2D heat propagation model.

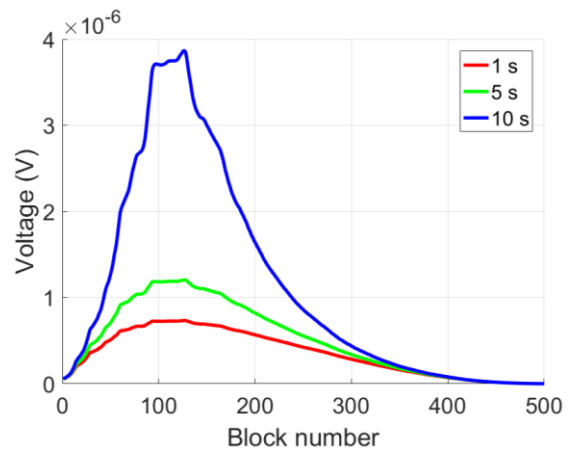


Fig. 160. Voltage of each block at different time using the 1D heat propagation model.

The propagation along the turns of the winding is observed to have an important impact on the conductor heating, which is spreading faster inside the whole coil. When the model is used with a constant current and background field without any global heating, the coil is transiting only because of the initial temperature chosen for this purpose. It makes the transition very slow so the influence of the 2D propagation is more pronounced. Furthermore, other simulations should be run using different initialization in order to study the influence of the 2D heat propagation compared to the 1D.

3.8.8 Conclusion

After the explanation of the model, the influence of the inputs has been studied starting with the parameters of the simulation (time step, number of blocks and subdivisions) to define the precision of the model, i.e. how many blocks are required for a good accuracy for example. In a second step, the impact of inputs used to run the model are investigated such as the current ramp, the initial value of the conductor at 77 K, self-field and the n value. It also underlines the numerous possibilities on what can be done with the model. However, for example, according to the proprieties of the conductor

layers, the results can be slightly different, and it is really difficult to know them with certainty. It has also been seen that some margins are necessary when the TapeStar is used: for the I_c values, some drops can be missed and for the n values more particularly because their theoretical values are still discussed.

The model shows promising results. It evaluates the area of the coil that dissipates first and the way it propagates along the winding. It also computes the temperature rise so hot spot can be localised. Nevertheless, running more simulations underlines the need of having more experimental data on wound samples, which is crucial to confirm the model's accuracy. The importance of the initialization of the I_c at 77 K, self-field with the constructor data is also expected to be validated with the experiments on wound samples.

In these simulations, a current ramp is used but in the next chapter, because of the noise level measurement, it is observed that the study of a magnet coil with many turns under high field is difficult using a current ramp. Three wound samples are studied and one of them has the main objective to detect and follow the transition. At this point, the experimental results are compared to the model simulations.

4 EXPERIMENTAL STUDY OF WOUND SAMPLES UNDER HIGH FIELD

In chapter 2, short REBCO samples have been studied under high fields with different orientations. The objective was twofold: to use the characterization for a numerical model as well as to get a first approach on how this conductor should be handled especially under high fields where they are easily damaged. The next logical step is then to study this conductor, when wound in small pancakes to study their behaviours.

In this section, wound samples are studied in high fields. Their magnetic and mechanical behaviours are investigated, as well as the coupling with the outer magnet and their performance in term of current capacity. To reach this goal, three wound samples with slightly different objectives are built.

These three sample coils have been wound during my PhD and studied under high magnetic fields: two insulated coils and one metallic insulated coil. The two insulated coils are my own work; I made the design, fabricated and studied them, with help from CNRS co-workers. The MI coil is a collaborative work with Thibault Lécresse; we defined the design together, I draw the assembly to fit the probe, we wound the coil in CEA, Saclay and tested it under high field in LNCMI, Grenoble assisted by both CNRS and CEA co-workers. T. Lécresse has done all the MI data processing.

Moreover, even if working inside a resistive magnet is supposed to create more noise in the measurement than a superconductive magnet [104], the wound sample is preferred to be tested inside a resistive magnet as there is less risk to trigger the emergency discharge of the outer magnet and furthermore, to damage it. In this extent, the wound samples, but also the final insert, are preferred to be first tested inside a resistive magnet to reduce the risk of a sudden discharge of the background field that can damage the winding. This is the reason why preliminary tests detailed in this chapter are all performed in a resistive background.

Details of the coils are given below, followed by their objectives, the description of the experimental setup and the main results of their study.

4.1 INSULATED COIL: MAGNETIC AND MECHANICAL BEHAVIOUR AND COUPLING ISSUES

4.1.1 First coil objectives: study of a 4 mm DP insulated coil

The three coils are designed to fit a measurement probe dedicated to work inside a 128 mm cold bore resistive magnet that generates up to 19 T in its centre.

The first wound sample is mainly fabricated to work on the winding process and monitor the behaviour of the coil without using any intrusive method. This first coil is fabricated to study the magnetic and the mechanical behaviours under high magnetic field. It has been studied inside both the 20 T resistive magnet at LNCMI and at a second time, inside an 8 T LTS coil at Tohoku University, in Sendai, Japan. Eventually, the performance of the coil in term of current are examined.

First, the coil is introduced, and the experimental studies are developed and finally their main results are shown.

4.1.2 Description of the insulated double pancake coil: fabrication and instrumentation

4.1.2.1 Double pancake coil fabrication

The first wound sample is a 4-mm double pancake whose tape is provided by the company SuperOx; the same length is used for the short sample characterisation under high magnetic field presented in section 2.6.2.1 and this winding. As a reminder, this conductor is chosen because at this time SuperOx was offering it with a convenient 10 μm thin polyimide coating, allowing a net gain in thickness as compared to classical Kapton tape insulation as explained in section 2.6.2.1. Each time the insulation has to be removed, the chemical solution detailed in section 2.6.2.1 is used.

In the following, this sample coil is called DP-INS and its photograph is shown in Fig. 161 (a) before being wrapped. This coil is a double pancake with no soldered joint in the middle of the winding. It means that the two pancakes are wound with the same conductor length (see section 1.4.1). For the layer jump, the conductor has to respect the hard bending minimum radius (see section 1.1.2.1), explained in [143]. The middle of the length is first fixed on the mandrel and then, half of the tape is saved on a satellite screwed on the mandrel while the other half is wound on the mandrel, as seen in Fig. 161 (b). Hence, the satellite follows the rotation while winding the first pancake.

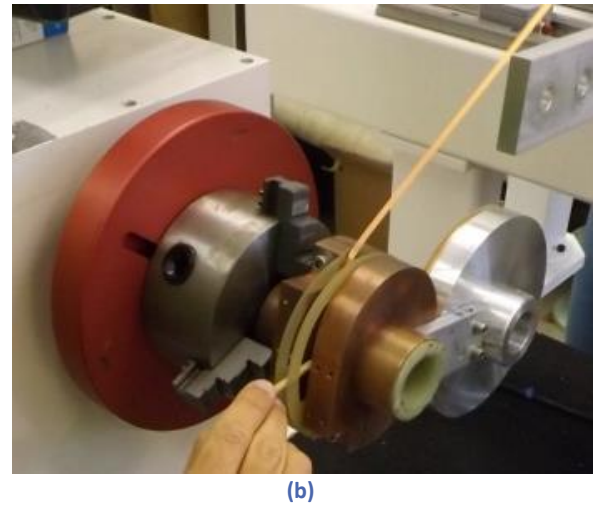
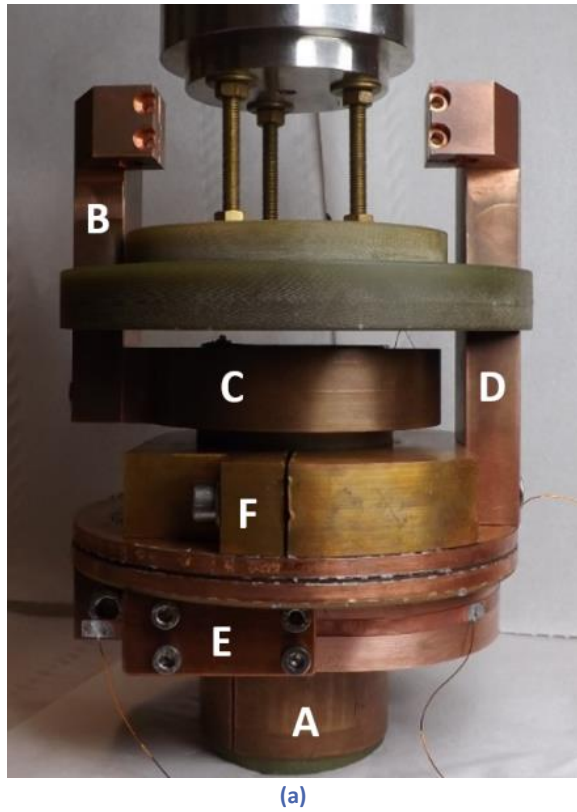


Fig. 161. (a) Double pancake assembly before wrapping. (b) Winding of the first pancake while the other half of the tape is set aside on a satellite.

In Fig. 161 (a), the final assembly of the sample coil is shown; it is mounted on the measurement probe, mentioned above, with a current capacity of 2000 A at 4.2 K [28]. The current comes from the power source through the measurement probe to the copper piece B to reach the cylinder C, which is tight on the inner copper mandrel A and allows the current to transfer down to part E. The tape is clamped on E and so the current can go through the winding. The other extremity is fixed on F which is screwed to D to allow the current to return and reach the power source. F and A are electrically insulated from each other with a glass fibre cylinder on which the coil is also wound to avoid electric contact between the copper cylinder and the winding. The input and the output of the current are set in such a way that the magnetic field produced by the coil is in the same direction as the one generated by the resistive magnet.

Eventually, the two last turns are soldered on themselves for mechanical reinforcement and to relieve a part of the mechanical stress. Finally, the winding is wrapped i.e. covered by an impregnated epoxy glass fibre. The coil has faced several damages during experiments, so its geometry has slightly evolved. Its final characteristics are presented in Table 9 as the experimental results presented in the section were conducted with this geometry. The characteristics changes are explained in section 4.1.7. The two pancakes can have a slightly different number of turns, which can be due to the non-homogeneous thickness of the insulated layer but also to the fact that the coil is not preloaded during the winding. After fabrication, the inductance is measured to be about 10 mH and the field coefficient is expected to be around 6 mT/A.

Characteristics of the coil	
Inner diameter (mm)	58
Outer diameter (mm)	108
Number of turns/pancake	170

Table 9. Characteristics of the double pancake coil DP-INS.

4.1.2.2 Instrumentation

The measurement probe is fully instrumented in a similar way as the one presented in section 2.5.2.1, in term of voltage taps and Cernox cryogenic temperature sensors.

Regarding the sample coil, non-intrusive instrumentation is desired at a first time, so only two voltage taps allow monitoring the whole winding. Temperature, magnetic field and mechanical strain due to Lorentz magneto-electrical stresses are also recorded. Cernox sensors are set up on the bottom and the top of the coil, on the copper pieces, to record any heat elevation during experiments. A Hall sensor is also placed in the middle of the coil to observe the magnetic field in the centre of the winding. The Arepoc Hall sensors (LHP-MU, [42]) have been chosen for the three wound sample studies, mostly for their accuracy and linearity in high field, at low temperature. They allow measuring only the component of the field that is perpendicular to the sensor as illustrated in Fig. 162 and show a very low sensitivity to temperature variations.

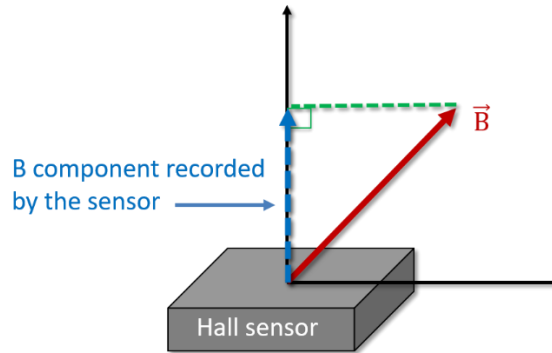


Fig. 162. Illustration of the Hall sensor measurement.

The mechanical behaviour has been monitored only on the DP-INS coil. The sample coil is also fully instrumented with six strain gauges, mounted on the sample coil. Four are glued on the outer layer of the coil, two on each pancake, not directly on the superconductor tape but on the fibre glass tape that wraps the winding. Two are directly glued on the superconducting tape, on the portion going to the clamp joining the current lead. The strain gauges are provided by Kyowa [144]. They are of the KFL-5-120-C1-16 type, recommended for 4 K operation [43] and glued with M-bond 600 [45] as the one used to assess a strengthening effect in [44].

4.1.2.3 Experimental protocol

Fig. 163 illustrates the experimental protocol of the DP-INS coil. The top graph shows the magnetic field measurement inside the sample and the bottom graph the current passing through the coil (in red) and the full coil voltage measurement (in blue). The background field is 8 T. When the

background field reached the target value, the current is ramped, creating a voltage inside the coil due to its inductance L , following the formula described below.

$$V = L \cdot \frac{dI}{dt} \quad 40$$

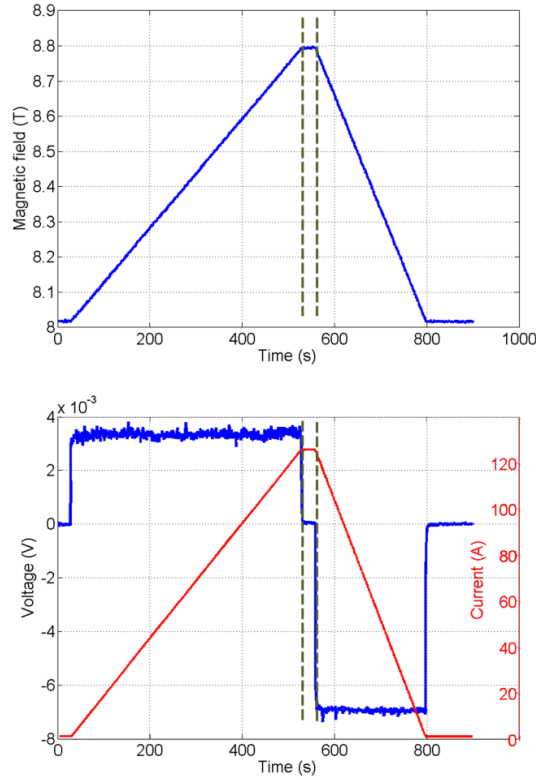


Fig. 163. Illustration of the study protocol used for the DP-INS coil. The top graph is the magnetic field measured inside the wound sample, on the bottom graph, the blue line is the full coil voltage and in red the current inside the coil.

By calculation, using the previous formula on the data presented in Fig. 163, the inductance is 14.8 mH, which is consistent with the one measured at room temperature. During the current ramp, as the voltage seems constant, the conductor is expected to be in a superconductive state. This is confirmed during the current plateau as the voltage goes back to zero and does not increase.

4.1.3 Magnetic behaviour

In the case of an insulated winding, the magnetic field increase is, as expected (see section 1.2.5), proportional to the current circulating in it, as illustrated in Fig. 163.

4.1.4 Mechanical behaviour of the insulated double pancake coil

Two strain gauges glued directly on the tape were lost at the beginning of the experiment and one was not perfectly aligned. Fig. 165 shows the measurements of the remaining three strain gauges that were correctly attached and still working under 8 T. The experimental values are compared to calculation (dotted red line), assuming the turns were acting independently [47]. The mechanical stress is calculated according to the field evaluated on the outside of the double pancake, using the following formula:

$$\sigma = J \cdot B_r \cdot r \quad 41$$

As expected the maximum stress is applied on the outer turn of the sample, the mechanical trend is calculated in Fig. 164.

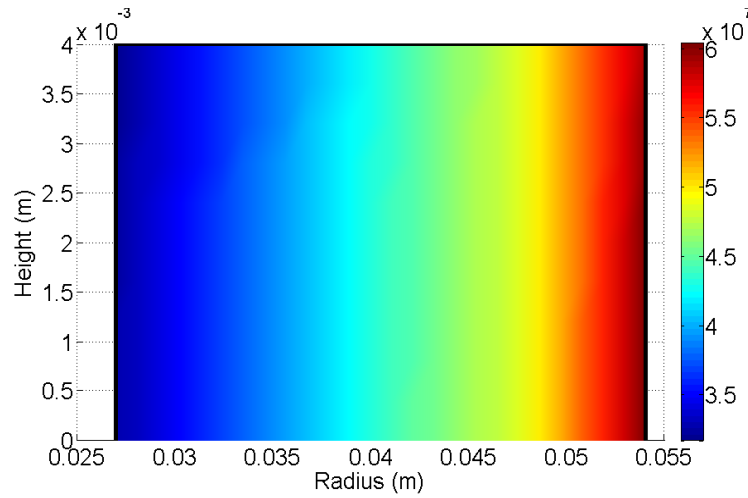


Fig. 164. Lorentz force JBr applied on the cross-section of the winding when 125 A are passing through the conductor under 8 T.

In Fig. 165, the maximum of the Lorentz force is given according to the current ramp. The maximum is taken on the outer layer of the coil, i.e. where the strain gauges are setup. An average Young's modulus value of the tape is used for the calculation, i.e. 205 GPa [46].

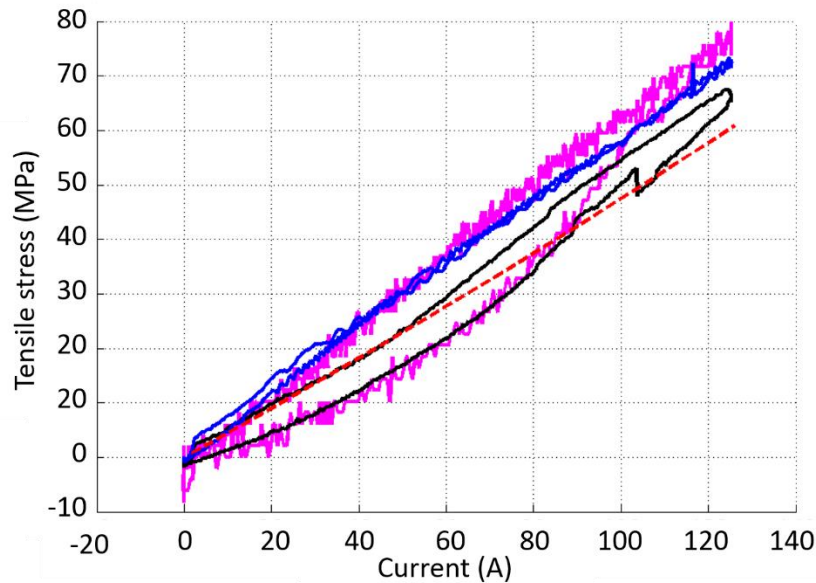


Fig. 165. Strain gauges measurements compared to simulation (red dotted line) under 8 T until 125 A.

In Fig. 165, the experimental measurements are found to be very close to the calculations, which is justifying the initial hypothesis for this wound sample.

4.1.5 Coupling issues

Section 1.2.4 develops coupling issues in a theoretical way. In this part, a practical experience of coupling is reported. This first sample was also tested in an LTS magnet as mentioned in 4. As the

sample is rather a small coil, the coupling was expected to be low and not able to induce a quench in the outer LTS magnet. However, the protection system of the outer magnet was imbalanced during a fast discharge of the HTS coil, from 200 A to 0 A in 3 seconds. The emergency discharge of the outer LTS magnet was triggered and induced its quench while generating 8 T. The whole event with the fast discharge is reproduced in Fig. 166. A field drop occurs first when the current was removed from the HTS insert (9.3 T to 8 T) and then when the outer magnet discharges in the sample in 10 seconds (from 8 T to 0 T). This discharge generated voltage values up to 2.8 V and it could have been worse if the respective geometries of both magnets were more adjusted, i.e. coupled. The background field is removed at a rather moderate rate, dictated by the emergency procedure.

Eventually, after this event, the sample is tested again and seems to be fully working even under field, as shown by some later tests performed in a resistive magnet, see section 4.1.6.2.

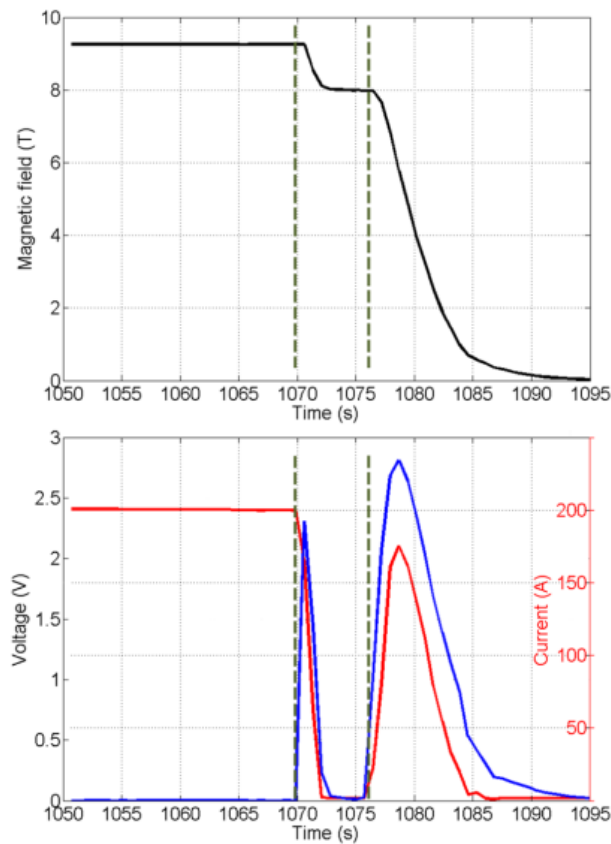


Fig. 166. The red curve is the current passing through the coil while removing the current and during the outer magnet quench. The coil voltage is the blue curve and the top graph shows the magnetic field measured at the coil centre. The two field drops correspond to the current decrease in the insert and then to the emergency field removal in the outer LTS magnet.

It would have been interesting to record the mechanical strain during this event but as the temperature happened to change a lot during a fast charge of the coil (discharge of the background field), the gauge measurements are distorted. This event comforted us to continue the next preliminary tests of quench inside resistive magnets rather than LTS magnets.

4.1.6 Experimental results: electrical behaviour

The DP-INS allows working on the general behaviours of an insulated REBCO coil. It has been chosen to be studied without an y intrusive method, therefore only the coil overall voltage measurement is recorded. In this section, the electrical behaviour of the double insulated pancake is studied first by calculation and then the experimental results are detailed.

4.1.6.1 Double pancake coil: calculation of the limiting critical current

First, the same limiting critical current calculation as in section 2.2.4 is performed, but this time for the wound sample coil only and not for a whole stack of pancakes anymore. Fig. 167 and Fig. 168 respectively show the parallel and the transverse components of the magnetic field on the cross-section of the wound sample, illustrated by the black lines. This magnetic field is the addition of the one generated by the resistive magnet and the magnetic field created by the wound sample. In this case, the background field is 8 T and 200 A are passing through the coil.

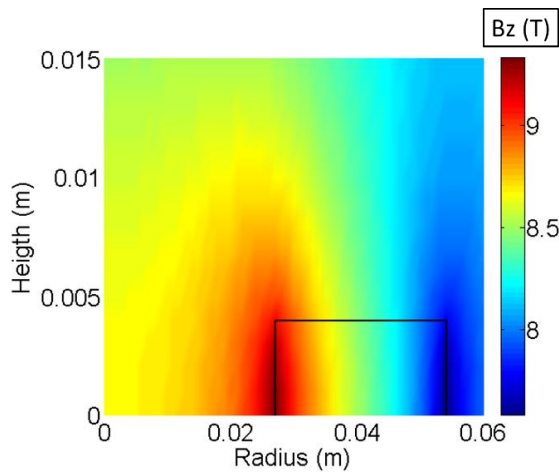


Fig. 167. Parallel component of the field (T), when 200 A is inside the coil, in an 8 T background field.

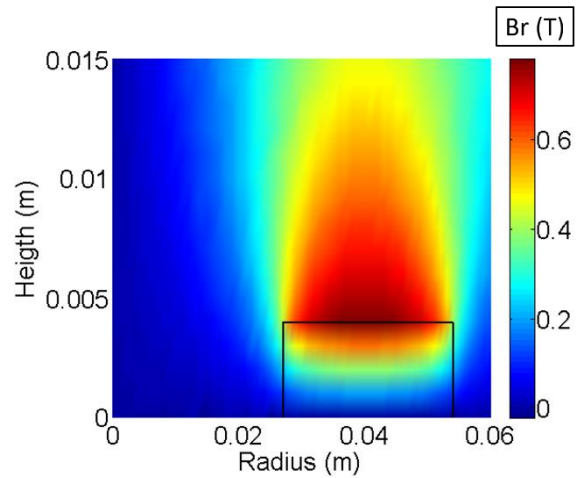


Fig. 168. Transverse component of the field (T), when 200 A is inside the coil, in an 8 T background field.

As the components of the field are evaluated over the whole section of the sample, it is possible to evaluate the critical current on each point of the winding using the previous short sample characterization (see section 2.6.4.1). Fig. 169 shows the value of the critical current on the whole cross-section of the wound sample in the same conditions as the graphs above. It means that only the cross-section of the winding is shown in Fig. 169 this time, and for each point of the winding a critical current is evaluated according to the components of the field applied on this area. The critical current still follows the trend of the transverse field and reaches its lowest values where the transverse field component is the highest.

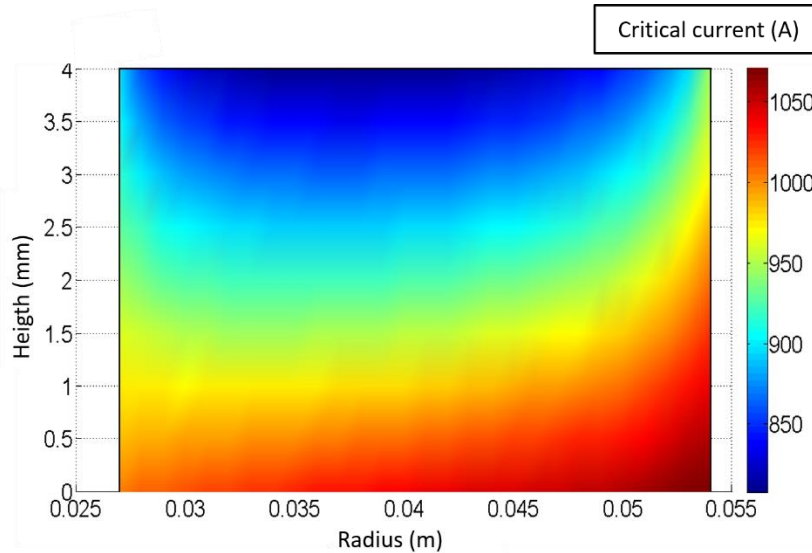


Fig. 169. Critical current (A) evaluated on the cross section of the wound tape according to the intensity of the field and its orientation.

4.1.6.2 Limiting critical current calculation and experimental coil performance

For large devices working under high fields, it is primordial to introduce a method, which considers the device's critical current according to both the magnetic field (including angle) it generates and the background magnetic field. The limiting critical current calculated for the DP-INS coil is plotted in Fig. 170. The red curve is set when the limiting critical current of the coil is taken as the lowest value evaluated on the cross-section of the wound sample and the black curve stands for a limiting critical current taken as the lowest value among all the average I_c calculated on the width of the conductor, for the whole wound length.

With this sample, the highest experimental values reached are 370 A, in self-field and 260 A, under 8 T. In all the following, only the red curve is used for calculation as the conductor behaviour in a field gradient is unknown. 370 A, self-field and 260 A, 8 T are respectively 22 % and 30 % lower than the calculated limiting I_c values. As a non-intrusive recording method is chosen, no transition could be recorded; the noise in the measurement is too high. Only current values reached with the coil in self-field and in field are introduced for this sample. These values are fixed before the experiment and consider as safe from a calculation point of view. Experimental I_c measurements are missing that could confirm the calculated margins. This is an area of potential improvement for future coils.

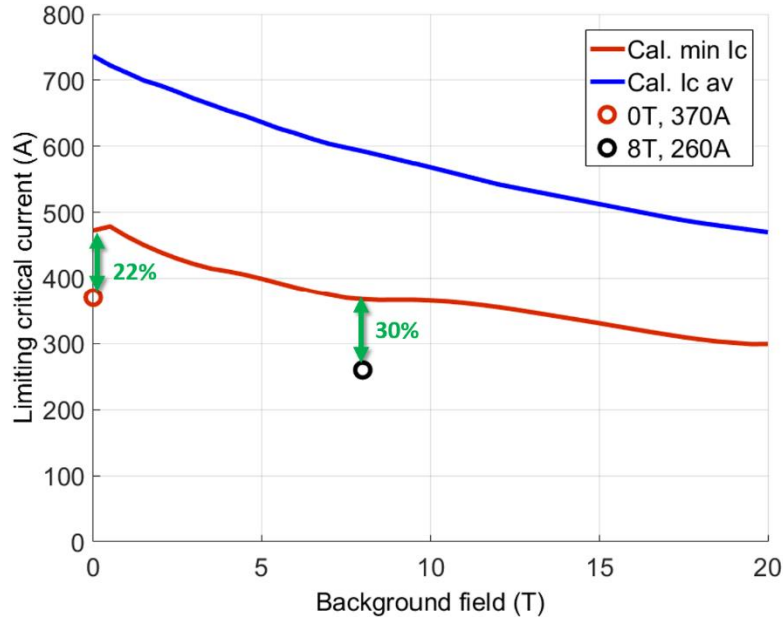


Fig. 170. Limiting critical current of the wound sample: the red curve is the minimum I_c , the blue one is when averaged on the conductor width.

4.1.6.3 Another limiting critical current evaluation method while ramping the current inside the coil and taking into account the inhomogeneity along the conductor

In this section, a slightly different method from the previous one is defined for which each graph is defined for a specific background field, including the tape current margin during current ramping, taking into account the 15 % inhomogeneity of I_c along the length. This method is presented in [145].

In Fig. 171 and in Fig. 172, the blue curve shows the different values of critical current according to the current inside the coil and the black line is the ramping current inside the coil. The two lines' intersection defines the limiting critical current of the coil. Fig. 171 and Fig. 172 are respectively calculated in self-field and with an 8 T background.

The blue curves are calculated while taking the minimum I_c of the cross section and the red ones when averaged on the width of the conductor. All dotted curves underline the 15 % critical current variations allowed by the provider at 77 K along the length of the tape due to its non-homogeneity. Even if the critical current is presumably higher, if the black line is already between the two dashed black lines, there is a large risk of quench. 260 A have been passed through the coil under 8 T, i.e. at 41 % of the critical current measured on short sample in identical conditions, and 45 % away from the limiting critical current of the coil. In self-field, 370 A have been carried by the coil, which means 34 % away from the limiting critical current of the coil, at 54 % of the short sample measurement of the tape in identical conditions.

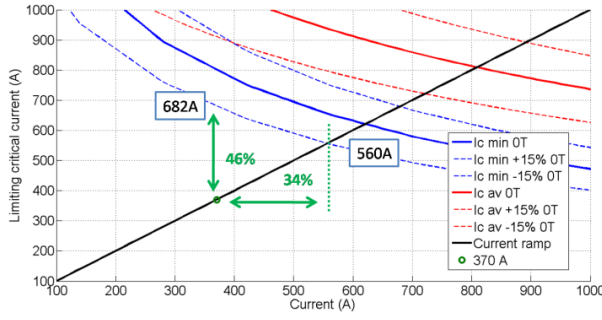


Fig. 171. Limiting critical current according to the current passing through the coil in self-field.

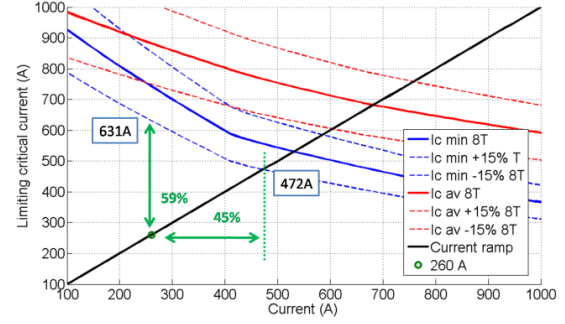


Fig. 172. Limiting critical current according to the current passing through the coil under 8 T.

This sample does not allow studying the electrical behaviour with precision as there is only one voltage measurement for the whole coil. The noise in the measurement is too high to allow recording a transition; a second insulated coil was wound with achieving this objective.

4.1.7 Conclusion

The sample has been damaged, fixed and wound again two times. The evolution of its characteristics is given in Table 10. The first time, the edge of one of the copper pieces was too sharp so one of the tape extremities was not clamped but soldered on the copper cylinder. This solder was too weak and burned. The copper cylinders where the conductor is clamped were machined again and several turns of the double pancakes were removed. The second time, the conductor burned close to the copper clamp, probably because of a too small contact with the copper or because of the mechanical effort, the conductor could have been ripped off. No transition was recorded before burning at the time of the event.

As the outer diameter was already smaller than the final geometry of the insert it was preferred to unwind the sample, increase the size of the inner mandrel and rewind the conductor.

Coil characterization	1 st winding	2 nd winding	3 rd winding
Inner diameter (mm)	50	54	58
Outer diameter (mm)	120	108	108
Number of turns/pancake	230	200	170

Table 10. Double pancake geometry of DP-INS according to the updates.

This first insulated double pancake allows recording the general behaviours of the coil using a relatively non-intrusive method; magnetic, mechanical behaviours and coupling issues have been investigated. This study is completed with a fully instrumented single pancake coil whose main objective is to record the transition propagation inside the winding.

4.2 INSULATED COIL: DETAILED STUDY OF THE TRANSITION INSIDE A WOUND SAMPLE IN HIGH FIELD

4.2.1 Objective of the coil

The second insulated pancake is fully instrumented in terms of voltage taps to record the internal behaviour of the coil. However, this is an intrusive method as the taps create extra steps between the layers and any solder can damage the conductor.

To be certain to record a transition even under high field and with high current, many voltage taps are set up in this second wound sample. Only natural quenches are interesting in this study, as there is no heater inside the winding; contrary to the last coil to be presented in this chapter, see section 4.4.1.3. Eventually, the intention is to make the two insulated coil studies complete each other. Moreover, to improve the voltage measurement clarity, a noise compensation coil (NCC) is wound around the sample coil [44], see section 4.2.3.2.

First, the sample is detailed, explaining how its fabrication and instrumentation are made to reach the objective of the experiments. Thereafter, the main experimental results are introduced.

4.2.2 Coil description: 6 mm SP insulated coil

4.2.2.1 Fabrication

In the following, this sample coil is called SP-INS; it is a 6-mm single pancake coil whose geometry is shown in Table 11. The geometry is similar to the one of the pancakes expected to be built for the final insert of the NOUGAT project [146]. The conductor width is 6 mm but the layer architecture is similar in terms of the nature and thickness of the tape studied during the short sample characterization as well as the previous wound sample, see section 2.6.2.1.

SP-INS sample coil characteristics	
Conductor width (mm)	6
Conductor thickness (mm)	~0.145
Number of turns	170
Inner diameter (mm)	60
Outer diameter (mm)	110
Inductance (mH)	1.16
Field coefficient (mT/A)	3.04

Table 11. Characteristics of the fully instrumented insulated single pancake coil SP-INS.

The workbench where the sample coil is set up before wrapping is shown in Fig. 173. The current goes to the sample through the copper cylinder A, which is soldered to the brass ring B. This latter is screwed to another brass ring C in order to allow the inside part to be reused for other wound samples. A REBCO tape is soldered on C and the same conductor bridges are soldered to join the outer turn of the wound sample, D. The inner turn of the sample is soldered on the brass mandrel E, where the current leaves the workbench to the probe. E is electrically insulated from A with Kapton tape. A draft of the assembly is drawn in Fig. 174. The conductor extremities are not clamped anymore but soldered (hence the choice of brass instead of copper for pieces B and E) and the contact surface is bigger than for the previous coil. Also, the mandrel has been thought more in details in order to be able to reuse the inner part of the assembly (A and B) as this part is only screwed to the outer part (C, D and E) where the coil is wound.

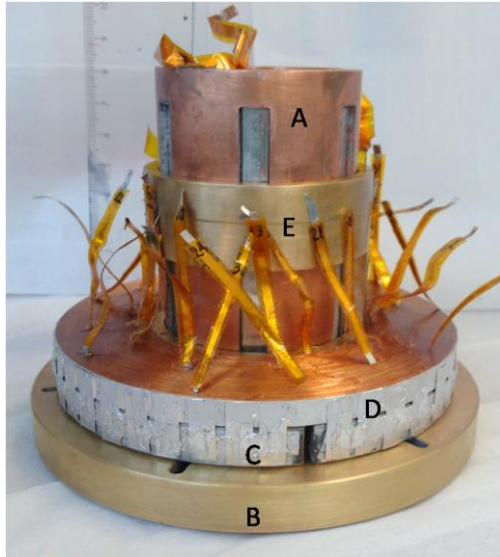


Fig. 173. Fully instrumented single pancake coil before wrapping.

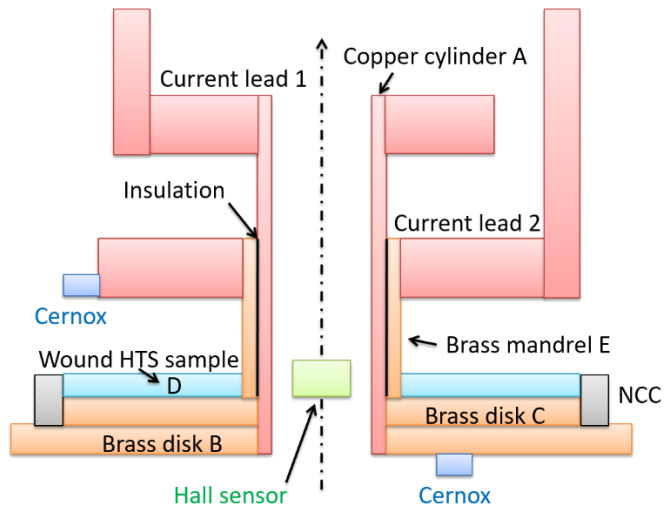


Fig. 174. Draft of the fully instrumented insulated coil assembly.

4.2.2.2 Instrumentation

The coil is fully-instrumented with 33 voltage taps that are arranged on every six turns of the winding as shown in Fig. 173 and illustrated in Fig. 175. The voltage taps are slightly shifted along the length in order to prevent geometry deformation and to scatter the extra step generated by the voltage taps inside the winding. The magnetic field is monitored in the centre of the sample coil using a Hall probe. The temperature is recorded all along the measurement probe but also close to the wound sample, with one Cernox sensor on the top and one on the bottom of the coil as illustrated in Fig. 176.

The last two turns are also soldered on themselves to back up the mechanical expanding stress. The coil is then wrapped in glass fibre reinforced tape and a noise compensation coil [104] is wound around the sample coil to reduce the noise due to the background resistive field; its position is shown in Fig. 175.

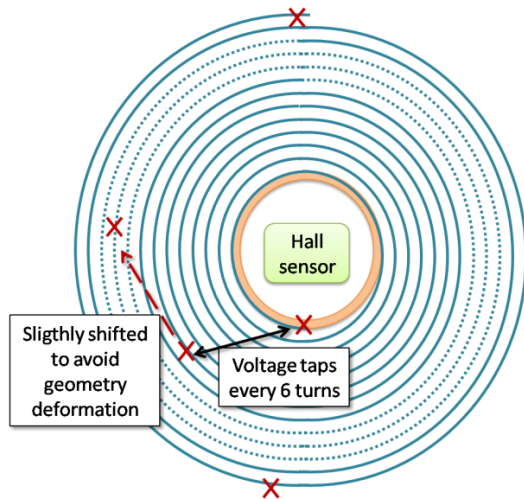


Fig. 175. Voltage taps inside the SP-INS winding.

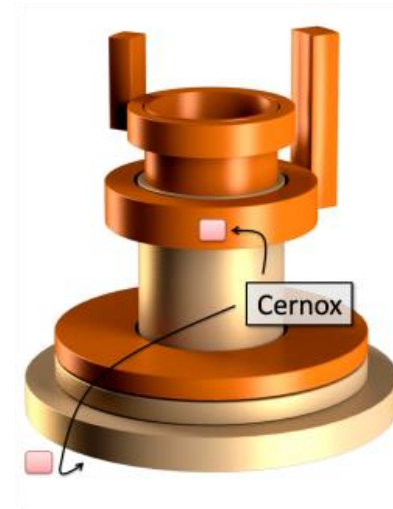


Fig. 176. Draft of the fully instrumented insulated coil assembly, details of the Cernox cryogenic temperature sensors position.

4.2.2.3 Experimental protocol

In order to reduce the noise measurement and to increase the clarity of the measurement; especially under high field, the experiments are done with a constant background field and a constant current passing through the coil. Thus, in a first step the background magnetic field is increased, only then, in a second step, the current is ramped by 50 A/s in the coil to reach the required value. This is shown in Fig. 177 where the background field is targeted at 19 T and the current at 300 A. Thereafter, the current, in a third step, can be removed from the coil and the background field can be set back to zero.

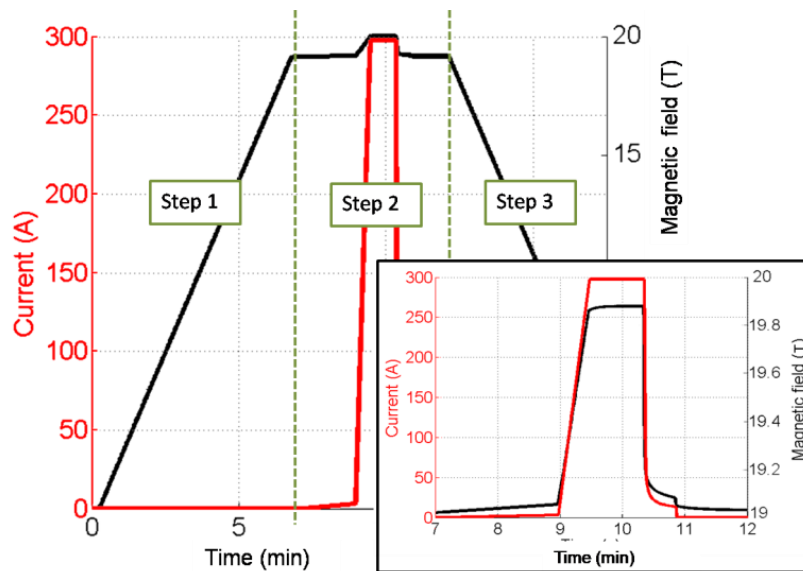


Fig. 177. Illustration of the experimental protocol for a background field fixed at 19 T and the current inside the coil reaching 300 A. The black curve is the magnetic field monitored by the Hall sensor in the middle of the wound sample SP-INS and the red line shows the current passing through the coil. The framed graph on the bottom right is a zoom of the second step.

The second step is underlined in Fig. 177 by the framed zoom when both plateau are reached. When the current is passing through the sample, it generates heat inside the mandrel and the inner turns of the winding are warmed up. This heating is then monitored thanks to the two Cernox placed at the top and the bottom of the coil. The temperature of the assembly increased slowly so the two Cernox sensors record approximately the same temperature during the experiments. When the temperature climbs high enough, the inner turns of the coil dissipate energy as illustrated in Fig. 178 for a background field of 17 T and a current of 250 A inside the coil.

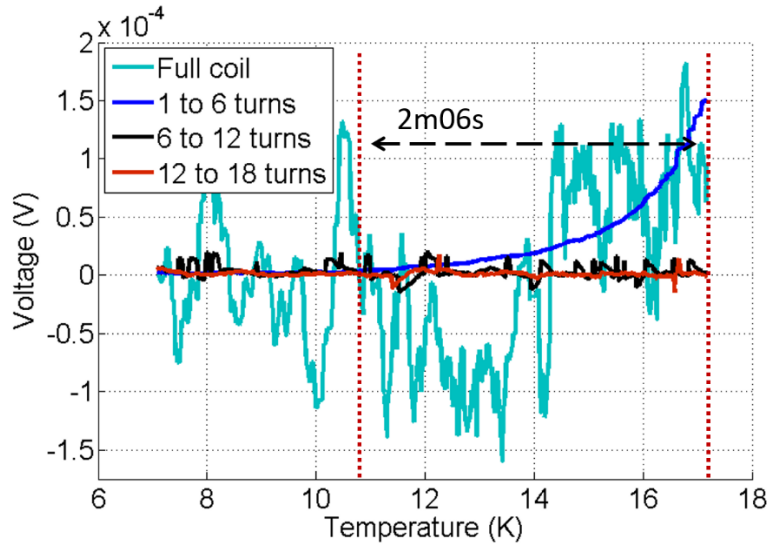


Fig. 178. Onset of transition of the inner turns while the background field is 17 T and 250 A is passing through the coil.

4.2.3 Noise level improvement

4.2.3.1 Experimental protocol

The experimental protocol is a first step in the noise level reduction. The limiting critical current calculation gives an idea of the experimental values and so the background field is increased as well as the current inside the winding while leaving enough margins not to damage the sample coil. Working with a constant field and constant current drastically decreases the noise level of the measurement.

4.2.3.2 Comparison with and without NCC

Moreover, the second step of the noise level measurement improvement is to wind a noise compensation coil (NCC). Its position is shown in Fig. 174, it is a 0.2 mm copper round wire wound around the superconducting coil in order to reach a higher inductance than the coil and allow compensating the noise generated by the outer resistive magnet. Thus, the main objective is to improve the signal-to-level ratio of the measurement.

Fig. 179, Fig. 180 and Fig. 181 show in blue the voltage measurement of the compensated signal and in black the REBCO sample alone centred on zero volt. Here, when the coil voltage measurement is plotted for the coil without compensation, the voltage increase due to the inductance is removed to allow a better comparison. The plots show cases where the current is ramped in self-field (Fig. 179), the current is constant in self-field (Fig. 180) and when the coil is in current plateau with an increase of the background field (Fig. 181).

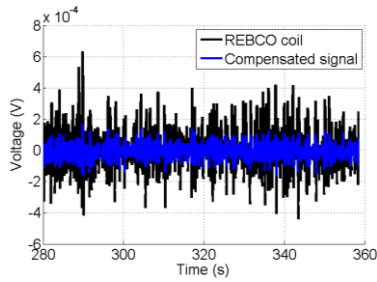


Fig. 179. Current is ramped from 50 A to 200 A.

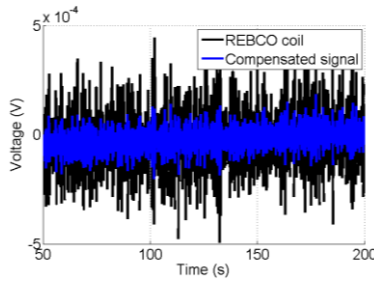


Fig. 180. Current plateau 200 A, self-field.

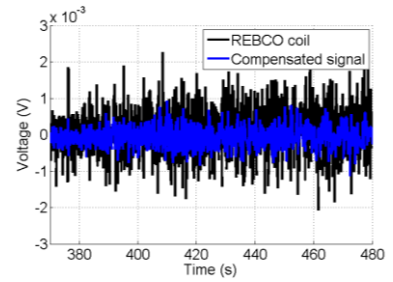


Fig. 181. 200 A circulating in the coil, the background field is ramped up to 3 T.

As the background field is increased, the level of noise becomes drastically higher as shown in Fig. 183. In this figure, the background field is ramped up to 14 T as 200 A is already passing through the coil.

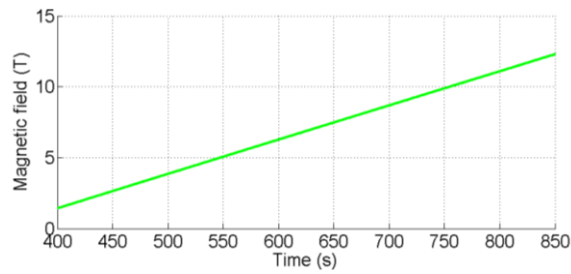


Fig. 182. Increase of the background field when 200 A is passing through the coil.

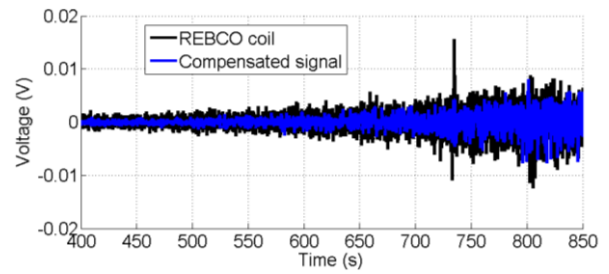


Fig. 183. Superconducting coil signal in red and compensated signal in blue when the background field is increased to 14 T, with 200 A passing through the coil.

Eventually, this noise level improvement allows recording the transition inside the winding as developed in the following.

4.2.4 Electrical behaviour

4.2.4.1 Definition of the coil working limitation

The main results are presented in Fig. 184; the coil has been studied from 150 A to 450 A up to 19 T according to the current passing through the coil. The voltage threshold has been chosen as 0.13 mV; the length of the first six turns measure approximately 1.146 m so it is a bit higher than 1 $\mu\text{V}/\text{cm}$ [48].

When both current and background field plateau are reached, the heating starts from the mandrel, hence the inner turns are expected to dissipate first. Fig. 184 shows the temperature attained when the six inner turns reach the voltage threshold while becoming resistive according to the background field and the current passing through the coil, i.e. each point represents an experiment.

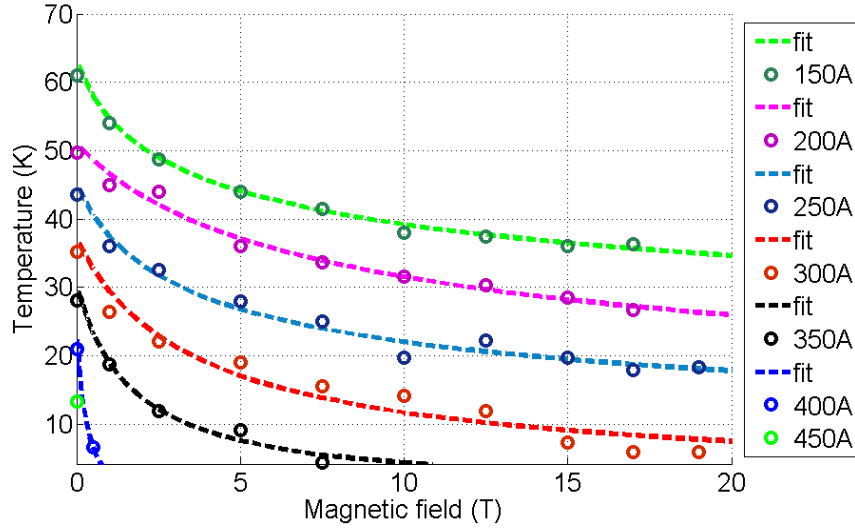


Fig. 184. Temperature reached when the coil starts its transition to a resistive state and reach the voltage threshold, according to the background field and the current passing through the coil.

For a given current, the curves have the same trend as for the short tape characterization according to the background magnetic field [147]. The dotted lines of Fig. 184 serve as visual guidance only for reading the experimental data and they have been plotted with the Kim's model (see section 2.7.1).

4.2.4.2 Extrapolation and comparison to calculation

One of the drawback of the experimental protocol is that measurements at 4.2 K cannot be conducted. Fig. 185 shows the temperature reached when the voltage threshold is attained according to the current. As the curves seem to follow a linear trend, the 4.2 K values can be extrapolated straightforward and are shown in green in Fig. 186 (a).

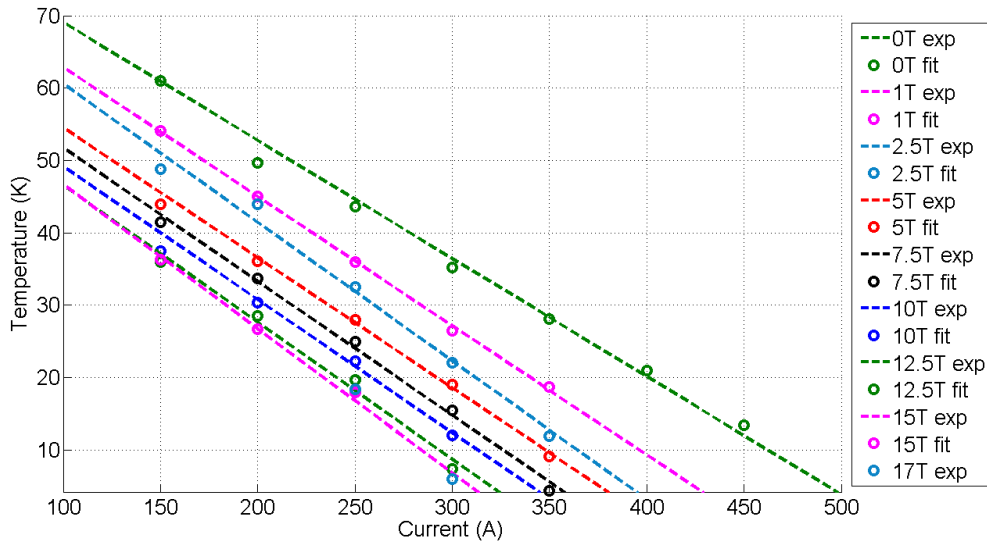


Fig. 185. Experimental results obtained on an instrumented insulated single pancake coil: set of temperatures when the voltage threshold is reached, for a given current and a given background field. The temperatures plotted vs the current for one magnetic field seem to follow a linear trend, which can be exploited to extrapolate currents at lower temperatures.

Fig. 186 (a) shows the comparison between the extrapolation of the experimental data at 4.2 K and the calculation of the limiting critical current of the coil according to the magnet field components on the magnet. The numerical results are calculated using both the background field and the field generated by the wound sample as well as the short sample characterization presented in [147] on another SuperOx tape. This latter is a 4 mm tape so a lift factor is used taking also into account the minimum I_c at 77 K, i.e. working with the ratio of the two different conductors measurement data. The black line plotted when the minimum critical current is calculated as explained in [147], in red the critical current is the minimum of the average on the width of the conductor and not just the lowest value anymore. The difference of the black and the green curves is only about 20 %, which is comforting as the coil performance is probably reduced because of the voltage taps all along the length of the winding and the soldering to join the current leads. It can be understandable that the green line is far away from the red line as the conductor behaviour is unknown in a field gradient as it is the case for a single pancake; even while working in field, the transverse component generated by the sample coil is non-negligible.

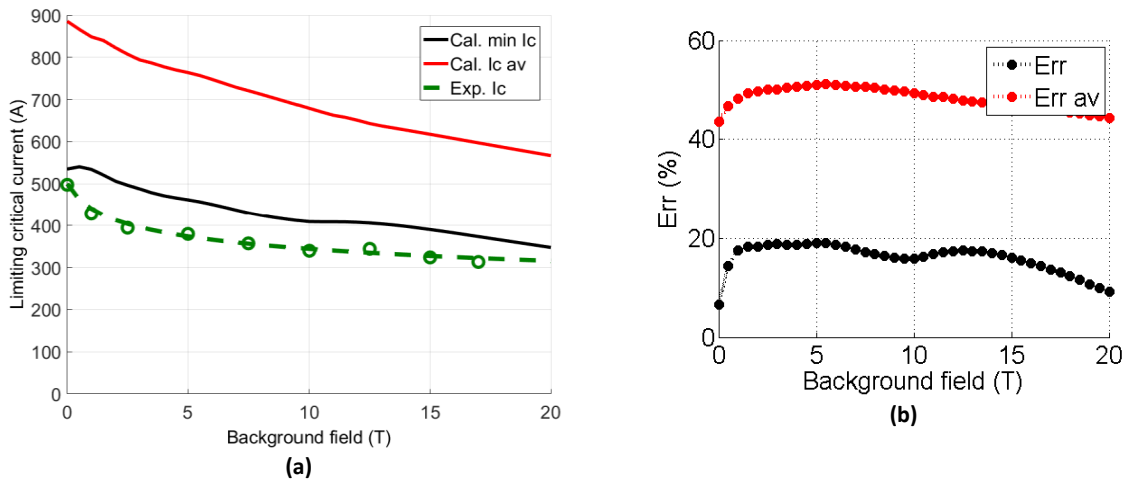


Fig. 186. (a) Limiting critical current evaluation: in green the data are evaluated according to the experiment presented in the paper; in black the curve is evaluated according to a short sample characterization applied on the field components while taking the lowest value and in red while taking the average on the width of the conductor. (b) Representation of the related errors.

4.2.4.3 Results: propagation along the turns

In this paragraph, couple of points of the Fig. 184 are analysed first for a similar amount of current inside the coil and then for a similar background field but with different currents passing through the wound sample.

Fig. 187 shows the propagation of the transition along the length of the conductor when 250 A are passing through the coil while there is no background field, i.e. the coil is working in self-field. As expected, every turn is becoming resistive ones after the others. The sample needs approximately 14 minutes and 20 seconds to reach the voltage threshold after the start of increase of the first six turns voltage.

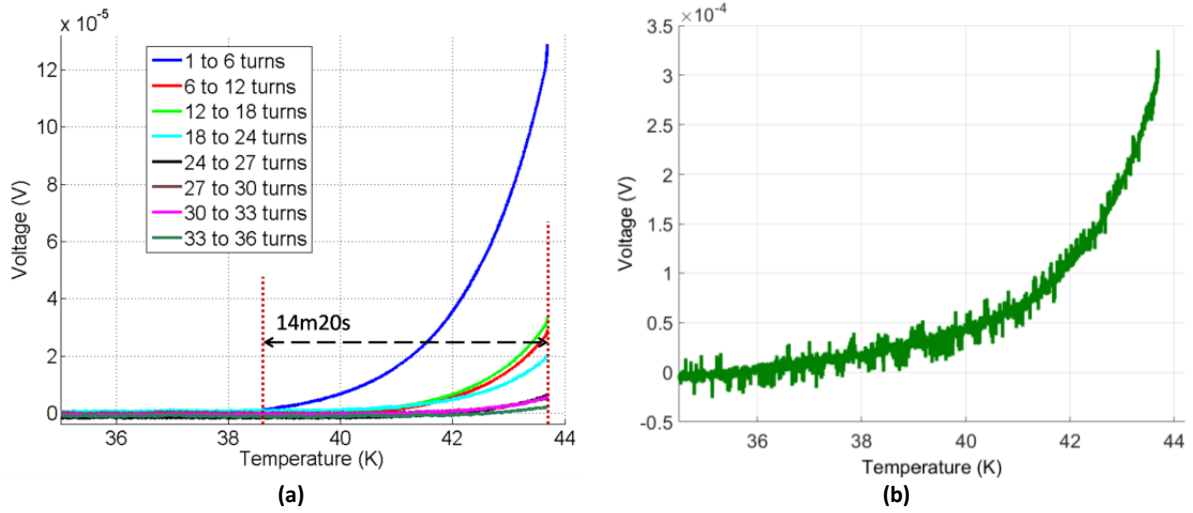


Fig. 187. (a) Inner turn voltages according to the temperature with 250 A passing through the coil, self-field. (b) Evolution of the full coil compensated voltage signal with increasing temperature.

Fig. 188 shows the same voltage measurements but for a background field of 17 T. First, the noise is much more important than in self-field. The temperature is also much lower than expected as the margin is lower when the background field is higher. In this configuration, the inner six turn's voltage needs 2 minutes and 6 seconds to reach the threshold after it starts to become resistive. This underlines lower margins for the same current but in a higher field.

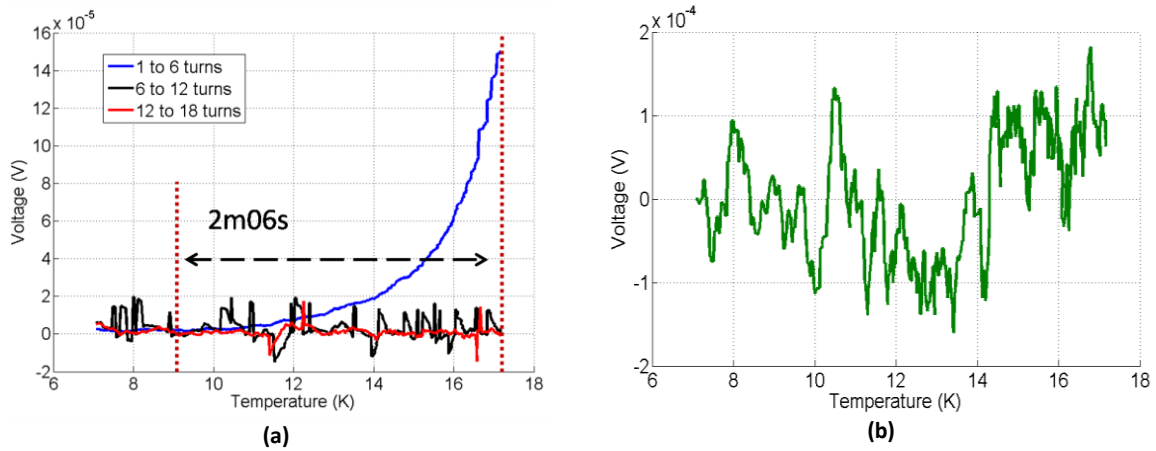


Fig. 188. (a) Inner turn voltages according to the temperature with 250 A passing through the coil, under 17 T. (b) is full coil compensated voltage signal.

In the case of a 17 T background field, only the voltage of the first six turns is increasing whereas many turns follow the trend of the first ones in self-field. This can be due to either the propagation velocity that slightly changes according to I_c but also to the heat that has more time to spread along the conductor in Fig. 187.

For both cases, the full coil voltage is also monitored but the transition can be recorded only in the first case (self-field) as the second one (background field) does not show a clear enough signal because of the noise level and the shorter time before reaching the voltage threshold when the inner turns' voltage starts to increase.

Experimental results are now compared for a similar background field but with a different amount of current inside the coil. Fig. 189 is plotted for a background field of 17 T as in Fig. 188 but the current passing through the coil is now 150 A. This time the inner voltage needs approximately 6 minutes and 46 seconds to reach the threshold after starting to show an increase of voltage; this time, the transition spreads into the turns of the coil even if it is less obvious than in self-field (Fig. 187). The delay is more than three times longer than for 250 A under the same background field, underlining again higher margins. The transition is also observed on the full coil measurement voltage.

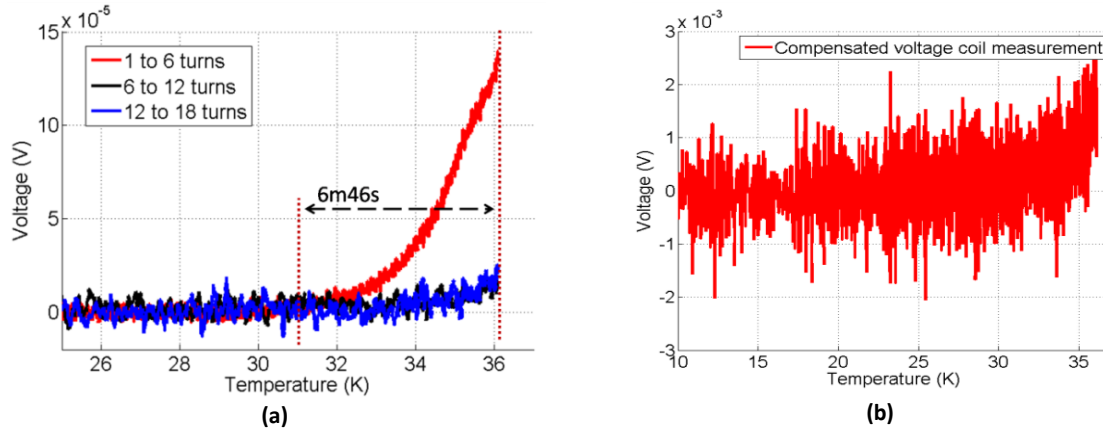


Fig. 189. (a) Propagations along the turns for 17 T and 150 A passing through the coil. (b) Full coil compensated voltage signal.

4.2.5 Comparison between experimental results and simulation

In this section, the experimental results obtained with the study of the fully-instrumented insulated single pancake are compared to the model developed in chapter 3. In section 4.2.4.2, it has been seen that in spite of the intrusive method allowing the detection and the recording of the transition inside the winding, the performance of the sample coil are only 20 % lower at 4.2 K than the expected, calculated with the experimental short sample characterization, see section 2.7.

At first, the global results are compared to the model simulations using the two different calculations of the limiting critical current previously introduced. In the second part, the full coil voltage measurements are compared to the signals evaluated with the model for some cases.

4.2.5.1 Comparison between model and experimental coil performance study: calculation of the critical current of the coil taken as the average value on the width of the conductor

The critical current of the coil is calculated here using the average of the critical current evaluated on the width of the conductor for each block and the minimum value of all blocks is taken as the critical current of the whole sample. For this comparison, the blocks along the length of the conductor are initialised with the Tapestar provided by the manufacturer, except that it is modified so that the minimum value is now equal to 65 A and not 180 A anymore. The experimental and numerical results are shown in Fig. 190.

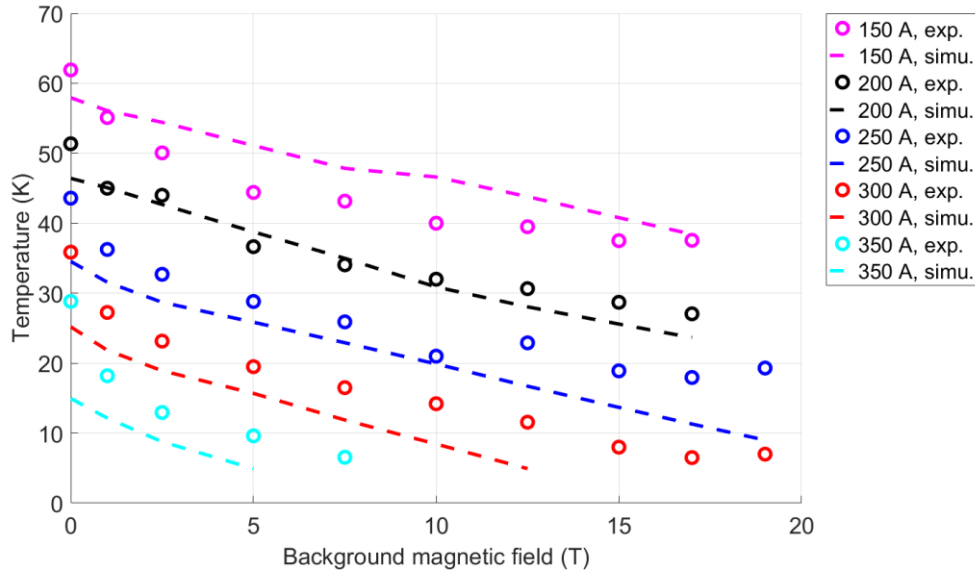


Fig. 190. Temperature of the winding when the voltage threshold is reached according to the background field and the current inside the coil.

In Fig. 190, the experimental and numerical curves do not follow the same trend. The numerical curves are approximately straight compared to the experimental data, which are more curved especially when the background field is lower than 5 T and saturate after 15 T. The shape difference can be due to the difference of measurements. For the experimental results, the first six turns are monitored whereas for the numerical results the threshold is set up on the full coil voltage at 0.1 mV/cm. As seen in section 4.2.4.3, it means that when the background field is lower than 5 T, a bigger part of the sample coil winding is transiting. Moreover, in the experiment, the winding is heating up from the inside and it is challenging to evaluate and therefore to implement it in the simulation. In this case the whole winding is warming up and it is not possible to monitor only six turns as bigger parts of the winding start transiting at the same time.

However, even if in this configuration the simulation at 200 A match the experimental data, there are some differences for the other values of current.

4.2.5.2 Comparison between model and experimental coil performance study: calculation of the critical current of the coil taken as the minimum value of the width of the conductor

The behaviour of the conductor under field gradients is unknown and for this reason, it is also interesting to work with the critical current calculated as the minimum value taken on the whole width of the wound conductor. In this configuration, only 20 % difference has been found at 4.2 K so this time the Tapestar is reduced so that its minimum value is now 75 A to match the experimental results at 200 A. The numerical and experimental results are compared in Fig. 191.

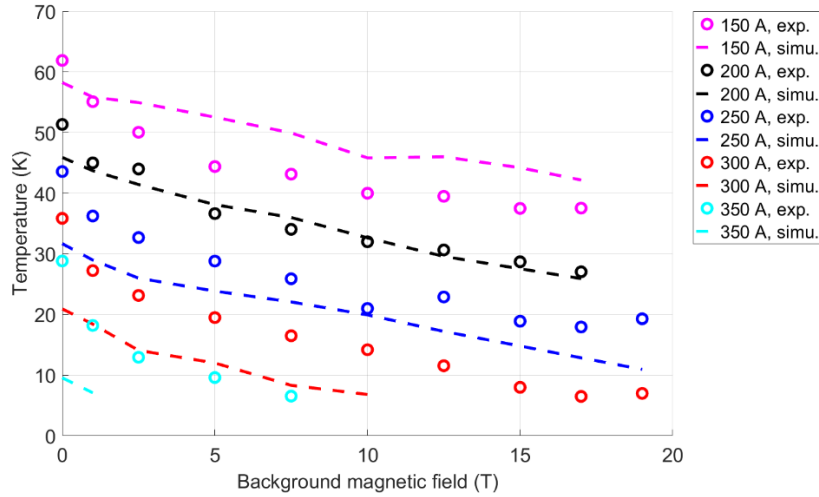


Fig. 191. Temperature of the winding when the voltage threshold is reached according to the background field and the current inside the coil.

In Fig. 191, the trend of the experimental and numerical curves is still not similar and this time the gap between both is bigger. Hence, even if the reduction of performance is lower using this calculation, the correlation between the experimental and numerical results for different current values is more important.

4.2.5.3 Comparison between model and experimental transition in a single pancake coil

In this section, the full coil voltage measurement is compared to the simulations when 250 A are passing through the coil for a self-field case and when it is working in a 17 T background field. For the model, the limiting critical current is calculated as the average of the critical current evaluated on the width of the conductor. In order to obtain the same temperatures as in the experiments the lowest value of the initial 77 K, self-field critical current values is now chosen to be 72 A. Fig. 192 shows the numerical and experimental voltage of the full coil when 250 A are passing through the coil at 17 T. Only the voltages of the six first turns are drawn from the experimental results because the signal is not clear enough on the whole coil and it has been seen in section 4.2.4.3 that only the six first turns are transiting. As it is mentioned in the previous section, the whole conductor is heated up here because it is difficult to quantify the heat generation of the winding during experiments.

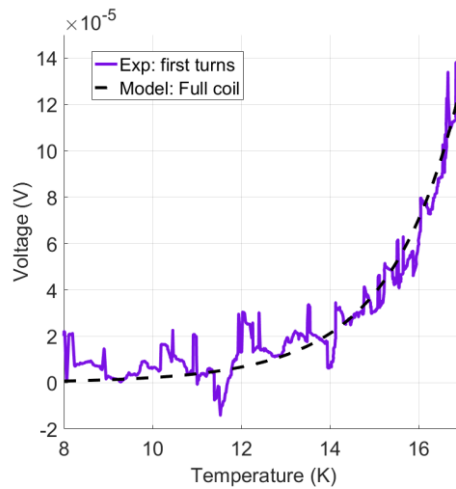


Fig. 192. Numerical and experimental voltages of the full coil when 250 A are passing through the winding at 17 T.

In this configuration, the fact that the whole conductor is heated up makes the transition homogeneous inside the winding. Fig. 193 and Fig. 194 respectively show the temperature and the voltage along the length of the conductor, according to the block number when the full coil voltage is 1 mV. The two figures underline the fact that the transition starts at the location of the defect observed on the I_c measurement given by the providers, see section 3.8.4.1. The temperature is homogeneous and the voltage on the blocks is spread mostly on one half of the length. With this simulation configuration the delay to reach the voltage threshold is only 4 seconds, compared to the 2 minutes in the experiment, see section 4.2.4.3.

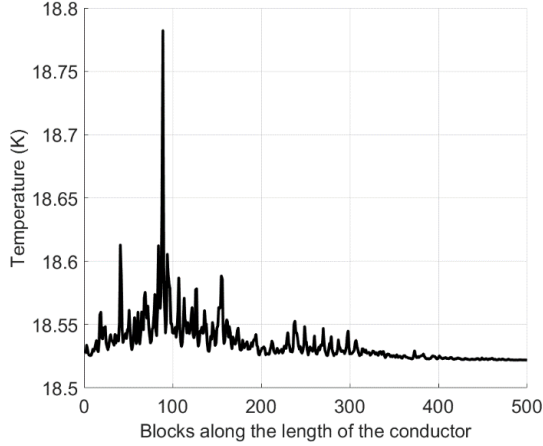


Fig. 193. Temperature along the length of the conductor when the full coil voltage is 1 mV, with global heating.

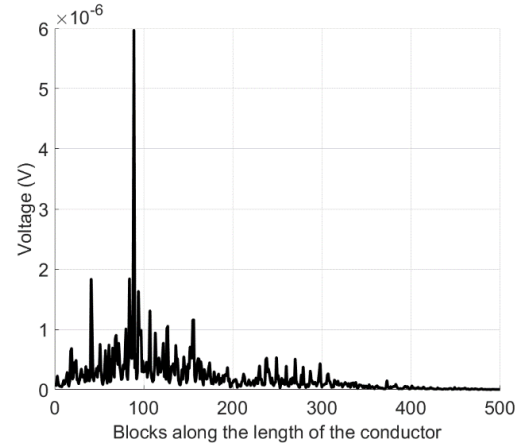


Fig. 194. Voltage along the length of the conductor when the full coil voltage is 1 mV, with global heating.

However, this transition location and propagation is still far from the experimental study as in this case, only the first six turns show a transition. Hence, another simulation is run without the global heating of the conductor. The temperature and the voltage along the length of the conductor when the full coil voltage is 1 mV are shown, respectively, in Fig. 195 and in Fig. 196. In this configuration, the initial temperature of the simulation is chosen so as the conductor does not need external heating to transit. The transition is localised on the defect (block 89) and significant voltage is visible on only six blocks. The temperature along the length of the conductor is not homogeneous anymore, ranging from 15 K up to more than 22 K. The delay to reach the voltage threshold is this time 3 minutes, longer than the 2 minutes recorded in the experimental study.

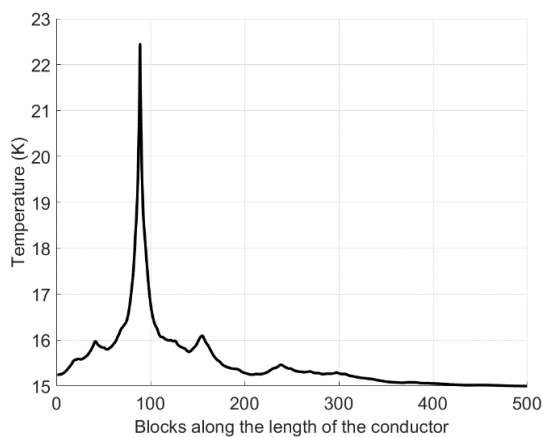


Fig. 195. Temperature along the length of the conductor when the full coil voltage is 1 mV, without global heating.

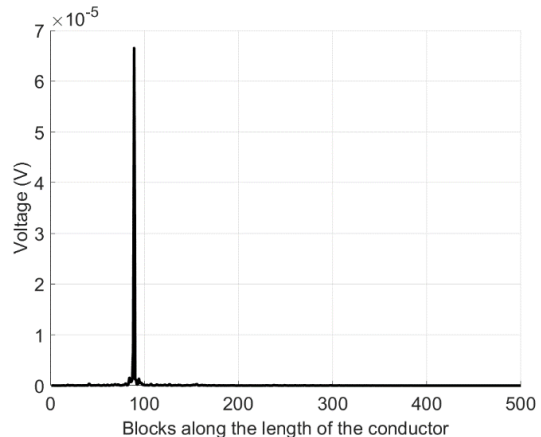


Fig. 196. Voltage along the length of the conductor when the full coil voltage is 1 mV, without global heating.

In this model, only the 1D heat propagation is used so the propagation is very slow, and the extremity of the conductor does not see any change of temperature unlike in the experiment. It is likely that an intermediate case between no heating and homogenous heating can be found which would match the experiment even better.

The start of the transition is not localised in the same area on the length of the conductor in the experiment and the simulation, which indicates that either the tape performance was reduced due to the inner contact soldering or that the performance fluctuation at 4.2 K, 17 T does not follow the same pattern as at 77 K, self-field.

4.2.6 Conclusion on the fully instrumented insulated single pancake

To conclude, the wound sample is still working even when a very intrusive method is used and after more than 50 transitions have started. During all these events, thanks to the experimental protocol, the coil is protected and does not face any damage as some experiments have been performed several times for verification and are found to have similar results. This is promising for magnet applications especially that for some experiments, where the coil could have been protected by monitoring only the full coil voltage. With the assumption that the required conditions to record a transition on a full coil can be found by calculation, this protocol would allow determining safely the operating limits of any coil. This operating zone definition is one of the main issues when working with insulated coils in large scale applications with appropriate margins as a magnet is unlikely to be damaged by an outside event. In this extent, investigation on safe operation margins would also help the implementation of a robust and precise detection/protection system.

The correlation between the experimental results and the simulations of the model is very promising even if the reduction of performance has to be slightly adapted according to the test. The model needs to be compared to more experimental results in order to understand these differences and then to reach the same values.

4.3 INTERMEDIATE CONCLUSION ON INSULATED COILS

Both insulated coil studies complement one another. The first wound sample is used to confirm calculation on magnetic and mechanical behaviours but also to study the coupling issues that need to be taken into account while working with a magnetic background field. In this study, the noise in the voltage measurement prevents the quench to be recorded. The second wound sample is aimed at working on the propagation of the transition inside the winding and safely defines at the same time the working limits of the coil. Eventually, under certain conditions, the quench is also recorded on the full coil voltage measurement, promising a safe quench detection.

The MI coil study is detailed below, underlining the main differences with an insulated coil as well as its self-protection ability.

4.4 COMPARISON WITH A MI COIL BEHAVIOUR

4.4.1 6 mm SP MI coil

4.4.1.1 Objectives

The third and last wound sample is a metallic insulated single pancake coil; it is called SP-MI in the following. As explained previously, the MI coil was made in second, between the two insulated coils. Its behaviour is also studied in detail using voltage taps implemented all along the conductor. Unlike the previous insulated coil, heaters are inserted inside the winding of the third coil to trigger quench. Hence, this coil is not used to study ‘natural’ quench but rather the transition is initiated by depositing locally some known energy inside the winding using the heaters.

The sample coil also faced voluntary as well as large unexpected discharges (the power supply of the facilities requires some tuning after a large upgrade and is being debugged) of the resistive background field so it allows studying coupling effect issues.

Here again, the goal is twofold: the sample coil is expected to show self-protection [116] and to provide some experimental contents for further simulations.

4.4.1.2 Details of the coil

The third wound coil is a metallic insulated single pancake coil (see section 1.4.6) that consists of a non-insulated superconductor tape co-wound with a thin Hastelloy tape provided by [148]; the sample is presented in Fig. 197. The two layers are wound under a tension of approximately 30 N which means a stress about 160/170 MPa for the metallic layer and 70 MPa for the superconductive tape. This assembly has been drawn and machined before the SP-INS coil. The main difference in the assembly is here the A part, which is no longer a tube but rather a bar of brass soldered with REBCO tapes. Apart from this, the design is similar, and the current follows the same path as for the SP-INS (see section 4.1.2.1).

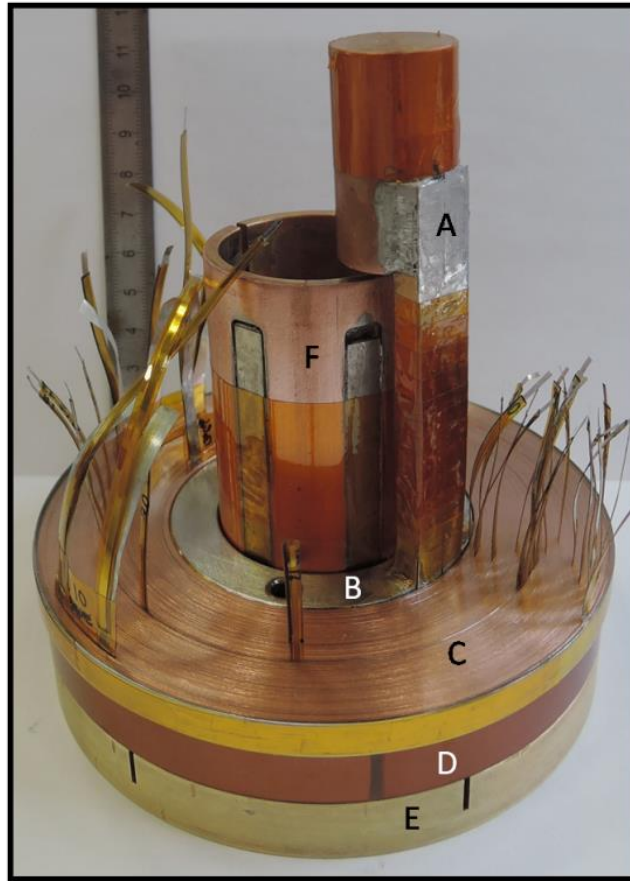


Fig. 197. MI coil after wrapping.

As the coil is expected to be self-protected [116] (see section 1.4.6.2), the conductor does not need as much copper as in the previous windings, the characteristics of the tape are presented in Table 12, inducing a lower total thickness that allows to wind more turns on the mandrel as highlighted in Table 13.

Conductor features	
Width (mm)	6
Copper layer (μm) x2	10
Total thickness (μm)	75
Hastelloy substrate (μm)	50
Ag layer (μm)	3
REBCO (μm)	~ 2
I_c min (77 K, self-field) (A)	205

Table 12. Conductor characteristics for the MI coil.

Coil characteristics	
Inner diameter (mm)	60
Outer diameter (mm)	110
Number of pancake	1
Number or turns/pancake	238
Field factor mT/A	3.615

Table 13. MI coil characteristics.

4.4.1.3 Instrumentation

The coil is a fully-instrumented 6-mm tape pancake with 33 voltage taps to monitor the quench propagation inside the winding. To facilitate the transition recording, three heaters are also placed inside the winding; the first one is between the first turns, the second in the middle and the third one on the outer turns. Both voltage taps and heaters are made with the same metallic ribbon whose thickness is 30 μm and isolated from the winding by Kapton tape as shown in Fig. 198. The same metallic layer is used for both the heaters and the voltage taps in order to avoid a damage of the instrumentation during experiment that may be caused by the high forces generated by the high current and the high background field.

Nevertheless, there is no difficulty for recording voltages as values are rapidly in the mV range and higher because of the current bypassing the turn-to-turn contact resistance during the transition, see section 1.4.6.2.



Fig. 198. Photography of one of the three heaters placed inside the winding.

The last couple of turns are also soldered on themselves and the wrapping is done with the co-wound metallic layer.

4.4.2 Field coefficient

In the case of NI or MI coil, the current may bypass turns (see section 1.4.7) and as its path is uncontrolled, the relationship between the magnetic field and the current is more complicated; this phenomenon is illustrated in Fig. 199. After energizing one of the heaters, the voltage increases inside the coil, which triggers the emergency discharge set up in the software to cut the current. When the current ramp is fast, the magnetic field curve does not follow the trend of the current anymore.

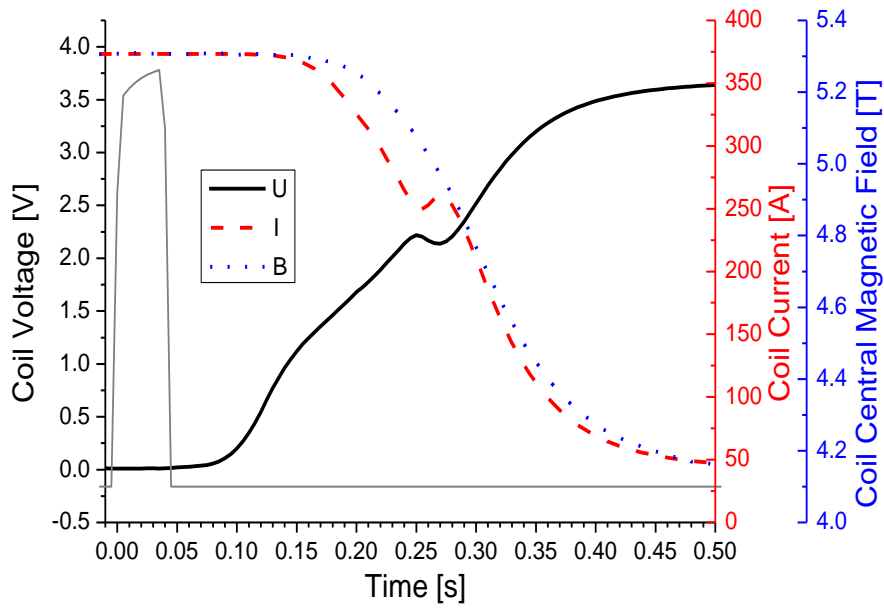


Fig. 199. MI coil measurements; full coil voltage, current and magnetic field at the centre of the coil are plotted.

Nevertheless, during experiments the coil field coefficient is close to the calculated value, which is comforting to build user magnet with MI coils, as illustrated in Fig. 200. To conclude, this magnetic field coefficient is only a concern when there is an unexpected discharge or a default.

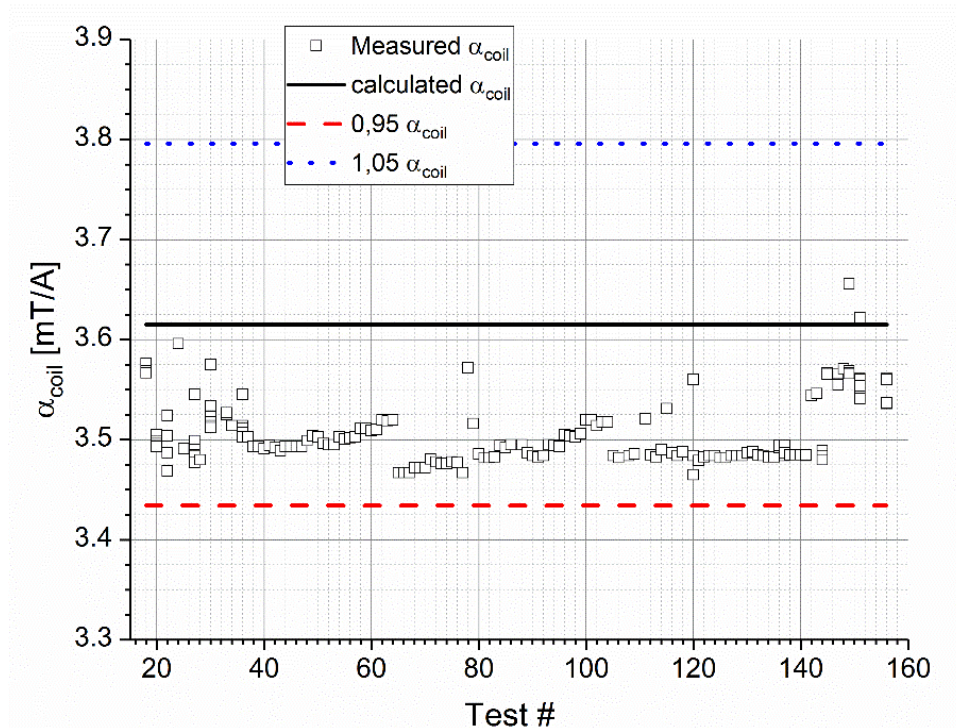


Fig. 200. 2017 tests magnet constant. Black line, red dash and blue dot are respectively the calculated magnet constant, the constant reduced by 5 % and the constant with 5 % added.

4.4.3 Coupling issues

Even if the MI coil was only tested inside a resistive magnet, it also faced a couple of unexpected discharges of the outer magnet. The measurements are shown in Fig. 201 and Fig. 202. Fig. 201 represents the whole coil voltage measurement (left axis) and the current inside the coil (right axis) and Fig. 202 shows both the background magnetic field alone (dotted line) and the magnetic field measured at the centre of the sample coil. The background field was at 16.5 T when unexpectedly discharged.

In Fig. 202, the plot of the external field is only approximated and not a direct measurement of the current inside the resistive outer magnet. It is assumed that the magnetic field generated by the sample coil follows the trend of the current and the magnetic field generated by the background field is then the difference of the measured field in the centre of the sample coil and the calculation of the field it generates. All the other curves are measurements.

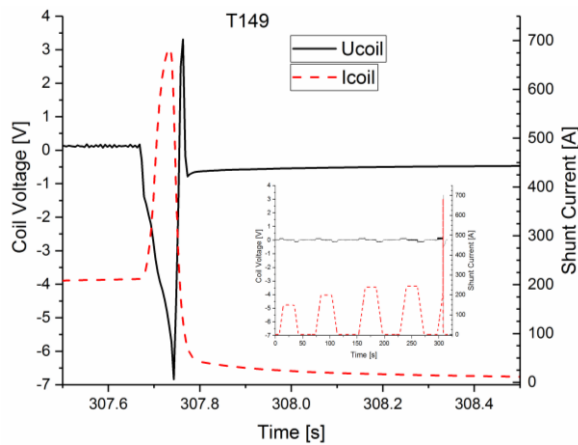


Fig. 201. Voltage measurement and current inside the coil during the unexpected background discharge.

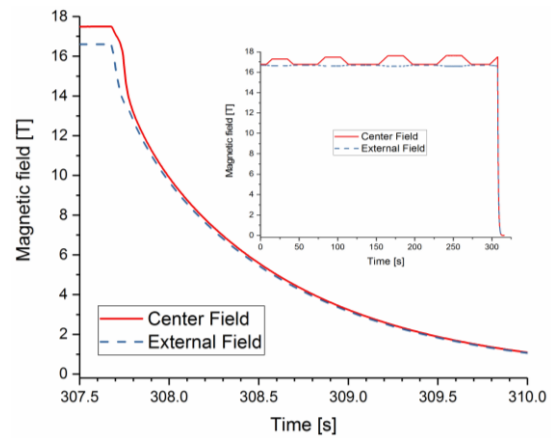


Fig. 202. Measured centre field and external field during unexpected discharged.

4.4.4 MI coil behaviour

Unfortunately, it was not possible to study natural quenches for the MI coil as the winding was damaged on the outer turns at the very beginning of the tests. It is damaged especially on the outer soldering on the current lead during the fast discharge of the outer magnet explained in the section dedicated to coupling, see section 4.4.3. This damage is thought to be caused by the mechanical stress during the fast increase and decrease of the current inside the coil because of the unexpected background discharge. Although one outer magnet's unexpected discharge is previously presented, the coil also faced another one but at lower field value, which damaged this time the inner current lead. Fig. 203 shows the resistance of the current leads before and after being damaged.

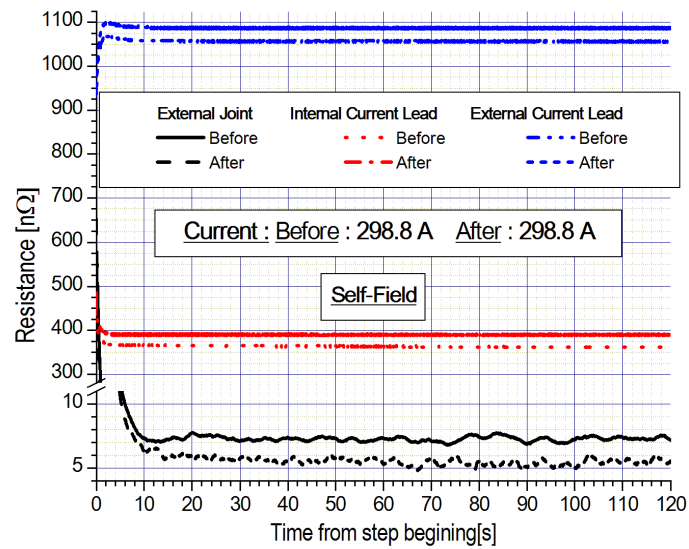


Fig. 203. Resistance of the damaged area of the winding before and after the outer discharges.

The heater in the middle of the winding allows initiating quenches without triggering the outer turns that are damaged. In Fig. 204, the energy provided to the heater to trigger a non-recovering transition is shown according to the current that is passing through the coil and the magnetic field background: this energy is called quench energy. This quench energy is only an approximation as an unknown part of it dissipates in the conductor especially as the pulse duration is rather long. The difference of energy needed while under high field or in self-field is very high.

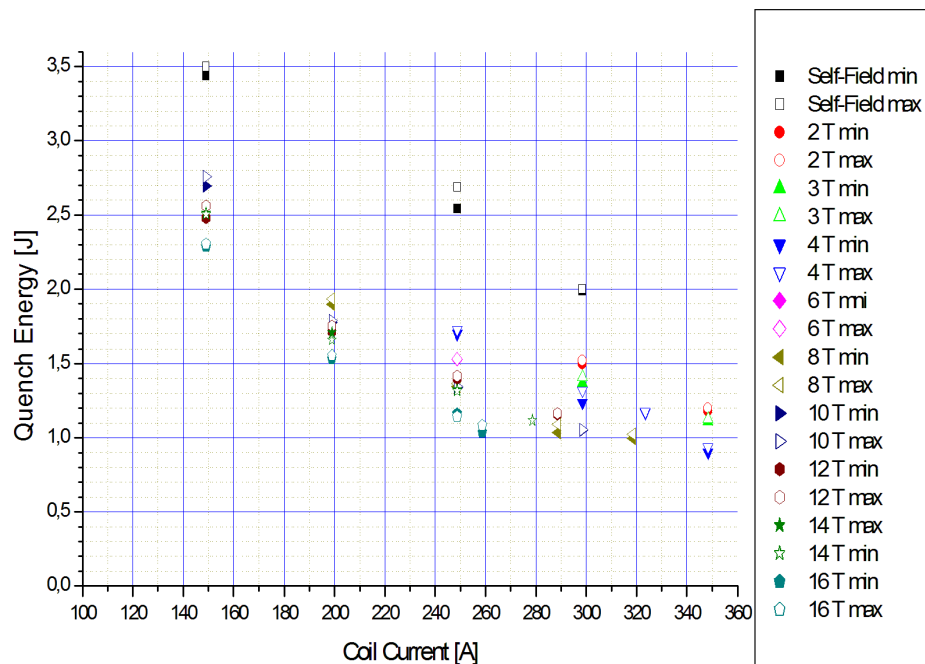


Fig. 204. Quench energy according to the magnetic field background and the current inside the coil.

It is also interesting to observe this quench energy only according to the magnetic background field as shown in Fig. 205. Over 5 T, the heat pulse duration values slightly start saturating and under 5 T the energy needed is much higher and the time twice longer. It is interesting to mention the pulse

duration because of the dissipation of the current inside the conductor, which highly depends on the pulse duration.

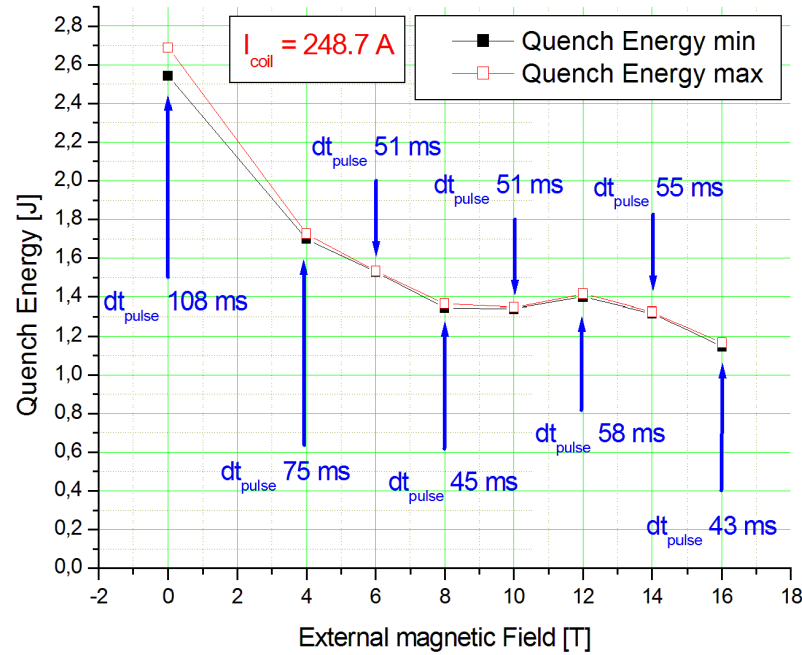


Fig. 205. Quench energy according to the magnetic field background, giving also the heat pulse duration.

On the three first graphs Fig. 206, Fig. 207 and Fig. 208, taken for a background field lower than 6 T, the propagation along the turns seems similar; the propagation is respectively given for a study in self-field, under 4 T and under 6 T.

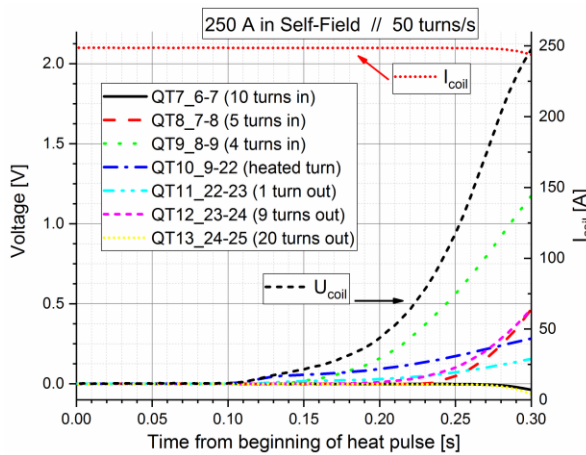


Fig. 206. Propagation of the transition after heat pulse for 250 A, self-field.

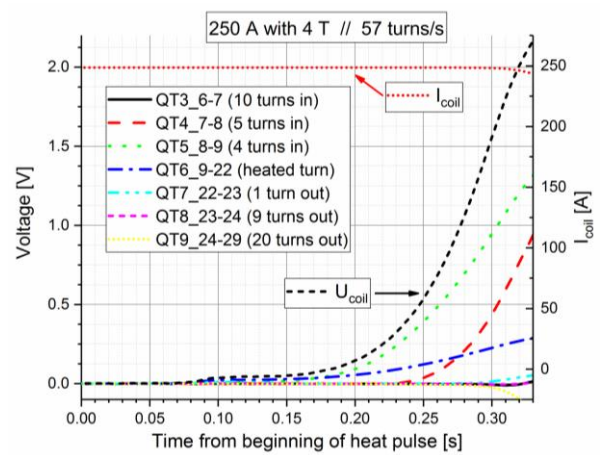


Fig. 207. Propagation of the transition after heat pulse for 250 A, 4 T.

The transition always starts with the 4 turns 'in' whereas under 16 T (see Fig. 209), even if the same turns start the transition, the 9 turns out quickly increase. On the contrary, under low field, this turn was only transiting slowly, especially in the case of a study under self-field.

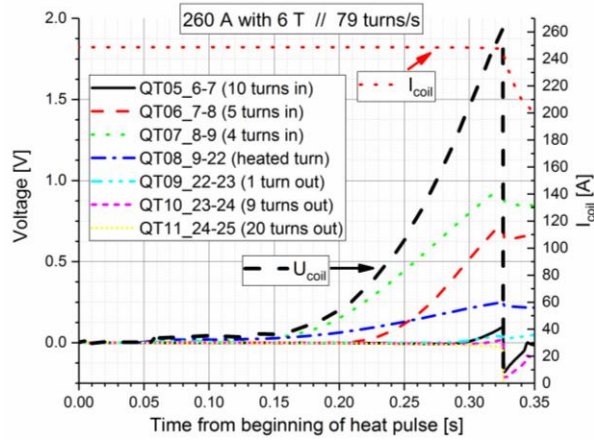


Fig. 208. Propagation of the transition after heat pulse for 260A, 6 T.

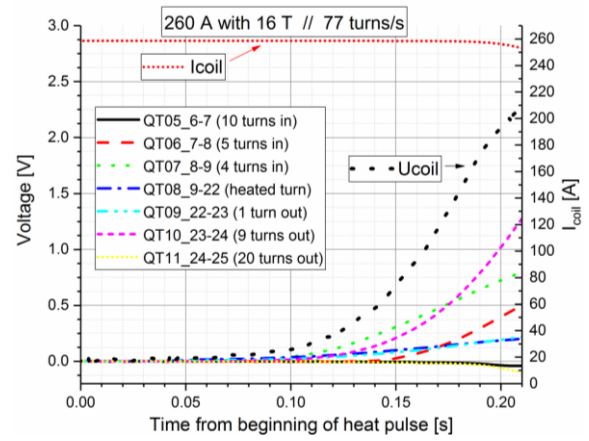


Fig. 209. Propagation of the transition after heat pulse for 260 A, 16 T.

Nevertheless, more than 200 transitions have been monitored and the coil remains undamaged. The self-protection ability of the MI coil can therefore be confirmed. However, the limiting critical current calculation of the coil could not be confirmed as the sample was damaged at the very beginning of the tests due to the unexpected background field discharges.

4.5 CONCLUSION

4.5.1 Summary

The three coil main characteristics are summarized below, in Table 14. They all tend to respect the final geometry of the insert according to what was decided at the time of their fabrication.

Coil characterization	DP INS coil	SP INS coil	SP MI coil
Inner diameter (mm)	56	60	60
Outer diameter (mm)	108	110	110
Number of pancake	2	1	1
Number or turns/pancake	170	170	238
Field factor mT/A	5.664	3.038	3.615

Table 14. Summary of the three coils studied under high field.

4.5.2 Assembly improvements

Each time the whole assembly has been slightly improved to help in the design assembly of the final insert prototype. For the first wound sample (SP-INS), the extremities of the tapes are clamped on massive copper pieces. The electric contacts do not seem to be good enough as the coil is damaged each time on this location. It is probably due to mechanical stresses on unprotected part of the conductor or a too small area of electric contacts.

For the MI coil, which is the second sample to be designed and wound, the current leads are also damaged, first the outer one and then the inner one even though the conductor is this time soldered. There is also a mechanical backup on the outer soldering but only on the pancake area so only half of the bridge surfaces are protected.

For the last sample (DP-INS), soldering is still used to connect the extremities of the conductor to the current leads. However, this time the inner current lead is a cylinder, making it stronger compared to a bar. Moreover, the outer soldering, i.e. the pancake but also the brass disk on which the outer bridges are soldered, is fully recovered by a glass fibre tape and the NCC. No damage has been recorded on the outer turns.

To conclude, the sample holder has been improved with these three studies that will help at designing the assembly of the final insert for the NOUGAT project

4.5.3 Chapter conclusion

Three wound samples have been successfully tested in order to improve our understanding of their behaviour under high field. The first wound sample (SP-INS) is dedicated to mechanical and magnetic studies as well as the coupling issues inside a LTS magnet. Simulation results have been confirmed each time by experiments. The second wound sample (DP-INS) is aimed at recording the propagation inside its winding using a very intrusive method. Even fully-instrumented, the coil is working under high field and more than 50 transition starts have been recorded. The winding remains undamaged during the experiments. The tests were performed several times and same temperatures were found. Even if it is only an approximation, the 4.2 K values were close to calculation taking into account that the coil performance could have been reduced because of the intrusive voltage measurements along the conductor length. Moreover, in certain specific conditions, when margins are high the coil could have been protected as the transition was detected on the full coil voltage measurement. The third wound sample (SP-MI) is fabricated to confirm the self-protection ability of the MI coil and the increase of time constants compared to NI coils. Both have been illustrated during experiments.

Both fully-instrumented wound samples provide plenty of experimental data for further simulations. The SP-INS is protected on the full coil voltage measurement but only for some specific conditions, rather when the operating margins are high.

These experimental results are also compared to the model previously detailed. Correlations have been found with success, nevertheless further work is still needed to better understand HTS magnets, especially in high magnetic fields.

5 CONCLUSION

The present work is part of the NOUGAT project, which aims at designing and building a 10 T REBCO insert working in a 20 T background field. The final prototype of this insert that is to be built at the end of the project is expected to use HTS conductor with no electrical insulation but rather to co-wound it with a metallic layer (MI coil) mostly for its self-protecting ability.

In the case of an insulated coil, the high heat capacity of REBCO and the inhomogeneity along the length can be the origin of a local hot spot, which is likely to cause irreversibly damage to the conductor. On the other hand, for a MI coil, in case of an inhomogeneity along the length of the conductor, the current bypasses the turn-to-turn contact resistance and prevents the winding from being damaged. Moreover, for an insulated coil, it is difficult to detect this local hot spot as the voltage signal is easily lost in a high noise level measurement environment. This phenomenon is caused by their low NZPV; it induces a local increase of the voltage, which does not spread along the length of the conductor. As a consequence, the voltage is not high enough to be recorded by the instrumentation before damaging the conductor. For a MI coil, even the detection is effortless to set up as the resistances of the turn-to-turn contact make the voltage quickly high and easily detectable. Nevertheless, MI coils cannot be considered for every kind of applications (SMES) and even when used for user magnets, their lower field linearity, stability and dynamics have to be considered. Hence, in parallel of the advancement of the project, insulated coils are investigated, especially to consider how to set up a reliable detection of the transition and a protection of the coil.

Hence, the present work is focused on the development and understanding of insulated coils even if some MI coil experimental results are presented, mostly for a comparison purpose. It is developed around three axes.

In a first step, the conductor is studied by itself without being wound under high field up to 23 T with various orientation and at several temperatures from liquid helium bath (4.2 K) to liquid nitrogen bath (77 K). This experimental short straight sample characterization is first aimed at having a recent set of data for the conductor as their performance is continuously improved. However, the purpose of this study is also to have a first approach on how carefully the conductor has to be handled while its limits are being tested, i.e. under high field with high current passing through the conductor. A high field measurement protocol was developed based on already existing experimental setups in the lab. With this protocol the tape of one supplier (SuperOx), for which data was not available in the literature at the time, was exhaustively characterized.

The second axis of this study is a magnet coil model whose purpose is to predict the location of the transition's beginning and how it propagates inside the winding of a single or double pancake. The results of the previous experimental short sample characterisation are implemented in this model to work with the most accurate and the latest performance values of the conductor. This model is the first to our knowledge to study the influence of initial tape inhomogeneity on coil quench behaviour. It is still under development, but first results show promising results allowing insightful comparisons with wound sample experimental studies.

Then, the third axis of the present work is the study of the conductor when wound in a coil and subject to high field at varying temperature: three coils are built and studied with slightly different purposes. Two insulated coils are designed, wound and their behaviours are investigated. The first one

is a double pancake, which allows studying its mechanical and magnetic behaviours. This wound sample allows confirming hypothesis made on the mechanical and magnetic calculations, but it also allows investigations on coupling issues as it faces a background field discharge while working inside an LTS magnet. It confirms the idea that it is better to study the quench phenomenon inside a resistive magnet rather than inside a superconducting magnet.

The second wound sample is, in terms of voltage taps, a fully-instrumented single pancake which allows recording the transition and its propagation inside the winding under high field up to 19 T, from 4.2 K to more than 60 K. An experimental protocol is investigated to decrease as much as possible the noise level measurement. In spite of the numerous voltage taps, which provide insurance for detecting the transition, this latter is also investigated on the full coil voltage measurement. The experimental protocol is then to work with the background field and current inside the winding when they are constant and only then the coil is heat up to work with the clearest voltage signals possible.

This second wound sample is a good promise for the use of REBCO conductors for high field applications as it has survived more than fifty starts of transition. Some experiments were performed several times and similar results were found, which prove that the coil was not damaged. It is seen as a big step for REBCO insulated coils for high field applications as this kind of intrusive method to monitor the voltages inside the winding is likely to damage the conductor, mostly because of the extra layer created by the soldered voltage taps. Hence, not only has the coil survived a transition that many times but also its performance was only 20 % under the calculated value, derived from the experimental short sample characterization. We have therefore proved that isolated REBCO coils can be protected safely.

The second interesting result of these experiments is that, even if each time the coil is protected, the increase of voltage is also observed (in some cases at least) on the entire coil voltage measurement. It means that, under some specific conditions, the coil could have been protected only using the global signal of the winding. In this extent, it is possible to study a working zone of the coil where the limits are defined safely using the full coil voltage measurement. If these conditions are understood and defined using simulation, a protocol to safely evaluate coil margins could be proposed and would help to setup a robust and reliable system of detection/protection of the magnet. The first comparison of the experimental results of this coil and the simulation of the model are really promising, even if it is difficult to quantify the heating of the coil during the experiments to be able to implement it in the model. However, when using a global heating of the conductor of the wound sample, the model corroborates the experimental results.

The third and last wound sample to be presented is a MI single pancake coil that is also fully instrumented. Results are only used here to underline the main advantages and disadvantages of such a winding technique.

In summary, the present work is an investigation on how a transition starts in an insulated winding and how it then propagates along the HTS conductor. The purpose is twofold: the first objective is to understand this behaviour so appropriate operating margins can be evaluated to allow one coil to work safely. The second main goal is to use this knowledge to implement reliable detection systems that should be set up to protect one coil. In the present work, preliminary comparisons between experimental results and first model simulations are compared and show promising results. Even if the model does not match the experimental contents yet, the beginning of the transition is

localised and the way it dissipates energy is evaluated inside the winding as well as the temperature rise along the conductor. However, the heating during the experimental study is difficult to quantify and therefore further simulations are required. An experimental protocol has also been proposed and successfully tested. Nevertheless, more experimental data and further model simulations are required to confirm these preliminary promising results.

6 APPENDIX

6.1 PROOF OF THE UNIQUE REAL POSITIVE SOLUTION

The function which is studied in the following is:

$$y \rightarrow x^n + ax - a \quad 42$$

with $a > 0$.

To prove the existence of this unique solution the trend of the function defined by the equation is studied. In a first time, n is even and then n is odd as n can have any value but also change during the model calculation according to the field and temperature.

The y function is continuous from \Re to \Re so it can be derivate on \Re and used to study y variations.

$$y' \rightarrow nx^{n-1} + a \quad 43$$

The assumption is made that n is at least higher than 10 (see section 2.6.3.2) so there is no use to study the cases where n is 0, 1 or 2. It means that n is always different from 0 as well as $n-1$.

6.1.1 Case with n is even

If n is even, $n-1$ is odd so it has to be d in \Re as $y'(d)=0$.

$$y'(d) = 0 \leftrightarrow nd^{n-1} + a = 0 \leftrightarrow d^{n-1} = \frac{-a}{n} \quad 44$$

$$d^{n-1} = \frac{-a}{n} < 0 \quad 45$$

Now, y' signs are studied.

$$y'(x) < 0 \leftrightarrow nx^{n-1} + a < 0 \leftrightarrow x^{n-1} < -\frac{a}{n} = d^{n-1} \leftrightarrow x < d \text{ as } d < 0 \text{ and } n-1 \text{ odd} \quad 46$$

y' is strictly negative on $]-\infty ; d]$ and strictly positive on $[d ; +\infty[$. It is also equal to zero in d .

So, y is strictly decreasing on $]-\infty ; d]$, strictly increasing on $[d ; +\infty[$ and has a minimum in d .

If $y(d)<0$, the polynomial has two real solutions, if $y(d)=0$, it has one unique real solution and if $y(d)>0$, it has no real solution. So $y(d)$ has to be evaluated.

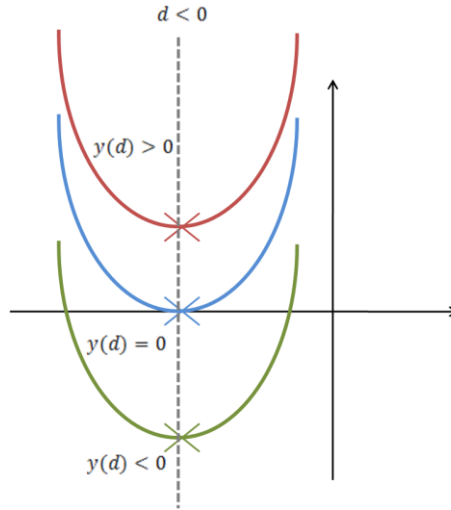


Fig. 210. Trend of the curve when n is even.

47

$$y(d) = d^n + d \cdot a - a = d \cdot d^{n-1} + d \cdot a - a = d \cdot \frac{-a}{n} + d \cdot a - a = ad \cdot \frac{n-1}{n} - a$$

with $a > 0$, $d < 0$, and $\frac{n-1}{n} > 0$ so $d \cdot a \cdot \frac{n-1}{n} < 0$

So we have $y(d) < 0$ and the polynomial has two real solutions.

Moreover $\lim_{x \rightarrow +\infty} y(x) = +\infty$ and $\lim_{x \rightarrow -\infty} y(x) = +\infty$

Because it is equivalent to x^n with n even in $+\infty$ and in $-\infty$.

It can be assumed that at least one of the solution is negative ($d < 0$); it is now shown that the other one has to be positive in all cases where n is even.

$y(0)$ is evaluated. If $y(0) < 0$, the polynomial has two real solutions, one positive and one negative. If $y(0) = 0$, 0 is one solution and the other one is negative and if $y(0) > 0$, the polynomial has two negative solutions.

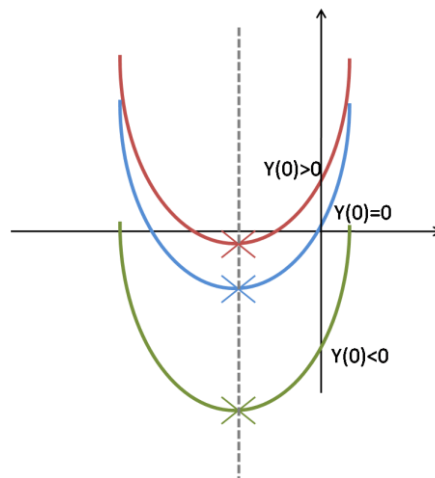


Fig. 211. Illustration of the trend of the curve according to the value of $y(0)$, when n is even.

$$y(0) = 0^n + 0 \cdot a - a = -a < 0 \quad 48$$

To conclude, if n is even, the polynomial has two real solutions, one is strictly negative and one is strictly positive. The same is shown when n is odd.

6.1.2 Case with n is odd

If n is odd, $n-1$ is even.

The following function is studied:

$$y \rightarrow x^n + x \cdot a - a \quad 49$$

With $a > 0$

And so the sign of its derivative is evaluated,

$$y' \rightarrow nx^{n-1} + a \quad 50$$

For all x in \mathbb{R} , $x^{n-1} > 0$ because $n-1$ is even. It is known that $n > 0$ and $a > 0$ so for all x in \mathbb{R} , y' is strictly positive.

So y is strictly increasing on \mathbb{R} .

Now, the limits of $y(x)$ in $+\infty$ and in $-\infty$ are studied.

$$\lim_{x \rightarrow +\infty} y(x) = +\infty \text{ and } \lim_{x \rightarrow -\infty} y(x) = -\infty$$

because $y(x)$ is equivalent to x^n with n odd in $+\infty$ and in $-\infty$.

So knowing that y is continuous on \mathbb{R} , it has to be a d as $y(d)=0$.

The sign of d is evaluated while calculating $y(0)$. If $y(0) < 0$, the polynomial has only one real strictly positive solution, if $y(0)=0$, it has only one solution equal to zero and if $y(0) > 0$, the polynomial has only one real strictly negative solution, as illustrated in Fig. 212

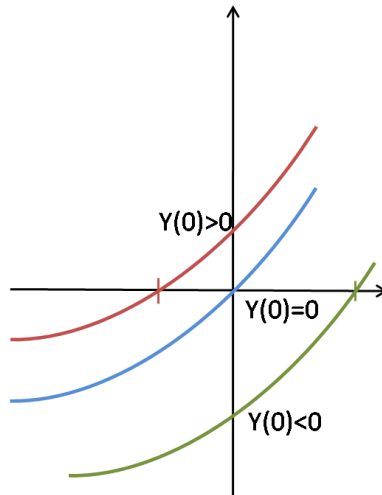


Fig. 212. Illustration of the curve when n is odd.

$$y(0) = 0^n + 0 \cdot a - a = -a < 0 \quad 51$$

To conclude, if n is odd, y has only one real strictly positive solution and so for all values of n , the polynomial has always one unique strictly positive solution. In summary, whatever n value, the equation always has one unique real positive solution.

6.2 MATERIAL PROPERTIES IMPLEMENTED IN THE MODEL

This appendix summarizes the material properties used in the model, taken from the literature. In the following, the silver and the copper data are respectively given with a RRR of 20 under 10 T and a RRR of 25 under 10 T.

6.2.1 Density

Density (kg.m^{-3})	
Silver	10 500
Copper	8 960
Hastelloy	8 220
Superconductive layer	6 400

Table 15. Density of the layer materials.

6.2.2 Specific heat capacity

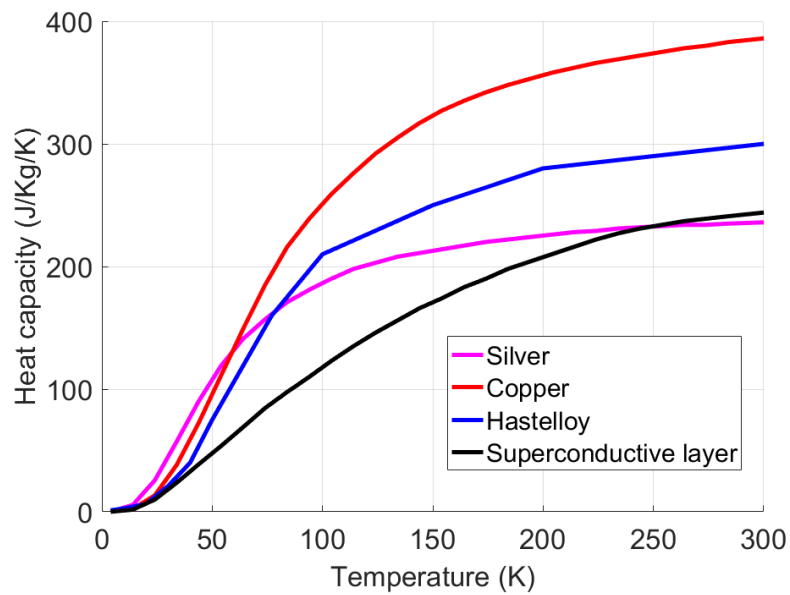


Fig. 213. Heat capacity of the layer materials.

6.2.3 Thermal conductivity

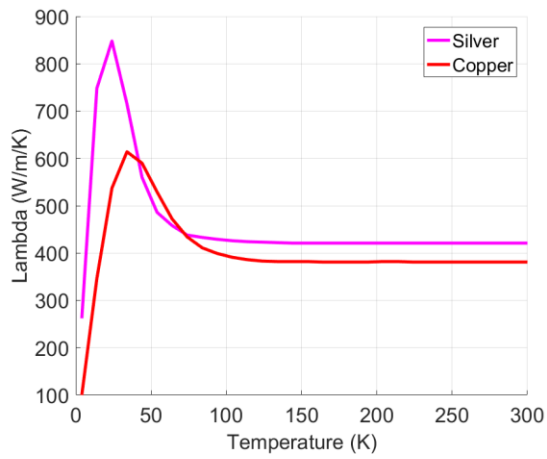


Fig. 214. Thermal conductivity of the silver and copper layers.

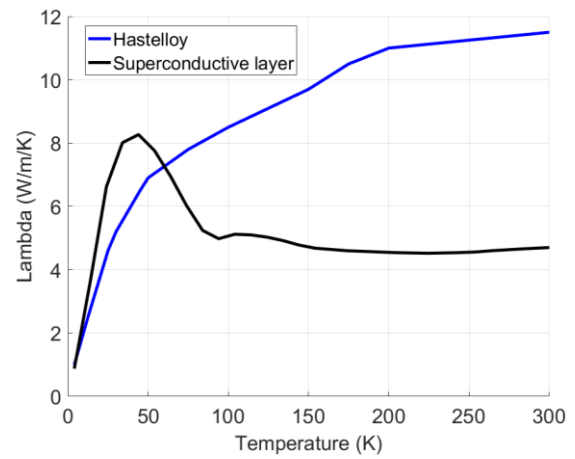


Fig. 215. Thermal conductivity of the Hastelloy and the superconductive layers.

6.2.4 Resistivity

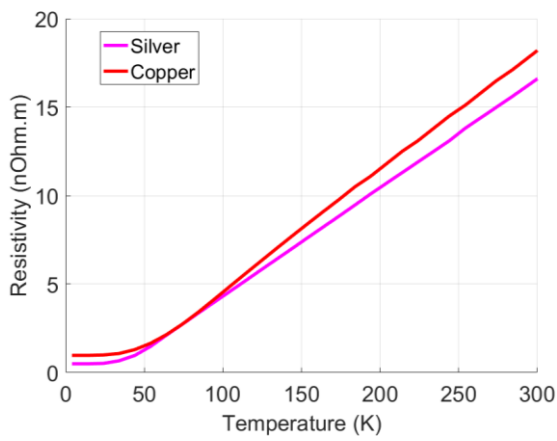


Fig. 216. Resistivity of the silver and copper layers.

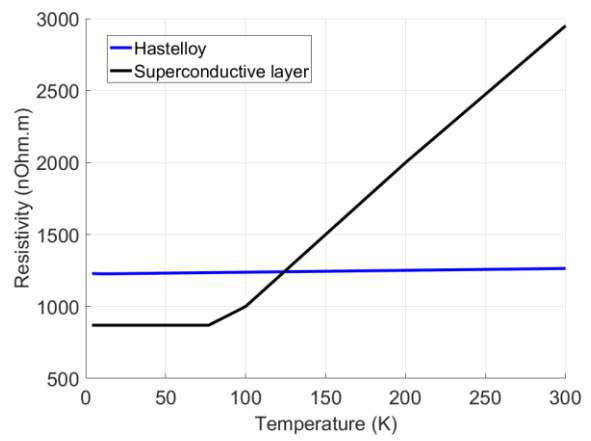


Fig. 217. Resistivity of the Hastelloy and the superconductive layers.

REFERENCES

- [1] S. Lee *et al.*, "Development and production of second generation high T_c superconducting tapes at SuperOx and first tests of model cables," *Supercond. Sci. Technol.*, vol. 27, 2014.
- [2] G. Majkic, E. Galstyan, Y. Zhang, and V. Selvamanickam, "Investigation of delamination mechanisms in IBAD-MOCVD REBCO coated conductors," *IEEE Trans. Appl. Supercond.*, vol. 23, no. 3, 2013.
- [3] H. Maeda and Y. Yanagisawa, "Recent Developments in High-Temperature Superconducting Magnet Technology (Review)," *IEEE Trans. Appl. Supercond.*, vol. 24, no. 3, 2014.
- [4] "SuperPower data." [Online]. Available: http://www.superpower-inc.com/system/files/SP_2G+Wire+Spec+Sheet_2014_web_v1_0.pdf.
- [5] J. Fleiter, "Development of high T_c superconducting cables for applications in CERN," 2014.
- [6] C. Zhou, K. A. Yagotintsev, P. Gao, T. J. Haugan, D. C. Van Der Laan, and A. Nijhuis, "Critical current of various REBCO tapes under uniaxial strain," *IEEE Trans. Appl. Supercond.*, vol. 26, no. 4, 2016.
- [7] D. N. Zheng *et al.*, "Magnetic susceptibilities, critical fields, and critical currents of Co- and Zn-doped $YBa_2Cu_3O_{7-x}$," *Phys. Rev. B*, vol. 49, no. 2, 1994.
- [8] "SuperOx data." [Online]. Available: <http://www.superox.ru/en/products/974-vtspprovod/>.
- [9] X. Hu *et al.*, "An experimental and analytical study of periodic and aperiodic fluctuations in the critical current of long coated conductors," *IEEE Trans. Appl. Supercond.*, vol. 27, no. 4, 2017.
- [10] J. H. Choi *et al.*, "Investigation of the key factors affecting the permanent damage of the REBCO coated conductor in overcurrent condition," *IEEE Trans. Appl. Supercond.*, vol. 25, no. 3, 2015.
- [11] C. Senatore, C. Barth, M. Bonura, M. Kulich, and G. Mondonico, "Field and temperature scaling of the critical current density in commercial REBCO coated conductors," *Supercond. Sci. Technol.*, vol. 29, 2016.
- [12] J. Pelegrín, E. Martínez, L. A. Angurel, Y. Y. Xie, and V. Selvamanickam, "Numerical and experimental analysis of normal zone propagation on 2G HTS wires," *IEEE Trans. Appl. Supercond.*, vol. 21, no. 3, 2011.
- [13] M. Daibo, S. Fujita, M. Haraguchi, Y. Iijima, and T. Saitoh, "Evaluation of the normal-zone propagation characteristics of REBCO coated conductors with laminated Cu tape," *IEEE Trans. Appl. Supercond.*, vol. 21, no. 3, 2011.
- [14] T. Verhaege *et al.*, "A new class of AC superconducting conductors," *IEEE Trans. Appl. Supercond.*, vol. 3, no. 1, 1993.
- [15] Z. P. Zhao and Y. Iwasa, "Normal-zone propagation in adiabatic superconducting magnets: I. Normal-zone propagation velocity in superconducting composites," *Cryogenics*, vol. 31, 1991.
- [16] M. Bonura and C. Senatore, "Temperature and Field Dependence of the Quench Propagation Velocity in Industrial REBCO Coated Conductors," *IEEE Trans. Appl. Supercond.*, vol. 27, no. 4, 2017.

- [17] H. Song and J. Schwartz, "Stability and Quench Behavior of $\text{YBa}_2\text{Cu}_3\text{O}_{7-x}$ Coated Conductor at 4.2 K, Self-Field," *IEEE Trans. Appl. Supercond.*, vol. 19, no. 5, 2009.
- [18] V. Selvamanickam, "Second-generation HTS Wire for Wind Energy Applications," in *Symposium on superconducting devices for wind energy, Barcelona, Spain*, 2011.
- [19] Y. Shiohara, T. Taneda, and M. Yoshizumi, "Overview of materials and power applications of coated conductors project," *Jpn. J. Appl. Phys.*, vol. 51, 2012.
- [20] M. Kumada *et al.*, "Development of 4 tesla permanent magnet," in *Particle Accelerator Conference, Chicago*, 2001.
- [21] "LNCMI Toulouse coils data." [Online]. Available: http://www.toulouse.lncmi.cnrs.fr/spip.php?page=article&id_article=94&lang=en.
- [22] S. Yoon, J. Kim, K. Cheon, H. Lee, S. Hahn, and S.-H. Moon, "26T 35mm all-GdBa₂Cu₃O_{7-x} multi-width no- insulation superconducting magnet," *Supercond. Sci. Technol.*, vol. 29, 2016.
- [23] S. Awaji *et al.*, "New 25 T Cryogen-Free Superconducting Magnet Project at Tohoku University," *IEEE Trans. Appl. Supercond.*, vol. 24, no. 3, 2014.
- [24] J. H. Liu *et al.*, "Development of YBCO insert for a 25 T all superconducting magnet," in *International conference on applied superconductivity and electromagnetic devices, Shanghai, China*, 2015.
- [25] J. Bascuñán, S. Hahn, Y. Kim, J. Song, and Y. Iwasa, "Design and Double-Pancake Coil Fabrication," *IEEE Trans. Appl. Supercond.*, vol. 24, no. 3, pp. 3–6, 2014.
- [26] Y. Wang, W. K. Chan, and J. Schwartz, "Self-protection mechanisms in no-insulation (RE)Ba₂Cu₃O_x high temperature superconductor pancake coils," *Supercond. Sci. Technol.*, vol. 29, 2016.
- [27] "Cedrat/Flux." [Online]. Available: <http://www.cedrat.com/en/software/flux.html>.
- [28] Y. Miyoshi *et al.*, "HTS coil test facility in a large bore 20 T resistive magnet at LNCMI," *IEEE Trans. Appl. Supercond.*, vol. 23, no. 3, 2013.
- [29] V. Braccini *et al.*, "Properties of recent IBAD–MOCVD coated conductors relevant to their high field, low temperature magnet use," *Supercond. Sci. Technol.*, vol. 24, 2011.
- [30] Y. Miyoshi, G. Nishijima, H. Kitaguchi, and X. Chaud, "High field I_c characterizations of commercial HTS conductors," *Phys. C*, vol. 516, 2015.
- [31] H. W. Weijers *et al.*, "High field magnets with HTS conductors," *IEEE Trans. Appl. Supercond.*, vol. 20, no. 3, 2010.
- [32] M. Solovyov *et al.*, "Non-uniformity of coated conductor tapes," *Supercond. Sci. Technol.*, vol. 26, 2013.
- [33] K. Tsuchiya *et al.*, "Critical Current Characterization of Commercial REBCO Coated Conductors at 4.2 and 77 K," *IEEE Trans. Appl. Supercond.*, vol. 27, no. 4, 2017.
- [34] Y. B. Kim, C. F. Hemstead, and A. R. Strnad, "Critical persistens currents in hard superconductors," *phys. Rev. Lett.*, vol. 9, 1962.
- [35] Z. Jiang *et al.*, "AC Loss Characteristics of YBCO Coated Conductors With Varying Magnitude of Critical Current," *IEEE Trans. Appl. Supercond.*, vol. 16, no. 2, 2006.

- [36] M. Xu, D. Shi, and R. F. Fox, "Generalized critical-state model for hard superconductors," *Phys. Rev. B*, vol. 42, no. 16, 1990.
- [37] T. Kiss, "In-field Characterization of Local I_c and n -indices as a Function of Longitudinal Coordinate in a Long- length GdBCO Coated Conductor," in *25th International Conference on Magnet Technology, Amsterdam*, 2017.
- [38] A. Badel, G. Escamez, and P. Tixador, "REBCO FCL modelling: Influence of local critical current non-uniformities on overall behavior for various tape architectures," *IEEE Trans. Appl. Supercond.*, vol. 25, no. 3, 2015.
- [39] Y. Xu *et al.*, "Distribution of AC loss in a HTS magnet for SMES with different operating conditions," *Phys. C*, vol. 494, 2013.
- [40] H. C. Jo *et al.*, "A Study on the Characteristic Evaluation of An HTS Coil with respect to the Winding Methods," *Supercond. Cryog.*, vol. 12, no. 4, 2010.
- [41] Y. Miyoshi *et al.*, "Performance tests of prototype high-field HTS coils in grenoble," *IEEE Trans. Appl. Supercond.*, vol. 25, no. 3, 2015.
- [42] "Hall sensor, Arepoc datasheet available at:" [Online]. Available: <http://www.arepoc.sk>.
- [43] "Strain Gages available :" [Online]. Available: http://www.kyowa-ei.com/eng/product/category/%0Astrain_gages/kfl/index.html.
- [44] T. Watanabe *et al.*, "Strengthening Effect of 'Yoroi-Coil Structure' Against Electromagnetic Force," *IEEE Trans. Appl. Supercond.*, vol. 25, no. 3, 2015.
- [45] "Available." [Online]. Available: <http://www.vishaypg.com/docs/11014/bond600.%0Apdf>.
- [46] C. C. Clickner *et al.*, "Mechanical properties of pure Ni and Ni-alloy substrate materials for Y-Ba-Cu-O coated superconductors," *Cryogenics*, vol. 46, 2006.
- [47] A. Otsuka and T. Kiyoshi, "High-field magnet design under constant hoop stress," *IEEE Trans. Appl. Supercond.*, vol. 18, no. 2, pp. 1529–1532, 2008.
- [48] J. Pitel, "Differences between two definitions of the critical current of HTS coils," *Supercond. Sci. Technol.*, vol. 26, 2013.
- [49] P. Tixador, *Les supraconducteurs*. Editions Hermes.
- [50] P. Jensen Ray, "Structural investigation of $\text{La}_{2-x}\text{Sr}_x\text{CuO}_{4+y}$: Following staging as a function of temperature," 2015.
- [51] "Open university, superconductivity course." [Online]. Available: <http://www.open.edu/openlearn/ocw/mod/oucontent/view.php?printable=1&id=2685>.
- [52] J. R. Waldram, *Superconductivity of metals and cuprates*, IOP. 1996.
- [53] G. Grissonnanche *et al.*, "Direct measurement of the upper critical field in a cuprate superconductor," 2013.
- [54] T. Sekitani, N. Miura, S. Ikeda, Y. H. Matsuda, and Y. Shiohara, "Upper critical field for optimally-doped $\text{YBa}_2\text{Cu}_3\text{O}_7$," *Phys. B*, vol. 346–347, 2004.
- [55] A. Goyal *et al.*, "High critical current density superconducting tapes by epitaxial deposition of

- YBa₂Cu₃O_x thick films on biaxially textured metals," *Appl. Phys. Lett.*, vol. 69, 1996.
- [56] V. S. Sarma, J. Eickemeyer, A. Singh, L. Schultz, and B. Holzapfel, "Development of high strength and strongly cube textured Ni-4.5% W/Ni-15% Cr composite substrate for coated conductor application," *Acta Mater.*, vol. 51, 2003.
 - [57] D. Verebelyi *et al.*, "Uniform performance of continuously processed MOD-YBCO-coated conductors using a textured Ni-W substrate," *Supercond. Sci. Technol.*, vol. 16, 2003.
 - [58] I. Iijima, N. Tanabe, O. Kohno, and Y. Iken, "In-plane aligned YBa₂Cu₃O_{7-x} thin films deposited on polycrystalline metallic substrates," *Appl. Phys. Lett.*, vol. 60, 1992.
 - [59] C. P. Wang, K. B. Do, M. R. Beasley, T. H. Geballe, and R. H. Hammond, "Deposition of in-plane textured MgO on amorphous Si₃N₄ substrates by ion-beam-assisted deposition and comparisons with ion-beam-assisted deposited yttria-stabilized-zirconia," *Appl. Phys. Lett.*, vol. 71, 1997.
 - [60] P. N. Arendt and S. R. Foltyn, "Biaxially Textured IBAD-MgO Templates for YBCO-Coated Conductors," *MRS Bull.*, vol. 29, 2004.
 - [61] C. Senatore, M. Alessandrini, A. Lucarelli, R. Tediosi, D. Uglietti, and Y. Iwasa, "Progresses and challenges in the development of high-field solenoidal magnets based on RE123 coated conductors," *Supercond. Sci. Technol.*, vol. 27, 2014.
 - [62] T. Takematsu *et al.*, "Degradation of the performance of a YBCO-coated conductor double pancake coil due to epoxy impregnation," *Phys. C*, vol. 470, 2010.
 - [63] S. Matsumoto *et al.*, "REBCO layer-wound coil tests under electromagnetic forces in an external magnetic field of up to 17.2 T," *IEEE Trans. Appl. Supercond.*, vol. 22, no. 3, 2012.
 - [64] U. P. Trociewitz *et al.*, "35.4 T field generated using a layer-wound superconducting coil made of (RE)Ba₂Cu₃O_{7-x} (RE = rare earth) coated conductor," *Appl. Phys. Lett.*, vol. 99, no. 20, 2011.
 - [65] A. Stenvall, R. Mikkonen, and P. Kováč, "Relation Between Transverse and Longitudinal Normal Zone Propagation Velocities in Impregnated MgB₂ Windings," *IEEE Trans. Appl. Supercond.*, vol. 19, no. 3, 2009.
 - [66] M. Stemmler, F. Merschel, M. Noe, and A. Hobl, "AmpaCity - Installation of advanced superconducting 10 kV system in city center replaces conventional 110 kV cables," in *International Conference on Applied Superconductivity and Electromagnetic Devices, Beijing, China*, 2013.
 - [67] J. F. Maguire *et al.*, "Progress and status of a 2G HTS power cable to be installed in the Long Island Power Authority (LIPA) grid," *IEEE Trans. Appl. Supercond.*, vol. 21, no. 3, 2011.
 - [68] G. Angeli, M. Bocchi, M. Ascade, V. Rossi, A. Valzasina, and L. Martini, "Development of Superconducting Devices for Power Grids in Italy: Update about the SFCL Project and Launching of the Research Activity on HTS Cables," *IEEE Trans. Appl. Supercond.*, vol. 27, no. 4, 2017.
 - [69] S. W. Schwenterly, S. P. Mehta, M. S. Walker, and R. H. Jones, "Development of HTS power transformers for the 21st century: Waukesha Electric Systems/IGC-SuperPower/RG&E/ORNL SPI collaboration," *Phys. C*, vol. 382, 2002.
 - [70] K. Funaki, M. Iwakuma, K. Kajikawa, M. Hara, J. Suehiro, and T. Ito, "for a 3MVA HTS Power Transformer," *IEEE Trans. Appl. Supercond.*, vol. 11, no. 1, 2001.

- [71] Y. Wang, J. Sun, Z. Zou, Z. Wang, and K. T. Chau, "Design and analysis of a HTS flux-switching machine for wind energy conversion," *IEEE Trans. Appl. Supercond.*, vol. 23, no. 3, 2013.
- [72] C. A. Luongo *et al.*, "Next generation more-electric aircraft: a potential application for hts superconductors," *IEEE Trans. Appl. Supercond.*, vol. 19, no. 3, 2009.
- [73] S. S. Kalsi, B. B. Gamble, G. Snitchler, and S. O. Ige, "The status of HTS ship propulsion motor developments," *IEEE Trans. Appl. Supercond.*, 2006.
- [74] "Electromagnet sketch." [Online]. Available: <http://www.ece.neu.edu/fac-ece/nian/mom/electromagnets.html>.
- [75] F. Debray, J. Dumas, C. Trophime, and N. Vidal, "DC high field magnets at the LNCMI," *IEEE Trans. Appl. Supercond.*, vol. 22, no. 3, 2012.
- [76] "MagLab resistive magnet record." [Online]. Available: <http://news.fsu.edu/news/science-technology/2017/08/22/national-maglab-achieves-new-world-record-strongest-resistive-magnet/>.
- [77] Cern, "100 years of Superconductivity, 50 years of superconducting magnets." [Online]. Available: https://indico.cern.ch/event/161849/contributions/1410628/attachments/188576/264762/100_years_supy_50_years_magnetsCERN.pdf.
- [78] Y. Yanagisawa *et al.*, "Operation of a 500 MHz high temperature superconducting NMR: Towards an NMR spectrometer operating beyond 1 GHz," *J. Magn. Reson.*, vol. 203, 2010.
- [79] J. R. Miller, "The NHMFL 45-T Hybrid Magnet System : Past , Present , and Future," *IEEE Trans. Appl. Supercond.*, vol. 13, no. 2, 2003.
- [80] C. Pes *et al.*, "Two-Dimensional and Three-Dimensional Mechanical Analyses of the Superconducting Outsert of the LNCMI Hybrid Magnet," *IEEE Trans. Appl. Supercond.*, vol. 26, no. 4, 2016.
- [81] P. Fazilleau, G. Aubert, C. Berriaud, B. Hervieu, and P. Pagnat, "Role and Impact of the Eddy Current Shield in the LNCMI-G Hybrid Magnet," *IEEE Trans. Appl. Supercond.*, vol. 26, no. 4, 2016.
- [82] G. E. Miller *et al.*, "Development of the Superconducting Outserts for the Series-Connected-Hybrid Program at the National High Magnetic Field Laboratory," *IEEE Trans. Appl. Supercond.*, vol. 18, no. 2, 2008.
- [83] D. W. Knight, *An Introduction to the Art of Solenoid Inductance Calculation with emphasis on radio-frequency applications*. 2016.
- [84] "NHMFL." [Online]. Available: <https://nationalmaglab.org/magnet-development/applied-superconductivity-center/plots>.
- [85] H. W. Weijers *et al.*, "Progress in the Development and Construction of a 32-T Superconducting Magnet," *IEEE Trans. Appl. Supercond.*, vol. 26, no. 4, 2016.
- [86] W. D. Markiewicz *et al.*, "Design of a Superconducting 32 T Magnet With REBCO High Field Coils," *IEEE Trans. Appl. Supercond.*, vol. 22, no. 3, 2012.
- [87] P. D. Noyes *et al.*, "Protection heater development for REBCO coils," *IEEE Trans. Appl.*

Supercond., vol. 22, no. 3, 2012.

- [88] S. Awaji *et al.*, “10T generation by an epoxy impregnated GdBCO insert coil for the 25T-cryogen-free superconducting magnet,” *Supercond. Sci. Technol.*, vol. 29, 2016.
- [89] Q. Wang *et al.*, “High magnetic field superconducting magnet system up to 25 T for ExCES,” *IEEE Trans. Appl. Supercond.*, vol. 23, no. 3, 2013.
- [90] Y. Iwasa, *Case studies in superconducting magnets: Design and operational issues (Second edition)*, Springer, 2009.
- [91] A. V. Polyakov, V. I. Shcherbakov, S. A. Shevchenko, and M. I. Surin, “Small layer-wound ReBCO solenoids,” *Phys. Procedia*, vol. 45, 2013.
- [92] F. Hornung *et al.*, “From Double-Pancake Coils to a Layer Wound 5 T RE BCO-HTS High Field Insert Coil Design,” *IEEE Trans. Appl. Supercond.*, vol. 27, no. 4, 2017.
- [93] S. Matsumoto *et al.*, “Generation of 24 T at 4.2 K using a layer-wound GdBCO insert coil with Nb3Sn and NbTi external magnetic field coils,” *Supercond. Sci. Technol.*, vol. 25, 2012.
- [94] S. W. Kim *et al.*, “Soldered double pancake winding of high temperature superconducting tape,” *IEEE Trans. Appl. Supercond.*, vol. 13, no. 2, 2003.
- [95] G. Dilasser, “Etude expérimentale et numérique des courants d’écrantage dans les aimants supraconducteurs à haute température critique REBCO,” 2017.
- [96] S. Hahn *et al.*, “A 78-mm/7-T Multi-Width No-Insulation ReBCO Magnet: Key Concept and Magnet Design,” *IEEE Trans. Appl. Supercond.*, vol. 24, no. 3, 2014.
- [97] T. Sung Lee *et al.*, “The effects of co-wound Kapton, stainless steel and copper, in comparison with no insulation, on the time constant and stability of GdBCO pancake coils,” *Supercond. Sci. Technol.*, vol. 27, 2014.
- [98] S. Yokoyama *et al.*, “Research and Development of the High Stable Magnetic Field ReBCO Coil System Fundamental Technology for MRI,” *IEEE Trans. Appl. Supercond.*, vol. 27, no. 4, 2017.
- [99] Y. Iwasa, “Protection of HTS magnets,” *Phys. C*, vol. 426–431, 2005.
- [100] J. H. Bae, H. Y. Park, B. Y. Eom, K. C. Seong, and S. K. Baik, “Thermal stability of YBCO coated conductor with different Cu stabilizer thickness,” *Phys. C*, vol. 470, 2010.
- [101] T. Minagawa, Y. Fujimoto, and O. Tsukamoto, “Study on Protection of HTS Coil Against Quench Due to Temperature Rise of Long Part of HTS Wires,” *IEEE Trans. Appl. Supercond.*, vol. 23, no. 3, 2013.
- [102] C. Oberly and Y. Iwasa, “Quench Protection of Magnets at Elevated Temperature,” in *DOE Wire Workshop, St. Petersburg, FL, USA*, 2005.
- [103] C. Lacroix, F. Sirois, and J.-H. F. Lupien, “Engineering of second generation HTS coated conductor architecture to enhance the normal zone propagation velocity in various operating conditions,” *Supercond. Sci. Technol.*, vol. 30, no. 6, 2017.
- [104] G. Nishijima, H. Kitaguchi, Y. Miyoshi, X. Chaud, F. Debray, and P. Tixador, “Transport Characteristics of a Bi-2223 Solenoid Coil in High Magnetic Fields,” *IEEE Trans. Appl. Supercond.*, vol. 24, no. 3, 2014.

- [105] K. J. Kim *et al.*, "Detection of AE signals from a HTS tape during quenching in a solid cryogen-cooling system," *Phys. C*, vol. 470, 2010.
- [106] F. Scurti and J. Schwartz, "Optical fiber distributed sensing for high temperature superconductor magnets," in *25th international conference on optical fiber sensors*, 2017.
- [107] Y. H. Choi, S. Hahn, J. B. Song, D. G. Yang, and H. G. Lee, "Partial insulation of GdBCO single pancake coils for protection-free HTS power applications," *Supercond. Sci. Technol.*, vol. 24, 2011.
- [108] N. Glowa, R. Wesche, and P. Bruzzone, "Quench Studies of YBCO Insulated and Noninsulated Pancake Coils," *IEEE Trans. Appl. Supercond.*, vol. 24, no. 3, 2014.
- [109] S. Hahn, D. K. Park, J. Bascuñán, and Y. Iwasa, "HTS pancake coils without turn-to-turn insulation," *IEEE Trans. Appl. Supercond.*, vol. 21, no. 3, 2011.
- [110] Y. Wang, H. Song, W. Yuan, Z. Jin, and Z. Hong, "Ramping turn-to-turn loss and magnetization loss of a No-Insulation (RE)Ba₂Cu₃O_x high temperature superconductor pancake coil," *J. Appl. Phys.*, vol. 121, 2017.
- [111] X. Wang, T. Wang, E. Nakada, A. Ishiyama, R. Itoh, and S. Noguchi, "Charging behavior in no-insulation REBCO pancake coils," *IEEE Trans. Appl. Supercond.*, vol. 25, no. 3, 2015.
- [112] K. Li *et al.*, "Coil Voltage Pulse at the Beginning of the Fast Discharge Operation of No-Insulation REBCO Coils," *IEEE Trans. Appl. Supercond.*, vol. 27, no. 4, 2017.
- [113] K. L. Kim *et al.*, "Effect of winding tension on electrical behaviors of a no-insulation ReBCO pancake coil," *IEEE Trans. Appl. Supercond.*, vol. 24, no. 3, 2014.
- [114] S. Kim, K. K. Seungyong Hahn, and D. Larbalestier, "Method for generating linear current-field characteristics and eliminating charging delay in no-insulation superconducting magnets," *Supercond. Sci. Technol.*, vol. 30, no. 3, 2017.
- [115] Y. H. Choi *et al.*, "The effects of partial insulation winding on the charge–discharge rate and magnetic field loss phenomena of GdBCO coated conductor coils," *Supercond. Sci. Technol.*, vol. 25, 2012.
- [116] T. Lecrevisse and Y. Iwasa, "A (RE)BCO Pancake Winding with Metal-as-Insulation," *IEEE Trans. Appl. Supercond.*, vol. 26, no. 3, 2016.
- [117] Y. Wang *et al.*, "Analysis and Comparison Between No-Insulation and Metallic Insulation REBCO Magnet for the Engineering Design of a 1-MW DC Induction Heater," vol. 27, no. 4, 2017.
- [118] R. Gupta *et al.*, "High field HTS R&D solenoid for muon collider," *IEEE Trans. Appl. Supercond.*, vol. 21, no. 3, 2011.
- [119] A. Voran, H. W. Weijers, W. D. Markiewicz, S. R. Gundlach, J. B. Jarvis, and W. R. Sheppard, "Mechanical Support of the NHMFL 32 T Superconducting Magnet," *IEEE Trans. Appl. Supercond.*, vol. 27, no. 4, 2017.
- [120] S. Hahn *et al.*, "Construction and Test of 7-T / 68-mm Cold-Bore," *IEEE Trans. Appl. Supercond.*, vol. 25, no. 3, 2015.
- [121] R. Gupta *et al.*, "Design , Construction , and Testing of a Large-Aperture High-Field," *IEEE Trans. Appl. Supercond.*, vol. 26, no. 4, 2016.

- [122] E. Pardo, J. Šouc, and J. Kováč, "AC loss in ReBCO pancake coils and stacks of them: modelling and measurement," *Supercond. Sci. Technol.*, vol. 25, 2012.
- [123] Y. Fu, O. Tsukamoto, and M. Furuse, "Copper stabilization of YBCO coated conductor for quench protection," *IEEE Trans. Appl. Supercond.*, vol. 13, no. 2, 2003.
- [124] H. M. Kim, J. Jankowski, H. Lee, J. Bascuñán, S. Fleshier, and Y. Iwasa, "Stability of bare and copper-laminated YBCO samples: Experimental & simulation results," *IEEE Trans. Appl. Supercond.*, vol. 14, no. 2, 2004.
- [125] Y. Wang *et al.*, "Detecting and describing the inhomogeneity of critical current in practical long HTS tapes using contact-free method," *Cryogenics*, vol. 47, 2007.
- [126] P. M. Leys, M. Klaeser, F. Schleissinger, and T. Schneider, "Angle-Dependent $U(I)$ Measurements of HTS Coated Conductors," *IEEE Trans. Appl. Supercond.*, vol. 23, no. 3, 2013.
- [127] Y. G. Kim, S. Hahn, K. L. Kim, D. G. Yang, and H. G. Lee, "Design consideration and optimization procedure for a no-insulation multi-width REBCO magnet," *Curr. Appl. Phys.*, vol. 15, 2015.
- [128] S. Iwai *et al.*, "Experimental Results of Screening-Current Field With 10-T Class Small REBCO Coil," *IEEE Trans. Appl. Supercond.*, vol. 26, no. 4, 2016.
- [129] H. Miyazaki *et al.*, "Screening-Current-Induced Magnetic Field of Conduction-Cooled HTS Magnets Wound With REBCO-Coated Conductors," *IEEE Trans. Appl. Supercond.*, vol. 27, no. 4, 2017.
- [130] K. Higashikawa *et al.*, "Scanning Hall-probe microscopy system for two-dimensional imaging of critical current density in RE-123 coated conductors," *Phys. C*, vol. 471, 2011.
- [131] T. Kiss *et al.*, "Comparison between Bi-2223 tape and RE-123 coated conductor from the view point of current transport properties influencing thermal stability," *Cryogenics*, vol. 80, 2016.
- [132] Y. Wang, S. Dai, X. Zhao, L. Xiao, L. Lin, and D. Hui, "Effects of critical current inhomogeneity in long high-temperature superconducting tapes on the self-field loss, studied by means of numerical analysis," *Supercond. Sci. Technol.*, vol. 19, 2006.
- [133] L. Rossi *et al.*, "Sample and length-dependent variability of 77 and 4.2 K properties in nominally identical RE123 coated conductors," *Supercond. Sci. Technol.*, vol. 29, 2016.
- [134] C. Senatore, C. Barth, M. Bonura, M. Kulich, and G. Mondonico, "Field and temperature scaling of the critical current density in commercial REBCO coated conductors," *Supercond. Sci. Technol.*, vol. 29, 2016.
- [135] A. Xu; *et al.*, "Angular dependent I_c at very high field in YBCO coated conductors, presented by J. Jaroszynski." Tallahassee.
- [136] E. J. McNiff, B. L. Brandt, S. Foner, L. G. Rubin, and R. J. Weggel, "Temperature anomalies observed in liquid 4He columns in magnetic fields with field-field-gradient products >21 T²/cm," *Rev. Sci. Instrum.*, vol. 59, 1988.
- [137] D. Abraimov *et al.*, "Double disordered YBCO coated conductors of industrial scale: high currents in high magnetic field," *Supercond. Sci. Technol.*, vol. 28, 2015.
- [138] A. Xu *et al.*, "Angular dependence of J_c for YBCO coated conductors at low temperature and very high magnetic fields," *Supercond. Sci. Technol.*, vol. 23, 2010.

- [139] A. V. Pan, I. A. Golovchanskiy, and S. A. Fedoseev, "Critical current density: Measurement vs. reality," *EPL (Europhysics Lett.)*, vol. 103, 2013.
- [140] A. L. Mbaruku, U. P. Trociewitz, X. Wang, and J. Schwartz, "Relationships between conductor damage, quenching and electromechanical behavior in YBCO coated conductors," *IEEE Trans. Appl. Supercond.*, vol. 17, no. 2, 2007.
- [141] Y. Yanagisawa *et al.*, "An ultra-thin polyimide insulation coating on REBCO conductors by electrodeposition produces a maximum overall current density for REBCO coils," *Phys. C*, vol. 495, 2013.
- [142] A. Badel, L. Antognazza, M. Therasse, M. Abplanalp, C. Schacherer, and M. Decroux, "Hybrid model of quench propagation in coated conductors for fault current limiters," *Supercond. Sci. Technol.*, vol. 25, 2012.
- [143] J. J. Himbele, "Contribution à l'étude d'un insert dipolaire supraconducteur à haute température critique pour accélérateur de particules, utilisent le concept de câble multi-rabans torsadé," 2016.
- [144] "Kyowa website." [Online]. Available: <http://www.kyowa-ei.com/>.
- [145] T. Benkel *et al.*, "Preliminary Tests and Margin Estimate for a REBCO Insulated 10 T Insert Under High Magnetic Field," *IEEE Trans. Appl. Supercond.*, vol. 27, no. 4, 2017.
- [146] F. Borgnolutti *et al.*, "Design Study of a 10-T REBCO Insert Solenoid," *IEEE Trans. Appl. Supercond.*, vol. 26, no. 4, 2016.
- [147] T. Benkel *et al.*, "REBCO Performance at High Field with Low Incident Angle and Preliminary Tests for a 10-T Insert," *IEEE Trans. Appl. Supercond.*, vol. 26, no. 3, 2016.
- [148] "Durnomag." [Online]. Available: <http://www.matthey.ch/en/home/>.